Probing Magnetostatic and Magnetotransport Properties of the Antiferromagnetic Iron Oxide Hematite

Dissertation zur Erlangung des Grades

„Doktor der Naturwissenschaften" (Dr. rer. nat.)

am Institut für Physik der

Johannes Gutenberg Universität Mainz

Andrew Ross

geb. in Guildford, United Kingdom

Mainz, 2020

JOHANNES GUTENBERG UNIVERSITÄT MAINZ

JG|U

Andrew Ross

Probing Magnetostatic and Magnetotransport Properties of the Antiferromagnetic Iron Oxide Hematite

Date of Oral Defence:February 16, 2021

Reviewers: Aus Datenschutzgründen entfernt / Removed due to data privacy

Supervisor: Aus Datenschutzgründen entfernt / Removed due to data privacy

MAINZ Supervisors: Aus Datenschutzgründen entfernt / Removed due to data privacy

Johannes Gutenberg-Universität Mainz
Kläui Lab,
Institut für Physik,
Staudingerweg 7,
55128, Mainz,
Deutschland

Abstract

With spin dynamics in the THz regime, a lack of stray fields and high stability in the presence of external magnetic fields, antiferromagnets have several benefits over ferromagnets for spintronics applications. The antiferromagnetic state can be used to store information and excitations of the magnetic order can be used for information transfer and processing in low power, high frequency devices. By utilising antiferromagnetic insulators with low magnetic damping as hosts for propagating spin currents, Joule heating in information transfer can be mitigated, overcoming one of the major limiting factors for device downscaling. The work presented in this thesis focusses on two aspects of antiferromagnetic spintronics for the development of real devices; utilising the spin Hall magnetoresistance to probe the magnetostatic properties of the antiferromagnetic state and demonstrating the long-distance transport of antiferromagnetic magnons for information transfer.

Making use of antiferromagnetic materials for magnetic bits relies on reliably encoding information into the antiferromagnetic state, parameterised by the Néel vector, which then needs to be read out. The equilibrium position of the magnetic state is determined by the present antiferromagnetic anisotropies which need to be overcome in a controlled manner in order to alter the magnetic state. Approaches to change the magnetic state include spin-orbit torques, thermal processes, strain or magnetic fields. In this thesis the insulating antiferromagnetic iron oxide hematite, the main component of rust, is studied. This readily available antiferromagnetic material is an attractive prospect for spintronics with a low magnetic damping and accessible spin flop field. By electrically detecting the equilibrium position of the Néel vector as a function of magnetic field and temperature in single crystals and thin films of this material, the key antiferromagnetic anisotropies are determined. Although the effective uniaxial anisotropy field in hematite thin films is found to be comparable to single crystals, the effective field generated by the antisymmetric exchange interaction is found to be four times larger due to distortions of the crystal lattice parallel to the c-axis. The growth of thin films of hematite on a substrate leads to an increase of the effective anisotropy field in the basal plane by two orders of magnitude. It is also found that the growth can also lead to a deviation of the antiferromagnetic anisotropy axis, introducing additional signals into the electrical measurements that need to be carefully considered when interpreting the equilibrium orientation of the Néel vector.

In pursuing fully antiferromagnetic devices where information transport, processing and storage all take place concurrently, information needs to be preserved over sufficient distances. However, previous reports have demonstrated that magnons coherently travel through antiferromagnets across nanometre distances before all the information is lost, which is too short for logic operations to occur. Therefore in this work this key issue

of spin-transport distance is investigated for the chosen hematite systems. The work reveals efficient long-distance spin transport in both the bulk and thin films of hematite, demonstrating that the low magnetic damping of this material is preserved even in thin films. The magnons are excited by either a polarised interfacial spin-bias or by local heating of the magnetic order and are found to be carried by different magnetic order parameters, either the Néel vector or a field induced magnetisation. This sharp distinction between the propagation mechanisms does not exist in ferromagnetic materials and presents an opportunity for the electrical excitation and detection of magnons without parasitic contributions from excess heat. In the presence of a multi-domain state, the magnon transport is observed to attenuate sharply due to the domain walls leading to scattering of incident magnons, where lower frequency magnons are observed to scatter more. Nevertheless, the intrinsic diffusion length scales of both thin film and bulk antiferromagnets are found to be orders of magnitude larger than previously reported. Overall these results demonstrate the feasibility and promise of antiferromagnetic hematite-based spintronic devices.

Zusammenfassung

Mit Spin-Dynamiken im THz-Regime, dem Fehlen von Streufeldern und der Stabilität gegenüber externen magnetischen Feldern haben Antiferromagneten zahlreiche Vorteile gegenüber Ferromagneten in spintronischen Anwendungen. Der antiferromagnetische Zustand kann für das Speichern von Informationen genutzt werden, während Anregungen der magnetischen Ordnung für Informationstransfer und -verarbeitung in Niedrigleistungs-, Hochfrequenzanwendungen gebraucht werden können. Durch die Verwendung von Antiferromagnetischen Isolatoren mit einer niedrigen magnetischen Dämpfung als Träger für Spinströme kann Joule'sche Verlustwärme im Informationstransfer vermieden werden, was einer der größten beschränkenden Faktoren in der Miniaturisierung von spintronischen Strukturen darstellt. Die in diesem Manuskript zusammengefasste Arbeit untersucht die magnetostatischen Eigenschaften des antiferromagnetischen Zustands und weist langreichweitigen Transport von informationstragenden Magnonen nach.

Die Verwendung von antiferromagnetischen Materialien als magnetische Bits setzt die zuverlässige Übersetzung von Informationen in antiferromagnetische Zustände voraus, ausgedrückt durch den Néel-Vektor, welcher ausgelesen werden können muss. Die Gleichgewichtsposition des magnetischen Zustands wird durch die Ausprägung antiferromagnetischer Anisotropien bestimmt, die in einer kontrollierten Art überwunden werden müssen, um den magnetischen Zustand zu manipulieren. Mechanismen um den magnetischen Zustand zu beeinflussen beruhen auf Spin-Orbit-torque, thermischen Prozessen, mechanischer Spannung oder Magnetfeldern. In dieser Arbeit wird der antiferromagnetische Isolator Hämatit, der Hauptbestandteil von Rost, untersucht. Dieses leicht verfügbare antiferromagnetische Material ist ein attraktiver Kandidat für Spintronik mit geringer magnetischer Dämpfung und leicht erreichbarem Spin-Flop-Feld. Durch die elektrische Bestimmung der Gleichgewichtslage des Néel-Vektors als Funktion des magnetischen Felds und der Temperatur in Einkristallen und dünnen Schichten dieses Materials werden die wichtigsten antiferrromagnetischen Anisotropien bestimmt. Auch wenn das effektive uniaxiale Anisotropiefeld in Hämatit Dünnschichten vergleichbar von dem mit Einkristallen ist, wird für das effektive Feld, das von antisymmetrischer Austauschwechselwirkung hervorgerufen wird, ein vierfach größerer Wert gefunden, weil die Kristallstruktur parallel zur c-Achse verzerrt ist. Das Wachstum von Hämatit Dünnschichten auf einem Substrat führt zu einer Steigerung des effektiven Anisotropiefelds in der Basalebene um zwei Größenordnungen. Außerdem wird eine Verschiebung der antiferromagnetischen Anisotropieachse auf Grund des Wachstums gefunden, die zu einem zusätzlichen Signal in den elektrischen Messungen führt, das bei der Bestimmung der Gleichgewichtsausrichtung des Néel-Vektors beachtet werden muss.

In der Entwicklung vollständig antiferromagnetischer Strukturen, in denen sowohl Informationsspeicherung, -transport als auch -verarbeitung stattfinden kann, müssen Informationen über ausreichend große Distanzen transportiert werden. Allerdings wurde Informationstransport mittels Magnonen bisher nur über Nanometerdistanzen nachgewiesen, was zu kurz für die praktische Umsetzung von logischen Operationen ist. Daher beschäftigt sich diese Arbeit mit diesem Kernaspekt der Reichweite von Spintransport im gewählten Hämatit-System. Die Untersuchung belegt effizienten langreichweitigen Spintransport in Volumenproben und dünnen Schichten von Hämatit, was beweist, dass die niedrige magnetische Dämpfung dieses Materials auch für dünne Filme erhalten bleibt. Die Magnonen werden entweder von polarisiertem Grenzschicht-Spinbias oder von lokalen Aufheizphänomenen der magnetischen Ordnung erzeugt und beruhen auf veschiedenen magnetischen Ordnungsparametern, entweder dem Néel-Vektor oder der feldinduzierten Magnetisierung. Diese scharfe Abtrennung zwischen den Ausbreitungsmechanismen ist in Ferromagneten nicht möglich und stellt deshalb eine Chance für den elektrischen Nachweis und die Erzeugung von Magnonen ohne parasitäre Beiträge von Aufheizphänomenen dar. Im Falle von Mehrdomänenzuständen, fällt der Magnonentransport scharf ab, weil die Domänenwände einfallende Magnonen streuen, insbesondere niederfrequente Magnonen. Nichtsdestotrotz ist die intrinsische Diffusionslänge sowohl von dünnen Schichten als auch des Volumenmaterials mehrere Größenordnungen länger als in allen anderen bekannten Materialien. Diese Ergebnisse belegen die Machbarkeit und positiven Eigenschaften Hämatit-basierter spintronischer Anwendungen.

Contents

Abbreviations

AFM - Antiferromagnet

AFMI - Antiferromagnetic Insulator

AMR - Anisotropic Magnetoresistance

AHE - Anomalous Hall effect

BEC - Bose Einstein Condensation

DMI - Dzayaloshinskii-Moriya Interaction

EA - Easy-Axis

EBL - Electron Beam Lithography

FM - Ferromagnet

FMI - Ferromagnetic Insulator

FMR - Ferromagentic Resonance

GMR - Giant Magnetoresistance

HM - Heavy Metal

HP - Holstein-Primakoff

ISHE - Inverse Spin Hall Effect

LH - Linear Horizontal

LV - Linear Vertical

NM - Normal Metal

MI - Magnetic Insulator

OHE - Ordinary Hall Effect

OMR - Ordinary Magnetoresistance

PEEM - Photoemission Electron Microscopy

PLD - Pulsed Laser Deposition

RSM - Reciprocal Space Map

SHE - Spin Hall Effect

SMR - Spin Hall Magnetoresistance

SOI - Spin Orbit Interaction

SSE - Spin Seebeck Effect

SSF - Spin Superfluid

STT - Spin Transfer Torque

XAS - X-ray Absorption Spectroscopy

XMCD - X-ray Magnetic Circular Dichromism

XMLD - X-ray Magnetic Linear Dichroism

YIG - Yttrium Iron Garnet ($Y_3Fe_5O_{12}$)

1 Introduction

Society's constant desire for more information and increased communication technology capacities has led to ever increasing amounts of computing power that is always accessible. Our need for more computation power in smaller devices is currently satisfied by the constant downscaling of transistors as the basic components of microprocessors. However, with the majority of energy consumption for a typical data centre being diverted to cooling [1], this process is approaching its limit due to, amongst other factors, unacceptable Joule heating [2]. Alternatives to conventional electronics are therefore being sought to allow for smaller, more powerful components with reduced Joule heating. The field of spintronics seeks to include the spin degree of freedom of the electron to improve the efficiency and overcome limitations of conventional electronics for information transport, processing and storage [3]. The inclusion of the spin degree of freedom opens potential advantages such as reduced power consumption and non-volatility [3]. Spintronics marked a turning point in the development of modern computing three decades ago, with the discovery of giant magnetoresistance (GMR) [4, 5]. Small, magnetic junctions with two clearly defined resistance states could then be used for information storage and the development of hard disk drives. A decade later, the all electrical control of the magnetic state of such junctions by spin-transfer torque (STT) led to the development of magnetic random access memory (MRAM) [6].

These initial concepts of GMR and STT were centred around spin-polarised charge currents, carrying information on both the spin and the charge of the electron. There also exists the possibility of pure spin currents, conveying solely information on the electron spin without the net motion of electrons and are beneficial for the development of increased energy efficiency. Pure spin currents can further be categorised into those mediated by diffusive electron motion and those carried by propagating spin wave excitations possible also in insulating magnetic systems [7, 8]. This second category further benefits from significant reductions in charge motion and Ohmic losses, especially if one utilises magnetic insulators where no charge motion is possible. The focus on spin wave excitations in magnetic insulators forms forms the sub-field of spintronics known as *magnonics*, where propagating magnons are excited and manipulated [8, 9], even showing interference effects. Magnons are the quasiparticles representing quantised spin wave excitations in magnetic systems and open up a range of possibilities for wave based computing where the phase of the spin waves introduce an additional information

carrier. The interaction of spin currents conceivably allows one to implement not only the transport of angular momentum via magnons but also logic operations and data processing through interference effects. By ultimately utilising magnons for both information transfer but also data processing, the energy loss that accompanies the conversion of magnons into electrical signals can be mitigated but requires materials with low magnetic damping that can host magnons across sufficient distances.

Aside from Joule heating preventing further downsizing of components, even with the discovery of GMR and tunnelling magnetoresistance, the focus on ferromagnetic materials gives rise to further problems. One problem comes from the magnetic stray fields produced by the ferromagnetic layers interfering with the magnetic state between neighbouring magnetic bits leading to data loss. A ubiquitous class of magnetic materials, that has until recently been overlooked, are those with antiferromagnetic ordering. One of the leading figures in developing the theory of antiferromagnetism, Louis Néel, commented when accepting his Nobel prize in 1970 that, whilst antiferromagnets "*are extremely interesting from the theoretical viewpoint*" they "*do not seem to have any applications*" [10]. However, these materials have many benefits over their ferromagnetic counterparts. They have no stray fields and superior stability in the presence of external magnetic fields. They further benefit from spin dynamics in the hundreds of GHz to THz regime, rather than the low GHz of ferromagnetic materials. Although these high frequencies will not lead to faster information transfer in magnonic systems, they will greatly increase the switching speeds of magnetic bits for information processing and storage [11]. By combining magnon spintronics and antiferromagnetic materials, i.e. *antiferromagnetic magnon spintronics*, the potential for reduced Joule heating alongside faster switching speeds has promoted great interest in antiferromagnetic insulators in recent years. However, the key advantages of antiferromagnetic materials also give rise to key problems; the stability of the magnetic order in externals fields makes altering the magnetic state challenging whilst accessing information on the internal magnetic anisotropies, especially in thin film antiferromagnets, that need to be thoroughly understood for applications is equally challenging. In the course of this thesis, great progress has been made in the field of antiferromagnetic spintronics, focussing on the manipulation of the antiferromagnetic order by, for example, spin-orbit torques [r4, 12] or strain [r18], whilst the magnetic state of antiferromagnetic components can be read by novel, interfacial magnetoresistance effects [r1, r9, 13–17]. However, reliable reading and writing of the antiferromagnetic order relies on a detailed understanding of the underlying antiferromagnetic anisotropies, where few reliable methods exist to access this information for bulk antiferromagnets and even fewer that are applicable to the thin film regime. With low magnetic damping [18, 19], insulating antiferromagnets have the potential for long distance magnon transport, with even dissipationless spin transport having been theoretically studied [20–23]. However experimentally evaluated magnon diffusion lengths in antiferromagnets have placed upper limits of only a few nanometers before all information is lost, presenting a considerable block to further progress, raising the question of whether long distance magnon transport is possible in antiferromagnets. The experimental work and results presented in this thesis contribute to these two key outstanding points; i) probing the antiferromagnetic anisotropies of bulk and thin film antiferromagnets through surface sensitive measurements and ii) demonstrating the generation, long distance transport and detection of magnonic spin currents in an antiferromagnetic insulator, albeit the magnon transport exists in the diffusive rather than non-diffusive regime.

This thesis is organised as follows, Ch. 2 will give a brief introduction to the concepts of magnetism in solids that is pertinent to the work in this thesis. The various energy terms that define the magnetic state of a solid will be discussed. The main material class of interest, antiferromagnets, will be introduced before finishing with an introduction to antiferromagnetic magnons. Moving on, Ch. 3 will discuss the spin transport phenomena that are utilised in the course of this thesis. This chapter starts by introducing the spin Hall effect and spin Hall magnetoresistance, a brief introduction to the thermal excitation of magnons by the spin Seebeck effect and an overview of the transport of magnons rounds out the discussion. An introduction to the main antiferromagnetic material of interest for this thesis, α-Fe_2O_3 (hematite) comes in Ch. 4 alongside an introduction to the experimental techniques regarding sample fabrication, characterisation and measurement setups used in this thesis. The experimental results obtained in this thesis are split into three chapters. Ch. 5 looks at the extraction of antiferromagnetic anisotropies by making use of the surface sensitive technique of spin Hall magnetoresistance finding good agreement with measurements of the key anisotropies by other techniques before being applied to thin film antiferromagnets where the anisotropies are unknown. These findings are presented in Ref. [r10] and Ref. [r14]. The long distance transport of information by magnons is shown in Ch. 6 in a bulk antiferromagnet, where the spin diffusion lengths for this material are demonstrated to be exceptionally large. The efficient transport of magnons relies on manipulating the orientation of the antiferromagnetic order parameter with respect to an interfacial spin accumulation between the insulating hematite and Pt wires, results which are published in Ref. [r3]. Ch. 7 then seeks to demonstrate the long distance transport of magnons in thin film hematite given that one would aim to functionalise thin films for future antiferromagnetic spintronic devices. Contrary to previous reports on the effective spin diffusion lengths of thin film antiferromagnets, a spin current persists over micrometers with effective diffusion lengths of hundreds of nanometers demonstrating that the magnetic damping of thin film hematite is still low. It is further found that the presence of an antiferromagnetic multi-domain structure attenuates the magnonic current with a critical threshold for scattering set by the frequency of the incident magnon. The results of this chapter are summarised in Ref. [r15]. Finally, Ch. 8 will summarise the main conclusions of this thesis and provide an outlook for potential future work.

2

Concepts of Magnetism

This chapter will focus on the basic concepts of magnetism that are of importance for the work performed in the course of this thesis. The magnetic susceptibility, a parameter that characterises the magnetic response of a material to a magnetic field, will be briefly introduced before a discussion of the magnetic free energy. With the key energy terms established, the materials of interest, antiferromagnets, will be introduced. Towards the end of the chapter, the quanta of magnetic excitation known as a magnon and the effect of a magnetic field on the antiferromagnetic dispersion relation will be introduced and explained.

2.1 Magnetic Susceptibility

All materials exhibit a form of magnetism known as diamagnetism, characterised by the negative response to a magnetic field $\boldsymbol{H}$ the magnetic susceptibility $\chi = \boldsymbol{H}/\boldsymbol{M}$ where $\boldsymbol{M}$ is the induced magnetisation. This negative response indicates that the induced magnetisation acts in order to oppose the impact of the applied field. Some materials also possess a form of magnetism known as paramagnetism that dominates over the diamagnetic contribution, characterised by an alignment of the induced magnetisation in an external field and thus $\chi > 0$. Furthermore, in some systems, the spontaneous alignment of the magnetic moments in the absence of a magnetic field can occur, leading to a long range magnetic order. The simplest type of spontaneously magnetised material has all of the magnetic moments aligned with both each other and the magnetic field. This type of magnetic order is known as ferromagnetism. Here the relationship between the magnetisation $\boldsymbol{M}$ and the applied field $\boldsymbol{H}$ is more complicated than in the case of dia- and paramagnets. When the magnetic field is removed, the material can maintain a net magnetic moment, which depends on the field history of the material [24, 25].

Another long range magnetic order that can emerge in the absence of an applied magnetic field is antiferromagnetism. Here, in the case of collinear antiferromagnetism, the moments align antiparallel to one another resulting in long range order but no long range, net magnetic moment. In this case, the response of the antiferromagnetic order to an applied field varies depending on the direction of the field relative to any preferred magnetic axis that may exist, as well as the magnitude of the applied field. A further magnetic ordering worth mentioning is ferrimagnetism. In this ordered state, there are

two magnetic sublattices $\boldsymbol{M}_1$ and $\boldsymbol{M}_2$, just like in an antiferromagnet, but now $\boldsymbol{M}_1 \neq \boldsymbol{M}_2$ and thus a sizeable net moment exists.

These long range magnetically ordered states can be destroyed by thermal fluctuations, allowing one to define a critical temperature below which spontaneous magnetic order is obtained and above which, paramagnetic behaviour dominates. In ferromagnets and ferrimagnets, this critical temperature is known as the Curie temperature, whilst for antiferromagnets, it is known as the Néel temperature. It is worth noting that ferro-, antiferro- and ferrimagnetism are by no means the only possible forms of magnetic order, but they are certainly the most prolific and of most relevance for the remainder of this thesis. Such other forms of magnetic order are discussed, for example, in Refs. [24] or [25].

Fig. 2.1a) presents a schematic for ferromagnetic order, where the arrows represent the magnetic moment of a single atom in the lattice. Fig. 2.1b) shows the same for a (collinear) antiferromagnetic material, with the different colours indicating different directions of the magnetic moment. A similar representation of a ferrimagnet would be similar to the antiferromagnet but the arrows of each colour would differ in size.

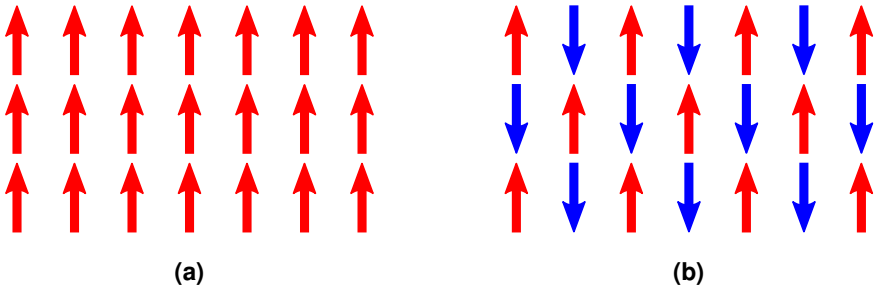

Figure 2.1: a) Sketch of a ferromagnetically ordered lattice with all magnetic moments aligned parallel to neighbouring moments. b) An antiferromagnetically ordered crystal lattice, where moments are aligned anti-parallel to each neighbouring moment.

2.2 Magnetic Free Energy

Regardless of the material composition, magnetic ordering originates from the electronic structure of the atoms within a solid. The ground state is determined by the magnetic free energy of the system, which is influenced by numerous factors, both intrinsic and external. The magnetic free energy $\mathcal{F}$ is given by,

$$\mathcal{F} = \mathcal{F}_{ex} + \mathcal{F}_{ani} + \mathcal{F}_{Zeeman} + ... \tag{2.1}$$

The various contributions to this magnetic energy to be discussed here, cover the dominant terms that are required to describe the antiferromagnetic materials investigated in the course of this thesis. These include the exchange energy ($\mathcal{F}_{ex}$), the Zeeman energy ($\mathcal{F}_{Zeeman}$), and the magnetic anisotropy energy ($\mathcal{F}_{ani}$), although other terms can be of importance; in particular the magnetic free energy for a ferromagnetic material requires the consideration of the magnetostatic dipolar energy [24, 25] . Whilst magnetostriction can be included as a term in the magnetic free energy, due to its importance in stabilising antiferromagnetic domains in thin films, the discussion of this energy will be reserved for Sec. 2.3.7 where it is of direct relevance. There is also an antisymmetric exchange interaction that can be included, but this will be discussed in Sec. 2.3.6.

2.2.1 Exchange Interaction

The exchange interaction acts between electron spins, allowing them to couple to one another, resulting in the formation of long range magnetic order. It arises due to both the classical Coulomb repulsion between the electrons and the quantum mechanical Pauli principle forbidding two fermions from occupying identical quantum states, i.e. both electrons cannot be in the same place with the same quantum number of spin. This interaction is the strongest contribution to the free energy and dominates the magnetic structure of antiferromagnetic materials. Although magnetic order is a macroscopic property, its origin lies in quantum mechanics and the overlapping wavefunctions of the individual electrons, thus a Hamiltonian can be derived to describe the exchange interaction. The derivation of this Hamiltonian $\mathcal{H}_{ex}$ presented here follows closely that found in Ref. [25].

A simple manifestation of the exchange interaction comes about in a H_2 molecule with a single electron attributed to each atom in the lowest atomic orbital, the 1s shell. The spatial position of each electron is then described by the quantum mechanical wavefunctions $\psi_1(\boldsymbol{r}_1)$ and $\psi_2(\boldsymbol{r}_2)$, where $\boldsymbol{r}_i$ describes the spatial coordinates of each electron. Furthermore, the spin state of each electron, whether up (↑) or down (↓), is described by the wavefunctions $\chi_1(\boldsymbol{s}_1)$ and $\chi_2(\boldsymbol{s}_2)$. The total system is then described by the product of the individual wavefunctions $\Psi(1,2)$. As electrons are indistinguishable particles, the total electron density must remain constant when the electrons are interchanged with one another, which can only be true if the total combined wavefunction is antisymmetric and

$$\Psi(1,2) = -\Psi(2,1). \tag{2.2}$$

This then places the system in a state with an antisymmetric singlet (symmetric triplet) spin state, χ_a (χ_s), alongside a symmetric (antisymmetric) spatial state, ψ_s (ψ_a), described further by the spin quantum number of the system of S=0 (S=1). The spatial wavefunctions can be written

$$\psi_s = \frac{1}{\sqrt{2}}(\psi_1 + \psi_2) \qquad \psi_a = \frac{1}{\sqrt{2}}(\psi_1 - \psi_2), \tag{2.3}$$

and the spin wavefunctions as,

$$\begin{aligned} \chi_s = |\uparrow_1,\uparrow_2\rangle; \quad \frac{1}{\sqrt{2}}\left(|\uparrow_1,\downarrow_2\rangle + |\downarrow_1,\uparrow_2\rangle\right); \quad |\downarrow_1,\downarrow_2\rangle, \\ \chi_a = \frac{1}{\sqrt{2}}\left(|\uparrow_1,\downarrow_2\rangle - |\downarrow_1,\uparrow_2\rangle\right). \end{aligned} \tag{2.4}$$

The two complete wavefunctions describing the two electrons in either the singlet, Ψ_S, or triplet, Ψ_T, state are then,

$$\Psi_S = \psi_s\chi_a \quad \text{and} \quad \Psi_T = \psi_a\chi_s. \tag{2.5}$$

A Schrödinger equation can be constructed as $\mathcal{H}(1,2)\Psi(1,2) = \mathcal{E}\Psi(1,2)$ for a Hamiltonian $\mathcal{H}$ and energy $\mathcal{E}$ in order to find the eigenstates corresponding to the energies of the two states,

$$\mathcal{E}_S = \int \Psi_S^*\mathcal{H}\Psi_S d\boldsymbol{r}_1 d\boldsymbol{r}_2 \quad \text{and} \quad \mathcal{E}_T = \int \Psi_T^*\mathcal{H}\Psi_T d\boldsymbol{r}_1 d\boldsymbol{r}_2. \tag{2.6}$$

The energy difference between the two states, known as the exchange integral, is then given as,

$$\mathcal{J} = \frac{\mathcal{E}_S - \mathcal{E}_T}{2} = \int \psi_1^*(\boldsymbol{r}_1)\psi_2^*(\boldsymbol{r}_2)\mathcal{H}\psi_1(\boldsymbol{r}_1)\psi_2(\boldsymbol{r}_2)d\boldsymbol{r}_1 d\boldsymbol{r}_2. \tag{2.7}$$

The total exchange energy between the two electrons can be written in the form,

$$\mathcal{E} = -2\frac{\mathcal{J}}{\hbar^2}\boldsymbol{s}_1 \cdot \boldsymbol{s}_2, \tag{2.8}$$

where $\boldsymbol{s}_1$ and $\boldsymbol{s}_2$ are the spins of the two electrons connected by the exchange integral and $\hbar$ is the reduced Planck's constant. The product $\boldsymbol{s}_1 \cdot \boldsymbol{s}_2$ can be expanded to $\frac{1}{2}[(\boldsymbol{s}_1 + \boldsymbol{s}_2)^2 - \boldsymbol{s}_1^2 - \boldsymbol{s}_2^2]$ with eigenvalues of either $\frac{1}{4}\hbar^2$ or $-\frac{3}{4}\hbar^2$ depending on whether the combined spin quantum number for the two electrons is 1 or 0. This then leads to the simple effective Hamiltonian $\mathcal{H} = (E_S + 3E_T)/4 - 2\mathcal{J}\boldsymbol{S}_1\boldsymbol{S}_2$. The first term is constant, allowing us to define the spin dependent exchange Hamiltonian as,

$$\mathcal{H}_{ex} = -2\mathcal{J}\hat{S}_1 \cdot \hat{S}_2, \tag{2.9}$$

where $\hat{S}_1$ and $\hat{S}_2$ are now dimensionless spin operators for each electron. It should be noted that this only considers the interactions between neighbouring electrons but it can easily be generalised for a lattice to include a sum over all possible pairs of atoms. In this case, $\mathcal{J}$ no longer takes a constant value but varies for different pairs of electrons, resulting in the exchange Hamiltonian for the so-called Heisenberg model,

$$\mathcal{H}_{ex} = -2\sum_{i>j} \mathcal{J}_{ij}\boldsymbol{S}_i \cdot \boldsymbol{S}_j, \tag{2.10}$$

where $i > j$ avoids double counting the same pair of spins[1].

Within a single atom, the exchange integral is generally positive in order minimise the Coulomb energy between two electrons. However, between neighbouring atoms, the electrons no longer have to remain localised to a single atom and the joint state serves to minimise the total energy. The value of $\mathcal{J}$ determines whether the interatomic exchange coupling is ferromagnetic, $\mathcal{J} > 0$, with a parallel alignment of the spins or antiferromagnetic, $\mathcal{J} < 0$, where an antiparallel alignment is preferred. However, calculating the exchange integral in systems with many delocalised electrons, orbital degeneracies, and competing exchange mechanisms proves challenging. It is instead often easier to adopt phenomenological descriptions of the exchange interactions supported by experimental measurements.

It is also worth noting that in real systems, there are many particles and thus many spins present, making a quantum mechanical approach impractical in such an ever increasing dimensional Hilbert space and instead a continuum approximation can be made [24].

2.2.1.1 Exchange in Oxides: Superexchange

The primary focus of this work is on insulating magnetic oxides where the electrons are strongly localised and hence, due to the short range nature of the exchange interaction, there is very little overlap between the electron wavefunctions of the magnetic ions.

[1] Frequently the exchange Hamiltonian can be defined without the factor of 2 and by counting each pair of spins twice.

Instead, the exchange interaction between the unpaired electrons of the ions responsible for the magnetic ordering is facilitated through a hybridisation with the 2p orbitals of the interceding oxygen atoms. This gives rise to a so-called *superexchange* interaction that can also be described by a Heisenberg Hamiltonian and commonly leads to antiferromagnetic and ferrimagnetic ordering rather than ferromagnetic ordering, although ferromagnetic ordering by superexchange is possible [26, 27]. In other words, there is a long-range exchange interaction between two non-neighbouring magnetic ions mediated by a non-magnetic ion between them. Fig. 2.2a shows an example of a superexchange bond for two Fe atoms via an oxygen atom. The superexchange interaction between two

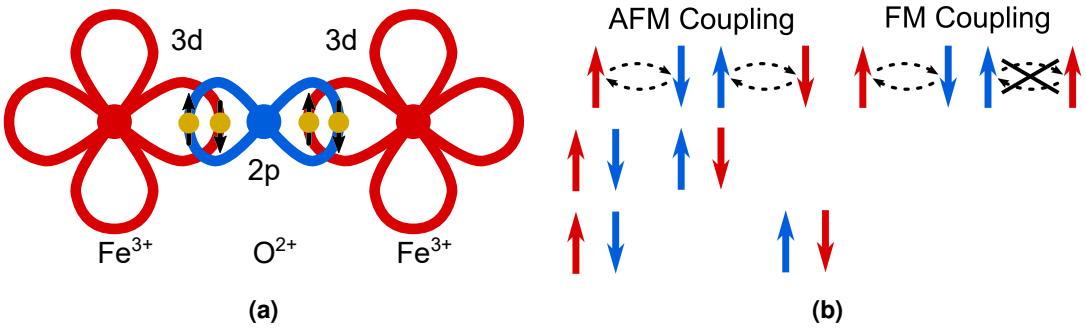

Figure 2.2: a) Example of the indirect superexchange interaction between the 3d atomic orbitals of two Fe atoms mediated by the 2p atomic orbital of an oxygen atom. b) Antiferromagnetic ordering is preferred due to the Pauli exclusion principle forbidding the electrons from occupying the same spin state.

atoms of Fe, a transition metal with an unpaired electron in the 3d orbital, and oxygen (for example), leads to the creation of a $3d^{n+1}2p^5$ state and the virtual exchange of two electrons from the oxygen 2p orbital to the unoccupied 3d orbitals of the iron. Due to the Pauli exclusion principle, antiferromagnetic ordering is preferred as it allows for the complete delocalisation of the electrons across the entire system, whilst ferromagnetic ordering would suppress electron hopping between the Fe atoms, as demonstrated in Fig. 2.2b. The strength and sign of the superexchange interaction is determined from the orbital degeneracy of the 3d states, as well as their occupation, alongside the interatomic distance and bond angle between the two metal atoms via the oxygen [26, 27]. This means that superexchange can even give rise to ferromagnetic alignment of the magnetisation depending on the symmetry and strength of the different exchange paths available in the material, but this is rare. An easy way to visualise this would be if, instead of a parallel positioning of the two Fe atoms and O atom in Fig. 2.2a, the two Fe atoms made a 90° angle with the O atom at the apex. In this case, the superexchange would be ferromagnetic as there is no overlap between the orbitals of the O atom and the 3d shell of the lower Fe atom.

2.2.2 Zeeman Interaction

When a single magnetic dipole $\boldsymbol{m}$ is situated in a static, external field $\boldsymbol{H}$ it experiences a torque given by,

$$\Gamma = \boldsymbol{m} \times \boldsymbol{H}. \tag{2.11}$$

By integrating across all angles between these two variables, we obtain the general expression for the potential energy of a single dipole in an external field [24]. The Zeeman

interaction for a magnetic material is then the net energy of the average magnetic moment, $\boldsymbol{M}$, in an external field and describes how the magnetisation is influenced by an external field. The form of this term,

$$\mathcal{E}_{Zeeman}\left(\boldsymbol{r}\right) \propto \boldsymbol{M}(\boldsymbol{r}) \cdot \boldsymbol{H}(\boldsymbol{r}), \tag{2.12}$$

demonstrates how the parallel alignment of the magnetisation in a ferromagnet and the external field leads to a minimum in the energy.

In a two sublattice collinear antiferromagnet however, this minimum instead occurs for the magnetic order aligned perpendicular to the field through minimising the Zeeman energy on both sublattices concurrently, providing there is no magnetic anisotropy delineating a preferred direction of the antiferromagnetic ordering and the applied magnetic field is not large enough to overcome the exchange energy between the sublattices. The case of an antiferromagnet with anisotropy will be covered in more detail in Sec. 2.3.5. In the absence of other contributions to the magnetic energy, in other words when a material lacks a long range magnetic order, this term describes the paramagnetic response to a magnetic field.

2.2.3 Magnetic Anisotropy

The Heisenberg form of the exchange energy is inherently invariant with respect to the coordinate system that one chooses. However, in magnetic materials, it is experimentally found that there are preferred crystallographic directions for the magnetic order, an effect known as magnetic anisotropy, with the preferred directions termed the *easy* directions or easy axes. The other directions, where it is harder to align the magnetic order, are known unsurprisingly as *hard* directions. This anisotropy is related to the crystal structure of the magnetic material, where a combination of the lattice and orbital moment via spin orbit coupling leads to changes in the wavefunction overlap between neighbouring spins in different directions. Such anisotropy leads to an additional energy contribution related to the work required to make the magnetic order lie along a direction other than the preferred easy direction. If there is a single preferred direction, i.e. a uniaxial anisotropy, the anisotropy energy depends on the angle between the magnetic order and the axis of anisotropy ϑ and has the form,

$$F_K = K_1 \sin^2 \vartheta + K_2 \sin^4 \vartheta, \tag{2.13}$$

where K_1 and K_2 are the first and second order anisotropy constants representing temperature dependent energy densities that tends to zero at the critical temperature for magnetic ordering [24, 25, 28]. In ferromagnetic materials, anisotropy can also arise from the shape of the sample, but this is not relevant for antiferromagnetic materials, the focus of this thesis. Information on the impact of this can be found in Refs. [24] and [25].

By minimising Eqn. 2.13, a phase diagram based on the values of K_1 and K_2 can be created, as depicted in Fig. 2.3. From this figure it is clear that the sign of the anisotropy constants define whether an antiferromagnetic material is one of the two most common structures, easy-plane or easy-axis. Ignoring the more exotic states represented, a general statement can then be made; positive anisotropy constants lead to an easy-axis antiferromagnet, whilst negative anisotropy constants result in an easy-plane antiferromagnet.

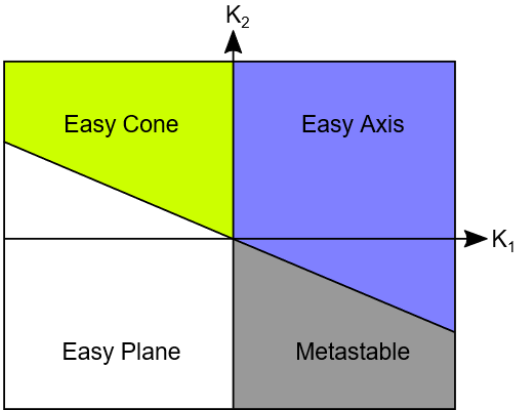

Figure 2.3: Magnetic phase diagram of different values of the anisotropy constants K_1 and K_2. Depending on the relative values, different anisotropy states will be stabilised. Fig. adapted from Ref. [24].

2.3 Antiferromagnetism

Having introduced the relevant energy terms for long range magnetic ordering, we now turn our attention to describing in more detail the material class of primary interest for this thesis, antiferromagnets (AFMs). As mentioned, AFMs are materials that have a spontaneous, long range magnetic order. However, they are crucially different from ferromagnets in that the net magnetic moment of the magnetic unit cell is zero, or has a value far smaller than the sum of the moments. Whilst antiferromagnetism normally refers to the complete absence of a net magnetic moment, materials with long-range, antiferromagnetic-like ordering with an additional average moment far smaller than the moment of a single ion per magnetic unit cell can also exist, the origin of which is discussed in Sec. 2.3.6 [29]. This type of AFM is termed a *weak ferromagnet*, and is usually closely related to compensated AFMs, sharing many similar properties and can be described in a similar way. Antiferromagnetic ordering exists up to the Néel temperature T_N above which the thermal fluctuations of the spins overcome the ordering and the material becomes paramagnetic.

Antiferromagnetism was discussed separately by Landau [30] and Néel [31–33] with respect to abnormal behaviour seen in some presumed paramagnetic materials. Both proposed a new magnetic ordering; for Néel, this was a staggered order where each magnetic moment is aligned antiparallel to its nearest neighbours (G-type antiferromagnetism), whilst Landau favoured layers of parallel moments, aligned antiparallel to neighbouring layers (A-type antiferromagnetism). Since these first discussions, numerous antiferromagnetic structures have been observed including both of these, with the first being reported by Shull and Smart, where they observed that the magnetic cell of MnO was twice that of the crystallographic cell by neutron scattering measurements [34].

The remainder of this section will introduce a phenomenological description of antiferromagnetism and the effect of a magnetic field on the antiferromagnetic ordering. Despite a lack of a demagnetising field that is relevant for ferromagnetic domain formation [24, 25], it has been observed that antiferromagnetic domains can also exist. The formation of these will also be discussed at the end of the section.

2.3.1 Types of Antiferromagnetism

Whilst on a global scale, antiferromagnetic materials all demonstrate a lack of net magnetic moment, how the moments are aligned relative to each other within the magnetic unit cell can vary greatly. There are several common types of three dimensional antiferromagnetic ordering, as well as the possibility for materials to display one dimensional chains of antiferromagnetically ordered spins [35], two dimensional layered antiferromagnets [36, 37] and two dimensional lattices [38].

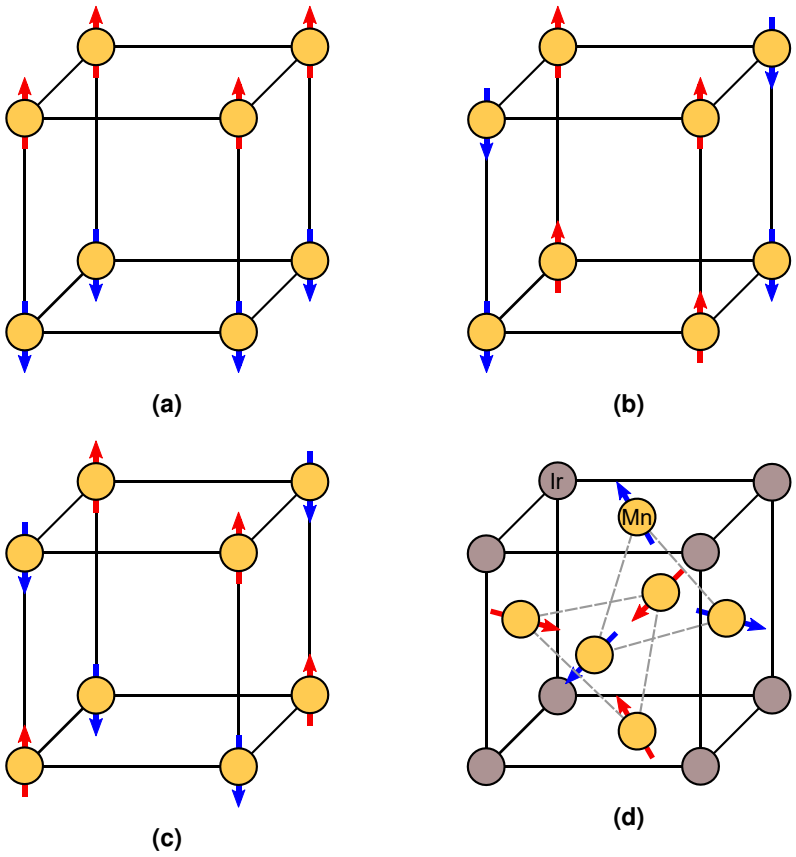

Figure 2.4: Schematic comparison of different types of antiferromagnetic ordering. a) A-type ordering where there are layers of ferromagnetically ordered moments. b) Shows C-type ordering where the moments experience antiferromagnetic coupling along two directions whilst c) demonstrates the antiferromagnetic coupling along three directions present in a G-type antiferromagnet. d) An example of a non-collinear antiferromagnetic ordering such as found in IrMn. Structure adapted from Ref. [39]

In an A-type antiferromagnet (Fig. 2.4a), the magnetic moments are coupled ferromagnetically within a given spin plane, but are antiferromagnetically coupled between neighbouring planes [24]. If, however, the intra-plane coupling is ferromagnetic and it is the inter-plane coupling that is antiferromagnetic, then the magnetic structure can be termed a C-type antiferromagnet (Fig. 2.4b). The third common type of antiferromagnet with both inter-plane and intra-plane antiferromagnetic coupling is known as a G-type antiferromagnet (Fig. 2.4c). These three types of antiferromagnetism are collectively known as collinear antiferromagnetism where the moments lie along common axes. There are further types of antiferromagnetism which are non-collinear in nature, for example, the metallic AFM IrMn shows a triangular lattice where the moments are rotated at 120° with respect to each other [39]. The antiferromagnetism is then provided

by three, rather than two, antiferromagnetically coupled moments (Fig. 2.4d). The work performed in this thesis focusses on AFMs with a collinear ordering, specifically type A antiferromagnetism, and thus the subsequent sections will also predominantly describe collinear AFMs.

2.3.2 Two Sublattice Model of Antiferromagnetism

Phenomenologically, the theory of antiferromagnetism proposed by Néel [31–33] allows for a semi-classical treatment based on sublattices of magnetic moments aligned along a collinear direction, where the magnetisation of each sublattice can be described by,

$$\boldsymbol{M}_j = \frac{1}{dV}\sum_f \langle \hat{\mathfrak{M}}_{jf} \rangle. \tag{2.14}$$

The summation is performed over the moments in a volume dV and $\langle \hat{\mathfrak{M}} \rangle$ is the quantum mechanical average of the magnetic moments of the j^{th} magnetic sublattice. The total magnetisation of the system is then the summation over N sublattices, where the number of sublattices is equal to the number of moments in the primitive magnetic unit cell,

$$\boldsymbol{M} = \sum_{j=1}^{N} \boldsymbol{M}_j. \tag{2.15}$$

In order to approximately describe the properties of such complicated magnetic structures, some magnetic sublattices can be combined, such as moments with the same orientation or those on the same lattice site regardless of orientation, until the N is reduced to two. Although this is only strictly applicable to simple AFMs such as MnF_2, it is also useful in describing more complex ordering. Thus, in most AFMs, the resulting magnetic unit cell consists of an equal number of moments in two opposing directions, ordered due to the exchange interaction, (c.f. Sec. 2.2.1). In order to guarantee a net antiparallel alignment of the spins, the sign of the total exchange integral $\mathcal{J}$ (Eqn. 2.7) between the two magnetic sublattices needs to be negative even if the exchange integral describing the intra-lattice exchange is not. The exchange interaction is mostly indirect in AFMs and in non-metallic crystals the indirect superexchange interaction via intermediate anions plays the major role (c. f. Sec. 2.2.1.1).

Having reduced the number of magnetic sublattices to two, the exchange energy between the sublattices can now be written as an effective field using the mean field approximation as,

$$H_E = \mathcal{J}_E \boldsymbol{M}_1 \cdot \boldsymbol{M}_2, \tag{2.16}$$

where $\mathcal{J}_E$ is now a mean field coefficient relating the exchange field H_E to the sublattice magnetisations $\boldsymbol{M}_1$ and $\boldsymbol{M}_2$ that have replaced the spin operators from before.

2.3.3 Weiss Model of Antiferromagnetism

A Weiss-like model can be developed for antiferromagnets similar to that of ferromagnets [40, 41], by considering the interaction between each sublattice. This model was developed by Néel [31–33] who was a PhD student under the tutorial of Pierre Weiss at the time he published his theory of ferromagnetism [24, 25, 42]. Here the basic ideas will be presented. If the nearest neighbours of each atom lie on the opposing sublattice,

then the molecular field acting on an atom of sublattice 1 can be written as

$$\boldsymbol{H}_{M_1} = -n_{11}\boldsymbol{M}_1 - n_{12}\boldsymbol{M}_2, \tag{2.17a}$$

and for an atom on sublattice 2 as,

$$\boldsymbol{H}_{M_2} = -n_{21}\boldsymbol{M}_1 - n_{22}\boldsymbol{M}_2, \tag{2.17b}$$

where $\boldsymbol{M}_1$ and $\boldsymbol{M}_2$ are the total magnetic moment of each sublattice and n_{ij} are constants of proportionality. If one assumes that the same type of atom lies on both sublattices, then $n_{11} = n_{22} = n_{ii}$ describes the molecular field constant for next-nearest-neighbour, *intra-sublattice* interactions and $n_{12} = n_{21}$ represents the same for nearest-neighbour *inter-sublattice* interactions. When a small magnetic field $\boldsymbol{H}$ is applied, Eqns. 2.17a and 2.17b then become,

$$\boldsymbol{H}_1 = \boldsymbol{H} + \boldsymbol{H}_{M_1} \tag{2.18a}$$

and,

$$\boldsymbol{H}_2 = \boldsymbol{H} + \boldsymbol{H}_{M_2} \tag{2.18b}$$

At thermal equilibrium, the spontaneous sublattice magnetisation is given by,

$$M_{1,2} = \frac{Ng\mu_B J}{2} B_J(x_{1,2}), \tag{2.19}$$

where $B_J(x_{1,2})$ is the Brillouin function, with $x_{1,2}$ representing the ratio of the Zeeman energy and thermal energy of each sublattice,

$$x_{1,2} = \frac{g\mu_B J}{k_B T}\boldsymbol{H}_{1,2}, \tag{2.20}$$

$N/2$ is the number of atoms with a permanent dipole moment on each sublattice and J represents the angular momentum of each moment, comprised of spin and orbital angular momentum. There is a critical temperature T_N where the sublattice magnetisation goes to zero due to thermal fluctuations, as shown in Fig. 2.5, above which, the material is paramagnetic and the application of a small magnetic field leads to a small induced moment directed along the field. By taking the small limit expansion of the Brillouin function and considering that there is no longer any AFM ordering, this induced moment $\boldsymbol{M}$ above T_N can be written as,

$$\boldsymbol{M} = \frac{Ng^2\mu_B^2 J(J+1)}{6k_B T}[2\boldsymbol{H} - (n_{ii} + n_{12})\boldsymbol{M}], \tag{2.21}$$

from which the temperature dependence of the susceptibility above the Néel temperature, $\chi = \boldsymbol{M}/\boldsymbol{H}$, can be written as,

$$\chi = \frac{C}{T + \theta_P}, \tag{2.22}$$

where the constants have been combined into the constant C and θ_P defines the paramagnetic temperature of the antiferromagnet,

$$\theta_P = \frac{1}{2}C(n_{ii} + n_{12}). \tag{2.23}$$

By considering the sublattice magnetisation at the Néel temperature in the absence of an applied field, T_N can be similarly calculated,

$$T_N = \frac{1}{2}C(n_{12} - n_{ii}). \tag{2.24}$$

The stronger the inter-sublattice exchange, n_{12}, and the weaker the intra-sublattice exchange, n_{11} or n_{22}, the higher the Néel temperature will be. In general, θ_P is very different from T_N, however, measuring the susceptibility above the Néel temperature and a subsequent extrapolation (Inset of Fig. 2.7) to find the value of θ_P alongside measurements of the actual T_N gives an insight into the strength of the exchange interactions of the AFM.

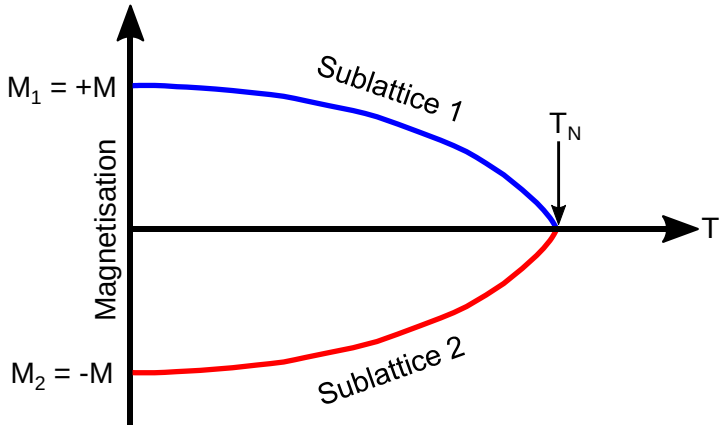

Figure 2.5: Temperature dependence of the sublattice magnetisations for the two sublattices of an antiferromagnet. The magnitudes are equal but opposite, maximum at 0 K and fall to 0 at the Néel temperature.

Below T_N, the sublattices develop a spontaneous magnetisation which follows a temperature dependence similar to a ferromagnet, Fig. 2.5. As both sublattice magnetisations follow the same temperature dependence, the two magnetisations are oppositely orientated and so the total magnetisation, $\boldsymbol{M}_1 + \boldsymbol{M}_2$, is zero at all temperatures. However, the staggered magnetisation of a collinear AFM can be defined by a non-zero ordering parameter known as the Néel vector, $\boldsymbol{n} = \boldsymbol{M}_1 - \boldsymbol{M}_2$, allowing for directions relative to the sublattice magnetisations to be defined.

2.3.3.1 Exchange Energy Scales

As an example, the different exchange energy paths in MnF_2 have been measured by means of neutron diffraction [43]. There are three possible exchange paths within the magnetic unit cell, shown in Fig. 2.6, whilst Table 2.1 lists the relevant strengths of the exchange parameters. As is clear, the negative inter-sublattice exchange $\mathcal{J}_2$ is far stronger than the intra-sublattice exchange paths $\mathcal{J}_1$ and $\mathcal{J}_3$ and thus determines the antiferromagnetic arrangement of the Mn sublattices.

2.3.4 Antiferromagnetic Susceptibility Below T_N

For the sake of simplicity, a uniaxial anisotropy is considered (Sec. 2.2.3) where the sublattice magnetisations are coincident with the easy-axis EA. For a small magnetic field applied parallel to the uniaxial anisotropy direction, the magnetic susceptibility below

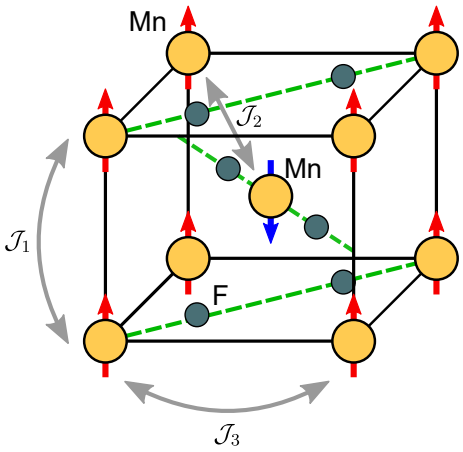

Figure 2.6: Magnetic unit cell of the easy-axis antiferromagnet MnF_2 showing the exchange paths between the two Mn sublattices. The gold atoms represent Mn and the green atoms represent F.

Exchange Parameter	Strength (meV)
$\mathcal{J}_1$	0.028
$\mathcal{J}_2$	-0.152
$\mathcal{J}_3$	- 0.004

Table 2.1: Relative strengths of the exchange paths in MnF_2 as measured by neutron scattering. Values from Ref. [43].

T_N within the molecular field theory varies as,

$$\chi_{||} = \frac{\boldsymbol{M}}{\boldsymbol{H}} = \frac{N\mu_B^2 g^2 J^2 B'_J(x_0)}{k_B T + \frac{1}{2}(n_{ii} + n_{12})\mu_B^2 g^2 J^2 N B'_J(x_0)}, \tag{2.25}$$

where $x_0 = \frac{g\mu_B J}{k_B T}[(n_{12} - n_{ii})M_0]$ is the equilibrium value of x in the absence of a magnetic field. At temperatures close to the Néel temperature, thermal fluctuations act to reduce the sublattice magnetisation, increasing the susceptibility. Conversely, as thermal fluctuations reduce at lower temperatures, the magnetic field has a smaller impact on the sublattice magnetisations and the susceptibility correspondingly lowers. At T = 0 K, the two sublattices experience no classical fluctuations and $\chi_{||} \to 0$. Above T_N the susceptibility again decreases, and the maximum value of $\chi_{||}$ occurs at the Néel temperature. The stronger the antiferromagnetic correlations, the lower this maximum value of the susceptibility will be.

If the magnetic field is applied perpendicular to the EA, the sublattice magnetisations begin to cant in the direction of the applied field by a small angle δ, opposed by H_E and a magnetic moment directed along $\boldsymbol{H}$ will appear. At equilibrium, the torque on each sublattice must be zero, i.e. $\boldsymbol{M}_1 \times (H + H_{M1}) = 0$. It then follows that $\boldsymbol{M}_1 H = n_{12}\boldsymbol{M}_1\boldsymbol{M}_2 \sin 2\delta$. By noticing that the field induced magnetisation along the applied field is related to the canting angle by $\boldsymbol{m}_\perp = 2M \sin\delta$, the susceptibility of an AFM for a magnetic field applied perpendicular to the sublattice magnetisation is,

$$\chi_\perp = \frac{1}{n_{12}}. \tag{2.26}$$

Again, reaching the value of the paramagnetic susceptibility at T_N, $\chi_\perp$ remains constant with temperature and independent of n_{ii} down to T = 0 K. The susceptibility of an antiferromagnet is also affected by the introduction of crystalline anisotropy. This crystalline anisotropy energy for a hexagonal crystal structure, for example, can be written as,

$$F_K = \frac{1}{2}K(\sin^2\vartheta_1 + \sin^2\vartheta_2), \tag{2.27}$$

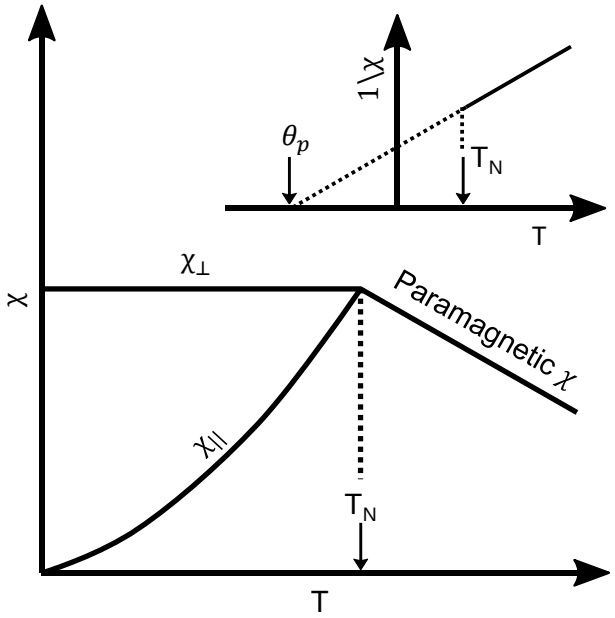

Figure 2.7: Susceptibility of an antiferromagnet as a function of temperature for a magnetic field applied parallel ($\chi_{||}$) and perpendicular ($\chi_\perp$) to the uniaxial anisotropy direction. Below the Néel temperature, the susceptibility is constant when measured perpendicular to the anisotropy axis whilst it drops from the paramagnetic value at T_N to 0 when measured parallel. The inset shows the inverse of the paramagnetic susceptibility above T_N. The extrapolation to 0 gives the paramagnetic temperature θ_P.

where K is a constant of the anisotropy energy and ϑ_1, ϑ_2 are the angles between the easy direction and the sublattice magnetisations, respectively $\boldsymbol{M}_1$ and $\boldsymbol{M}_2$. If the values of ϑ_1 and ϑ_2 are small, then the results for antiferromagnets with a uniaxial anisotropy also hold for other crystal symmetries such as cubic or orthorhombic. The anisotropy energy can also be written in terms of the equivalent magnetic fields acting on each sublattice $H_{K,1}$ and $H_{K,2}$,

$$\chi_\perp = \frac{1}{n_{12} + K/2M_0^2}. \tag{2.28}$$

If the molecular field is large compared to the anisotropy field then $\chi_\perp \approx 1/n_{12}$, or in other words, Eqn. 2.26 is recovered.

2.3.5 Effect of a Large Applied Field

If the applied magnetic field is larger than that in the previous section, the response of the antiferromagnetic sublattices is different. The simplest case to envision is that of the magnetic field being applied perpendicular to the sublattice magnetisations. As the magnetic field increases in magnitude, the canting angle δ continues to increase until the two sublattices lie parallel to the applied field and to each other, as shown in Fig. 2.8a. The field that this occurs at needs to be strong enough to overcome the exchange interaction keeping the sublattices antiparallel to one another, in other words $2H_E$, where H_E is the effective field created by the exchange energy.

When the magnetic field is applied parallel to the uniaxial anisotropy, providing the sublattice magnetisations remain collinear with it, the free energy of the antiferromagnet changes by an amount $\delta\mathcal{F}_T = -\chi_{||}(\boldsymbol{H}^2 \text{ / } 2)$. If on the other hand, the sublattice

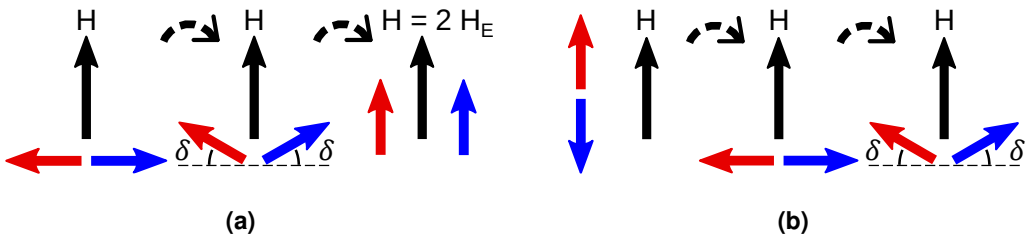

Figure 2.8: a) Effect of an increasing magnetic field perpendicular to the sublattice magnetisations which continue to cant until the field overcomes the exchange field. b) Effect of an increasing magnetic field parallel to the sublattice magnetisations. At some critical field, the sublattice magnetisations rotate perpendicular to the applied field then begin to cant. In rare cases, a field parallel to the easy-axis induces a spin flip where the spins align parallel to each other and the field, bypassing the spin flop configuration.

magnetisations are perpendicular to the easy-axis, providing the anisotropy constant is small, the change in the free energy is then $\delta\mathcal{F}_T = -\chi_\perp(\boldsymbol{H}^2$ / 2). Considering that $\chi_\perp > \chi_{||}$ for an antiferromagnetic material below the Néel temperature (see Fig. 2.7), it stands to reason that the perpendicular alignment of the sublattice magnetisation and anisotropy direction would be the ground state of the antiferromagnet. If $K \neq 0$, then the change in the free energy now includes the anisotropy, $\delta\mathcal{F}_T = K - \chi_\perp(\boldsymbol{H}^2/2)$ for the perpendicular alignment meaning that, providing the value of the applied field is not too large, the parallel alignment is now that with the lowest energy. These two states then become equal in energy at some critical magnetic field, $H_c^{\parallel}$ given by,

$$-\frac{1}{2}\chi_{||}(H_c^{\parallel})^2 = K - \frac{1}{2}\chi_\perp(H_c^{\parallel})^2,$$
$$\text{or,} \tag{2.29}$$
$$H_c^{\parallel} = \left[\frac{2K}{\chi_\perp - \chi_{||}}\right]^{1/2}.$$

Below $H_c^{\parallel}$, the sublattice magnetisations will be collinear to the EA, whilst for $\boldsymbol{H} > H_c^{\parallel}$, they will lie perpendicular. This transition is known as *spin flopping* with the critical spin flop field $H_c^{\parallel}$. There is also the possibility of a metamagnetic transition for $\boldsymbol{H}\|EA$ where the spin flop is bypassed and the moments of both sublattices abruptly reorientate to be parallel to each other and $\boldsymbol{H}$. This is known as a *spin flip* transition [24].

A spin flop can be more easily achieved in AFMs with a low Néel temperature since $\chi_\perp - \chi_{||}$ is larger, making $H_c^{\parallel}$ relatively small. Spin flopping was first observed in $CuCl_2{\cdot}2H_2O$ [44, 45] and has since been observed in numerous other AFMs such as Cr_2O_3 [46], α-Fe_2O_3 [47] and MnF_2 [48]. Through measurements of the Néel temperature, the susceptibility above T_N, AFM resonance, and the spin flop field, the anisotropy constants can be easily evaluated, however these measurements are more applicable to single crystalline bulk samples, placing significant limitations on the evaluation of antiferromagnetic anisotropies in thin film AFMs.

2.3.6 Antisymmetric Exchange and Weak Ferromagnetism

At the beginning of this section, it was briefly mentioned that there is a type of antiferromagnet that is not completely compensated, yet the net magnetic moment is not of the

order of an elementary magnetic moment like in ferrimagnets. This sub-class of antiferromagnets is known as weak ferromagnets, and there are several materials that present such a structure, including those known as orthoferrites with the composition XFe_2O_3. This net moment was a cause of confusion when it was first observed and suggestions of ferromagnetic impurities [49] or uncompensated poles at domain walls [50] were put forward in an attempt to explain it. It is now known that this moment originates from a canting of the magnetic sublattices, however, the Heisenberg exchange is isotropic and cannot explain the origin of such a canting. In the case of one of the most studied antiferromagnets showing this structure, α-Fe_2O_3, Dzyaloshinskii recognised that the canting could not be ruled out by the symmetry of the lattice [51]. By using Landau's theory of second order phase transitions [24, 25], he demonstrated that when the two magnetic sublattices $\boldsymbol{M}_1$ and $\boldsymbol{M}_2$ lie in the the c-plane of this antiferromagnet, they can be rotated from π by about 10^{-4} radians. However, if the moments lie parallel to the c-axis, Dzyaloshinskii concluded that there would be no net moment in the absence of an applied magnetic field. He termed these two states, "State II" and "State I" respectively. Whether an antiferromagnet exhibits either state depends on which state has the lowest energy at a given temperature.

A microscopic origin of the canting was later provided by Moriya [52] by using the superexchange formalism of Anderson [26]. Through a combination of superexchange and spin-orbit coupling, he showed that the constant of this anti-symmetric exchange has the form $D \sim \frac{\Delta g}{g} J$, where $\Delta g = g - 2$ is the contribution to the g-factor from the orbital moment. However, experimental values of Δg are at odds with the theoretical expectations, returning negative values in α-Fe_2O_3 [53, 54]. Since this interaction originates from the spin-orbit interaction of two magnetic ions mediated by an non-magnetic atom, this leads to an antisymmetric exchange interaction between the ground state of one magnetic ion with the excited state of another. This interaction favours the alignment of the antiferromagnetic moments perpendicular to each other, in a plane perpendicular to the vector of the interaction, in order to reduce the energy. The Dzyaloshinskii-Moriya interaction (DMI) is represented by an antisymmetric Hamiltonian, which is then added to the total Hamiltonian of the magnetic state,

$$\mathcal{H}_D = F_D = -\mathcal{D} \cdot [\boldsymbol{M}_1 \times \boldsymbol{M}_2], \tag{2.30}$$

where $\mathcal{D}$ is a vector that lies along a high symmetry axis and $\boldsymbol{M}_1$ and $\boldsymbol{M}_2$ are the sublattice magnetisations. This higher-order effect can occur in materials where ions are coupled via superexchange and there is a broken inversion symmetry within the unit cell of the bulk material. It serves to cant the moments of an antiferromagnet away from the antiferromagnetic axis. This canting angle is normally small due to the relative strengths of the DMI and the exchange, $\mathcal{D}/\mathcal{J} \approx 10^{-2}$. Such a canting, and hence weak moment, only appears when the spins lie perpendicular to the high-symmetry axis that $\mathcal{D}$ lies along. If the spins lie parallel to this axis, then $\mathcal{D}$ has no impact on the equilibrium position of $\boldsymbol{n}$ and no canted moment appears. It can, however, have an impact when a magnetic field is applied perpendicular to $\mathcal{D}$ as will be discussed in Ch. 4. It should also be noted that not all uniaxial antiferromagnets have an antisymmetric exchange interaction. Notably Cr_2O_3 possesses the same crystal structure as α-Fe_2O_3 but no DMI as $\mathcal{D}$ disappears when there is an inversion symmetry with respect to the centre between the two magnetic ions.

Such an antisymmetric exchange can exist wherever there is a broken inversion sym-

metry, which doesn't only include the symmetry of the crystal structure of a material but can also include the broken symmetry across the interface between two layers. This is known as the interfacial Dzyaloshinskii-Moriya interaction (i-DMI) which appears at the interface between a magnetic material and a non-magnetic material with a large spin-orbit coupling [55]. It has been intensely studies in recent years due to its ability to stabilise Néel type domain walls with a fixed chirality, leading to complex spin structures, such as skyrmions [r7, 55–58].

2.3.7 Antiferromagnetic Domains

In ferromagnets, magnetic domains form as a natural consequence of the magnetic free energy (c.f. Sec. 2.2) as they serve to reduce the magnetostatic energy that comes with the stray and demagnetising fields outside of the sample [24, 25]. Fig. 2.9a shows a single domain ferromagnetic sample with a large stray field. By forming a second domain, the strength of this stray field can be reduced (Fig. 2.9b) or completely suppressed by the formation of a closed domain structure (Fig. 2.9c). However, the formation of increasing numbers of domains doesn't necessarily lead to an indefinite reduction of the magnetic free energy.

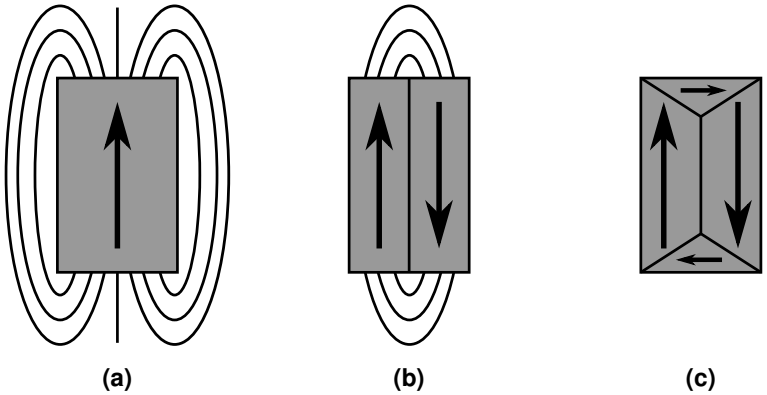

Figure 2.9: Possible domain configurations for a cubic ferromagnet. a) Schematic of a monodomain sample. At the edge of the sample, a demagnetising field is created in order to satisfy Maxwell's second equation. b) A 180° domain wall is created in order to reduce the strength of the stray field. c) The formation of additional 90° domain walls between areas where the magnetisation is orientated by 90° allows for the stray field to be suppressed.

Within a single domain, the magnetisation is homogeneous and aligned along a common direction, which changes orientation between neighbouring domains in a region known as a domain wall, which costs energy. Eventually, the reduction in the magnetostatic energy and the gain in domain wall energy balance one another and an equilibrium state is reached. Whilst it is quite easy to see why a ferromagnetic material will form domains, there is no energetic reason for antiferromagnetic domains to form as the net magnetisation is zero and no reduction of the magnetostatic energy should occur.

Despite this, in order to explain the magnetic susceptibility of some antiferromagnetic materials, Néel proposed antiferromagnetic domains separated by domain walls that can be displaced by small magnetic fields [59] and they have since been observed in numerous materials [60–66]. Li discussed the formation of domains as an interplay between the change of entropy due to the increased disorder and the wall energy, but the contribution to the free energy by the change in entropy is far too small [50]. The

magnetoelastic interaction, also known as magnetostriction, describes the deformation of a magnetic material when a magnetic field is applied and vice versa [67]. The magnetoelastic nature of antiferromagnetic domains has been demonstrated in the literature for domains where the magnetic axis changes orientation [68–70]. However, it doesn't explain the stabilisation of domains where the magnetic axis of each domain is parallel [71, 72]. The formation of such domains is related to the spontaneous nucleation of domains at defects and pinning sites when the antiferromagnet is cooled through the Néel temperature [73] or from the meeting of two 90° domain walls when the antiferromagnet is driven above the spin flop [72]. At some point, two domains that have nucleated separately meet and may form a 180° domain wall, depending on the orientation of $\boldsymbol{n}$ in each. The character of the domain walls in both ferro- and antiferromagnets can be classified as either Néel-like or Bloch-like, depending on how the magnetisation rotates across the domain wall; respectively perpendicular or parallel to the plane of the wall.

The direct observation of magnetic domains in antiferromagnets is not as simple as for ferromagnets. Polarised light can be used to observe non-180° domains in materials with a large magnetostriction, where the crystal structure distorts due to the magnetic ordering along the direction of the moments. In neighbouring domains, the distortion will be along different crystallographic directions, and hence, when the polarised light passes through the material, the birefringence within the material allows for domains to be resolved [60, 74]. The observation of domains in this manner was restricted to AFM single crystals but has recently been transferred to thin film AFMs by making use of the Voigt and Kerr effects [75] The domains in materials with a large magnetostriction can also be investigated with X-ray diffraction topography [76, 77] which allows for the strain distribution to be revealed. Different domains will result in different diffraction angles, allowing them to be imaged [76, 77]. Rather than relying on the magnetostrictive distortion, neutron scattering can also be used to image the spin arrangement of antiferromagnets. As neutrons possess a magnetic dipolar moment, they are scattered not only by the nucleus via the strong interaction but also from the unpaired electrons of the magnetic atoms through the dipolar interaction. This results in coherent, magnetic Bragg scattering when there is magnetic ordering. Depending on the orientation of the magnetic moments, the scattered neutron intensity will vary, allowing for point-by-point maps to be made of the magnetic ordering in a sample. Indeed, neutron diffraction was the technique by which antiferromagnetic order was first conclusively established [34]. X-ray magnetic linear dichroism-photoemission electron microscopy (XMLD-PEEM: Sec. 4.2.6) can also be utilised for AFMs without a large magnetostriction, where linearly polarised X-rays elicit photoemitted electrons depending on the AFM state, allowing one to observe antiferromagnetic domains for regions with different orientations of the Néel vector $\boldsymbol{n}$ [r1, r4, r15, r17, 62, 78]. This is the main technique used for the domain imaging used in the course of this thesis.

2.4 Magnons

For a simple chain of spins aligned ferromagnetically along the same direction at finite temperature, the flip of a single spin is the lowest form of excitation above the ground state expected from the Heisenberg picture, however it is energetically very expensive. In order to reverse a single spin, an energy of $2\mathcal{J}$ is required, twice that available at the magnetic ordering temperature $k_B T_c = \mathcal{J}$ from the molecular field approximation

[24]. Instead of a single spin changing orientation, the spin flip is shared amongst every element of the chain, leading to a periodic displacement of the spin direction away from equilibrium. Each spin then precesses around the equilibrium position with some phase difference from its neighbours, spatially separated by a distance a, resulting in a periodic oscillation. By taking the distance between two points that are precessing in phase with one another, one can define a wavelength, λ, and correspondingly a frequency, ω. Just as how elementary excitations of the crystal lattice give rise to phonons, such an excitation of the magnetisation can be described as a massless pseudo-particle called a magnon representing the reversal of a single integer spin and thus obeying Bose-Einstein statistics [79–81]. This is schematically shown in Fig. 2.10.

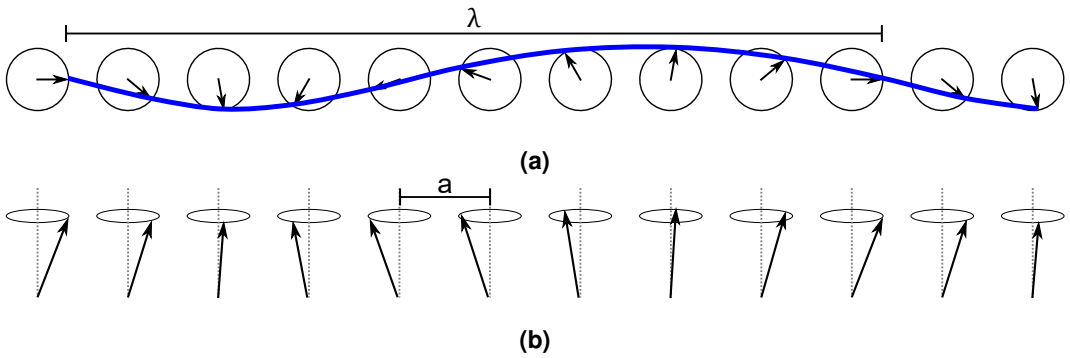

Figure 2.10: Ferromagnetic magnon in a one dimensional chain. a) Top view of magnetic moments deviating from the equilibrium position, tracing out a wave of wavelength λ between two spins precessing in phase. b) Side view of magnetic moments in the spin chain spatially separated by a.

As magnons are fluctuations of the magnetic order, they require a finite temperature. At T = 0 K, there are no thermally activated fluctuations of the magnetic order and thus magnon excitations are not possible. However, at finite temperature, there exist so called *thermal* magnons with a maximum frequency determined by the thermal energy of the system $\hbar\omega \approx k_B T$. At higher temperatures, there are then more available magnon states. Magnons are capable of transferring angular momentum, and therefore information, without the need for electron motion, making them a topic of increased research interest birthing the specific sub-field of spintronics known as magnonics, a field in which a lot of the work in this thesis is based [8, 9, 82].

2.4.1 Antiferromagnetic Magnons

Magnon excitations can also exist in antiferromagnetically ordered materials [83–85], albeit with a different dispersion relation [86]. If we now consider a similar chain of magnetic moments to before, but this time with an exchange interaction that leads to antiferromagnetic ordering between nearest neighbours, the effect of flipping a single spin also leads to every spin in the chain reversing its direction at an energy cost of $8\mathcal{J}$. This far exceeds the energy available at the magnetic ordering temperature $k_B T_N \sim 2\mathcal{J}$ and thus such a localised spin flip is not energetically possible. Just as for the ferromagnetic spin chain, the spin flip is instead shared amongst all of the available spins. A schematic for a magnon produced in a two sublattice antiferromagnet is depicted in Fig. 2.11 where the moment of each sublattice precesses around a common equilibrium position.

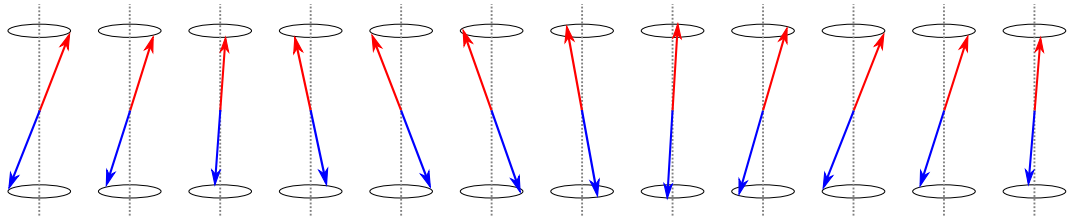

Figure 2.11: Side view of an antiferromagnetic magnon for a circularly polarised magnon mode. The two sublattices are both perturbed from a equilibrium position, leading to the creation of a magnon.

The magnon dispersion for an easy-axis AFM in the absence of a magnetic field can be derived by making use of the Holstein-Primakoff (HP) [80] approach to express the spin operators of the two AFM sublattices in terms of boson operators creating and annihilating magnons [87, 88]. Starting from a two sublattice AFM with an easy-axis anisotropy, in the absence of a magnetic field the Hamiltonian for the system can be written as the sum of the exchange energy and the anisotropy energy,

$$\mathcal{H} = \sum_{i \neq j} \left(S_i^+ S_j^- + S_i^- S_j^+ + 2 S_i^z S_j^z \right) - K \sum_{i,j} \left(S_{i,j}^z \right)^2, \tag{2.31}$$

where $S_i^+ \left(S_i^- \right)$ is the raising (lowering) spin operator of an individual spin, S_i^z the z component of the spin, and K the anisotropy constant which is negative to promote an easy-axis anisotropy. The first HP transformation relates the raising (lowering) spin operators to annihilation (creation) operators of spin deviations $a_i \left(a_i^\dagger \right)$ and $b_i \left(b_i^\dagger \right)$ for sublattice 1 and 2 respectively. A transformation is then made from the localised field operators to boson operators,

$$a_i = N^{-1/2} \sum_k e^{i\vec{k}\cdot\vec{r}_i} a_k \qquad \text{and} \qquad b_i = N^{-1/2} \sum_k e^{i\vec{k}\cdot\vec{r}_i} b_k, \tag{2.32}$$

where N is the number of spins on each sublattice and $\vec{k}$ is the wavevector. Introducing these operators into the Hamiltonian in Eqn. 2.31 alongside a binomial expansion, the Hamiltonian is now of the form,

$$\mathcal{H} = E_0 + \mathcal{H}^{(2)} + \mathcal{H}^{(4)} + \mathcal{H}^{(6)} + \ldots \tag{2.33}$$

The first term is a constant and the second, quadratic term can be expanded to read [87, 88],

$$\mathcal{H}^{(2)} = \gamma\hbar \sum_k \left(H_E + H_K \right) a_k^\dagger a_k + \left(H_E + H_K \right) b_k^\dagger b_k + \gamma_k H_E \left(a_k b_{-k} + a_k^\dagger b_{-k}^\dagger \right), \tag{2.34}$$

where $\gamma_k = (1/z) \sum_\delta \exp\left[i\vec{k} \cdot \vec{\delta} \right]$ is a material specific structure factor with $\vec{\delta}$ being vectors connecting the z nearest neighbours of the opposite sublattice. Magnon creation (annihilation) operators $\alpha_k^\dagger \left(\alpha_k \right)$ and $\beta_k^\dagger \left(\beta_k \right)$ are produced from the boson operators via a Bogoliubov transformation [89] which can then be substituted into 2.34 resulting in,

$$\mathcal{H}^{(2)} = \hbar \sum_k \left(\omega_{\alpha k} \alpha_k^\dagger \alpha_k + \omega_{\beta k} \beta_k^\dagger \beta_k \right), \tag{2.35}$$

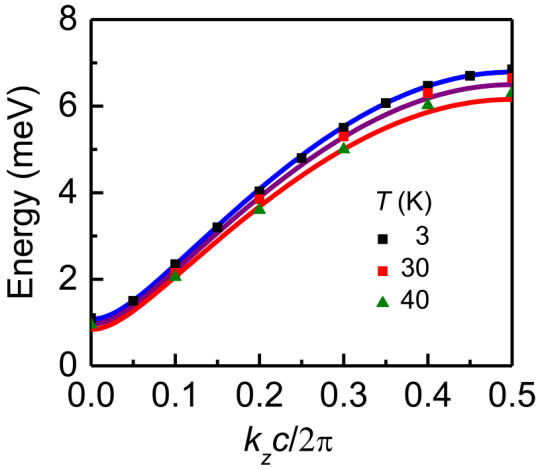

Figure 2.12: Magnon dispersion for the body-centric easy-axis antiferromagnet MnF_2 as measured by neutron scattering for a wavevector parallel to the c-axis. Reprinted from S. M. Rezende *et al.*. Introduction to antiferromagnetic magnons. *J. Appl. Phys.* **126** (2020), with the permission of AIP Publishing.[88]

where $\omega_{\alpha k}$ and $\omega_{\beta k}$ are the frequencies of the two magnon modes. These two frequencies will be derived separately in the next section for the case of an applied magnetic field exciting resonant excitations of the two modes and a relationship will be derived to show how these frequencies evolve with increasing field. One of the simplest easy-axis AFMs is the body-centric MnF_2. The magnon dispersion of this AFM in the absence of a magnetic field with the wavevector parallel to the c-axis, as measured by neutron scattering, is shown in Fig. 2.12 for several temperatures, with solid curves being theoretical calculations.

In the dispersion relations of both ferromagnetic and antiferromagnetic magnons, at a wavenumber of $k = 0$, excitations can still be excited at a finite frequency due to the presence of magnetic anisotropy leading to a so-called *magnon gap*. Unlike in ferromagnetic materials where the magnons are circularly polarised, in antiferromagnets linear polarisations can also exist [42, 90]. The situations where these two polarisations are relevant, as well as the effect of a magnetic field on the magnon dispersion of the $k = 0$ modes, will be discussed in the next section in the context of antiferromagnetic resonance [46, 90–92]. This technique is identical to ferromagnetic resonance, a common investigative technique for measuring FMs, but requires much larger applied fields and frequencies to excite resonance due to the increased strength of the exchange interaction found in antiferromagnets.

2.4.2 Effect of a Magnetic Field on the Antiferromagnetic Magnon Dispersion

Antiferromagnetic resonance was first theoretically studied by Kittel [91], Nagamiya [93] and, Keffer and Kittel [94], with the first experimental investigations performed on Cr_2O_3 and MnF_2 [95, 96]. By exciting the magnetisation of an antiferromagnet through the application of both a static external field and an additional alternating magnetic field, the coherent precession of the magnetic moments represents the continuous creation of magnons with a given frequency. For an antiferromagnet with a uniaxial anisotropy, providing the basal plane anisotropy in the plane perpendicular to the easy-axis can be

neglected, the effect of resonant driving fields on the magnon dispersion can be derived. For a complete discussion and derivation of the antiferromagnetic resonance, one can consult for example Ref. [42] and the references therein. Here, the key effects of a magnetic field on the excited sublattices will be addressed following similar arguments to those presented in Ref. [42]. Equally one can follow the concept of transformations from spin operators to magnon operators and maintain the terms containing a magnetic field from the previous section [88]. An understanding of the effect a magnetic field has on the magnon dispersion is key for the discussions of antiferromagnetic magnon transport that will be presented in later chapters.

2.4.2.1 Easy-axis Antiferromagnets

We will start with an easy-axis antiferromagnet with a magnetic field applied either parallel or perpendicular to the easy direction. In order to find the characteristic frequencies of an antiferromagnet, the eigenfrequencies of oscillations in the state below the spin flop need to be evaluated. Using linearised equations of motions for each magnetic sublattice, driven at some frequency ω, two independent equations can be obtained [91, 93, 94],

$$\left[\pm\omega - i\alpha\omega - \gamma(\boldsymbol{H} + H_E + H_K)\right] m_{1\pm} - \gamma H_E m_{2\pm} = -\gamma M h_{\pm}, \tag{2.36a}$$

$$\gamma H_E m_{1\pm} + \left[\pm\omega - i\alpha\omega - \gamma(\boldsymbol{H} - H_E - H_K)\right] m_{2\pm} = \gamma M h_{\pm}, \tag{2.36b}$$

where α is the Gilbert damping of the oscillations, γ is the gyromagnetic ratio, and H_E, H_K and $\boldsymbol{H}$ are respectively the exchange, anisotropy and applied fields. In order to find the eigenfrequencies, the determinant of this system of equations is set to zero and, for $\alpha = 0$, there are two frequencies ω_+ and ω_- given by,

$$\frac{\omega_{\pm}}{\gamma} = H_c \pm \boldsymbol{H}, \tag{2.37}$$

where H_c is the spin flop field and given by,

$$H_c = \sqrt{H_E H_K}. \tag{2.38}$$

At zero applied field, $\omega_+/\gamma = \omega_-/\gamma = \omega_0/\gamma = H_c$. The resonant frequencies can be very large in antiferromagnetic materials as compared to ferromagnets. For example, in Cr_2O_3 ω_0 is in excess of 135 GHz [46] as compared to a resonance frequency in $Y_3Fe_5O_{12}$ (YIG) of 4.5 GHz at 75 mT [97]. The two resonant frequencies, ω_+ and ω_-, correspond to a right circular and left circular precession of the magnetisation respectively, as shown in Fig. 2.13a.

Eqn. 2.37 shows that, with increasing applied magnetic field, below the critical field for the spin flop, the frequency of each mode changes linearly, with one approaching zero. Above the critical field for the spin flop, the magnetic field is now perpendicular to the magnetic moments of the two sublattices which lie in the plane perpendicular to the easy-axis and the eigenfrequencies of the excited magnons become,

$$\frac{\omega_1}{\gamma} = \left(H^2 - 2H_E H_K\right)^{\frac{1}{2}}, \tag{2.39a}$$

$$\omega_2 = 0. \tag{2.39b}$$

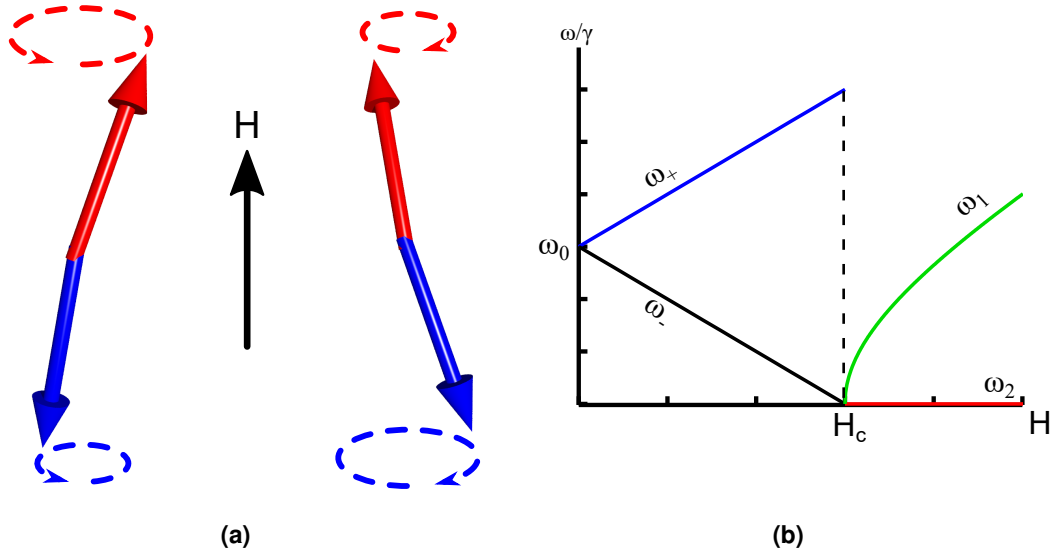

Figure 2.13: a) Possible magnon modes for an antiferromagnet with a uniaxial anisotropy and a magnetic field applied parallel to the easy-axis. This results in a left circularly or right circularly polarized magnon mode. The two colours represent the two magnetic sublattices. b) Dispersion of magnon modes in an easy-axis antiferromagnet as a function of applied field from Eqns. 2.37 and 2.39. At a critical field H_c, the antiferromagnetic order under goes a spin flop transition and the modes become linearly polarised. At the critical field, one mode disappears whilst the other changes character across the transition.

Following the rotation of the sublattice magnetisations at the spin flop field, the second mode, ω_2 represents an infinitely slow rotation of $\boldsymbol{M}_1$ and $\boldsymbol{M}_2$ around the easy-axis without a change of energy of the system and thus exhibits an eigenfrequency of zero. In reality, the presence of anisotropy within the basal plane means that ω_2 is not exactly zero but is very low compared to the other eigenfrequencies of the system and is known as a soft mode. For the first mode in Eqn. 2.39, the induced magnetisation of each sublattice is excited as,

$$m_{1x} = m_{2x}, \qquad m_{1y} = m_{2y}, \qquad m_{1z} = -m_{2z}, \tag{2.40}$$

where m_{ij} is the j^{th} component of the magnetisation of sublattice i. Whilst the modes below the spin flop are circularly polarised, the mode described by Eqns. 2.39a and 2.40 is one with a linear polarisation. One can think of the difference between these two polarisations as follows: a circular polarisation confines the moments of $\boldsymbol{M}_1$ and $\boldsymbol{M}_2$ to move on the surface of a sphere whilst for linear polarisation, the moments are confined to move in a plane. A more correct statement is that the modes of the spin flop phase are in fact highly elliptical. The ellipticity strongly varies with wavenumber and for magnons at the boundaries of the Brillouin zone the magnon modes are circular [88]. The field dependence of the k = 0 magnon modes given in equations 2.37 and 2.39 is graphically shown in Fig. 2.13b.

Rather than applying the field parallel to the easy-axis, if the field is applied perpen-

dicular, resonance modes can also appear at the frequencies $\omega_{\perp 1}$ and $\omega_{\perp 2}$ [42],

$$\frac{\omega_{\perp 1}}{\gamma} = \left(H_c^2 + H^2\right)^{\frac{1}{2}}, \tag{2.41a}$$

$$\frac{\omega_{\perp 2}}{\gamma} = \left(H_c^2 - \frac{H_K}{H_E}H^2\right)^{\frac{1}{2}}. \tag{2.41b}$$

However, these modes are generally not observable as the fields and frequencies required become exponentially large and above the realm of what is attainable in a laboratory setting [46].

2.4.2.2 Easy-Plane Antiferromagnets

If instead of an easy-axis antiferromagnet, we consider one with an easy-plane anisotropy, i.e. the sublattice magnetisations lie antiparallel to one another but within a plane rather than along a single axis, the results are similar to the uniaxial case above the spin flop. For the magnetic field applied within the easy-plane, perpendicular to the moments Eqns. 2.39a and 2.39b remain valid. However, due to the fact that the anisotropy constant is negative for an easy-plane antiferromagnet rather than positive, i.e. $K < 0$, the sign of H_K is different. For the magnetic field applied perpendicular to the easy-plane, the behaviour is slightly different and the two possible modes are described by,

$$\frac{\omega_{\perp 1}}{\gamma} = H\sqrt{1 + \frac{|H_K|}{2H_E}}, \tag{2.42a}$$

$$\frac{\omega_{\perp 2}}{\gamma} = \left(2H_E|H_K| - \frac{|H_K|}{2H_E}H^2\right)^{\frac{1}{2}}. \tag{2.42b}$$

Fig. 2.14 shows the field dependence of the magnon modes in an easy-plane antiferromagnet for the field within the easy-plane, $\omega_{||1}$ and $\omega_{||2}$, and perpendicular to the easy-plane, $\omega_{\perp 1}$ and $\omega_{\perp 2}$. It is interesting to note that, unlike in an easy-axis antiferromagnet, the field dependence of $\omega_{\perp 1}$ approaches zero in the absence of an applied field. In reality, this mode indeed has a finite value at zero field caused by the presence of an in-plane anisotropy. Just as in the spin flop phase of an easy-axis AFM, the magnon modes at k = 0 are effectively linear, however they become increasingly more elliptical as one moves through the Brillouin zone.

It is worth mentioning that the above theory can also be applied to antiferromagnets with more complex magnetic structures consisting of more than two magnetic sublattices. However, the number of eigenmodes is equal to the number of sublattices. Combining and reducing the number of sublattices to two in order to apply this theory results in one obtaining only the lowest two frequency branches.

In conclusion, the lowest two magnon branches from an antiferromagnet can be calculated for different ground states as a function of magnetic field by utilising a relatively simple model. At zero field, these magnon branches have a finite value and thus there is a gap if there exists a finite anisotropy, with the exception being one of the easy-plane modes. In easy-axis antiferromagnets, below the critical field for a spin flop, there are two circularly polarised modes, one being left circularly polarised and the other right. However, above the critical spin flop field and in easy-plane antiferromagnets, the modes

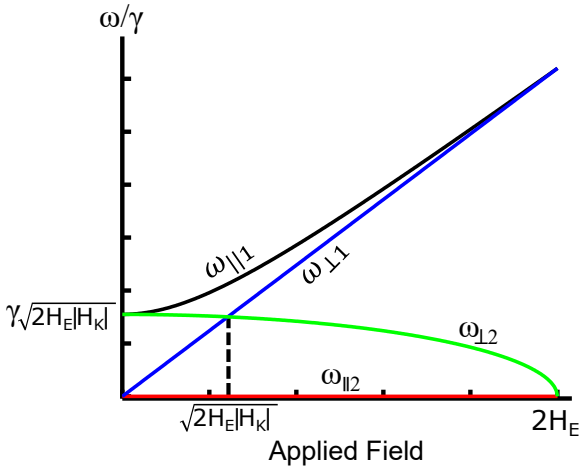

Figure 2.14: Field dependence of the magnon excitations in an antiferromagnet possessing an easy-plane anisotropy, generated from Eqns. 2.39 (with a negative anisotropy constant) and 2.42.

are linearly polarised in the centre of the Brillouin zone, but adopt some ellipticity at the edges. This distinction is important, because angular momentum can only be carried by circularly polarised magnons.

3

Spin Transport Effects

The research field of spintronics makes use of the transfer of spin angular momentum of the electron, frequently alongside the electron charge but not implicitly, for information processing and other technologies. This chapter will briefly introduce the main spintronic effects of interest that make up the basis of the experimental results reported in the course of this thesis. The key topic of conversion between the charge and spin of the electron is discussed through the spin Hall effect followed by a brief venture to the closely related phenomena of spin Hall magnetoresistance as a tool for probing the magnetic textures of insulating materials. Information transport in insulators can be achieved with an absence of charge motion by making use of pure magnon currents which can be produced in several ways including the thermally activated spin Seebeck effect and electrical injection, which will also be introduced and discussed before concluding with a small overview of magnon transport in antiferromagnetically ordered materials.

3.1 Hall Effects

In 1881, Edwin Hall observed that a current flowing in a metal, in the presence of perpendicular an external magnetic field, led to a measurable voltage transverse to both, an effect known as the (ordinary) Hall effect (OHE). This was the first of many closely related effects to be discovered [98]. The applied magnetic field generates a Lorentz force on the flowing charge carriers, leading to a deflection that depends on the charge of the carrier, i.e. whether it is an electron or hole, leading to carriers of differing charges being deflected in opposite directions and a measurable electromagnetic potential building up, opposing the further migration of charge carriers. A few years later, the anomalous Hall effect (AHE) was observed by Hall in iron magnetised out of the sample plane where, in the absence of an applied magnetic field, a transverse voltage is still produced which changes sign if the magnetisation of the iron is switched [99]. Such an effect is not limited to out-of-plane magnetised materials. For example, in-plane magnetised ferromagnetic metals with an in-plane charge current will also produce a transverse Hall-like effect, known as the planar Hall effect (PHE), based on the spin dependent scattering of the charge carriers when the in-plane magnetisation is parallel or perpendicular to the direction of the current.

3.1.1 Spin Hall Effect

Since Hall's first measurements, a group of interconnected effects has since been discovered. One such effect of central interest in the work performed in the course of this thesis is known as the spin Hall effect (SHE) allows for the interconversion of charge and spin, a critical requirement in spintronics, in order to create and detect pure spin currents [7]. As a charge current flows through a material with a large spin orbit interaction (SOI), the electrons are deflected based on their spin, leading to a net transverse flow of angular momentum. Although similar to the AHE in a ferromagnetic material, where the electrons are asymmetrically deflected by SOI leading to a spin flow with an accompanying electron flow, the SHE leads to no net charge transport. This effect allows for the generation of a pure spin current flowing perpendicular to a charge current, and thus represents a completely electrical method of generating a pure spin current, see Fig. 3.1a. The reciprocal process, the inverse spin Hall effect (ISHE), allows the conversion of a spin current into a charge current which is then detectable as a voltage, Fig. 3.1b. Whilst the details of this effect as revealed from the past two decades of research cannot be discussed in full, some excellent reviews on the theoretical and experimental progress made in the field of the SHE can be found in Refs [7], [99] and [100]. Here, a brief history of the effect's discovery and a small overview will be given.

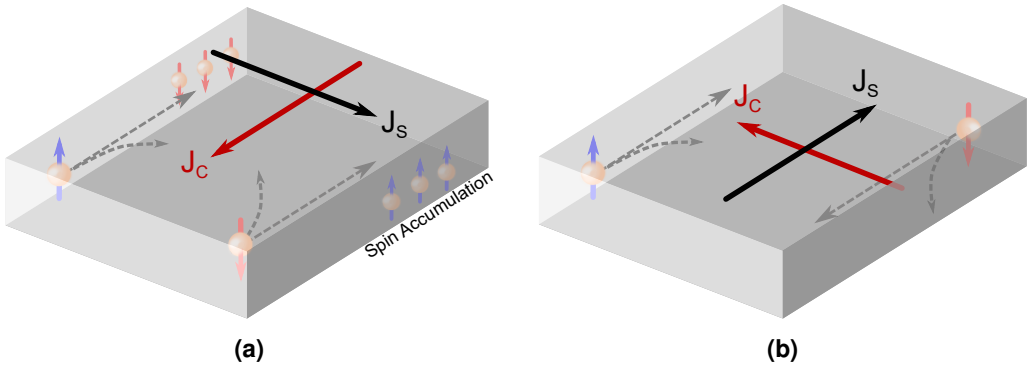

Figure 3.1: a) Sketch of the spin Hall effect. A flowing charge current produces a polarised spin current in the transverse direction due to the spatial separation of opposing electron spins. b) Sketch of the inverse spin Hall effect where a spin current is re-converted into a charge current.

The SHE was predicted by D'yakonov and Perel who looked at the spatial separation of spins in semiconductors depending on the spin polarisation, based on the concepts of asymmetric Mott scattering [101]. Following this initial work, the existence of the effect was all but forgotten until it was given new life at the turn of the millennium by the works of Hirsch [102] and Zhang [103]. In the early years of SHE research, there was intense theoretical debate on the the origin of the effect, with both extrinsic [102, 103] and intrinsic [104, 105] SHE mechanisms proposed. Eventually, the SHE was observed directly in 2004 by the magneto-optical Kerr effect [106]. In this case, it was attributed to extrinsic scattering whilst the intrinsic SHE was claimed shortly after by photoluminescence measurements [107]. The inverse of the SHE (ISHE) was later observed by Saitoh *et al.* by means of ferromagnetic resonance measurements of a $Y_3Fe_5O_{12}$/Pt bilayer leading to a measurable voltage in the Pt, a technique known as *spin pumping* [108].

The theoretical understanding of the SHE has its roots in the description of the AHE, but rather than correlating the charge degrees of freedom via relativistic SOI, the SHE correlates the charge of the electron with its spin [99]. Although the charge of the electron

is conserved, the spin is not and as such is subject to decay and dephasing occurring on short timescales due to the SOC that is itself required for the SHE. It has further been established that one can ascribe three possible contributions to the SHE; the intrinsic SHE and two extrinsic contributions that can be separated into skew scattering and side jump scattering. The intrinsic contribution originates from the electronic band structure of the material under investigation and depends heavily on the influence of the SOC, making it calculable from a theoretical basis [104, 105, 109]. This is often the dominant mechanism for the SHE in pure 3d, 4d and 5d transition metals [99, 110–112] and the transverse resistivity of the material under investigation due to the SHE ρ_{xy}^{int} scales in a simple model with the square of the resistivity ρ_{xx}^2 just like the intrinsic AHE [111, 113].

The skew scattering contribution covers inelastic scattering from impurities forming a local disorder potential that, through SOC, results in the trajectories of electrons with differing spin polarisations being altered differently (See Fig. 3.2a). This contribution tends to dominate in nearly perfect crystals. The experimental characterisation of the skew scattering thus requires a detailed understanding of the disorder of the material being investigated in order to separate it from other effects where it is found is to be proportional to the resistivity of the material under consideration, i.e. $\rho_{xx} \propto \rho_{xy}^{Skew}$ [7, 100, 113–115]. The final term, the side jump contribution, covers contributions to the SHE resistivity that are not covered by the intrinsic or skew scattering contributions and scales with ρ_{xx}^2 [100, 113]. There are several possible sources of side jump depending on the strength of the SOC but a basic (semi-) classical argument for this contribution comes from elastic scattering of electrons with different spin polarisations by impurities [100, 116, 117] (see Fig. 3.2b). Clearly separating these contributions in an experimental setting is challenging but several works have made detailed systematic studies of the intrinsic [112, 118] and extrinsic [114, 115, 119–121] SHEs

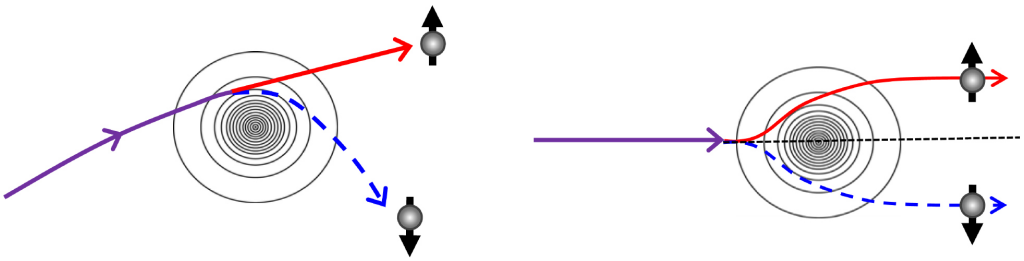

Figure 3.2: a) Sketch depicting skew scattering. b) Sketch depicting side jump scattering. Figs. reproduced from Ref. [100].

The efficiency of the conversion from a charge current $\boldsymbol{J}_c = \boldsymbol{J}_\uparrow + \boldsymbol{J}_\downarrow$ to a spin current $\boldsymbol{J}_s = \boldsymbol{J}_\uparrow - \boldsymbol{J}_\downarrow$, where $\boldsymbol{J}_{\uparrow(\downarrow)}$ represent the flow of spin up (down) electrons with a spin polarisation $\boldsymbol{\sigma}$, is quantified via the spin Hall angle θ_{SH}, empirically given by,

$$\boldsymbol{J}_s \propto \theta_{SH}(\boldsymbol{\sigma} \times \boldsymbol{J}_c), \tag{3.1a}$$

$$\boldsymbol{J}_c \propto \theta_{SH}(\boldsymbol{\sigma} \times \boldsymbol{J}_s), \tag{3.1b}$$

The values of θ_{SH} reported for various materials vary wildly depending on the method used to produce the sample, the measurement technique used, the properties of the interfaces between the different components of the heterostructure being measured etc..

Material	Spin Hall Angle (θ_{SH})	Method	Source
Pt	0.0037 - 0.11	Non-local, SP, SMR	[7] and the references therein.
W	(-0.14) - (-0.33)	SP, STT-FMR	[7] and the references therein
Au	0.0033 - 0.12	SP, Non-local	[7] and the references therein
$Cu_{1-x}Ir_x$	0.021 - 5	Non-local, SSE	[119, 120]

Table 3.1: Examples of spin Hall angles, θ_{SH}, for various materials as measured by various techniques. Even a single material can have a range of spin Hall angles. (SP:spin pumping, SMR: spin Hall magnetoresistance, STT-FMR: spin transfer torque-ferromagnetic resonance, SSE: spin Seebeck effect)

Table 3.1 lists θ_{SH} for a few materials showing the wide variety in the measured values. Some entries were taken from the substantive summary provided in Ref. [7].

The primary material of interest for the work performed here is platinum (Pt) for which a large positive value for θ_{SH} is usually reported, however tungsten (W) and tantalum (Ta) are both commonly utilised. One problem that can possibly arise from using Pt is the possibility of a proximity induced magnetisation arising when placed in contact with a magnetic layer since Pt is close to the Stoner criterion for the onset of ferromagnetism [122, 123], although whether this accounts for the SMR effect (see next section) in such systems is contested [124–126].

3.1.2 Spin Hall Magnetoresistance

Only days apart in 2013, two research groups reported that the direction of the magnetic moment in the ferrimagnetic insulator (FMI) YIG ($Y_3Fe_5O_{12}$) could be detected via electrical measurements of a Pt layer grown on top of the magnetic insulator[1] [13, 128]. In response to an applied charge current through the Pt layer, the SHE generates a spin current directed towards the YIG/Pt interface where a spin accumulation $\boldsymbol{\mu}_s$ builds up. The resistance of the Pt top layer depends on the relative orientation between the polarisation of $\boldsymbol{\mu}_s$ and the magnetic moment $\boldsymbol{m}$ of the YIG [13, 124, 128, 129]. The application of an external field $\boldsymbol{H}$ can then change the direction of $\boldsymbol{m}$ leading to a modulation of the Pt resistance as a function of θ, the angle between $\boldsymbol{m}$ and $\boldsymbol{\mu}_s$. The resistance of the Pt is maximised when $\boldsymbol{m} \perp \boldsymbol{\mu}_s$ and the spin current is absorbed by the magnetisation of the YIG (see Fig.3.3a). When $\boldsymbol{m} \| \boldsymbol{\mu}_s$, the generated spin accumulation is reflected by the magnetisation (see Fig.3.3b). The reflected part of $\boldsymbol{\mu}_s$ is reconverted to a charge current by the ISHE, causing the net current flow to be larger and the resistance of the Pt is correspondingly minimal. This effect is known as spin Hall magnetoresistance (SMR). The majority of SMR studies have focussed on normal metal (NM)/FMI heterostructures where $\boldsymbol{m}$ follows $\boldsymbol{H}$, resulting in what is conventionally known as positive SMR [13,

[1] It is worth noting that a couple of years before this, a magnetoresistance effect was reported in Pt/Co/Pt originating from the Co/Pt interface [127]. This effect was also due to spin Hall magnetoresistance but it was not recognised at the time.

124, 130–132]. The SMR also appears in completely metallic systems where the FMI is replaced by a metallic ferromagnet [127, 133–136] and can display unidirectional behaviour based on the differing diffusion properties between majority and minority spins [137–140]. Furthermore the effect is observed in antiferromagnetic insulators where it is sensitive to both the antiferromagnetic Néel order [r1, r10, r19, r14, 14, 15, 141], but also the possible emergent moment from canting of the sublattices or the interface [r9, r19, 142].

Theory of the Spin Hall Magnetoresistance

The theoretical explanation of SMR was published shortly before the experimental results [129]. This phenomenology has since been extended to include AFM/NM bilayers where the Néel vector is also relevant [143]. Within the NM, the diffusive spin current perpendicular to the flowing charge current, originating due to the SHE, approaches the NM/vacuum interface where it must tend to zero. Meanwhile at the NM/FMI interface (z=0), it is governed by the complex spin mixing conductance per unit area $G_{\uparrow\downarrow}$ and the spin accumulation $\boldsymbol{\mu}_s$ [129, 144, 145],

$$e\boldsymbol{j}_s^{z=0}(\boldsymbol{m}) = G_r \boldsymbol{m} \times (\boldsymbol{m} \times \boldsymbol{\mu}_s) + G_i\,(\boldsymbol{m} \times \boldsymbol{\mu}_s), \tag{3.2}$$

where $\boldsymbol{m}$ is the vector representing the magnetic moment of the FMI and $G_r\,(G_i)$ is the real (imaginary) part of $G_{\uparrow\downarrow}$. The component flowing in the $\hat{z}$ direction then leads to an additional charge current in the xy-plane due to the ISHE which is modulated depending on the reflection that occurs at the FMI/NM interface. The longitudinal and transverse Hall currents are then modified by terms related to the spin Hall effect of $\mathcal{O}(\theta_{SH}^2)$. Expressions can be derived for the change in the resistivity of the NM due to the SMR for both the longitudinal ($\Delta\rho_{long}$) and transverse ($\Delta\rho_{trans}$) components,

$$\Delta\rho_{long} \propto \Delta\rho_1 \left(1 - m_y^2\right), \tag{3.3a}$$

$$\Delta\rho_{trans} \propto \Delta\rho_1 m_x m_y + \Delta\rho_2 m_z, \tag{3.3b}$$

where ρ_1 and ρ_2 are constants proportional to θ_{SH}^2, dependent on the the material parameters of the NM and, respectively, the real and imaginary components of $G_{\uparrow\downarrow}$ [129]. The magnetisation enters through the x (m_x), y (m_y) and z (m_z) components.

Temperature dependent measurements of the SMR demonstrate that generally the SMR ratio decreases with decreasing temperature although the explanations provided are not congruent. Ref. [131] attributes the decrease to a dependence of the spin diffusion length of the Pt with T, whilst $G_{\uparrow\downarrow}$ and the spin Hall angle are temperature independent. Ref. [132] meanwhile suggest a temperature independent spin diffusion length but a temperature dependent spin Hall angle of the Pt, yet also maintain a temperature independent value of $G_{\uparrow\downarrow}$ whilst Ref. [146] attribute the change in the SMR ratio to a variation in the interface transmissivity to spin, i.e. a temperature dependence of $G_{\uparrow\downarrow}$.

Alongside the SMR, there is also the possibility of anisotropic magnetoresistance (AMR) due to proximity induced magnetism in the neighbouring heavy metal. Here the resistance of a magnetic material is modulated as a function of the angle between the magnetisation and the probing current, however this can be disentangled by choosing the plane the magnetic field is rotated in, Fig. 3.3c – Fig. 3.3f, since the angular dependences of the SMR and AMR are distinctly different.

The above discussion has mostly focussed on explanations of the SMR for insulating ferromagnets, however it is antiferromagnets that are of more interest at the present

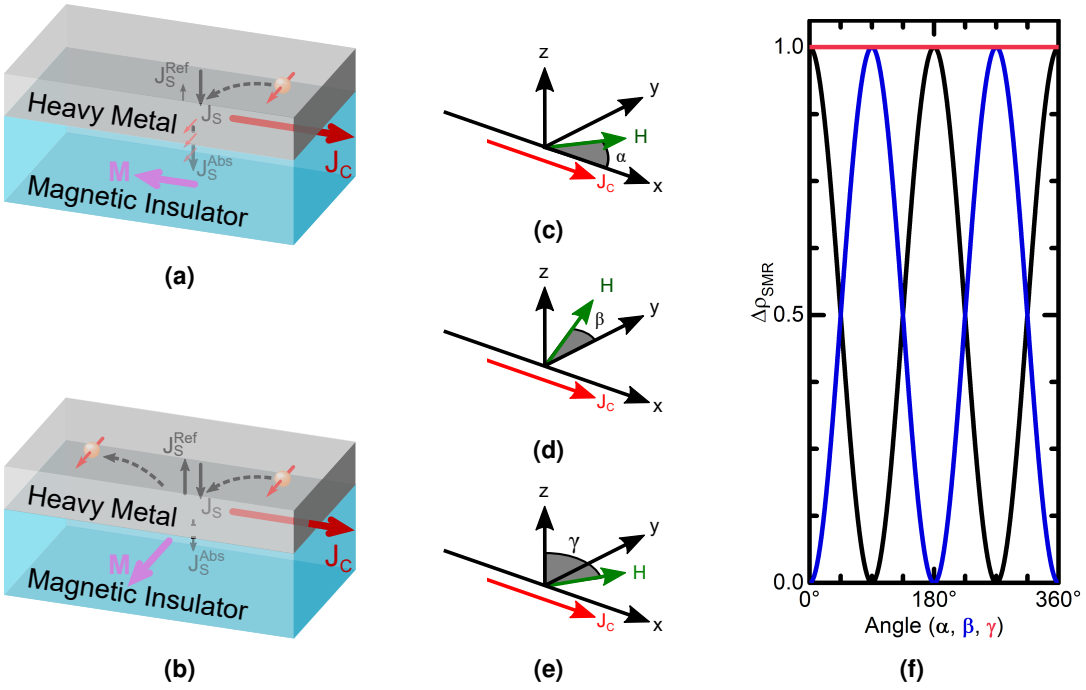

Figure 3.3: a) Sketch of the SMR mechanism in a heavy metal/magnetic insulator bilayer. For a perpendicular alignment of the magnetic order parameter and the spin accumulation, a spin current is absorbed resulting in a higher resistance state. b) For a parallel alignment, there is a large reflected spin current that is reabsorbed by the ISHE, resulting in a lower resistance state. c) - e) Sketches of the coordinate systems for the α, β and γ angle defining rotation in the xy-, yz- and xz-planes, respectively. f) Ideal behaviour of the heavy metal resistance in the three planes for a ferromagnetic insulator in the absence of AMR as a function of the angle between the charge current and the magnetic order parameter.

moment. It has recently been theoretically shown that the phenomenological explanation of the SMR can easily be extended to antiferromagnets [143]. The magnetisation of the ferromagnet is replaced by the magnetic ordering parameters of the antiferromagnet; the Néel vector $\boldsymbol{n}$ and the field induced magnetisation $\boldsymbol{m}$. Eqn. 3.2 is then modified to include the Néel vector but further to this, $G_{\uparrow\downarrow}$ now represents the transfer of angular momentum from the heavy metal not only to $\boldsymbol{m}$ but also to $\boldsymbol{n}$ [143],

$$e\boldsymbol{j}_s = G_r^m \boldsymbol{m} \times (\boldsymbol{m} \times \boldsymbol{\mu}_s) + G_i^m (\boldsymbol{m} \times \boldsymbol{\mu}_s) + G^n \boldsymbol{n} \times (\boldsymbol{n} \times \boldsymbol{\mu}_s), \tag{3.4}$$

where G_r^m (G_i^m) and G^n represent the real (imaginary) magnetic and Néel spin mixing conductances respectively, on the assumption of no sublattice symmetry breaking of the antiferromagnetic interface. Experimentally, one would then expect the resistivity of the HM layer to be modulated as a function of the angle between $\boldsymbol{n}$ and $\boldsymbol{\mu}_s$. In general, the minimum in the magnetic free energy of an AFM comes for a perpendicular alignment of $\boldsymbol{n}$ and $\boldsymbol{H}$, which would mean that the SMR would present a 90° phase shift relative to the FM case and be best described by $\sin^2\alpha$ (rather than a $\cos^2\alpha$ function) for an in-plane magnetic field. However, this relies on the assumption that $\boldsymbol{n}$ is free to rotate with $\boldsymbol{H}$. Indeed, SMR has been observed in AFMs, with the first report demonstrating *positive* SMR [142], but other more recent reports showing a *negative* SMR with the expected 90° shift of the signal with respect to the FM case [r1, 14, 15]. There is furthermore disagreement about the role of the emergent magnetic moment $\boldsymbol{m}$ in canted AFMs with

both 'positive" [r9, r19] and "negative" signals observed [r10, r14]. The case of AFM-SMR and its suitability for the extraction of AFM anisotropies will be discussed in further detail in Ch. 5 based on results obtained in the course of this thesis. These results have been summarised in Refs. [r10] and [r14].

3.1.3 Other Magnetoresistance Effects

As well as the OHE and SMR, the application of a magnetic field also leads to additional magnetoresistive effects, where the electrical resistance of the material changes value, with different symmetries with respect to the magnitude and direction of the applied field and associated magnetisation direction. These other effects can also come into play when making measurements of the SMR such as contributions from the parabolic ordinary magnetoresistance (OMR) that can appear in metals [r1, 16, 147]. The different magnetoresistive effects can be distinguished by those that directly depend on the applied magnetic field such as the OMR or those that depend indirectly on the magnetisation of the materials under investigation like AMR.

3.2 Spin Seebeck Effect

The classical Seebeck effect [148] (and the reciprocal process known as the Peltier effect [149]) is the generation of a charge current (thermal gradient) in response to a thermal gradient (charge current) and is used extensively in thermoelectic generators. Just as there exists a spin analogue for the Hall effect, there is also a spin analogue for the Seebeck effect, the spin Seebeck effect (SSE), first claimed to be observed by Uchida *et al.* in the ferromagnetic metal permalloy (Py:$Ni_{81}Fe_{19}$) [150]. The SSE is the production of a spin current by thermally generated collective excitations (the spin Peltier effect has also been reported [151]). Although doubts were raised about the true origin of the signal seen in this initial work, with multiple groups unable to replicate the initial result e.g. [152, 153], a thermally induced signal that was dependent on the magnetisation was observed in a ferrimagnetic insulator in contact with a heavy metal in a different geometry that allows one to rule out certain parasitic effects [154, 155]. Experiments with the addition of a copper interlayer were able to remove any doubts about the validity of the SSE as a mechanism to excite magnonic spin currents. However the observation of a spin Seebeck effect on the femtosecond timescale, where there is not enough time for a thermal gradient in the magnetic insulator itself to develop, also demonstrates the potential for a contribution from the thermal gradient across the interface [119]. Aside from the commonly used ferrimagnetic insulator YIG, the spin Seebeck effect has also been observed in other iron garnets such as the compensated garnet gadolinium iron garnet (GIG: $Gd_3Fe_5O_{12}$) [155], spin ferrites like $NiFe_2O_4$ [153, 156] and the paramagnetic garnet $Gd_3Ga_5O_{12}$ (GGG) [157]. In the case of AFMs, the SSE is only observed when a significant field induced magnetisation $\boldsymbol{m}$ appears. This condition has been met in, for example, the easy-axis insulating AFMs Cr_2O_3 [158, 159] and MnF_2 [160] at high magnetic fields and low temperatures.

3.3 Transport of Magnons

The field of magnonics relies on the generation, transport, interaction and detection of magnons. The generation of magnons can be achieved in several ways including

the previously mentioned spin Seebeck effect. However, regardless of the excitation mechanism used, the created magnons travel away from the point of excitation, in the simplest model, in a diffusive manner. Making use of magnons for devices relies on understanding the magnon transport properties of different materials [8, 9, 82]. This section will discuss the concept of fully electrical, non-local measurements of magnon transport in magnetic insulators, followed by a discussion of the works investigating the transport of magnons through antiferromagnetic materials.

3.3.1 Non-local Spin Injection and Transport of Magnons

In the course of this thesis, magnon transport has been investigated in the so-called *non-local* geometry whereby the magnetic material under investigation is contacted with two spatially and electrically isolated electrodes produced by electron beam lithography (Sec. 4.2.5.2). One electrode acts as the source of magnon excitation (*injector*), whilst the other serves to detect the magnon transport some distance away (*detector*). This geometry was first used to investigate the long distance propagation of magnons in the insulating ferrimagnet $Y_3Fe_5O_{12}$ (YIG) in 2015 by Cornelissen *et al.* [161] and Goennenwein *et al.* [162] and allows for the complete electrical excitation and detection of magnons without the need for microwave [97, 108, 163] or thermal [154, 155, 164] excitations of a spin current in a magnetic insulator. Following the application of this geometry to YIG, it has since been applied to several other ferro(i)magnetic insulators [165, 166]. Through a gate electrode placed between the injector and detector, this geometry also allows for active manipulation of the magnon transport [r5, 167–169]. This additional electrode then allows for either a direct manipulation of the magnon population in the magnetic insulator [167, 168] or to locally manipulate the magnetic order and by extension the local transport properties through magnetic fields and heat [r5].

The concept of a normal metal/ferromagnetic insulator/normal metal (NM1/FMI/NM2) trilayer, where a charge current passed through NM1 induces a voltage in NM2 and vice versa, was first proposed by Zhang and Zhang [170, 171] in response to an experimental paper a few years before [172]. The proposed mechanism by which this voltage was induced, magnon mediated current drag, is similar to the Coulomb drag seen in two-dimensional electron gases separated by an insulator where the electrical current carried by one electron gas induces a voltage in the other [173]. The one dimensional trilayer geometry considered allows the magnon current to flow perpendicular to the plane of the individual layers. The passing charge current in NM1 leads to a transverse spin current due to the SHE and a spin accumulation builds up at the interface between NM1 and the FMI. The total angular momentum across the interface needs to be conserved in the transfer between the spin current in the NM (with density δm_s) and the magnon current in the MI (with density δm_m), resulting in the boundary condition at the NM1/HM interface of,

$$G_{em}\delta m_s\left(0^-\right) - G_{me}\delta m_m\left(0^+\right) = 0 \tag{3.5}$$

where the G_{em} and G_{me} are two coefficients that represent the interfacial conductance for the conversion between the electron and magnon spin currents. The first term is the creation of a magnon current in the presence of an electron spin accumulation whilst the second term is the inverse effect, the creation of a spin current in the presence of a magnon accumulation. There is then *s-d* exchange coupling due to an overlapping of electron wavefunctions in NM1 and the MI which acts as a *spin-bias* across the interface

of the form [171],

$$\mathcal{H}_{sd} = -\mathcal{J}_{sd}\sqrt{\frac{S}{2N_s}}\sum_{\boldsymbol{k},\boldsymbol{q},\boldsymbol{k'}}\left(a^{\dagger}_{\boldsymbol{q}}c^{\dagger}_{\boldsymbol{k}\uparrow}c_{\boldsymbol{k'}\downarrow} + a_{\boldsymbol{q}}c^{\dagger}_{\boldsymbol{k'}\downarrow}c_{\boldsymbol{k}\uparrow}\right)\delta_{\boldsymbol{k'}} = \boldsymbol{q} + \boldsymbol{k} \tag{3.6}$$

where $\mathcal{J}_{\text{sd}}$ is the exchange integral for the system, $a^{\dagger}_{\boldsymbol{q}}$ ($a_{\boldsymbol{q}}$) are the creation (annihilation) operators for magnons, and $c^{\dagger}_{\boldsymbol{k}\uparrow}$ ($c_{\boldsymbol{k}\uparrow}$) and $c^{\dagger}_{\boldsymbol{k}\downarrow}$ ($c_{\boldsymbol{k}\downarrow}$) are the creation (annihilation) operators for spin up and spin down electrons. Furthermore, S is the spin per atom of the FMI and N_{s} is the number of atomic spins of the FMI at the interface. This theory disregards spin transfer torques for the transfer of angular momentum, contrary to SMR [13, 129], but instead focusses on the creation of high frequency magnons allowed at finite temperatures ($\hbar\omega$ = k_BT). At equilibrium, the net transfer of angular momentum in the form of a spin current across the interface is zero. However, in the presence of a non-equilibrium spin or magnon distribution (whether an accumulation or depletion), a net spin current flows across the interface.

This theory then accounts for both the excitation of non-equilibrium magnons polarised based on the polarisation of $\boldsymbol{\mu}_s$ in the ferro(i)magnetic insulator at the NM1/FMI interface and for the creation of a spin current in response to a magnon accumulation at the FMI/NM2 interface. At the FMI/NM2 interface, the amplitude of the magnon accumulation or depletion is smaller that that below the injector due to relaxation processes. Nevertheless, angular momentum is *pumped* into NM2 where it polarises the spin of conduction electrons diffusing from the interface. These induce a transverse charge motion due to the ISHE and thus a measurable voltage. Although the diffusion and relaxation of non-equilibrium magnons was first investigated in a non-local geometry with electrodes deposited atop the magnetic insulator YIG [161, 162] (see Fig.3.4), electrically driven magnon transport was also later demonstrated in a Pt/YIG/Pt trilayer system, the geometry described by Zhang and Zhang, confirming the validity of the non-local geometry employed elsewhere [174, 175]. However, the production of such trilayers is challenging from an experimental point of view, and the 2D non-local geometry is far more practical. Furthermore, it has the distinct advantage over the 1D trilayer system in that the transport properties of the excited magnons can be easily investigated by varying the separation between the two electrodes.

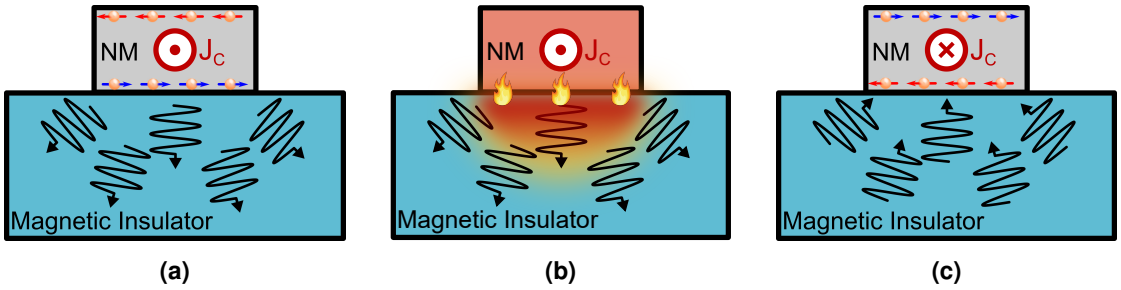

Figure 3.4: Schematic of non-local magnon excitation in a magnetic insulator. A charge current $\boldsymbol{J}_c$ passing through a normal metal (NM) injector leads to an excitation of magnons a) that diffuse away from the injector. This occurs due to either the interfacial spin accumulation from the SHE and also via b) Joule heating and the thermally induced SSE. c) The spin current is reconverted to a charge current in a NM detector by the ISHE and is the reciprocal of a).

Alongside magnons excited by the spin accumulation at the NM1/FMI interface, the passing charge current leads to Joule heating of the magnetic insulator below and thus a

thermal excitation of magnons via the SSE (Fig. 3.4b). This then gives rise to a non-local SSE [176–178]. Furthermore, one must be careful when drawing parallels between the local and non-local SSEs given that the local effect will be sensitive to all excited magnon modes [179] whilst the non-local effect will only be sensitive to the modes that allow for the long distance propagation and that arrive at the detector.

The dependence on the propagation length of magnons with respect to frequency has been studied in ferromagnets and antiferromagnets, whereby lower energy magnons have longer propagation lengths [164, 180–182]. The propagation length is maximal close to the frequency gap before decreasing with higher frequency [164, 182]. This frequency dependence for ferromagnets and antiferromagnets is given by [164],

$$\xi_{FM}(\omega) \propto \frac{1}{2\alpha\hbar\omega}\sqrt{1-\left(1-\frac{\hbar\omega-2d_x}{\mathcal{J}}\right)^2}, \tag{3.7a}$$

$$\xi_{AFM}(\omega) \propto \frac{\sqrt{H_0^2-(\hbar\omega)^2}}{\alpha H_0\hbar\omega}\sqrt{1-\left(\frac{\sqrt{H_0^2-(\hbar\omega)^2}}{2|\mathcal{J}|}-2\right)^2}, \tag{3.7b}$$

where $\mathcal{J}$ is the exchange and d_x is an anisotropy constant.

Magnon Chemical Potential

Whilst the described theory may demonstrate the creation and absorption of magnons, it has several shortcomings when it comes to explaining the diffusive transport of the excited magnon current $\mathbf{j}_m$, not least the fact that it cannot distinguish between electrically and thermally excited magnons since it considers only a net magnon population. Instead, long range magnon transport in magnetic insulators is explained based on the concept of a magnon chemical potential μ_m [183] rather than the magnon density or magnon temperature. The magnon chemical potential has also been theoretically discussed in the context of AFMs [184, 185]. It is reasonable to assume that the magnon-phonon relaxation is fairly efficient such that the diffusive magnon transport is described by [183, 185, 186],

$$\mathbf{j}_m \propto \nabla\mu_m \tag{3.8}$$

The magnon chemical potential has been directly detected in YIG [187]. It has been shown to be directly modified by the spin accumulation that builds up in a neighbouring heavy metal electrode as well as the deposited heat from the Joule heating, exponentially decaying with distance on the length scale of l_m [183–185, 187].

3.3.2 Magnon Transport Through Antiferromagnets

The transport of magnons in AFMs has been mostly studied in what can be termed a *vertical* geometry where the sample under investigation consists of a trilayer of a FMI/AFM/HM as shown in Fig. 3.5 [r2, r8, 97, 164, 188, 189]. One way in which this geometry is utilised involves the spin current being generated in the FMI by either the SSE [r2, 164, 190] or by ferromagnetic resonance [97, 188], and this then flows towards the FMI/AFM interface. Passing into the AFM layer, the spin current is then attenuated before passing into the HM capping layer, which can be in principle any metal with a significant spin Hall angle. The spin current is then converted into an easily detectable voltage by the ISHE. At each interface, the FMI/AFM and AFM/HM interfaces, the transmission of the spin current across the interface will rely on the spin mixing conductance

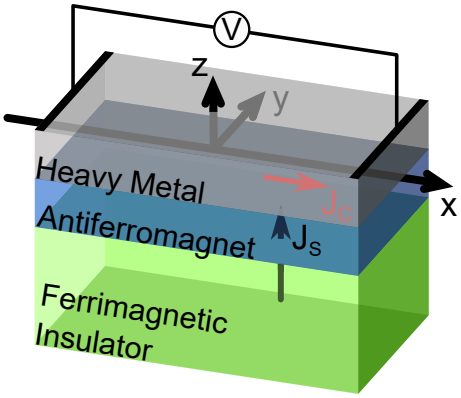

Figure 3.5: Schematic demonstrating the vertical geometry that has been employed to investigate magnon transport through antiferromagnets. The spin current $\boldsymbol{J}_s$ is generated in the ferrimagnetic insulator, diffuses across the antiferromagnet before being detected in a heavy metal.

of each [144, 145, 191, 192]. Alongside this there is also the intrinsic decay of the spin current through the AFM layer which relies on the magnon population of the AFM as well as the (frequency dependent) propagation length (Eqn.3.7b). Such trilayers can also be used in reverse whereby the spin current now originates from the SHE in the HM layer. It flows towards the HM/AFM interface and then diffuses across the AFM before being reflected or absorbed by the magnetisation of the FMI layer below, resulting in a modulation of the HM resistance [r8, 193]. In this case, the reflected spin current passes through the AFM layer twice and is thus exposed to twice the attenuation effects and can exhibit a change of sign in the SMR signal depending on whether the FMI or AFM layer dominates [r8]. Metallic AFMs can also be employed which take the role of both the AFM and the HM in a single layer [164]. Regardless of which method is used, the transport properties and spin diffusion lengths of several AFMs can evaluated by varying the thickness of the inserted antiferromagnetic layer including insulating antiferromagnets of different structures [r2, r8, 188, 190] and metallic antiferromagnets such as IrMn [164, 194, 195] or FeMn [194–196]. Table 3.2 gives a list of some antiferromagnetic spin diffusion lengths that have been evaluated in this manner.

Regardless of method, antiferromagnetic ordering or conductivity, all of the works listed in Table 3.2 have in common that the evaluated spin diffusion lengths are in the range of 1-10 nm. However, one would at least expect that, even if antiferromagnets are incapable of transporting a magnon current efficiently, that there would be a difference between metallic and insulating antiferromagnets since in the latter case the lack of conduction electrons should lead to a significantly lower magnetic damping. However this is not observed. One possible explanation could be the varying characteristic frequencies of the FMI and AFM layers where, even though some of the magnon mode frequencies will overlap, the majority of the AFM modes will lie at far higher frequencies given the much larger exchange energy. Given the inverse relationship between the frequency and the propagation length scale, with the maximum propagation length occurring for frequencies just above the frequency gap [164, 182] (Eqn. 3.7a and Eqn. 3.7b), the propagation length of the FM magnons that exceed the AFM magnon gap will be very small. This then means that the majority of the magnons reaching the FMI/AFM interface will have frequencies lying in the AFM magnon gap, and thus should not illicit a significant response, instead driving evanescent magnon excitations far below the AFM

Insulating Antiferromagnets:

AFM	Ordering	Spin Diffusion Length (nm)	Method	Source
NiO	Easy-plane	1-10	SMR, SP, SSE	[r2, r8, 188, 197, 198]
Cr_2O_3	Easy-axis	1.6	SP	[188]
a-NiFeO	Amorphous	6.3	SP	[188]
a-YIG	Amorphous	3.9	SP	[188]
CoO	Easy-plane	2	SP	[190]

Metallic Antiferromagnets:

IrMn	Polycrystalline	1-10	SSE	[164]
$Fe_{50}Mn_{50}$	Polycrystalline	0.8-6	SP	[194–196]
$Ir_{20}Mn_{80}$	Polycrystalline	0.7	SP	[194, 195]

Table 3.2: Table of evaluated antiferromagnetic spin diffusion lengths for differing insulating and metallic antiferromagnets by various methods. (SMR: spin Hall magnetoresistance, SSE: spin Seebeck effect, SP: spin pumping)

resonance frequency [164, 192].

As well as varying the thickness of the inserted antiferromagnetic layer, changing the environmental temperature for the measurements can also allow for an investigation into the magnon transport properties of the antiferromagnetic layer [r2, 164, 197, 199, 200]. As the thickness of an antiferromagnet is reduced below a certain point, the Néel temperature correspondingly reduces [201, 202], allowing for the investigation of the diffusion of magnons through the antiferromagnetic layer both above and below T_N if the film is thin enough. Several works claim to see an enhancement of the signal at T_N of this AFM layer, even labelling it as a spin analogue of colossal magnetoresistance [200], i.e. *spin colossal magnetoresistance*, whereby the spin conductivity of the trilayer can be enhanced by changing the temperature [197, 199, 200, 203, 204]. The overall temperature dependence of the trilayers follows the temperature dependence of the antiferromagnetic susceptibility, which is maximal in the region of the Néel temperature. Additionally, the reduction of the magnetic anisotropy of the antiferromagnetic layer as the Néel temperature is approached from below leads to increased thermal fluctuations. There are thus more excitations available to carry angular momentum from the ferro(-i)magnetic layer to the heavy metal detection layer. Other reports, however, have failed to see such an enhancement [r2, 189]. There have also been reports of an enhancement of the spin signal for very thin layers of AFM material and further signal suppression as the thickness increases beyond the extracted spin diffusion length [188, 190–192, 198] but other groups fail to see such an enhancement [r2, 193] or even a change of sign in the measured signals with increasing thickness [r8, 196]. Regardless of the existence of these enhancements, from whichever origin, the measured values of the spin diffusion lengths still fail to exceed 10 nm.

Given that AFMs have been shown to host spin waves [83–85], the question now arises as to how are such excitations transported across large distances, especially in AFMs with a low magnetic damping. From a theoretical point of view, AFMs should be as efficient as FMs in transporting magnons [185, 205]. A spin accumulation should be able to excite propagating magnons in easy-axis AFMs where the electron-magnon coupling and heat transfer at the HM/AFM interface is considerable stronger than in FM based systems [184, 206]. In a FMI, there is only one magnon polarisation able to carry angular momentum as a spin current whilst in a two-sublattice AFM, both magnon modes contribute to the spin transport. The total z component of the spin angular momentum carried by the AFM magnons is then given by $\sum_{i,j}\left(S_i^z + S_j^z\right)$, where i, j represent the spins on the i^{th}, j^{th} lattice sight. This can be written in terms of magnon creation (annihilation) operators for the two modes (c.f. Sec. 2.4.1) as [88, 191],

$$S^z = \sum_k \left(-\alpha_k^\dagger \alpha_k + \beta_k^\dagger \beta_k\right), \tag{3.9}$$

and a spin current density operator can be constructed for a volume V as,

$$\vec{J}_S^z = \frac{\hbar}{V}\sum_k \left[-\vec{v}_{\alpha k}\alpha_k^\dagger \alpha_k + \vec{v}_{\beta k}\beta_k^\dagger \beta_k\right], \tag{3.10}$$

where $\vec{v}_{ik}$ is the group velocity of the i^{th} mode. In the absence of a magnetic field, the two modes are degenerate and the group velocities are equal. Given that each mode carries equal but opposite angular momentum, there is no net spin current. This degeneracy is lifted in a magnetic field and a net spin current is possible [88, 205, 207]. With increasing magnetic field, the condition for the AFM spin flop will eventually be reached. In the vicinity of the spin flop transition, when Gilbert damping dominates the transport time scale, the conductance of the surviving magnon mode shows a sharp increase [205, 207]. In the case of the non-interacting regime, where there is no magnon-magnon scattering, this would lend itself to an algebraic decay of the spin conductance with distance and the AFM tends towards a zero spin resistivity [205, 207]. However, structural transport experiences a bottleneck in the diffusive regime caused by the interfacial resistance at the NM/AFM interfaces [207]. The spin-bias transport signal in the diffusive regime would then experience an enhancement in the region around the spin flop [207]. A more detailed discussion on AFM magnons and the corresponding dispersion relations of magnons in AFMs with different magnetic structures can be found in Sec.2.4.1.

The non-local technique was used to investigate long distance, diffusive transport of magnons through the antiferromagnetic insulator hematite (α-Fe_2O_3). Whilst there are obviously strong parallels that can be drawn with the non-local measurements that have been performed on YIG and other FMIs, there are key differences when the measurements are performed in AFMs. These results are presented in Ch. 6 and Ch. 7, and published partly in Refs. [r3], [r15], and [r13].

3.3.2.1 Non-Diffusive Transport

In recent years, theoretical interest has arisen concerning how to transport spin currents in a non-diffusive manner [20–22, 208, 209], a so-called spin-superfluid transport (SSF), the spin analogue of superconductivity, where a phase gradient of the magnetic order facilitates the transport of spin excitations in a dissipationless manner [210].

Through techniques such as laser heating or parametric pumping [211, 212], Bose-Einstein condensation (BEC) of magnons can be initiated in the ferrimagnet YIG and also in antiferromagnets such as $CMnO_3$ and CsMnFl [83–85]. The question then arises of how to transport such a BEC of magnons as, once the excitation is turned off, the magnons quickly return to having a distribution of momentum states. Several theoretical works have argued that true SSF is not possible in ferromagnetic materials, including YIG. This is due to long range dipolar coupling of the magnetic moments disrupting the state and thus coherent transport is not possible, preventing the transport of magnons in the low dissipation regime [23, 209, 213]. However, in antiferromagnetic materials, the dipolar coupling is very weak compared to other interactions and it has been predicted that a spin current may be transported through an AFMI where the only losses would come from the intrinsic magnetic damping of the material, rather than from the numerous other dissipation paths that normally lead to diffusive transport [20, 23].

If a HM1/AFMI/HM2 trilayer is considered, similar to the geometry originally proposed for non-local magnon drag [170, 171] (Sec. 3.3.1), then an electrical current applied in the left hand HM electrode would lead to a spin accumulation building up at the HM1/AFMI interface. This spin accumulation would then exert a torque on the Néel vector of the AFMI. Considering an AFMI with an easy-plane symmetry, oriented such that $\boldsymbol{n}$ is parallel to the direction of travel, a spin accumulation perpendicular to the easy-plane and a small magnetic field is applied parallel to the spin accumulation, i.e. perpendicular to $\boldsymbol{n}$. If the torque exerted by $\boldsymbol{\mu}_s$ on $\boldsymbol{n}$ is sufficient, a precession of $\boldsymbol{n}$ can be excited across the length of the AFMI. This precession would then travel incident on the AFMI/HM2 interface, pumping angular momentum into HM2, which subsequently generates an electronic spin current that is reconverted into a charge current via the ISHE. If there is, as found in real materials, an in-plane anisotropy, there would exist a critical spin accumulation required to overcome this anisotropy and induce the coherent precession of $\boldsymbol{n}$ [20, 21]. The transported signal is expected to decay algebraically rather than exponentially with distance with the remaining losses arising from the inherent Gilbert damping of the magnetic material. A simplified example of this is shown in Fig. 3.6 where the non-diffusive transport is shown as a simple linear decay [20, 21, 208]. In reality, this would be represented by some non-exponential function on a given length scale unlike diffusive transport, which experiences an exponential decay [161].

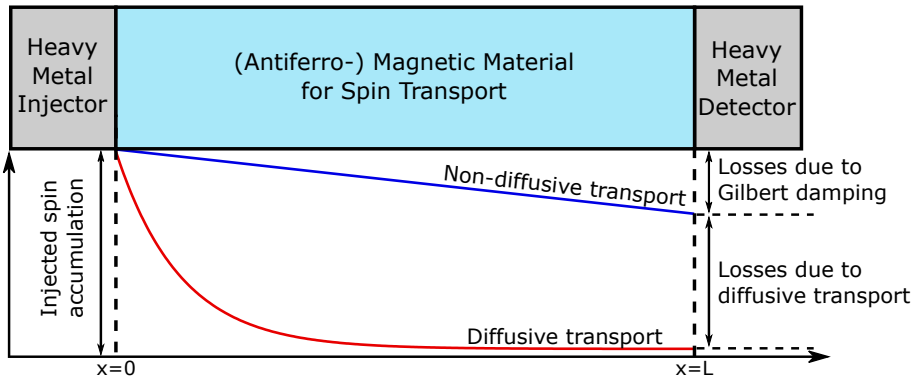

Figure 3.6: Simplified schematic comparison of diffusive (red) versus non-diffusive (blue) transport through a magnetic material bounded by a heavy metal source and sink of spin current. The two transport regimes show a different decay as a function of distance.

However, all of the work on magnon transport in AFMs presented in Ch. 6 and Ch. 7 exists in the diffusive regime and at the time of writing, no conclusive evidence of SSF

in AFMs has been experimentally presented. There have been some experimental reports on long distance spin transport where the distance dependence does not follow an exponential decay [169, 214, 215]. In Ref.[214], the authors claim non-diffusive transport in thin films of the AFM Cr_2O_3, which appears to show some of the hallmarks of true non-diffusive magnon transport. Meanwhile, spin transport was also claimed via the quantum Hall effect in the antiferromagnetic ground state of graphene at ultra low temperatures [215] and later the 2D antiferromagnet $MnPS_3$ was also reported to host long distance magnon transport [37]. The reports on both Cr_2O_3 and $MnPS_3$ both rely solely on thermally activated spin transport at low temperatures, with no evidence of a spin-bias, implying that the non-coherent thermal excitation has transformed into a coherent precession of the Néel vector [23]. This proves a challenge for evaluating the spin transport properties [r3, 216, 217]. However, the absence of a spin-bias signal at low temperature does not indicate that the interfaces are poor, but is only due to the diffusive nature of the transport. Although the spin-bias signal results in a strongly localised source for the excited magnons, thermal gradients arising from the Joule heating of the injector can extend far from the source and thus care needs to be taken when analysing the transport length scales of thermally generated signals [176, 218–220]. One can also not be certain that the thermal gradient of each device is identical due to variations in the local resistivity of wires, as well as the Joule heating of the injector leading to large local heating (e.g. +70 K in YIG at 300 K for a reasonable injector current [221]) whilst a nearby detector can experience large temperature gradients and heating [221]. This then keeps both the detector and the injector above the temperature of the phonon peak, especially when the local environmental temperature is a few Kelvin [37, 214]. The spatial distribution of the thermal gradient can also lead to additional contributions to the signals the are generated far from the injector where the “distance” is measured to the detector. Additionally, the spin Seebeck signal can be driven in different regimes depending on the thickness of the sample as compared to the spin diffusion lengths [220], and the “non-local” signal can be dominated by heat backflow at large separations.

Meanwhile, non-diffusive transport relies on the coherent rotation of $\boldsymbol{n}$ across the length scales investigated but in thin film antiferromagnets, it is unlikely that a single magnetic domain exists [73, 222, 223] meaning that the magnon current will encounter magnetic domain walls that disrupt the SSF state [224]. Given these problems, it is inconclusive whether the transport regime investigated in Refs [37, 214] is a diffusive thermal regime, a non-diffusive regime or a mixture of both, especially when distances were not extended until the signal disappeared below the noise level. In order to conclusively demonstrate a non-diffusive transport regime, one would need to utilise a single domain antiferromagnet where a spin-bias signal is observed with a clear threshold in spin current density. This signal would need to be verified as a function of distance until the signal falls below the noise levels of experimental measurements and further supported by measurements utilising electrical contacts with low SOC and opposite signs of the spin Hall angle.

The observations in Ref.[169] make use of an additional electrode between the injector and detector of the magnon current. A large current is passed through this central electrode in order to generate a significant spin accumulation at the interface with the underlying YIG. This additional spin accumulation *pumps* magnons into the YIG, modifying the local magnon chemical potential [187]. The flowing magnon current between the injector and detector passes through this region with the modified magnon density

that can lead to an enhancement of the spin current depending on the polarisation of the magnon current. When utilising YIG at room temperature, one has to be careful of electrical effects, where by the resistance of the YIG is heavily reduced [221] and in the presence of a large SOT, the spin conductance can become non-linear due to the excitation of sub-thermal magnons where the energies are on the order of the magnetostatic energy [225]. This effect is effectively the compensation of the magnetic damping by SOT that is observed in nanostructures [226, 227] occurring in a non-local geometry, where the non-diffusive transport only occurs in the region of the compensated damping and becoming diffusive elsewhere. For the observations in Ref.[215], the authors report on AFM graphene devices with only 2 separations. Given that a key determination of a non-diffusive, SSF regime comes from the decay of the signal with distance, it is impossible to ascertain if the observations reported come from SSF or not.

4

Hematite and Experimental Techniques

This chapter will introduce the main material of interest for the work performed in the course of this thesis, the insulating antiferromagnet α-Fe_2O_3, known as the mineral hematite and is the main component of rust. The experimental works performed in this thesis make use of different crystal orientations as well as different orientations of electrical measurement geometries with respect to the magnetic axes. An overview can be found in the appendix Sec. A.8. Aside from the magnetic structure, the temperature and magnetic phase transitions will be discussed before moving to an introduction of the experimental techniques used for the results obtained in this thesis, from the production of samples to the mechanisms by which measurements were made.

4.1 Hematite

One of the antiferromagnetic phases of iron oxide is known as hematite, α-Fe_2O_3 . This common insulating antiferromagnet crystallises in the corundum structure, space group $R\bar{3}m$, and has a Néel temperature $T_N \approx 955\,\mathrm{K}$ in the bulk [228–231]. The structure was first investigated as early as 1925 by Pauling and Hendricks [232] who suggested the iron atoms were positioned in-planes organised along the c-axis. The structure was later refined further to show that the oxygen atoms lie in a close packed hexagonal structure with iron atoms symmetrically occupying two thirds of the octahedral interstices. This means that the positions of the six nearest neighbour oxygen atoms of each iron atom are slightly distorted and conversely, the nearest neighbour iron atoms of each oxygen do not form a regular tetrahedron [233–236]. This crystal structure is shown in Fig. 4.1a. Below T_N, the magnetic moments lie within the basal plane of the tetragonal structure. There is a ferromagnetic coupling within this plane and an antiferromagnetic interplane coupling along the c-axis (see Tab.4.1 for relative strengths). There also exists a small canting of the moments within the basal plane caused by an antisymmetric exchange interaction (DMI) which results in a net magnetic moment $\boldsymbol{m}$ perpendicular to the antiferromagnetic Néel vector $\boldsymbol{n}$, schematically shown in Fig. 4.1b (c.f. Sec. 2.3.6). However, the basal plane is not devoid of anisotropy with the crystalline structure serving to define a three-fold crystalline symmetry within the plane with an associated magnetocrystalline anisotropy field. There then exists three energetically degenerate directions within the basal plane favoured by $\boldsymbol{n}$ in this AFM phase. There is also a contribution from the intrinsic magnetoelastic anisotropy, but as seen in Tab.4.1,

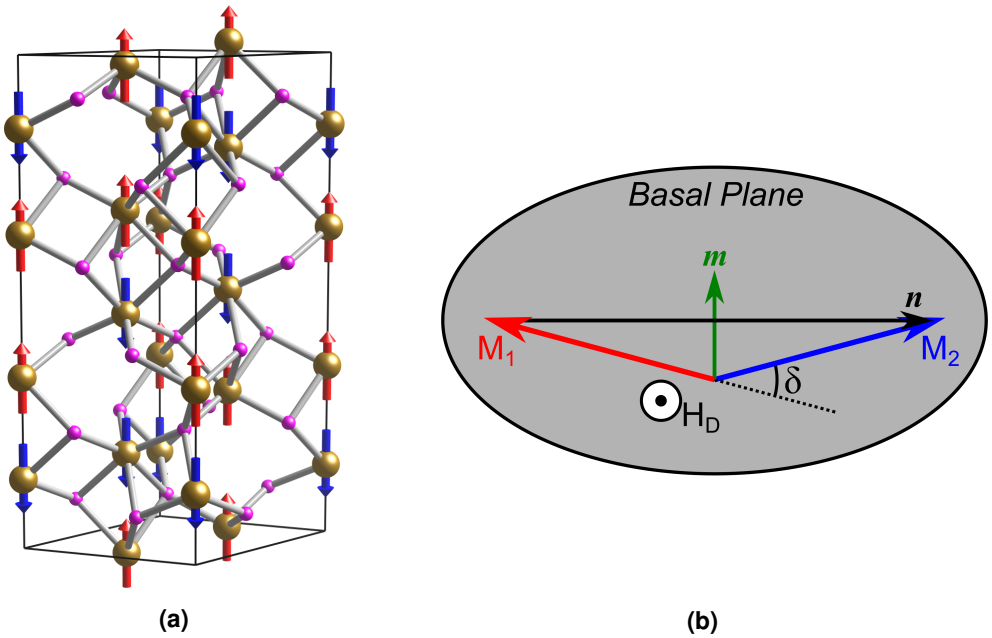

Figure 4.1: a) Unit cell of hematite α-Fe_2O_3 produced using VESTA [237]. The gold coloured atoms represent the Fe atoms whilst the pink coloured atoms indicate the oxygen positions. The spins of the Fe atoms (red and blue arrows) are aligned along the c-axis and represent the antiferromagnetic phase at low temperatures. At high temperatures, b) the spins rotate 90° to lie in-plane and the effective field created by the Dzyaloshinkii-Moriya interaction H_D along the c-axis leads to a canting of the spins within the basal plane, resulting in a canted moment $\boldsymbol{m}$ perpendicular to the Néel vector $\boldsymbol{n}$. The canting angle δ is highly exaggerated for illustration purposes.

both this and the basal plane anisotropy are far smaller than the other terms. When additional stresses are applied to hematite, both of these anisotropies are masked by the net magnetoelastic effects that arise and are an order of magnitude larger than the inherent values [238, 239]. The full magnetic free energy (c.f. Sec. 2.2) of hematite is then given by [29],

$$\begin{aligned}\mathcal{F} = &-\boldsymbol{H}\cdot(\boldsymbol{M}_1+\boldsymbol{M}_2)+\mathcal{J}\boldsymbol{M}_1\cdot\boldsymbol{M}_2-\mathcal{D}\cdot[\boldsymbol{M}_1\times\boldsymbol{M}_2]\\ &-\frac{K_1}{2}\left(\cos^2\vartheta_1+\cos^2\vartheta_2\right)-\frac{K_2}{2}\left(\cos^4\vartheta_1+\cos^4\vartheta_2\right)\\ &+K_E\cos\vartheta_1\cos\vartheta_2+\frac{K_B}{2}\left[\sin^6\vartheta_1\cos 6\left(\varphi_1+\beta\right)+\sin^6\vartheta_2\cos 6\left(\varphi_2+\beta\right)\right]\\ &-\frac{K_{ME}}{2}\left(\sin^2\vartheta_1\sin^2\varphi_1+\sin^2\vartheta_2\sin^2\varphi_2\right),\end{aligned} \tag{4.1}$$

where the first term is the Zeeman term, the second the exchange energy, the third is the DMI contribution and the next two terms are the first and second order anisotropies. Then follows terms describing the anisotropic exchange, basal plane anisotropy and intrinsic magnetoelastic anisotropy, without additional stresses. The angles represent the polar (ϑ and φ) coordinates of a spin on sublattice 1 or 2 with respect to the c-axis, whilst β is an angle from an arbitrary direction in the crystallographic basal plane. The anisotropic exchange ($\propto K_E$) contributes as an additive term to the first order anisotropy whilst $K_B, K_{ME} \ll K_2 \ll K_1$. The exchange term meanwhile encompasses the ex-

change energy between all nearest neighbours, but only the five closest contribute significantly [240]. Even then, the exchange term is dominated by the antiferromagnetic coupling between planes (see Tab.4.1) [240]. Obviously Eqn. 4.1 is challenging to interpret so it is more convenient to introduce equivalent mean fields for each term given by,

$$H_E = -\mathcal{J}M, \quad H_D = \mathcal{D}M, \quad H_{K_1} = \frac{K_1}{M}, \\ H_{K_2} = \frac{K_2}{M}, \quad H_B = \frac{K_B}{M} \quad \text{and} \quad H_{ME} = \frac{K_{ME}}{M}, \tag{4.2}$$

where M represents either $\boldsymbol{M}_1$ or $\boldsymbol{M}_2$. Tab.4.1 lists the magnitudes of these effective fields as well as some other magnetic parameters for undoped hematite. At tempera-

Quantity	Value	Source
H_E	830 T - 1040 T	[29, 240, 241]
Exchange Constants		
Interplane	J_3 = -2.56 meV, J_4 = -2.00 meV	[240]
Intraplane	J_2 = 0.14 meV	[240]
H_D	2.1 T	[29]
$H_{K_1}(T = 0\,\text{K})$	22 mT	[241, 242]
$H_{K_1}(T = T_M)$	-1.18 mT	[241, 242]
$H_{K_2}(T = 0\,\text{K})$	6 mT	[241, 242]
$H_{K_2}(T = T_M)$	3.6 mT	[241, 242]
H_B	0.068 μT	[239]
H_{ME} (stress free)	75 μT	[243]
Spontaneous Magnetisation ($T > T_M$)	2.1 kA/m	[238]
Canting angle ($T > T_M$)	0.065°	[29]
Sublattice Magnetisation ($T = 0$)	900-920 kA/m	[29, 240]
Band Gap	2.1 eV	[29]
Spin Wave Velocity		
$v \| c$-axis	24 km/s	[240]
$v \perp c$-axis	31.6 km/s	[240]

Table 4.1: Magnetic properties of undoped hematite. $H_E \propto (J_1 + 3J_3 + 6J_4)\, S_B + 3J_2 S_A$ where the first term is the (strong, antiferromagnetic) interplane coupling and the second term is the (weak, ferromagnetic) intraplane coupling. J_1 is much smaller than J_3 and J_4.

tures above the Morin transition (see next section), H_{K_2} does not play a role [241, 242], whilst below the transition temperature, both H_{K_1} and H_{K_2} contribute as an additive (temperature dependent) anisotropy field along the c-axis [29, 241].

4.1.1 The Morin Transition

At some critical temperature below T_N, the magnetic moments spontaneously rotate to lie parallel to the c-axis, adopting an easy-axis phase (Fig. 4.1a) and the canted

moment now disappears as seen in Fig. 4.2 from the drop in the magnetisation. This temperature is known as the Morin transition temperature and occurs at $T_M \sim 260$ K in very pure samples of hematite [29, 228, 229, 239, 241, 244, 245]. Despite the name, it was actually first observed in 1914 [246] and then again in 1939 [247] before the namesake F. J. Morin reported this transition [228].

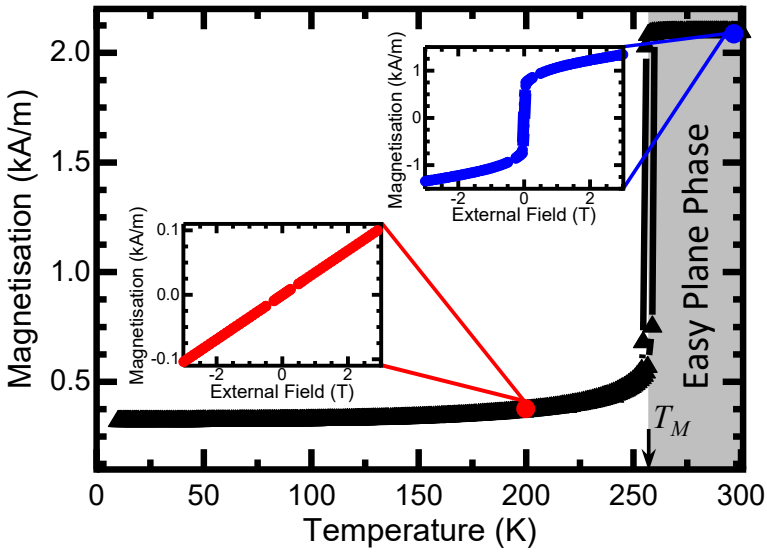

Figure 4.2: Temperature dependence of the magnetic moment of a α-Fe_2O_3 single crystal for a magnetic field applied perpendicular to the c-axis. The Morin transition is visible from a sudden drop in magnetisation at T_M. The insets show measurements of the magnetic moment as a function of magnetic field above (blue) and below (red) T_M evidencing the canted moment in the form of a hysteresis.

A model was proposed to explain the Morin transition through the temperature dependences of the two contributing anisotropies H_{K_1} and H_{K_2} [29, 248]. Given the magnetic structure of hematite above and below the transition, this means that the total anisotropy along the c-axis has to change sign to promote either an easy-axis (> 0) or easy-plane (< 0) antiferromagnet. This would occur if the underlying contributions to H_{K_1} and H_{K_2} have different temperature dependencies and signs. The microscopic interactions have been identified to be magnetic-dipole anisotropy (for H_{K_1}) and single-ion anisotropy (both H_{K_1} and H_{K_2}) where each interaction has a different temperature dependence [249–251]. The magnetic-dipole anisotropy describes differences in the dipolar interaction between two atoms connected along different crystallographic directions [252]. Meanwhile the single-ion anisotropy represents variations in the crystal field generated by all atoms, as felt by a single atom [253]. Given that the crystal structure is not cubic, the crystal field along different crystallographic directions will be inherently anisotropic. Given that H_{K_2} does not apply above T_M [29, 242], and shows weak temperature dependence (remaining around 60 mT from 0 K to about 200 K before dropping gradually to 36 mT at T_M [29, 241]), this indicates that it is the temperature dependence of H_{K_1} that dictates the Morin transition. In terms of the effective fields, the Morin transition occurs when,

$$H_{K_1} = \frac{H_D^2 - 2H_E H_{K_2}}{2H_E}. \tag{4.3}$$

Using the values listed in Tab.4.1, this results in $H_{K_1} = H_{SI} + H_{MD} =$ -1.18 mT. The temperature dependence of the two microscopic anisotropy fields H_{SI} (single-ion

anisotropy) and H_{MD} (magnetic-dipolar anisotropy) are shown in Fig. 4.3. As can be seen, the required value of H_{K_1} occurs just below the intersection (where $H_{SI} - H_{MD} =$ 0) of the two lines, when $T/T_N = 0.282$. For T_N = 965 K, this gives an estimate of $T_M \sim$ 269 K, in excellent agreement with the experimentally observed values [228, 229, 239, 241, 244, 245]. This agreement is made all the more remarkable when considering that this quantitative analysis made use of mean field theory which is based on several simplifying assumptions. Furthermore the value of the exchange field used to estimate the intersection point may be too low and the experimental measurements used to obtain the 0 K values of the anisotropies on which the temperature dependence is based also carry a considerable uncertainty.

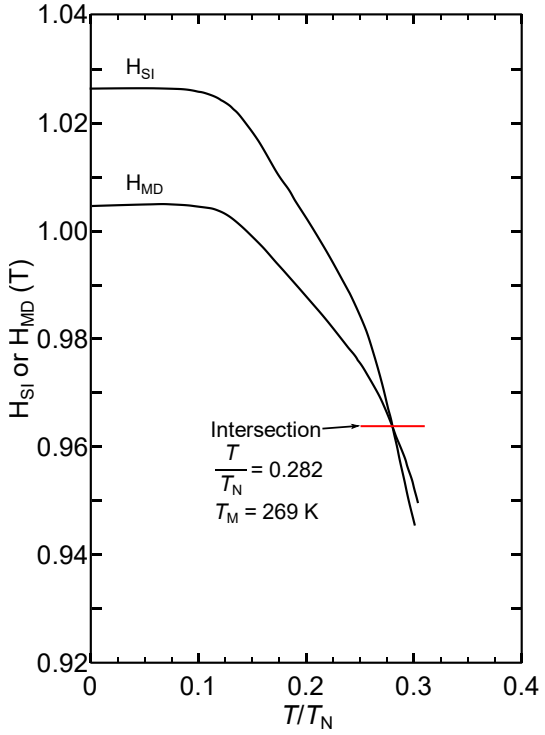

Figure 4.3: Temperature dependence of the single-ion and magnetic-dipole anisotropy fields for hematite. At the Morin transition, $H_{K_1} = H_{SI} + H_{MD} =$ -1.18 mT, just below the intersection point. Fig. adapted from [248].

4.1.1.1 Altering T_M Through Dilute Doping

Although antisymmetric exchange exists in all $XFeO_3$ orthoferrites only α-Fe_2O_3 and $DyFeO_3$ have been shown to have a first order Morin transition from an easy-plane to easy-axis phase [254], however one can slightly tune this temperature by dilute doping [228, 255, 256]. It is worth mentioning that other orthoferrites can show reorientation transitions, but they are not of the same type as the Morin transition. Ref. [254] summarises some of these transitions. If the Morin temperature can be controlled, then the range over which the easy-axis or easy-plane phases are stabilised can be enhanced, even for example allowing for the easy-axis phase at room temperature [230]. The effect of adding dilute dopants to pure hematite crystals has been shown to reduce the Morin transition for the case of almost every dopant investigated including Ti^{4+} [228], Sb^{5+} [255] and Sn^{4+} [256]. However, three dopants have been shown to actually increase the Morin transition in bulk samples and dilute concentrations; Ru^{3+} [257], Rh^{3+} [236] and Ir^{4+} [230].

Whether an impurity increases or decreases T_M will depend on how it modifies H_{MD} and H_{SI}. For example, by substituting ferric ions for trivalent dopants with $S = 0$, given the lack of a magnetic moment on the impurity, this will reduce the number of ferric ions and thus reduce H_{MD}. If the impurity has a net moment, this will also directly modify H_{MD}. The introduction of impurities also modifies the crystal structure itself with atoms smaller than Fe leading to a contraction of the lattice and larger atoms a corresponding expansion. Either way, the net effect is again a modification of H_{MD}. Furthermore, the size of the impurity atom will lead to shifts in the crystalline field, with smaller atoms leading to a reduction of the crystalline field felt by neighbouring ferric ions and the inverse for larger impurities, modifying H_{SI} through higher order SOC terms The net result is that the introduction of impurities will alter both H_{SI} and H_{MD}. This then means that H_{K_1} and H_{K_2} will also vary and thus the Morin temperature will change. In order to increase the Morin transition, the difference between H_{SI} and H_{MD} needs to be increased. This happens with Ru^{3+} for example, where the larger than iron atomic radius and S =1/2 lead to a large modification of H_{SI} [257]. Aside from impurities affecting the Morin transition, vacancies have also been shown to have an influence on the magnetic properties of hematite [258–260] whilst Verbeeck *et. al.* found indications that the value of T_M, as well as the temperature range for the transition, is affected by the morphology and crystallinity of the sample under investigation [261].

The effect of dopants on the Morin transition in bulk hematite does not always apply in thin films and nanoparticles, where the reduction in size can introduce other effects that compete in modifying the critical anisotropy terms. For example, Ir^{4+} doped thin films show $T_M > 400$ K [262], just as in bulk hematite [230], however, interestingly, Sn and Ti can also increase T_M in thin films despite lowering it in bulk crystals, as shown in Fig. 4.4 [263].

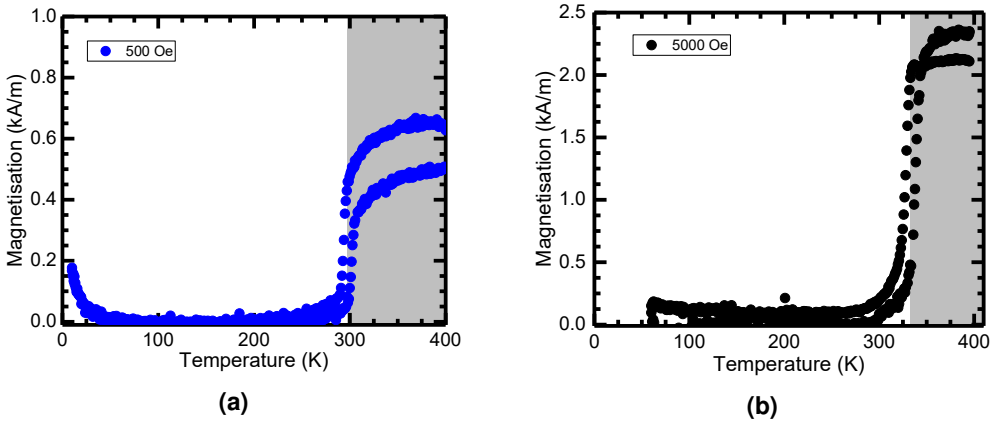

Figure 4.4: SQUID magnetometry measurements on hematite thin films doped with 1% by weight of a) Sn, field cooled under 500 Oe, or b) Ti, field cooled under 5000 Oe. The magnetic moment drops substantially at the Morin transition, which is close to or above room temperature. The shaded area indicated the $>T_M$ region.

4.1.2 Spin Flopping in Hematite

As hematite displays a uniaxial anisotropy below T_M, the observation of a spin flop for a field applied along this axis was not surprising [53, 264]. This critical field $H_c^{\parallel}$ has been measured as a function of temperature by several authors by multiple bulk techniques

[241, 265–267]. The additional Dzyaloshinskii-Moriya (DMI) term serves to lower the value of $H_c^{\parallel}$ with increasing temperature and becomes increasingly more important near the Morin transition. This critical field is then described by a slightly modified version of Eqn. 2.37 from Sec. 2.4.2,

$$H_c^{\parallel 2} = 2H_E(H_{K_1} + H_{K_2}) - H_D^2, \tag{4.4}$$

where H_E is the exchange field, H_{K_1} and H_{K_2} are the effective anisotropy fields, and H_D is the DMI field.

Another side effect of the additional DMI term is that a field applied perpendicular to the easy-axis (EA) also leads to a transition of the sublattice moments to the basal plane [238, 245, 268–275]. Just below the Morin transition, the critical field for this transition is relatively low, allowing for it to be observed with small applied fields [238, 268, 272, 273]. Meanwhile larger fields have been used to observe this transition down to low temperatures which show that it is fairly constant from 0 K to 100 K with a value of $H_c^{\perp} \sim$16.2 T before decreasing towards T_M [245, 269, 274, 275]. The critical field for this *perpendicular* spin reorientation $H_c^{\perp}$ is described by,

$$H_c^{\perp} = \frac{2H_E H_{K_1} - H_D^2}{H_D}. \tag{4.5}$$

One can note that the second order anisotropy doesn't enter the final expression for $H_c^{\perp}$ even with if an extensive consideration of the hematite free energy is made [29].

4.1.3 Magnon Dispersion in Hematite

The additional DMI and higher order anisotropy terms also lead to additional modification of the field dependence of the k = 0 magnon modes previously discussed in Sec. 2.4.2 for a simple uniaxial antiferromagnet. For a magnetic field applied parallel to the easy-axis, below the spin flop and $T < T_M$ [241, 242, 270, 275],

$$\frac{\omega_+}{\gamma} = \frac{\omega_0}{\gamma} + \boldsymbol{H}, \tag{4.6a}$$

$$\frac{\omega_-}{\gamma} = \frac{\omega_0}{\gamma} - \boldsymbol{H}, \tag{4.6b}$$

where the zero field frequency ω_0/γ is given by Eqn. 4.4. One can note that these equations are very similar to those given in Eqn. 2.37 of Ch. 2, where the critical field is now modified by the additional effective field created by the DMI term. The general form is similar to that shown in Fig. 2.13b of Ch. 2. These modes have been observed by numerous authors, for example by Foner and Williamson [53], and Elliston and Troup [54] for a range of frequencies up to 120 GHz.

The more complex issue arises for the magnetic field applied perpendicular to the easy-axis. Unlike in a simple easy-axis antiferromagnet discussed in an earlier chapter, where $\boldsymbol{H} \perp EA$ leads to oscillations of the magnetisation but no spin transition (Eqns 2.41) [46], a consequence of the DMI is to smoothly rotate the moments away from the EA as the magnitude of the field is increased. This more complex nature of hematite leads to two uncoupled modes given by [241],

$$\left(\frac{\omega_1}{\gamma}\right)^2 = \boldsymbol{H}^2 + \left(\frac{\omega_0}{\gamma}\right)^2 - 4H_E H_{K2} \sin^2\vartheta + 2H_E H'_M, \tag{4.7a}$$

$$\left(\frac{\omega_2}{\gamma}\right)^2 = \cos^2\vartheta\left[\left(\frac{\omega_0}{\gamma}\right)^2 - 12H_E H_{K2}\sin^2\vartheta\right] + 2H_E H'_M, \tag{4.7b}$$

where,

$$\sin\vartheta = \frac{\boldsymbol{H}H_D}{2H_E\left(H_{K1} + 2H_{K2}\cos^2\vartheta\right) - H_D^2}, \tag{4.8}$$

and H'_M represents a magnetostrictive field which is equal to $H_M\sin\vartheta$. The value of ϑ, which represents the angle between the magnetic moments and the direction of the uniaxial anisotropy, can be calculated numerically depending on the applied field. In the work of Morrison *et al.* [241] where these equations were derived, the small basal plane anisotropy is omitted. The field dependence of these modes is shown in Fig. 4.5a. The critical feature of the magnon dispersion of hematite that is of importance for some of the work in this thesis is the closure of the magnon gap of the lower branch for a field applied both parallel to the easy-axis at the traditional spin flop but also when the field is perpendicular to the easy-axis.

The mode given by Eqn. 4.7b has readily been observed [241, 270]. The second mode possible (Eqn. 4.7a) requires frequencies in excess of 300 GHz and fields in excess of 16 T at low temperatures [245, 276].

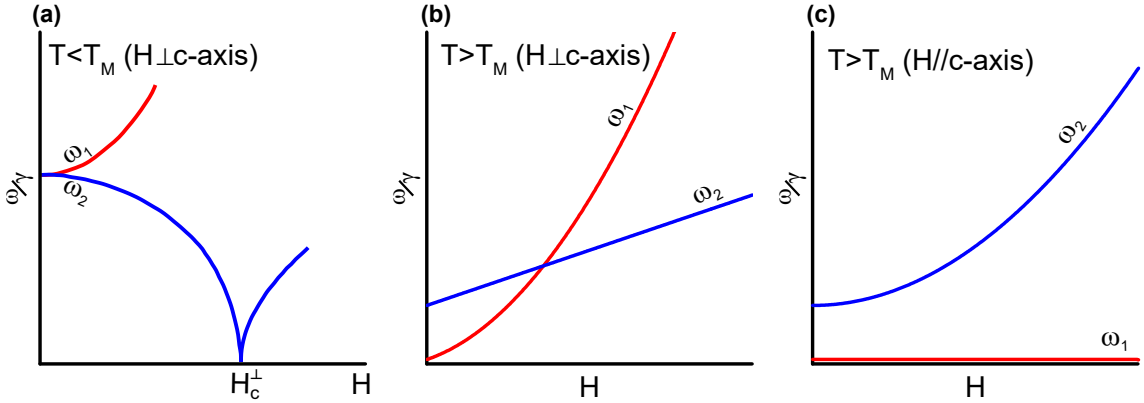

Figure 4.5: a) Magnon dispersion for hematite for $\boldsymbol{H}$ applied perpendicular to the easy-axis below T_M. At some critical field $H_c^{\perp}$, the additional Dzyaloshinskii-Moriya interaction leads to a smooth reorientation of the magnetisation. At this critical field, the magnon branch of one mode falls to zero just as in the conventional spin flop. The magnetic field below $H_c^{\perp}$ leads to a smooth canting and rotation of $\boldsymbol{n}$. This figure is based on Fig. 1 from Ref. [270]. b) Magnon dispersion for hematite above T_M based on Eqns 4.9 with $\varepsilon = \pi/2$, i.e. $\boldsymbol{H}$ in the basal plane. c) Magnon dispersion for hematite above T_M based on Eqns 4.9 with $\varepsilon = 0$, i.e. $\boldsymbol{H}$ perpendicular to the basal plane and parallel to the c-axis.

In the case of $T > T_M$ in the easy-plane phase, there also exist resonant modes for a magnetic field applied within the basal plane that are slightly modified from those of a purely easy-plane antiferromagnet due to the additional DMI and subsequent in-plane canting. The derivation of the following equations can be found in, for example, Refs. [29, 42, 277, 278], but for completeness, they will be stated,

$$\left(\frac{\omega_1}{\gamma}\right)^2 = \boldsymbol{H}\sin\varepsilon\left(\boldsymbol{H}\sin\varepsilon + H_D\right) + 36H_E H_{KB}\cos 6\beta + 2H_E H_M, \tag{4.9a}$$

$$\left(\frac{\omega_2}{\gamma}\right)^2 = -2H_E H_{K_1} + H^2\cos^2\varepsilon + H_D\left(\boldsymbol{H}\sin\varepsilon + H_D\right) + 6H_E H_{KB}\cos 6\beta + 2H_E H_M, \tag{4.9b}$$

where H_{KB} is the effective field arising from the basal plane anisotropy, H_M is the effective magnetostrictive field arising from the inherent magnetoelastic interaction of hematite, however additional strains can also be induced by effects such as the glue used in sample mounting [239]. Meanwhile, ε is the polar angle of the applied field and β is the in-plane angle from some basal plane crystallographic axis. These modes have been observed by numerous authors, for example Refs. [47, 53, 54, 241, 276, 279]. The resulting dispersion for Eqns. 4.9 is shown in Fig. 4.5b for a magnetic field in the basal plane ($\varepsilon = \pi/2$) and Fig. 4.5c for a magnetic field perpendicular to the basal plane ($\varepsilon = 0$) and the same value of β.

4.1.4 Thin Film Hematite

Small particles of hematite have shown reduced values of T_M with particles below a certain size remaining in the easy-plane phase down to liquid helium temperatures [280]. As the particle size decreases, the lattice parameters increase leading to a decrease of the magnetic-dipole anisotropy field [280]. However, the surface morphology and spin-pinning have also been proposed in order to explain the decrease of T_M, with unsupported nanoparticles showing a Morin transition whilst supported ones did not [281]. Meanwhile, high quality epitaxial films have been shown to possess a Morin transition albeit with a suppressed temperature from that of the bulk [262, 263, 282]. The spin flop along the c-axis has also been observed in thin films of hematite in both XMLD [263] and magnetisation [282] measurements. Just as in bulk hematite, close to the Morin transition the critical field to induce a spin flop falls to around zero and increases with decreasing temperature.

For the work performed in the course of this thesis, thin films of hematite were obtained through a collaboration with the group of Professor Avnar Rothschild from the Technicon Institute of Technology, Israel. These films were grown by pulsed laser deposition from a stoichiometric Fe_2O_3 target in an oxygen pressure of 10 mTorr at 800 ℃ on orientated sapphire substrates (Al_2O_3) and detailed in Ref. [283]. Sapphire was chosen due to it sharing the corundum structure with similar lattice constants. It has also been shown that hematite grows well with a Cr_2O_3 buffer layer between the substrate and film as the lattice constants of hematite are more similar to those of Cr_2O_3 than the sapphire itself, however, in this case one would have two antiferromagnets with different values of T_N and different anisotropies, not least one with a DMI, on top of one another. Since this would dramatically complicate the interpretation of the results, the work in this thesis has focused on the simpler system of hematite directly grown on a substrate. The structural and magnetic characterisation of the films that are immediately relevant for the later transport measurements will be introduced in later chapters.

4.2 Techniques

This section will detail the techniques used in the course of this thesis in order to produce, characterise and measure samples. Although multiple samples for the work presented here were grown via pulsed laser deposition (PLD), these samples were grown through collaboration rather than by the author and so this technique will not be discussed here. Details of the PLD growth can be found in Ref. [283].

4.2.1 Superconducting Quantum Interference Device (SQUID) Magnetometry

Static magnetic properties of magnetically ordered materials can be investigated via magnetometry using a superconducting quantum interference device (SQUID) [284] such as the curves shown in Figs. 4.2 or 4.4. A SQUID consists of a superconducting loop interrupted by Josephson junctions; one in an RF-SQUID or two in a DC-SQUID [284]. The sample under investigation is passed through a pickup coil, generally a second-order gradiometer, situated within a superconducting magnet, which induces a current obeying Lenz's law [285]. This current is then converted to a magnetic flux in the Josephson junctions which can support integer multiples, or "quanta", of magnetic flux $\Phi_0 = h/2e$. In order to maintain a balanced state, a coupled feedback loop is used that generates a voltage directly related to the magnetic moment of the sample. For more information on the operation of a SQUID, one can consult for example Ref. [285] or, for a more detailed discussion, Ref. [284].

SQUID magnetometry is a bulk measurement technique, which means that it measures not only the magnetic material but also the induced moment of all other components in the system. These other contributions can come from substrates and layers without a net magnetic order, as well as from the mounting equipment required to install the sample. In the case of additional paramagnetic or diamagnetic contributions, these can be eliminated in field dependent measurements as linear contributions to the signal. However, sometimes, these contributions can be too large and mask the signal from the films deposited atop the substrate.

In order to obtain the true magnetisation of the sample under investigation, the total magnetic moment returned by the SQUID is corrected for the contributions from the substrate and sample environment, then divided by the volume of the magnetic material. Further data correction is then required to account for the geometry used in the initial calibration [286]. For a $5\,\mathrm{mm}\times5\,\mathrm{mm}$ sample in our measurement geometry, this accounts for a multiplication factor of 1.012 when the in-plane magnetisation is investigated or 0.979 when mounted for out-of-plane investigations. For a $5\,\mathrm{mm}\times10\,\mathrm{mm}$ sample, this factor becomes 1.112 for in-plane measurements whilst the SQUID magnetometer used here (a Quantum Design MPMS XL) does not allow for such a sized sample to be mounted out-of-plane given the internal diameter of the system is only 7 mm.

4.2.2 X-Ray Diffraction

The crystallographic order of thin films has been investigated through X-ray diffraction (XRD) making use of a Bruker D8 DISCOVER X-ray diffractometer. To generate a parallel monochromatic beam of X-rays with a wavelength of $\lambda(K_\alpha) \simeq$1.54Å, a copper X-ray source, a Göbel mirror and a Ge based monochromator is used. The X-rays with a wavevector $\vec{k}_i$ are sent towards the sample under investigation under some angle of incidence θ. These X-rays are then reflected by the sample with a wavevector $\vec{k}_r$ and detected by a detector with the same angle of incidence on the other side of the sample ω. When the scattering vector $\vec{Q} = \vec{k}_i - \vec{k}_r$ is equal to the reciprocal lattice vector $\vec{G}$, reflexes will occur [287]. If one knows the crystal structure and the lattice constants, the diffraction pattern then allows one to identify the crystal orientation by varying the angle of incidence in a 2θ-ω measurement [287]. This then leads to the Bragg condition of

constructive interference,

$$n\lambda = 2d_{hkl}\sin\theta, \tag{4.10}$$

where n is an integer, d_{hkl} is the separation between planes with the Miller indices (hkl). These peaks further be investigated through a measurement known as a rocking curve

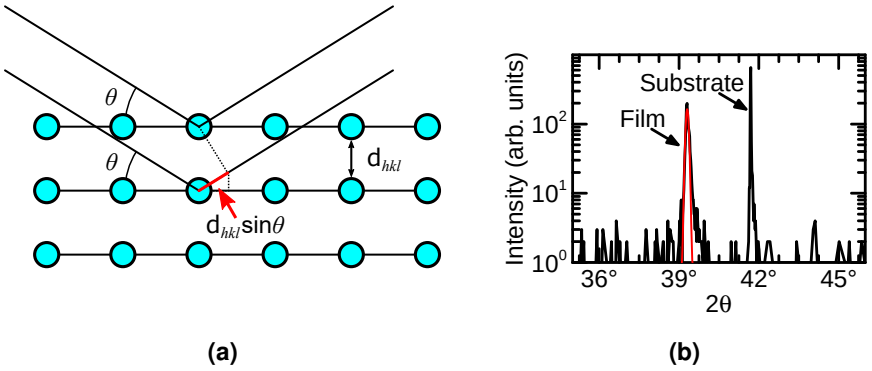

Figure 4.6: a) Figurative illustration of X-ray reflection from the crystal lattice. b) Typical XRD scan for α-Fe_2O_3 grown on a sapphire substrate. A Gaussian fit reveals the peak scattering angle of the film which can be used to deduce the crystal lattice constant out-of-plane.

whereby θ is fixed and ω is "rocked" around the ideal angle of diffraction giving information about the mosaicity of the crystal planes. Meanwhile, the in-plane crystallinity can be investigated if the sample is tilted about the polar angle χ in order to have a component of the momentum transfer occurring in-plane.

4.2.3 Sputtering

The heavy metals used in this thesis were deposited by means of sputtering. Sputtering is a physical vapour deposition technique, meaning that it relies on the ejection of the atomic species to be deposited from a target source and its subsequent adherence to the substrate. A great resource that delves into the physics of sputtering is the *Handbook of Sputtering Technology* [288]. This versatile process is dominated by the transfer of momentum between a bombarding ion and the target, which can be a large range of materials. A gaseous species is used as a precursor in order to catalyse the process. In most cases argon is employed, however krypton can be used and oxygen can be added into the mix in the case of reactive sputtering. The reason an inert gaseous species is used is because these atoms are ionised during the process and an inert gas prevents any chemical reactions with the target atoms. A voltage bias is applied between the substrate and the target, leading to the acceleration of free electrons in the chamber due to the electric field. These electrons inelastically collide with the argon atoms, leading to an ionisation of the atoms and liberating additional electrons that go on to ionise further atoms. These ions then accelerate towards the target, causing atoms to be ejected from the surface that subsequently adhere to a substrate positioned above. In order to have a sustained discharge at a lower argon pressure, magnets are placed below the target. These magnets confine the secondary electrons from the ionisation process near the surface of the target, increasing the efficiency of the ionisation and the sputtering process. Details of the sputtering parameters used in the course of this thesis can be found in Appendix Sec. A.4

4.2.4 Electron Beam Lithography

Lithography is the term used to describe the transfer of a design onto a thin layer of photoresist, where the photoresist is matched to the radiation being used, i.e. ultraviolet light or electrons [289]. In industrial applications, optical lithography has been optimised for structures down to 14 nm [290], but in university research, structures of such a size, for example the nanowires used in non-local measurements during this thesis (Sec. 4.2.5.2) are typically achieved by means of electron beam lithography (EBL) [291]. The sample is prepared by first cleaning the surface in order to remove contaminants, before a polymer photoresist is applied via spincoating to achieve a thin, homogeneous layer. Additional solvent residues are removed and polymer chains become cross linked via a baking step at elevated temperatures. Finally, in the case of insulating surfaces such as frequently utilised here, a conductive resist is spun and baked. The desired pattern is then transferred to the resist by a rastered focussed electron beam. The incoming electrons lead to a modification of the structure of the resist such that the exposed regions have different chemical activity when the sample is developed in chemical solvent (developer). For a *positive resist*, the developer removes the resist from the areas that were exposed whilst a *negative resist* is washed away from all areas that were not exposed. The structure is then created by either the deposition of material onto the exposed regions with the remaining resist and unwanted material then being removed together, a process termed *lift-off*, or by *etching* the regions that are unprotected by resist, see Fig. 4.7. It is common when performing an etching process that the material layer of interest is deposited prior to the spin coating and lithography process before being etched into the desired pattern. Several parameters can be adjusted to optimise the EBL process. The acceleration voltage of the electrons generally controls the feature size but higher voltages come at the cost of an increased penetration depth which may result in additional secondary electrons emitted by the substrate that unwantedly expose the resist. Details of the resists, spincoating recipes and exposure parameters can be found

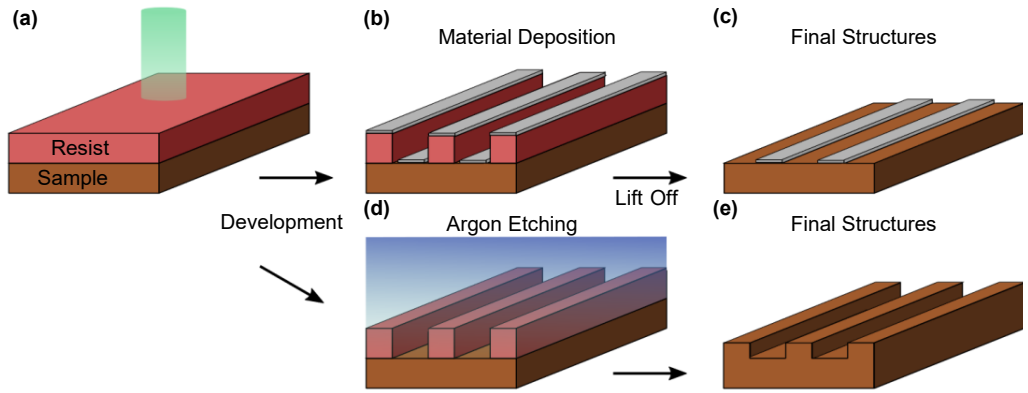

Figure 4.7: Cartoon sketch of the electron beam lithography process. a) A sample is coated with an electron-sensitive resist. A focused electron beam is then used to expose the resist. b) For a lift-off process, the resist is removed during development in regions dependent on the resist used and material is deposited. c) The resulting structure is then left behind. d) Alternatively in an etching process, argon plasma is used to etch into the layer below the resist e) resulting in the desired structure.

in Appendix Sec. A.3.

4.2.5 Electrical Measurements

Two different measurement geometries were utilised to obtain the results herein presented; local SMR measurements and non-local magnon transport measurements. Whilst both rely on similar experimental setups, the exact geometries differ. The two will be briefly described separately before the experimental setup itself is introduced.

4.2.5.1 Local SMR Measurements

For the local SMR measurements, Hall bar structures were utilised defined by EBL (Sec. 4.2.4) followed by the deposition (Sec. 4.2.3) of Pt and a subsequent lift off process (see Fig. 4.7). The structures consist of a central bar to carry a charge current provided by either a Keithley model 2400 sourcemeter or a Keithley 6221A operating in *Delta Mode*. Meanwhile contact pads situated along this central bar allow for the measurement of a voltage making use of a Keithley model 2182A nanovoltmeter. Depending on the configuration of the nanovoltmeter relative to the central bar, the *longitudinal* or *transverse* voltages can be measured, which carry different information. It is worth mentioning that Delta Mode works by applying a direct current that is inverted at a frequency of $50\,\mathrm{Hz}$ so that the current traces a square wave. When used in conjunction with a Keithley model 2182A nanovoltmeter, the voltage is measured for a positive and negative current, the average is then calculated and returned. This method results in a lower noise in the measured signal (a noise floor of $\sim$1-2 nV vs 30 nV) but can only be used to capture a single voltage at once and fails to record effects that are symmetric in current. In order to gather the same information as a single measurement with the Keithley 2400, four measurements would be needed. The reduction in noise comes from an increase in measurement speed that allows for far more data points to be captured. Furthermore, fewer cables are required which introduce additional noise, as well as Delta Mode being optimised by Keithley for low noise measurements. Meanwhile, the nanovoltmeter as a stand alone instrument not used in Delta Mode has an inherent noise floor that scales with the resistance of the device under investigation and is one of the main sources of noise. Finally, given the strong temperature dependence of the resistivity of Pt, small temperature drifts can mask the small SMR signals, so care needs to be taken to reach thermal equilibrium before commencing with a measurement. A sketch of a Hall bar with electrical contacts is shown in Fig. 4.8.

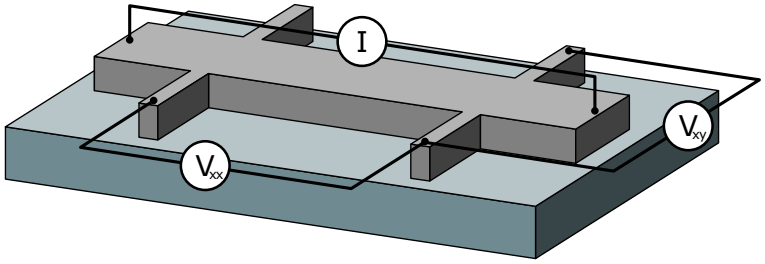

Figure 4.8: Sketch of a Hall bar (e.g. made of Pt) atop a magnetic insulator (e.g. α-Fe_2O_3) with electrical contacts indicated. The charge current is passed through the central bar whilst either a longitudinal V_{xx} or transverse V_{xy} voltage is measured.

4.2.5.2 Non-local Measurements

In order to investigate the transport of magnons in magnetic insulators, a method to excite the magnons in the material under investigation and detect them after propagating

some finite distance needs to be developed as mentioned in Sec. 3.3.1. In the course of this thesis, a non-local geometry consisting of three wires was prepared using EBL (Sec. 4.2.4) and the subsequent magnetron sputtering (Sec. 4.2.3) of a metal, in most cases the heavy metal platinum, followed by lift off. A scanning electron micrograph of a typical structure is shown in Fig. 4.9, showing three wires of platinum atop a film of α-Fe_2O_3 with electrical contacts and circuit indicated. Electrical contacts consisting of a bilayer of Cr/Au or Ti/Au were also defined by EBL and sputtering. The purpose of the three wire geometry is to allow for two distances to be measured simultaneously per device, not only increasing efficiency in utilising space and measurement time but also allowing for verification of any signal seen.

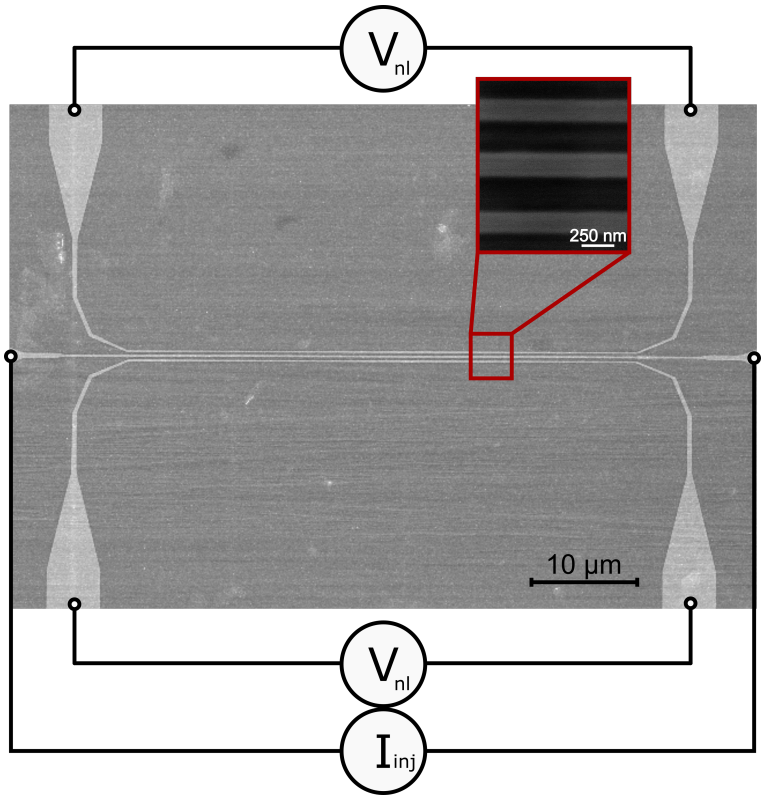

Figure 4.9: Scanning electron microscope image of a typical non-local structure used in this thesis consisting of three wires atop a film of α-Fe_2O_3. A charge current is passed through the central wire and a voltage measured in the top and bottom wires. The electrical contacts used are indicated. Adapted with permission from Ref. [r15]. Copyright 2020 American Chemical Society.

A charge current I_{inj} is provided by a Keithley model 2400 sourcemeter passed through the central wire, and a voltage is measured by means of a Keithley model 2182A nanovoltmeter connected to either the top and bottom wires that act as detectors. The distance between the injector and detector can be varied in order to investigate the distance dependence of any measured signal, as required to extract the spin diffusion length of the excited magnons. In order to avoid device breakages, currents for non-local devices were maintained below a current density of $3.5\times10^{11}\,\mathrm{A\,m^{-2}}$ unless stated otherwise. Unlike the SMR measurements, these measurements are less sensitive to temperature drifts during the measurements given that the signal is a probe of the spin conductance of the magnetic insulator. However, noise still enters from the experimental setup which can be reduced by averaging, although the noise floor of the setup used lies around $\sim$30 nV.

Separation of Electrical and Thermal Signals

Given that the electrical excitation of magnons will inherently lead to Joule heating of the magnetic insulator, the measured voltage in the detector will contain contributions from both. These two can be disentangled in two ways; the first is by noticing the symmetry of each signal with current. As the electrical contribution to the density of the magnon chemical potential below the injector is directly related to the interfacial spin accumulation [187], it thus presents a linear dependence with current. It should be noted that at very large current densities in the injector, the signals can display non-linearities but these are related to the additional deposited heat altering the insulting nature of the magnetic insulator [221]. The torque exerted by the spin accumulation at the injector/magnetic insulator interface can also result in non-linearities through locally compensating the magnetic damping, even leading to auto-oscillations of the magnetic order [169, 225–227]. The thermal excitation mechanism is related to the thermal power deposited into the magnetic insulator, in other words it is proportional to the square of the current. In the course of this work a direct current was used as an excitation, meaning that both signals are detected simultaneously. In order to separate them, the polarity of the current can be reversed and the signals will behave differently. The electrical signal is then odd with current I_{inj} whilst the thermal signal is even. The signals can then further be expressed as non-local resistances.

$$R_{el} = \frac{V(I^+) - V(I^-)}{2I_{inj}}, \tag{4.11a}$$

$$R_{th} = \frac{V(I^+) + V(I^-)}{2I_{inj}^2}, \tag{4.11b}$$

where $V(I^+)$ ($V(I^-)$) is the voltage measured for a positive (negative) current. Alongside the current dependence, there is also the symmetry of the signal with respect to the orientation of the magnetic field. This is discussed further, as well as the differences between the method used here and lock-in based measurements in Appendix Sec. A.2.

It should also be clarified that if the injector and detector electrodes have the same sign of the spin Hall angle, the resulting measured voltage is negative when the contacts are measured symmetrically.

4.2.5.3 Experimental Setup for Electrical Measurements

Regardless of the geometry employed, samples are then installed inside the variable temperature insert of a superconducting cryostat, an Oxford Instruments VSM MagLab capable of magnetic fields up to 12 T and temperatures from 300 K down to 1.9 K by means of liquid helium cooling. Although the magnet is a solonoid, the sample can be mounted in either an in-plane or out-of-plane configuration on a *uniaxial* rod, or alternatively mounted on a piezorotating element (model number ANRv51/RES/LT controlled by a ANC350) from Attocube, attached to a self-made *rotating rod*, designed by Dr. L. Baldrati with extensive input by the author and constructed by the author with assistance from Dr. L. Baldrati. This piezorotating element is capable of functioning in high magnetic fields, at cryogenic temperatures and with 360° of endless rotation. However doing a full rotation is not practical as there is a blind spot in the encoder between 320° and 360°. Furthermore, endless rotation would lead to the cabling required for electrical contacting of samples under investigation suffering undue stress and possibly breaking.

The piezorotator works by means of a DC voltage passed to the element. In order to not break the element or deposit excessive heat, this voltage is not applied constantly, so the rotation takes place with a ratchet-esque behaviour. The speed of rotation is then defined by the size of this voltage and the frequency at which the voltage is applied, where each time the voltage is applied, the element rotates a finite amount. The amount it rotates depends on the voltage applied and the temperature the rotation takes place at. It also rotates far slower at low temperatures than at room temperature (e.g. 180° of rotation in ∼1.5 hours at 300 K as compared to ∼6 hours at 4 K for 60 V). Given that larger voltages are required to enable rotation at lower temperatures, this also leads to additional heat deposited in the sample space, which can introduce additional noise. Through two possible sample boards, shown in Figs. 4.10 and 4.11, a sample can be rotated through three orthogonal planes (xy, xz and yz) whilst in a static field, making use of control programs written by the author using the graphical programming language Labview.

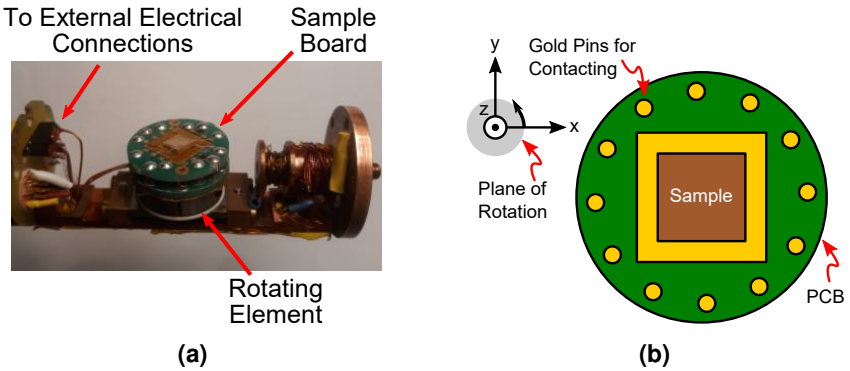

Figure 4.10: a) Photograph of one of the sample boards designed to be used on the rotating sample rod. This board allows for a sample to be rotated such that a magnetic field remains in the sample plane. The sample board is the green PCB whilst the metallic piezorotating element can be seen below. b) Schematic of the in-plane sample board when viewed from above. The board allows for a magnetic field to be rotated in the xy-plane.

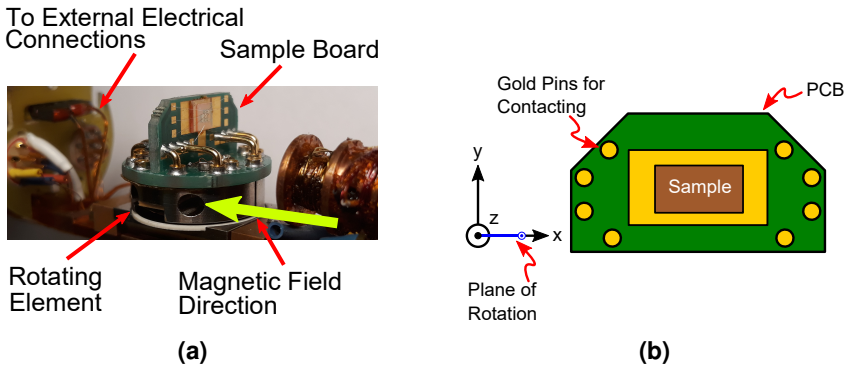

Figure 4.11: a) Photograph of one of the sample boards designed to be used on the rotating sample rod. This board allows for a sample to be rotated such that a magnetic field rotates in an out-of-plane manner, either parallel or perpendicular to the charge current of the sample depending on the orientation of the sample mounting. The sample board is the green PCB and allows for 8 electrical connections. b) Schematic of the out-of-plane sample board when viewed from the side. The board allows for a magnetic field to be rotated in the xz plane of the sample board.

4.2.6 X-ray Magnetic Linear Dichroism

As mentioned earlier in Sec. 2.3.7, one method of investigating AFMs is to make use of X-ray synchrotron radiation through the technique X-ray magnetic linear dichroism (XMLD). A detailed description of this effect, and the related X-ray magnetic circular dichroism, can be found in Ref. [292].

The X-ray beam from a synchrotron is focussed onto the surface of the sample under investigation and the material properties are investigated based on X-ray absorption spectroscopy (XAS). This is a non-invasive technique where the X-ray absorption coefficient depends on the magnetic order and crystal structure of the material under investigation [292]. Given that the momentum of the incident X-ray photon needs to be conserved, this results in the absorption of the photon completely by an electron, prompting it to move to an excited state if the photon energy matches the transition energy. An example of this comes for 3d transition metals where the 2p state is split due to SOC into the $2p_{1/2}$ and $2p_{3/2}$ states. These then act as the initial states for the transition to the 3d shell, termed the L_2 and L_3 absorption edges respectively. When the photon is absorbed, the electron undergoes a spin flip whereby a spin up electron becomes a spin down electron after the transition and vice versa. In the presence of SOC, this leads to a net spin inequality depending on the polarisation of the incident X-ray [292]. In a magnetic material, the absorption characteristics are linked to the magnetic characteristics and the density of states at the Fermi level for different electron spins. Due to the Fermi principle forbidding electrons from swapping bands from minority spins to majority spins and vice versa, the transition in response to the absorbed X-ray can be used as a spin detector. Collinear magnetic ordering leads to a non-spherical distortion of the atomic orbitals due to SOC and the X-ray absorption will then be different for X-rays polarised parallel or perpendicular to the spin axis [292]. XMLD makes use of this difference between the absorption of X-rays with a linear vertical (LV) or linear horizontal (LH) polarisation. XAS measurements can then be made with both polarisations where the intensity of the signal is then the spacial average across the beam size. The XMLD signal is calculated from the differences in the XAS spectra,

$$\text{XMLD} = \frac{\text{LV-LH}}{\text{LV+LH}} \tag{4.12}$$

This then averages out the non-magnetic contributions, leaving behind the dichroism originating from the magnetic order. Different transitions result in different peak energies and the incoming photon energy can be tuned to the binding energy of the element of interest. This can then also be extended to insulating materials, but results in additional peaks at the elemental edges that are not seen in the pure metallic form of the same element. An example of the XAS spectra for an Fe based oxide is shown in Fig. 4.12, alongside the difference for the two polarisations. The two features in the difference then corresponds to the XMLD at the L_2 and L_3 peaks.

XMLD - Photoemission Electron Microscopy (XMLD-PEEM)

Following the excitation of the electrons from absorbing the incident X-ray radiation, holes are left in the lower core levels. The subsequent recombination leads to the emission of secondary electrons which have a propagation distance of a few nm in a solid material. Electrons that manage to escape the surface are then accelerated by a high extraction voltage and focussed through a series of magnetic lenses to a luminescent screen imaged by a CCD camera, enabling the spatially resolved investigation of the

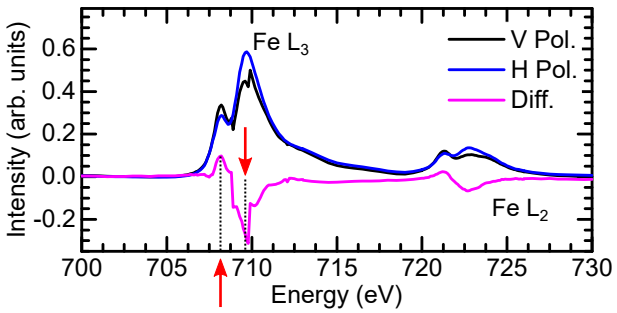

Figure 4.12: Example of X-ray absorption spectroscopy at the Fe L_2 and L_3 edges in a α-Fe_2O_3 film with linear vertical (black) and linear horizontal (blue) polarised X-rays. The difference between the two polarisations (pink) reveals dichroism at the two edges.

XMLD effect. The methodology to image the AFM domains in an oxide used in this thesis makes use of a two images taken at energies corresponding to the different peaks of the multiplet one obtains from a XAS measurement (indicated by the red arrows in Fig. 4.12). These peaks should correspond to a maximum and minimum in the magnetic dichroism. The magnetic contrast is then revealed through the asymmetry between the two energies for a single polarisation. This then allows for regions with different orientations of the Néel vector to be revealed through different levels of grey-scale contrast that correspond to the number of emitted electrons from each region. In order to increase the contrast, this process is repeated many times and the resulting dichroism images averaged together. An example of magnetic domains revealed in this manner is shown in Fig. 4.13 where areas of grey contrast represent domains with parallel alignments of $\boldsymbol{n}$, separated by broad domain walls (the white contrast).

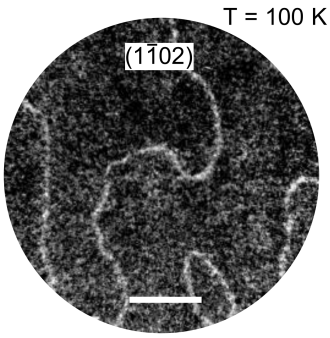

Figure 4.13: Example XMLD-PEEM image of the domain structure of the antiferromagnetic oxide α-Fe_2O_3 orientated with the (1$\bar{1}$02) direction out of the sample plane. The grey area represent domains with a parallel alignment of $\boldsymbol{n}$ separated by broad 180° domain walls. The white contast comes from the out-of-plane component of the Néel vector. The white scale bar represents 2 µm. Adapted with permission from Ref. [r15]. Copyright 2020 American Chemical Society.

The propagation length of the secondary electrons then sets a threshold on the penetration sensitivity of PEEM, making it a highly surface sensitive technique and allows one to build up a map of the AFM domain structure. There are also several limitations; first, given that it relies on emitted electrons, XMLD-PEEM is only suitable for metallic samples and thus insulators need to be “capped” by a thin metal layer to prevent discharges. This metal layer should be thinner than the probing length of the technique in order to access information about the underlying AFM. Second, it requires a finite angle between

the Néel vector of neighbouring domains as it cannot distinguish between antiparallel directions of $\boldsymbol{n}$ and thus cannot be used to resolve domains separated by 180° domain walls, unless the wall where $\boldsymbol{n}$ rotates is wider than the resolution of XMLD-PEEM which is about 25 nm. This resolution is dictated, among other things, by the resolution of the CCD camera and the electron optics used for focussing.

5

Determining Antiferromagnetic Anisotropies from Spin Hall Magnetoresistance Measurements

Antiferromagnetic (AFM) materials are the main focus of this thesis and show great promise for next generation spintronics devices with spin dynamics in the THz regime and the potential for increased packing of magnetic bits due to an absence of stray fields. Functionalising AFMs relies on finding efficient ways to manipulate the equilibrium orientation of the Néel vector, for example using electric fields [293, 294], Néel spin-orbit torques [295, 296], interfacial spin-orbit torques [r4, 12] or strain [r18]. As well as modifying the equilibrium orientation of the Néel vector, such changes need to be detected. They can, for example, be evidenced by magnetic imaging [r4, r17, 297] (c.f. Sec. 4.2.6) or detected by electrical magneto-transport measurements based on even functions of the magnetic order parameter such as the planar Hall effect [295, 296] or spin Hall magnetoresistance (SMR) [r1, 14, 15]. Whilst such measurements can be used to detect switching events, they rely on a change in the average orientation of $\boldsymbol{n}$ and it is not immediately clear how one can use magneto-transport measurements to determine the antiferromagnetic anisotropies and other key magnetic properties. In order to access key values, such as the magnetic anisotropy, techniques such as AFM resonance can be used to investigate the spin flop phenomena [46, 92, 241, 271]. One can also make use of techniques like neutron scattering [240], magnetic susceptibility measurements [46, 244, 269] or Mössbaurer spectroscopy [236, 267, 272]. However, these established techniques rely on large scale facilities or on having sufficient material to produce a measurable signal or effect. Given that spintronic devices ultimately aim to use thin layers, such techniques are not suited for the task at hand.

In this chapter, spin Hall magnetoresistance (c.f. Sec. 3.1.2) will be shown to be a versatile tool for investigating the antiferromagnetic anisotropies of insulating antiferromagnetic rust α-Fe_2O_3, also known as the mineral hematite. This material has a low magnetic damping [r13, 19] and an accessible spin flop field meaning that the antiferromagnetic order can be manipulated. The interfacial nature of the SMR, makes it an ideal technique for probing antiferromagnets, theoretically down to a single layer of AFM material. However, additional problems can arise given the possible dependence of the SMR

on the magneto-crystalline symmetry [298], or even the structural symmetry [299] as well as the net signal potentially vanishing for multi-domain states [r1, 15]. This chapter starts with the extraction of the magnetic anisotropies of a bulk hematite crystal using spin Hall magnetoresistance to probe the antiferromagnetic state as a function of magnetic field and environmental temperature. The values resolved from the surface sensitive measurements match well those measured elsewhere by other techniques for bulk α-Fe_2O_3 and the Morin phase transition temperature can be resolved from the behaviour of the spin flop field. The technique is then applied to thin films of α-Fe_2O_3 in later sections of the chapter, where the strengths of the magnetic anisotropies are previously unknown. Not only can the strengths of the key magnetic anisotropies of hematite thin films be resolved, it is also observed that growth induced deviations of the antiferromagnetic axis introduces additional features into the signal. An overview of the measurements performed in this chapter can be found in the Appendix Sec. A.8. The results of the first section have been published in Ref. [r10] whilst the results of the latter half are published in Ref. [r14].

5.1 Extraction of Magnetic Anisotropies of Bulk Hematite

The first experimental results to be presented in this chapter will discuss the magnetic anisotropies of a bulk crystal of antiferromagnetic hematite α-Fe_2O_3, probed by the spin Hall magnetoresistance [r10]. Measurements are performed at temperatures both above and below the Morin transition temperature T_M, where the antiferromagnetic order is respectively easy-plane and easy-axis. Making use of a simple model, the magnetic anisotropies can be extracted from these surface sensitive measurements and found to be in a good agreement with volume sensitive measurements.

The experimental devices for electrical measurements were produced by the author. The electrical measurements were performed by the author with Dr. R. Lebrun of JGU. The experimental data were analysed by the author with Dr. R. Lebrun and Prof. O. Gomonay of JGU, and Dr. S. Bender of Utrecht University in the Netherlands. The analytical calculations were performed by Prof. O Gomonay of JGU with input from Dr. S. Bender of Utrecht University and Dr. A. Qaiumzadeh of NTNU in Trondheim, Norway. The results of this section have been published as a research article in Ref. [r10].

5.1.1 Analytical Model of the Spin Hall Magnetoresistance in Bulk Hematite

The transport measurements in the next sections (Sec. 5.1.3 – Sec. 5.1.7) were analysed by making use of an analytical model of the spin Hall magnetoresistance in order to determine the underlying antiferromagnetic anisotropies. As mentioned in the introduction of this section, these calculations were performed by Prof. O Gomonay of JGU with input from Dr. S. Bender of Utrecht University and Dr. A. Qaiumzadeh of NTNU in Trondheim, Norway. This model will be introduced here [r10]. In general, the SMR response of a heavy metal/antiferromagnet system depends on both the field induced/canted moment $\boldsymbol{m}$ and the Néel vector $\boldsymbol{n}$ [143]. Assuming that the contribution dependent on $\boldsymbol{n}$ outweighs that of $\boldsymbol{m}$, the SMR $\Delta R/R$ can be written as [r10, 143],

$$\frac{\Delta R_{jk}}{R_{jk}} = \rho_0 \begin{cases} 1 - (\boldsymbol{n} \cdot \boldsymbol{\mu}_s)^2, & j = k, \\ n_j n_k, & j \neq k, \end{cases} \tag{5.1}$$

where $j, k = x, y$ are the coordinates parallel and perpendicular to the direction of the charge current $\boldsymbol{j}_c$, as defined later in Fig. 5.2. The constant ρ_0 depends on the spin-mixing conductance $G^{\uparrow\downarrow}$ [143–145] at the Pt/α-Fe_2O_3 interface and in the most general case depends on both $\boldsymbol{m}$ and $\boldsymbol{n}$ [143]. The spin accumulation $\boldsymbol{\mu}_s$ due to the spin Hall effect in the Pt layer lies within the xy-plane, perpendicular to the direction of $\boldsymbol{j}_c$ [7, 100]. As discussed in Sec. 4.1, the antiferromagnetic structure of hematite is stabilised by a temperature dependent uniaxial anisotropy field that is positive at temperatures below the Morin transition temperature T_M. At $T = T_M$, this effective anisotropy field changes sign to stabilise the high temperature, easy-plane phase. The application of a magnetic field leads to a rotation of $\boldsymbol{n}$ in both states. Below T_M, a magnetic field at any angle to the easy-axis (EA) leads to a smooth reorientation of $\boldsymbol{n}$ due to the antisymmetric exchange interaction (DMI), leading to a final state of $\boldsymbol{n} \perp \boldsymbol{H}$ [29, 241]. By minimising the potential energy,

$$w_{pot} = 2M_s \left[\frac{1}{2} H_E \, \boldsymbol{m}^2 + H_D \left(n_X m_Y - n_Y m_X \right) - \boldsymbol{H} \cdot \boldsymbol{m} \right] + w_{ani}, \tag{5.2}$$

the equilibrium orientation of the Néel vector in the presence of a field $\boldsymbol{H}$ can be calculated. In Eqn. 5.2, M_s is the sublattice magnetisation, H_E is the exchange field, H_D is the effective field produced by the Dzyaloshinskii-Moriya interaction directed along the c-axis. Meanwhile, $\boldsymbol{m}$ is the magnetisation of the antiferromagnet which encompasses both the field-induced magnetisation and the canted moment of hematite and is related to the Néel vector by the two conditions $\boldsymbol{n} \cdot \boldsymbol{m} = 0$ and $\boldsymbol{n}^2 + \boldsymbol{m}^2 = 0$. The anisotropy energy w_{ani} depends on both the anisotropy field parallel to the c-axis $H_{an}^{\parallel}(T)$[1] and is temperature dependent [29, 239, 241], and the anisotropy field that exists in the plane perpendicular to the c-axis $H_{an}^{\perp}$, defined as,

$$w_{ani} = 2M_s \left[-\frac{1}{2} H_{an}^{\parallel}(T) \, n_Z^2 - \frac{1}{6} H_{an}^{\perp} \left(n_X^2 - n_Y^2 \right) \left(4 \left(n_X^2 - n_Y^2 \right)^2 - 3 \left(n_X^2 + n_Y^2 \right)^2 \right) \right]. \tag{5.3}$$

The in-plane anisotropy field encompasses all possible anisotropies in-plane including the basal plane anisotropy and magnetoelastic anisotropy (c.f. Sec. 4.1). This anisotropy serves to select one of three degenerate easy-axes in the easy-plane phase and is included in order to avoid multiple solutions with $H_E \gg H_D \gg H_{an}^{\parallel}, H_{an}^{\perp}$. For more details on the structure of hematite, please refer back to Sec. 4.1 or Ref. [29]. The coordinate system of Eqn. 5.2 is related to the crystallographic axes such that $\boldsymbol{Z}$ is along the EA and differs from the experimental xyz coordinate frame used in Fig. 5.2 where $\boldsymbol{x}$ is the in-plane component of $\boldsymbol{Z}$. The general expression for the critical magnetic field required to induce a reorientation of $\boldsymbol{n}$ when $\boldsymbol{H}$ makes an angle χ with the easy-axis can be written as [r10],

$$H_{cr}(\chi_H) = \frac{H_c^{\perp 2} - H_c^{\parallel 2}}{2H_c^{\perp}} |\sin\chi| + \frac{1}{2H_c^{\perp}} \sqrt{\left(H_c^{\perp 2} - H_c^{\parallel 2} \right)^2 \sin^2\chi + 4 H_c^{\perp 2} H_c^{\parallel 2}}, \tag{5.4}$$

where $H_c^{\perp}$ is is the critical field for a spin reorientation when $\boldsymbol{H}$ is perpendicular to the easy-axis. Meanwhile, $H_c^{\parallel}$ is the same for $\boldsymbol{H}$ parallel to the EA, i.e. the classical spin flop. These cases of Eqn. 5.4 were previously discussed in Sec. 4.1, but to reiterate,

[1] In Ch. 4, it was discussed that there are two anisotropy fields of different origins in hematite parallel to the c-axis. Here $H_{an}^{\parallel}$ represents the net effective anisotropy field directed along this direction.

the spin flop field is defined as $H_c^{\parallel} = \sqrt{H_E H_{an}^{eff}}$ where the effective anisotropy $H_{an}^{eff} = H_{an}^{\parallel} - H_D^2/H_E$ is introduced. The DMI induced spin-reorientation field can then be written as $H_c^{\perp} = {H_c^{\parallel}}^2/H_D$. Eqn. 5.4 will then be used to fit the angular dependence of the critical magnetic fields in order to determine the strengths of the effective uniaxial anisotropy and the DMI fields.

5.1.2 Experimental Details

Single crystals of hematite[2] was commercially obtained from SurfaceNet GmbH, orientated such that the surface plane was the crystallographic $(1\bar{1}02)$ plane (r-plane). The crystal structure of hematite is shown in Fig. 5.1 with the r-plane superimposed on top. Below the Morin transition temperature T_M [228], α-Fe_2O_3 adopts an easy-axis antiferromagnetic structure where the Néel vector $\boldsymbol{n}$ lies parallel to the crystallographic c-axis (see Fig. 5.1). There is then a finite angle between the antiferromagnetic axis and the sample plane of 33°, i.e. a component of $\boldsymbol{n}$ appears within the sample plane. A magnetic field applied also within the sample plane then subtends a finite angle to $\boldsymbol{n}$ of 33° when $T < T_M$. Above T_M, where $\boldsymbol{n}$ rotates 90°, the easy-plane is similarly inclined at 33° to the surface normal. This crystallographic orientation was chosen over one which places $\boldsymbol{n}$ perfectly in- or out-of-plane for two reasons; (i) this crystal orientation results in a chemically stable surface [300] (see Sec. A.9) and (ii) the inclined nature of $\boldsymbol{n}$ allows a finite angle to be made with an applied magnetic field $\boldsymbol{H}$ within the sample plane, breaking the degeneracy of the spin flop phase at high magnetic fields for $T < T_M$.

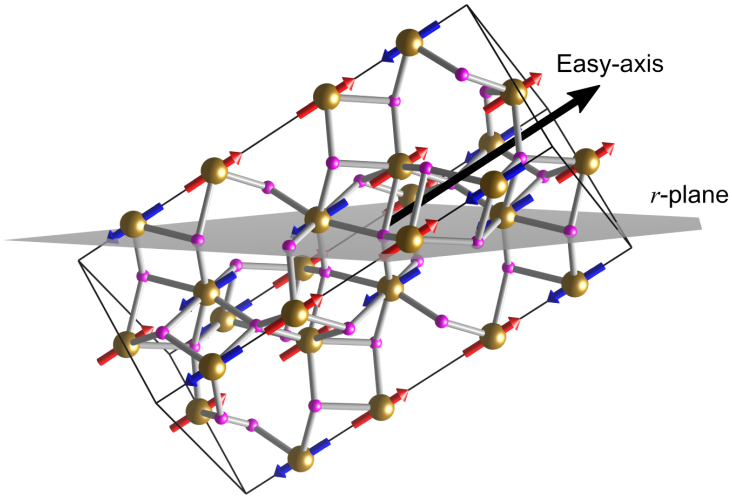

Figure 5.1: Unit cell of α-Fe_2O_3. The gold atoms represent Fe whilst the pink atoms are placed at the oxygen sites. The easy-axis, which is coincident with the crystallographic c-axis, is indicated and represents the direction parallel or perpendicular to the Néel vector $\boldsymbol{n}$ when below or above the Morin transition temperature T_M, respectively. The grey plane indicates the r-plane, inclined at 33° to the c-axis. The figure is orientated such that the r-plane would represent the sample surface to emphasis the orientation of the easy-axis. Figure created with VESTA [237].

Hall bars were defined via electron beam lithography (EBL, Sec. 4.2.4) and the deposition of 7 nm Pt by DC sputtering (Sec. 4.2.3) in an Ar atmosphere. Electrical contact pads of Cr(6 nm)/Au(32 nm) were defined by a second EBL step. A charge current $\boldsymbol{j}_c$ is

[2] Crystal dimensions were 5 mm × 5 mm × 500 µm

passed through the Hall bar either parallel (along $\boldsymbol{x}$) or perpendicular (along $\boldsymbol{y}$) to the in-plane EA component. Meanwhile a longitudinal resistance (R_{xx} or R_{yy} for the two current directions) or transverse resistance (R_{xy} or R_{yx} for the two current directions) is detected. These resistances were measured for both a positive and negative sense of the current polarity and averaged. More details of the measurement methods can be found in Sec. 4.2.5.1. Schematics of these two geometries are shown in Fig. 5.2a and Fig. 5.2b for the current along $\boldsymbol{x}$ or $\boldsymbol{y}$, respectively.

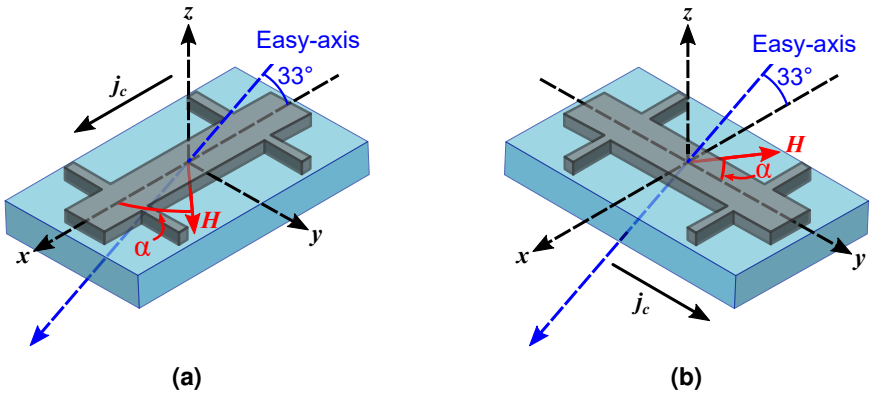

Figure 5.2: Schematic of devices used to investigate SMR in $(1\bar{1}02)$ orientated bulk α-Fe_2O_3. Pt Hall bars are defined by electron beam lithography and orientated such that the charge current passes parallel (a) or perpendicular (b) to the in-plane projection of the easy-axis.

Spin Hall magnetoresistance (SMR) measurements and the determined magnetic anisotropies will discussed for both the easy-axis and easy-plane phases of the hematite crystal, i.e. at temperatures both below and above T_M. The value of T_M can be measured by magnetometry measurements making use of a SQUID (c.f. Sec. 4.2.1) by measuring the magnitude of the canted moment in the basal plane $\boldsymbol{m}$ with reducing temperature. At the Morin transition temperature, $\boldsymbol{m}$ disappears and the measured magnetisation falls. Fig. 5.3 shows the magnetisation of r-plane α-Fe_2O_3 for a magnetic field applied within the crystallographic basal plane. The insets of the same figure show the presence of a hysteresis, and thus canted moment, above T_M, and an absence of a hysteresis below. From these measurements, the value of T_M can be determined as 257 K$\pm$1 K.

Having established the value of T_M, the SMR response will be discussed depending on the orientation of the anisotropy relative to the patterned devices and thus the direction of current flow. In ferromagnets with a low anisotropy, the magnetisation follows the applied field above the saturation of the magnetic order. Meanwhile, in an easy-axis antiferromagnet, the projection of the Néel vector $\boldsymbol{n}$ depends entirely on the magnitude of the applied magnetic field relative to the EA direction. This means that the orientation of the patterned devices can lead to drastically different responses, even above the critical fields (Eqn. 5.4). Here, two key orientations will be discussed. First, the Hall bar parallel to the easy-axis (Fig. 5.2a), followed by Hall bars patterned perpendicular to the easy-axis (Fig. 5.2b) which will allow the role of the crystal anisotropies with respect to the crystalline orientation to be probed.

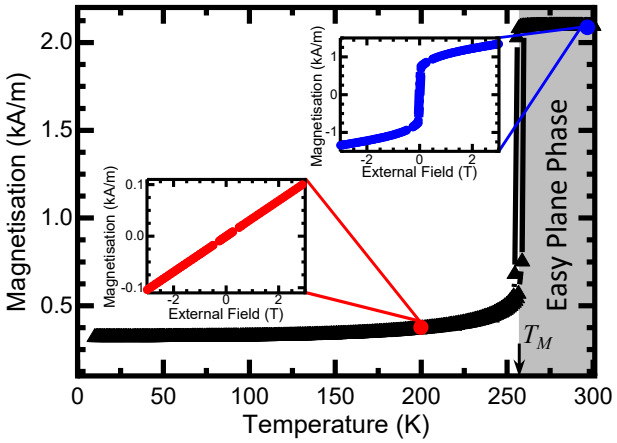

Figure 5.3: Magnetisation of bulk r-plane hematite measured by SQUID. The canted moment for $T > T_M$ leads to a measured magnetisation and the presence of a hysteresis (inset in blue). Due to the Morin transition at $T = T_M$, the canted moment disappears (inset in red) and the magnetisation drops abruptly.

5.1.3 Probing the Magnetic Anisotropies of Bulk Hematite Using Hall Bars Parallel to the Easy-Axis

The first orientation of Hall bar lies parallel to the surface in-plane component of the easy-axis, i.e. the charge current flows along the geometric $\boldsymbol{x}$ direction (Fig. 5.2a). This means that the spin accumulation $\boldsymbol{\mu}_s$ that builds up at the Pt/α-Fe_2O_3 interface due to the spin Hall effect will be polarised perpendicular to the easy-axis, i.e. $\boldsymbol{\mu}_s \| \boldsymbol{y}$ [7, 100]. In the absence of a magnetic field, the projection $\boldsymbol{n} \cdot \boldsymbol{\mu}_s$ is therefore zero and both cases given by Eqn. 5.1 are similarly zero, i.e. there is no SMR response in either the longitudinal (R_{xx}) or transverse (R_{xy}) configuration. Before the experimental results are shown, expectations can be made for how the Néel vector will behave under an applied field $\boldsymbol{H}$. For $\boldsymbol{H} \| \boldsymbol{x}$, i.e. parallel to $\boldsymbol{j}_c$, $\boldsymbol{n}$ will reorient at $H_{cr}(33°)$ and lie parallel to the geometric $\boldsymbol{y}$ axis, increasing the projection $\boldsymbol{n} \cdot \boldsymbol{\mu}_s$ in Eqn. 5.1. In the case of $\boldsymbol{H} \| \boldsymbol{z}$, $\boldsymbol{n}$ will again reorientate, albeit at $H_{cr}(123°)$, and again settle into a new equilibrium position of $\boldsymbol{n} \| \boldsymbol{y}$, increasing $\boldsymbol{n} \cdot \boldsymbol{\mu}_s$ and lowering the recorded magnetoresistance. Finally, when $\boldsymbol{H} \| \boldsymbol{y}$, although $\boldsymbol{n}$ will reorientate at $H_{cr}(90°)$, the projection $\boldsymbol{n} \cdot \boldsymbol{\mu}_s$ will remain unchanged and thus the SMR response will remain unchanged as well. From the values of $\boldsymbol{H}$ required to illicit a reorientation of $\boldsymbol{n}$, information on the strengths of the effective uniaxial anisotropy and the DMI will be gained.

With this in mind, we can turn our attention to the experimental observations. Fig. 5.4 shows the change in the longitudinal resistance ΔR_{xx} for a magnetic field $\boldsymbol{H}$ parallel to $\boldsymbol{x}$, $\boldsymbol{y}$ and $\boldsymbol{z}$, normalised to the resistance in the absence of a magnetic field. According to Eqn. 5.1, the increase in $\boldsymbol{n} \cdot \boldsymbol{\mu}_s$ for $\boldsymbol{H} \| \boldsymbol{x}$ and $\boldsymbol{H} \| \boldsymbol{z}$ should lead to a decrease in the SMR ratio, an expectation that is mirrored by the experimental data. The SMR ratio continues to decrease until $\mu_0 \boldsymbol{H} \sim 7\,\mathrm{T}$ ($\mu_0 \boldsymbol{H} \sim 9\,\mathrm{T}$) for $\boldsymbol{H} \| \boldsymbol{x}$ ($\boldsymbol{H} \| \boldsymbol{z}$) where it reaches a minimum and begins to increase again. Utilising Eqn. 5.1 alongside the equilibrium position of the Néel vector and an expression for the magnetic anisotropy, we can calculate the expected SMR response for these two orientations of $\boldsymbol{H}$, shown in Fig. 5.4 by the solid lines. From zero field, the calculated response anticipates a decrease of the SMR ratio before a saturation. This minimum corresponds to the complete rotation of the Néel vector where the saturation indicates that the equilibrium position of $\boldsymbol{n}$ remains unchanged.

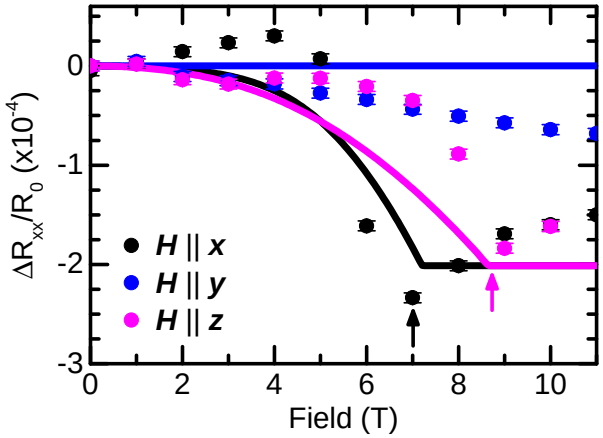

Figure 5.4: Longitudinal spin Hall magnetoresistance ΔR_{xx} normalised to the zero-field resistance of the device R_0 at 200 K for Pt Hall bars on r-plane α-Fe_2O_3 with $\boldsymbol{j}_c$ parallel to the in-plane projection of the easy-axis. A magnetic field is applied along $\boldsymbol{x}$ (black), $\boldsymbol{y}$ (blue) or $\boldsymbol{z}$ (magenta). The solid lines are the calculated SMR response. The arrows indicate the critical field $H_{cr}(\chi)$ for the reorientation of $\boldsymbol{n}$. Figure adapted from data published in Ref. [r10].

From the experimentally observed critical magnetic fields, the magnetic anisotropies can be calculated to be $H_D = 2.72$ T, $H_{an}^{eff} = 23.8$ mT at 200 K [r10]. The calculations also rely on an exchange field of $H_E = 1040$ T [239], which is a bit higher than some other authors have measured but measurements of such a large exchange field rely on accurate measurements of, for example, the Néel temperature which can be altered by impurities in the investigated samples. There is the obvious difference between the experimental and theoretical curves above the reorientation field, where the experimental data increases. The SMR ratio defined by Eqn. 5.1 does not consider that the application of a magnetic field perpendicular to $\boldsymbol{n}$, such as above the spin reorientation and spin flop, leads to a canting of $\boldsymbol{n}$ in the direction of $\boldsymbol{H}$. This results in a field induced canting $\boldsymbol{m}$ directed along $\boldsymbol{H}$ such that $\boldsymbol{n}^2 + \boldsymbol{m}^2 = 1$. In other words, the projection of $\boldsymbol{\mu}_s \cdot \boldsymbol{n}$ again decreases, which experimentally observed as an increase of the SMR response.

Alternatively, the magnetic field is applied in the sample plane and perpendicular to the charge current $\boldsymbol{j}_c$ ($\boldsymbol{H} \| \boldsymbol{y}$). For this orientation of the magnetic field, $\boldsymbol{n}$ remains in the plane perpendicular to $\boldsymbol{H}$ for all values of the applied magnetic field. Given that the projection $\boldsymbol{\mu}_s \cdot \boldsymbol{n}$ is zero in the absence of the magnetic field, the rotation of $\boldsymbol{n}$ in the xz-plane does not alter this and one would expect that there is no change in the SMR with increasing magnetic field. This expectation is shown as the solid line in Fig. 5.4, and this particular geometry cannot be used to obtain information on the effective uniaxial anisotropy or effective DMI field when the reorientation is confined to this plane. Just as for the other field orientations, there is a deviation between the constant of the theoretical expectations and the experimental curves of Fig. 5.4 for $\boldsymbol{H} \| \boldsymbol{y}$. The experimental data shows a sustained decrease with increasing magnetic field, indicating an increase of $\boldsymbol{\mu}_s \cdot \boldsymbol{n}$. The increasing magnetic field leads to a canting of $\boldsymbol{n}$ in the direction of $\boldsymbol{H}$ and an emerging field induced magnetisation $\boldsymbol{m}$ leading to a residual signal. Some studies on canted antiferromagnets have shown that the SMR can be dominated by the canted/field-induced magnetisation, even in the presence of a Néel vector [r9, r19] and thus consideration of both $\boldsymbol{n}$ and $\boldsymbol{m}$ is needed to interpret AFM-SMR results fully, which

the model considered here based purely on effects of $\boldsymbol{n}$ fails to account for.

5.1.3.1 Angular Dependence of the Spin Hall Magnetoresistance

If the magnitude of the magnetic field is fixed, the angular dependence of both the longitudinal SMR ΔR_{xx} and transverse SMR ΔR_{xy} response can be investigated for an in-plane magnetic field. The field dependence of the previous section provides information on the underlying antiferromagnetic anisotropies, meanwhile the angular dependence of the signal can shed light on the symmetry of the magnetic structure. Given the dependence of the SMR on the $\boldsymbol{y}$ component of $\boldsymbol{n}$ in Eqn. 5.1, this should give rise to a maximum resistance for $\boldsymbol{n} \perp \boldsymbol{\mu}_s$ and a minimum at $\boldsymbol{n} \| \boldsymbol{\mu}_s$ [143]. This same expectation can be made considering the experimental data in Fig. 5.4, where the signal should move between the two extremes of $\boldsymbol{H} \| \boldsymbol{x}$ and $\boldsymbol{H} \| \boldsymbol{y}$. If $\boldsymbol{n}$ is completely free to move, such as when a magnetic field exceeds the anisotropy field in an easy-plane AFM, then the signal will smoothly modulate with a $\sin^2 \alpha$ functional form, where α is the angle between the field and the charge current $\boldsymbol{j}_c$ [r1, 14, 15]. This is 90° shifted with respect to the current direction as compared to ferromagnetic materials where the magnetisation $\boldsymbol{m}$ is parallel to $\boldsymbol{H}$ [13]. The SMR dominated by the orientation of $\boldsymbol{n}$ rather than $\boldsymbol{m}$ is therefore colloquially known as *negative* SMR, although *positive* AFM-SMR has been reported [r9, r18, r19, 142, 301] indicating that a hard distinction cannot universally be made.

In the case of an AFM with a uniaxial anisotropy, such a smooth rotation of $\boldsymbol{n}$ is unlikely given that a spin flop will only occur when $\boldsymbol{H}$ is within a few degrees of the easy-axis direction [46]. One would then expect abrupt changes in the SMR when the spin flop condition is reached, i.e. *spikes* in ΔR_{xx}. However, due to the antisymmetric exchange of hematite that led to the spin reorientations in Fig. 5.4, $\boldsymbol{n}$ can smoothly rotate with the magnetic field, providing that $\boldsymbol{H}$ exceeds $H_{cr}(\chi)$ (Eqn. 5.4). Fig. 5.5

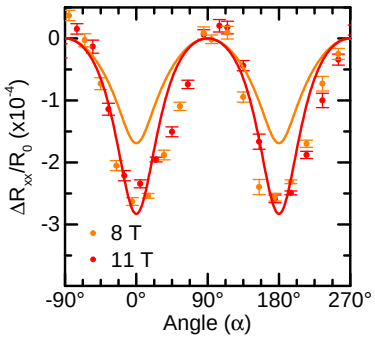

Figure 5.5: Angular dependence of the longitudinal spin Hall magnetoresistance ΔR_{xx} at 200 K, normalised by the zero-field resistance R_0 for a magnetic field $\boldsymbol{H}$ rotated in the xy-plane through an angle α. The magnitude of $\boldsymbol{H}$ is 8 T (orange) or 11 T (red). The solid curves are calculated making use of H_D = 2.72 T, H_{an}^{eff} = 23.8 mT and $H_{an}^{\perp}$ = 1.54 µT. Figure adapted from data published in Ref. [r10].

shows the change in the longitudinal resistance for a magnetic field rotated in the sample plane for two magnetic fields, 8 T in orange and 11 T in red. As expected, there is a smooth modulation of the signal as a function of the in-plane angle between a maximum resistance at 90°/270° and a minimum at 0°/180° indicative of AFM-SMR. Both magnetic fields in Fig. 5.5 are greater than $H_{cr}(33°)$ ($\boldsymbol{H} \| \boldsymbol{x}$ in Fig. 5.4). The value of $H_{cr}(90°)$ should lie between the two fields chosen for Fig. 5.5, however, as seen in Fig.

5.4, $H_{cr}(90°)$ is not visible in this geometry. The solid lines in Fig. 5.5 represent the calculated SMR response from Eqn 5.1 – Eqn. 5.3, making use of the anisotropy field strengths extracted from the uniaxial measurements alongside a basal plane anisotropy field of $H_{an}^{\perp} = 1.54\,\mu\text{T}$ obtained from later measurements above T_M (Sec. 5.1.6). This solid line shows a smooth modulation between the two extremes, but it is not quite the $\sin^2\alpha$ response of easy-plane antiferromagnets [r1, r14, 14–17] demonstrating that the fields here do not completely overcome the magnetic anisotropies, allowing a free rotation of $\boldsymbol{n}$. The calculated SMR signal also expects a reduction in the response for 8 T as compared to 11 T that is not seen in the experimental data. However, just as in Fig. 5.4, the deviations from the calculated response may originate from the large magnetic fields inducing a canting $\boldsymbol{m}$ of the Néel vector that is not taken into account here.

As well as the longitudinal SMR response, the transverse SMR ΔR_{xy} can also be investigated as a function of the in-plane angle. According to Eqn. 5.1, the transverse SMR will depend on the x and y components of the Néel vector n_{xy} as opposed to the longitudinal SMR which relies only on the y component of $\boldsymbol{n}$ [r1, 15, 143]. The angular

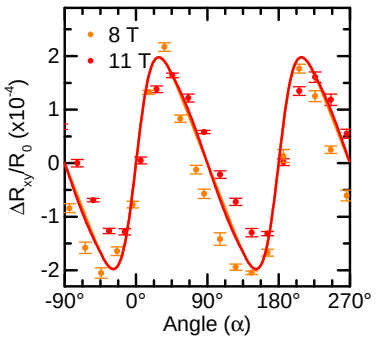

Figure 5.6: Transverse spin Hall magnetoresistance ΔR_{xy} at 200 K for Hall bars with $\boldsymbol{j}_c$ parallel to the in-plane projection of the easy-axis for a magnetic field rotated in the xy-plane through an angle α. The curves are normalised by the zero-field longitudinal resistance R_0. These curves are calculated making use of $H_D = 2.72\,\text{T}$, $H_{an}^{eff} = 23.8\,\text{mT}$ and $H_{an}^{\perp} = 1.54\,\mu\text{T}$. Figure adapted from data published in Ref. [r10].

dependence of ΔR_{xy} is shown in Fig. 5.6 for a magnetic field rotated in the sample plane for $\mu_0\boldsymbol{H} = 8\,\text{T}$ (orange) and 11 T (red). As compared to Fig. 5.5, the extrema occur at $\pm 45°$, confirming the dependence on n_{xy}. Fig. 5.6 is again accompanied with the calculated SMR response from Eqn. 5.1 – Eqn. 5.4. The calculated response matches well the experimental results indicating that whilst ΔR_{xx} may suffer from additional contributions from $\boldsymbol{m}$, ΔR_{xy} is described well by a model centred around $\boldsymbol{n}$.

5.1.4 Probing the Magnetic Anisotropies of Bulk Hematite Using Hall Bars Perpendicular to the Easy-Axis

By virtue of the relative orientation of $\boldsymbol{j}_c$ and $\boldsymbol{n}$ in the absence of a magnetic field, the reorientation of the Néel vector was not visible in Fig. 5.4 when a magnetic field was applied along $\boldsymbol{y}$. This indicates that the relative orientation of the magnetic anisotropy and the measurement devices can give rise to differences in the SMR response, potentially limiting the ability to access key magnetic anisotropies. This was also demonstrated in NiO thin films, where inclination of the easy-plane with respect to the surface normal gave rise to a significant SMR response for a magnetic field rotated in all three principle planes [r1]. If the easy-plane and the sample plane are the same, then a significant

SMR response would only be visible in the xy-plane [14, 15]. This section will discuss the SMR response for a Pt Hall bar patterned perpendicular to the in-plane easy-axis component for temperatures both above and below the Morin transition, starting with $T < T_M$. This geometry is shown in Fig. 5.2b and a charge current is passed parallel to the geometric $\boldsymbol{y}$ axis. The interfacial spin accumulation $\boldsymbol{\mu}_s$ that builds up due to the spin Hall effect (c.f. Sec. 3.1.1) is then polarised along the geometric $\boldsymbol{x}$ axis, parallel to the EA in-plane component. Whilst the previous geometry in Fig. 5.4 relied on the y component of $\boldsymbol{n}$, the electrical response for this geometry then relies on the component of $\boldsymbol{n}$ parallel to $\boldsymbol{\mu}_s$, i.e. the x component n_x.

The longitudinal SMR response ΔR_{yy} for this geometry is first investigated below T_M for a magnetic field $\boldsymbol{H}$ along the three principle directions, parallel to the charge current ($\boldsymbol{H} \| \boldsymbol{y}$), perpendicular to the charge current ($\boldsymbol{H} \| \boldsymbol{x}$) and out of the sample plane ($\boldsymbol{H} \| \boldsymbol{z}$). The response of $\boldsymbol{n}$ to the magnetic field is the same as described in the previous section, but this time we are interested in n_x, which changes for all three field directions at the spin reorientation. The experimental curves are shown in Fig. 5.7, alongside fits based on Eqn. 5.1 – Eqn. 5.4 indicated by the solid lines. In the absence of a magnetic field,

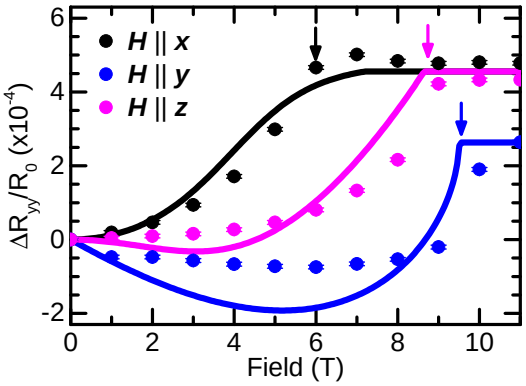

Figure 5.7: Longitudinal spin Hall magnetoresistance ΔR_{yy} at 200 K for Hall bars orientated such that $\boldsymbol{j}_c$ is perpendicular to the in-plane projection of the easy-axis. The magnetic field is applied parallel to $\boldsymbol{x}$ (black), $\boldsymbol{y}$ (blue) or $\boldsymbol{z}$ (magenta). The signal is normalised by the zero-field resistance R_0. The solid lines represent the calculate SMR response using $H_D = 2.72$ T, $H_{an}^{eff} = 23.8$ mT and $H_{an}^{\perp} = 1.54$ µT. Figure adapted from data published in Ref. [r10].

the projection of $\boldsymbol{n}$ on $\boldsymbol{\mu}_s$ is maximal and the application of a field will lead to a reduction of n_x for all three directions of the magnetic field according to Eqn. 5.4. The calculated response from Eqn. 5.1 – Eqn. 5.4 matches well the experimental results based on a DMI field of $H_D = 2.72$ T, an effective anisotropy field of $H_{an}^{eff} = 23.8$ mT, an in-plane anisotropy field of $H_{an}^{\perp} = 1.34$ µT. The orientation results in the same reorientation fields as seen before and requires the same values for the magnetic anisotropies in order to replicate the field response, demonstrating that, although the shape differs, the underlying magnetic anisotropies responsible for the reorientation of $\boldsymbol{n}$ can be determined from both geometries.

Unlike in Fig. 5.4, when $\boldsymbol{H}$ is applied perpendicular to the EA along the geometric $\boldsymbol{y}$ direction, the SMR response ΔR_{yy} registers the reorientation of $\boldsymbol{n}$ that occurs due to the DMI (Fig. 5.7). The reorientation of $\boldsymbol{n}$ that occurs for $\boldsymbol{H} \| \boldsymbol{y}$ at $H_{cr}(90°)$ maintains $\boldsymbol{n}$ in the geometric xz-plane. This leads to a reduction of n_x and thus is visible for the geometry of Fig. 5.2b with $\boldsymbol{j}_c \| \boldsymbol{y}$, even though it was not evident for the previous geometry with $\boldsymbol{j}_c \| \boldsymbol{x}$

(Fig. 5.4). This highlights the importance in measurements of AFM-SMR of the device geometry with respect to the magnetic anisotropy axes. The calculated SMR response for this magnetic field direction, indicated by the solid blue line in Fig. 5.7 deviates somewhat from the experimental results at low magnetic fields. The calculation assumes that, when $\boldsymbol{H}\|\boldsymbol{y}$, $\boldsymbol{n}$ remains confined to the xz-plane. In other words, given that $\boldsymbol{n}$ initially lies below the sample plane, it first rotates into the sample plane, increasing $\boldsymbol{n}\cdot\boldsymbol{\mu}_s$ before continuing out of the sample plane where $\boldsymbol{n}\cdot\boldsymbol{\mu}_s$ decreases. Experimentally, $\boldsymbol{n}$ will not rotate in a fixed plane, but rather trace a smooth arc with a component parallel to $\boldsymbol{y}$ as well as an emergent moment $\boldsymbol{m}$ due to $\boldsymbol{H}$ being perpendicular to the Néel vector.

5.1.4.1 Angular Dependence of the Spin Hall Magnetoresistance

Just as in Sec. 5.1.3, the spin Hall magnetoresistance can also be investigated for a fixed magnetic field as a function of the angle between the charge current $\boldsymbol{j}_c$ and field $\boldsymbol{H}$. For Hall bars orientated such that $\boldsymbol{j}_c$ flows perpendicular to the in-plane component of the Néel vector, i.e. $\boldsymbol{j}_c\|\boldsymbol{y}$, the angular SMR should display a stronger field dependence than for Fig. 5.5 and Fig. 5.6 when $\boldsymbol{j}_c$ was parallel to $\boldsymbol{x}$. This statement is made based on the field dependence of ΔR_{yy} in Fig. 5.7. The angular dependence of the longitudinal SMR response ΔR_{yy} is shown in Fig. 5.8, normalised to the resistance of the device at zero-field, for three values of the magnetic field. The magnitude is maintained around the critical field for $\boldsymbol{H}\|\boldsymbol{x}$ (6 T, orange points), the critical field for $\boldsymbol{H}\|\boldsymbol{y}$ (11 T, brown points), and at an intermediate value (8 T, red points). The amplitude of the longitudinal SMR is negative, confirming that the Néel vector dominates the response, and is maximal for 6 T. This is expected from the curves in Fig. 5.7, where the largest difference between $\boldsymbol{H}\|\boldsymbol{x}$ and $\boldsymbol{H}\|\boldsymbol{y}$ occurs at the spin flop $\mu_0\boldsymbol{H}=6$ T. In contrast to this, when the field is maintained at 11 T, ΔR_{yy} transitions between the two saturation values of Fig. 5.7. These two saturation values originate from the small differences in the reduced projection n_x for the two "spin flop" states. The intermediate field of 8 T meanwhile spans the two states with $\boldsymbol{n}$ smoothly rotating through some range of angles, whilst for others (angles closer to the $\boldsymbol{y}$ direction), the field is not sufficient to rotate $\boldsymbol{n}$ away from the easy-axis. For each value of the magnetic field in Fig. 5.8, calculated

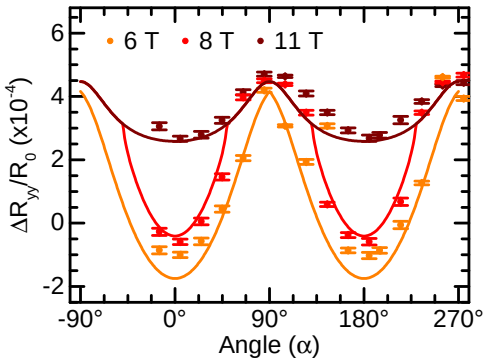

Figure 5.8: Longitudinal SMR response ΔR_{yy} for a magnetic field rotated in the xy plane through an angle α and normalised to the zero-field resistance. The charge current $\boldsymbol{j}_c$, and hence $\alpha=0°$, are coincident with $\boldsymbol{y}$. The solid lines represent the calculated SMR response using $H_D=2.72$ T, $H_{an}^{eff}=23.8$ mT and $H_{an}^{\perp}=1.54$ µT. Figure adapted from Ref. [r10].

SMR responses are plotted as solid lines based on Eqns 5.1 – 5.4.

The corresponding transverse SMR response ΔR_{yx} is shown in Fig. 5.9 alongside the calculated responses as solid lines. Although there is minimal field dependence,

ΔR_{yx} is maximal for $\mu_0 \boldsymbol{H} = 6$ T. The agreement between the calculated response based on the n_{yx} component of $\boldsymbol{n}$ confirms further that the canted moment and field induced magnetisation $\boldsymbol{m}$ have no impact on the spin Hall magnetoresistance of this system, unlike other systems where the transverse and longitudinal responses may be dominated by different magnetic order parameters [r19].

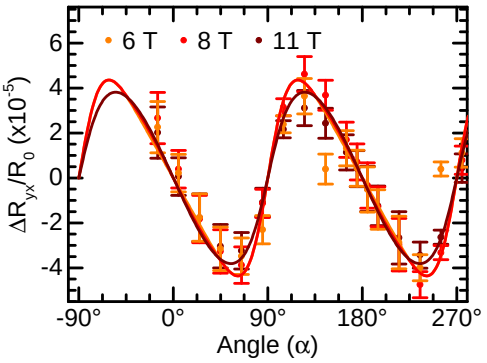

Figure 5.9: Transverse SMR response ΔR_{yx} for a magnetic field rotated in the xy plane through an angle α and normalised to the zero-field resistance. The charge current $\boldsymbol{j}_c$, and hence $\alpha = 0°$, are coincident with $\boldsymbol{y}$. The solid lines represent the calculated SMR response. Figure adapted from Ref. [r10].

It is worth noting that the transverse SMR ΔR_{yx} for devices orientated such that $\boldsymbol{j}_c$ is parallel to $\boldsymbol{y}$ is one order of magnitude smaller than for the devices orientated 90° in Fig. 5.6, although the general functional form is similar. This difference originates from the magnitude of n_{yx} that appears in this orientation, highlighting further the importance in device orientation relative to the magnetic anisotropies when considering the SMR response.

5.1.5 Angular Dependence of the Spin Reorientation Field H_{cr}

From Fig. 5.7, the value of H_{cr} could be extracted easily from the saturation of the SMR response ΔR_{yy}. By understanding the behaviour of H_{cr} with angle between the EA and $\boldsymbol{H}$, the role of the DMI field can be probed in order to further reinforce the spin Hall magnetoresistance as a true probe of the bulk antiferromagnetic state. Given that a minimum in the value of H_{cr} should occur for $\boldsymbol{H}$ parallel to the EA, the variation of H_{cr} as a function of χ can be investigated by applying the magnetic field in the xz-plane. In this plane, there will be no contributions from any possible anisotropic magnetoresistance due to proximity induced magnetism in the Pt Hall bar [13, 129]. Fig. 5.10 shows the SMR response ΔR_{yy} for several magnetic fields within the xz-plane perpendicular to $\boldsymbol{j}_c$, defined by the angle β between $\boldsymbol{H}$ and $\boldsymbol{x}$ within this plane. When $\boldsymbol{H}$ is along the EA, this then corresponds to $\beta = -33°$, in other words, there is a phase shift of 33° between the experimental frame of reference with the angle β and the frame of reference used in Eqn. 5.4 with the angle $\chi = \beta + 33°$. For an angle of $\beta = -30°$ (i.e. $\chi = 3°$), the experimental data in Fig. 5.10 (black points) displays a sharp jump in the value of ΔR_{yy} between $\mu_0 H = 5$ T and $\mu_0 H = 6$ T. This behaviour for ΔR_{yy} is what one would expect for the classical spin flop ($\chi \approx 0°$ gives rise to a first-order transition), where $\boldsymbol{n}$ abruptly reorientates as compared to $\chi \neq 0°$, where ΔR_{yy} continuously increases up to a saturation value as $\boldsymbol{n}$ smoothly rotates [29]. As β is increased, $\boldsymbol{H}$ will eventually lie within the basal plane, i.e. perpendicular to the easy-axis, when β approaches 60°. Here, H_{cr} should approach

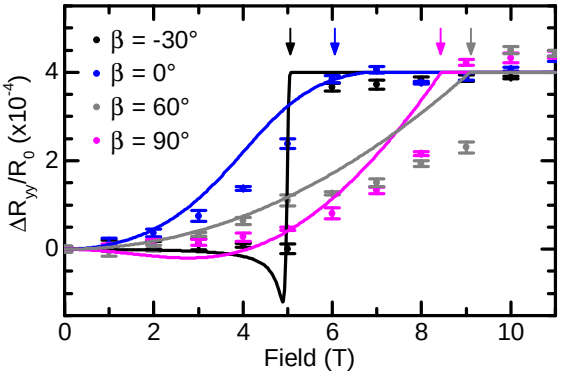

Figure 5.10: Longitudinal spin Hall magnetoresistance ΔR_{yy} at 200 K for Hall bars perpendicular to the in-plane projection of the easy-axis, normalised by the zero-field resistance of the device R_0. The applied magnetic field $\boldsymbol{H}$ subtends different angles β to $\boldsymbol{x}$, where $\boldsymbol{H}$ parallel to the easy-axis corresponds to β = -33°. Figure adapted from Ref. [r10].

the maximum value, experimentally seen at $\mu_0 \boldsymbol{H} \approx 10$ T, a value consistent with reports making use of antiferromagnetic resonance at comparable temperatures [241]. Increasing β further such that $\boldsymbol{H} \| \boldsymbol{z}$ at $\beta = 90°$, the critical field decreases as the angle between $\boldsymbol{H}$ and the EA decreases again. For all values of β shown in Fig. 5.10, the calculated responses, shown as solid lines, match the experimental points well. There is a sharp suppression of the calculated response when β = -30°. This originates from the 3° of misalignment between the field and the easy-axis direction inducing tilting of $\boldsymbol{n}$ as $\boldsymbol{H}$ approaches H_{cr}.

The magnetic field required for the saturation of ΔR_{yy} H_{cr} can be extracted from Fig. 5.10 as a function of β. This results in the black experimental data points shown in Fig. 5.11. Using Eqn. 5.1 – Eqn. 5.4, H_{cr} can be calculated as a function of the

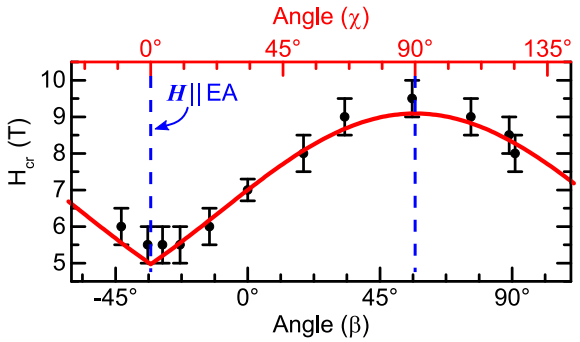

Figure 5.11: Critical magnetic field H_{cr} for the reorientation of $\boldsymbol{n}$ as a function of the angle β between the applied field $\boldsymbol{H}$ and $\boldsymbol{x}$ for a magnetic field in the geometric xz-plane. The top axis shows the angle χ from the easy-axis, related to β as $\chi = \beta + 33°$. The dashed lines indicate the point where the magnetic field is parallel or perpendicular to the easy-axis. The red line shows the calculated value of H_{cr} according to Eqn. 5.4. The region below the red line indicates the easy-axis phase under the applied field. Figure adapted from Ref. [r10].

angle χ between the magnetic field and the EA. This calculated angular dependence, bearing in mind that $\chi = \beta + 33°$, is shown in Fig. 5.11 by the solid red line. The magnetic fields above the solid line represent the spin flop phase and those below represent the easy-axis phase. One can note that the calculated variation of H_{cr} matches well the experimentally extracted values of Fig. 5.11. By comparing the experimental values of $H_{cr}(\beta)$ with the calculated values for $H_{cr}(\chi)$ in Fig. 5.11, we can extract the values for

the internal DMI field and the effective anisotropy field in order to compare with previous measurements that make use of volume measurements. From this fitting we obtain the values listed in Tab. 5.1 and represent the values used in the calculations of Fig. 5.4 – Fig. 5.10. These values are then consistent with the values extracted by volume

Field	Value	Ref.
H_D	2.72 T	Calculated Here
H_{an}^{eff}	23.8 mT	Calculated Here
H_D	2.11 T[a]	Ref. [29]
H_{an}^{eff}	$\sim$22 mT	Ref. [29]

Table 5.1: Values of the effective internal DMI field H_D and the effective anisotropy field H_{an}^{eff} extracted from spin Hall magnetoresistance measurements compared to values from literature.

[a]This value is based on the spontaneous magnetisation about T_M. The authors of Ref. [53] determine H_{DMI} to be $\sim$4 T from resonance measurements but the authors comment that this is too large. The hematite crystals of Ref. [53] are natural rather than synthetic so may lead to impurities that alter the effective fields, leading to terms that are not accounted for in the simple theory applied by the authors of Ref. [53].

measurements and demonstrate that the surface sensitive nature of the spin Hall magnetoresistance can be used to extract the antiferromagnetic anisotropies, even when the volume is too small to enable more traditional measurement techniques. This result proves useful for the latter half of this chapter where the spin Hall magnetoresistance will be used to investigate the antiferromagnetic anisotropies of thin films of hematite [r14].

5.1.6 Probing the Magnetic Anisotropies of the Easy-Plane Phase of Bulk Hematite

Having established that the spin Hall magnetoresistance can be used for the easy-axis phase of hematite below the Morin transition temperature T_M, the easy-plane phase can also be investigated for both a charge current $\boldsymbol{j}_c$ parallel and perpendicular to the in-plane projection of the c-axis in order to determine the strength of the anisotropy within the easy-plane $H_{an}^{\perp}$ [r1]. At $T > T_M$, the Néel vector now lies in the plane perpendicular to the crystallographic c-axis,[3] the same plane that $\boldsymbol{n}$ adopts above the spin flop field of the easy-axis phase. In the absence of a magnetic field to break the degeneracy, there are then three degenerate easy directions for $\boldsymbol{n}$ to lie within this plane. For the geometry such that $\boldsymbol{j}_c$ passes parallel to the geometric $\boldsymbol{x}$ direction, the interfacial spin accumulation $\boldsymbol{\mu}_s$ will then be polarised within the easy-plane. Meanwhile $\boldsymbol{j}_c \| \boldsymbol{y}$ will result in $\boldsymbol{\mu}_s$ polarised perpendicular to the easy-plane. Fig. 5.12 shows the relationship between the Pt Hall bar and the antiferromagnetic easy-plane shaded in red, which is inclined to the geometric yz-plane towards the x-axis by 33°.

A magnetic field within the easy-plane will lead to a rotation of $\boldsymbol{n}$ within the plane to lie perpendicular to $\boldsymbol{H}$ once the magnitude of the applied magnetic field is able to over-

[3]The c-axis is now the hard-axis perpendicular to the easy-plane.

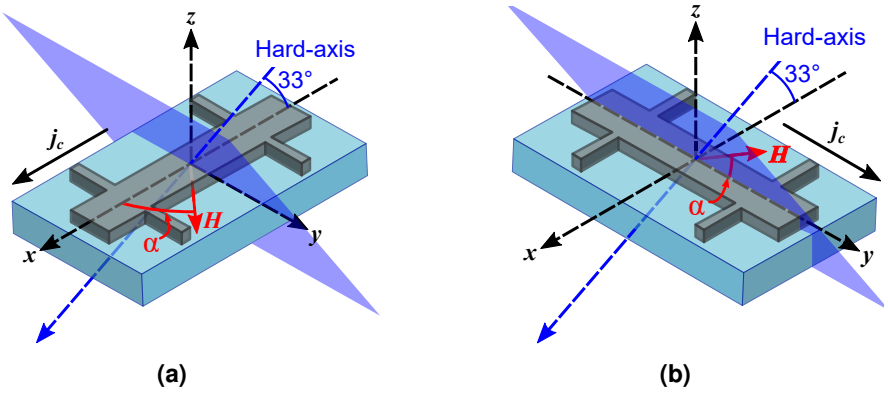

Figure 5.12: Schematic of devices used to investigate SMR in $(1\bar{1}02)$ orientated bulk α-Fe_2O_3 for $T > T_M$. Pt Hall bars are defined by electron beam lithography and orientated such that the charge current passes parallel (a) or perpendicular (b) to the in-plane projection of the hard-axis. The hard-plane is inclined in the xz-plane and indicated by blue plane.

come the in-plane anisotropy. Once $\boldsymbol{H} > H_{MD}$, the degeneracy between the different domains is completely broken and a mono-domain state is created [r1, 15, 17]. This is more obvious in thin film samples, such as thin film NiO, where the growth process introduces additional stress, defects and magnetic anisotropy into the sample, correspondingly increasing the value of field required to create a mono-domain state H_{MD} [r1, 15]. Once a mono-domain state has been created, the SMR response saturates given that there is no additional contributions to the magnetic signal from the Néel vector once it reaches its new equilibrium position (Eqn. 5.1). With knowledge of H_{MD}, one can calculate the in-plane anisotropy required [r1]. If $\boldsymbol{H}$ is applied along the hard-axis, there will be no reorientation of $\boldsymbol{n}$ given that all three degenerate directions represent equilibrium positions. As for a magnetic field parallel to the geometric x-axis, this will break the degeneracy due to the finite component of $\boldsymbol{H}$ within the easy-plane, however, this may not produce a mono-domain state as several equilibrium positions of $\boldsymbol{n}$ may exist.

With these established expectations for the behaviour of $\boldsymbol{n}$ we can consider the impact on the SMR response for the two geometries in Fig. 5.12 as $\boldsymbol{H}$ is rotated within the xy-plane. By investigating the angular dependence of ΔR_{xx} and ΔR_{yy}, the anisotropy in the basal plane can be determined. For the case of $\boldsymbol{j}_c \| \boldsymbol{x}$, $\boldsymbol{H}$ parallel to the y-axis (i.e. perpendicular to $\boldsymbol{j}_c$) will lead to $\boldsymbol{n}$ maintaining an equilibrium position in the xz-plane (i.e. within the easy-plane). As $\boldsymbol{H}$ is rotated towards $\boldsymbol{x}$, the average value of n_y should increase, leading to a minima in the value of ΔR_{xx}. The angular dependence for the device orientated such that $\boldsymbol{j}_c$ is parallel to $\boldsymbol{x}$ is shown in Fig. 5.13a, where indeed we see a modulation between a minima for $\boldsymbol{H} \| \boldsymbol{j}_c$ (i.e. $\alpha = 0°$) and a maxima for $\boldsymbol{H} \perp \boldsymbol{j}_c$.

When $\boldsymbol{j}_c$ is now passed within the easy-plane ($\boldsymbol{j}_c \| \boldsymbol{y}$), the angular dependence will now depend on n_x. For $\boldsymbol{H} \| \boldsymbol{y}$, $\boldsymbol{n}$ will lie within the xz-plane, i.e. there will be a finite value of n_x. Meanwhile, the magnetic field applied parallel to the hard-axis will lead to n_x being zero. From these two states, the SMR response ΔR_{yy} should then modulate between a low resistance state when $\boldsymbol{H} \| \boldsymbol{y}$ (i.e. $\alpha = 0°$[4]) and a high resistance state when $\boldsymbol{H} \perp \boldsymbol{x}$.

[4] α is always calculated with respect to the axis of the charge current $\boldsymbol{j}_c$.

This modulation is experimentally seen in Fig. 5.13b.

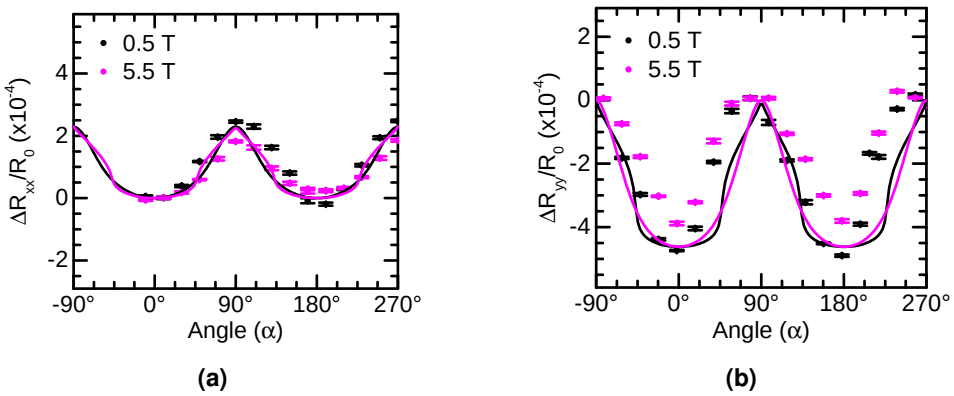

Figure 5.13: Angular dependence of the longitudinal spin Hall magnetoresistance ΔR_{jj}, where $j = x, y$, for a magnetic field rotated in the xy plane, normalised to the zero-field device resistance. a) Longitudinal SMR response for $\boldsymbol{j}_c \| \boldsymbol{x}$. b) Longitudinal SMR response for $\boldsymbol{j}_c \| \boldsymbol{y}$. These curves are measured at $T = 280$ K and thus above the Morin transition temperature. The antiferromagnetic structure is therefore an easy-plane. The solid lines represent the calculated SMR response. Figure adapted from Ref. [r10].

The modulation of both ΔR_{xx} and ΔR_{yy} due to the reorientation of $\boldsymbol{n}$ within the easy-plane is driven mostly by the in-plane anisotropy field $H_{an}^{\perp}$. The absence of a field dependence in Fig. 5.13, where the two curves of each geometry were taken at $\mu_0 \boldsymbol{H} = 0.5$ T and $\mu_0 \boldsymbol{H} = 5.5$ T, indicates that the critical "spin flop" field of the easy-plane phase is less than 0.4 T [r1]. This places an upper limit on $H_{an}^{\perp}$ of 1.6 µT. By fitting the angular dependence for both $\boldsymbol{j}_c$ along $\boldsymbol{x}$ (Fig. 5.13a) and $\boldsymbol{j}_c$ along $\boldsymbol{y}$ (Fig. 5.13b), we can find that, with the previous extracted values in Tab. 5.1, $H_{an}^{\perp} = 1.54$ µT. This value is consistent with our expected upper limit, whilst the calculated responses in Fig. 5.13 highlight the expected behaviour of the Néel vector for a magnetic field moving through both the easy-plane and hard-axis. Meanwhile, the weak field dependence not only provides an upper limit for the critical field, but also indicates that the canted moment $\boldsymbol{m}$ that increases linearly with $\boldsymbol{H}$ has a negligible contribution to the SMR.

Although also visible when comparing Fig. 5.4 and Fig. 5.7, it is more obvious in Fig. 5.13 that the geometry with $\boldsymbol{j}_c \| \boldsymbol{y}$ gives rise to a larger response than $\boldsymbol{j}_c \| \boldsymbol{x}$. This may be due to differences in the lithographic process, for example the relationship between a measurement devices "length" and the beam rastering direction, or due to the crystal symmetry along the two directions promoting differences in the interface transparency. However, from the measurements performed here it is challenging to determine why one geometry shows a larger response. The electrically measured SMR response is a combination of a series of events from the application of the charge current and its conversion to a spin current to the interaction between the spin current and the magnetic material. In order to ascertain the underlying cause of this difference, measurements would need to be performed as a function of the Pt thickness as well as for other crystal orientations. In a later section, measurements on two orientations of thin film hematite demonstrate nearly one order of magnitude difference in the recorded SMR response. A similar effect has also been observed in, for example, $CoFe_2O_4$ where the SMR response differs depending on the relative crystal orientation parallel to $\boldsymbol{j}_c$ [299]. Whilst SMR is a powerful tool to investigate the magnetic anisotropies based on the behaviour with field,

the absolute value of the SMR needs to be approached with caution.

5.1.7 Temperature Dependence of the Magnetic Anisotropies of Bulk Hematite

This final section will discuss the behaviour of the magnetic anisotropies of bulk hematite as a function of temperature by detecting the change in the spin flop field with temperature. As detailed in an earlier chapter (Ch. 4, Sec. 4.1), the magnetic anisotropies of hematite are the main driver of the Morin transition. The two magnetic anisotropies H_{K_1} and H_{K_2} compete with one another to produce a net, effective anisotropy field H_{an}^{eff} directed along the c-axis [239]. Whether hematite is in the easy-axis phase or easy-plane phase then depends on the sign of this effective anisotropy field, where at $T = T_M$, H_{an}^{eff} changes sign. This then implies a corresponding temperature dependence of the spin reorientation field H_{cr} (Eqn. 5.4). Such a temperature dependence has been observed in volume measurements such as antiferromagnetic resonance, where the spin flop field is constant from low temperatures until about 100 K – 150 K before decreasing in magnitude, reaching zero at the Morin transition temperature T_M. Given the differences in the SMR response for temperatures less than and greater than T_M, it stands to reason that the Morin transition itself can be detected by SMR, allowing one to produce a magnetic phase diagram as a function of temperature and field.

The temperature dependence of the SMR response for devices aligned such that $\boldsymbol{j}_c \| \boldsymbol{x}$ (i.e. the geometries shown in Fig. 5.2a and Fig. 5.12a) is shown in Fig. 5.14. As a magnetic field is swept parallel to the charge current, the reorientation of $\boldsymbol{n}$ that

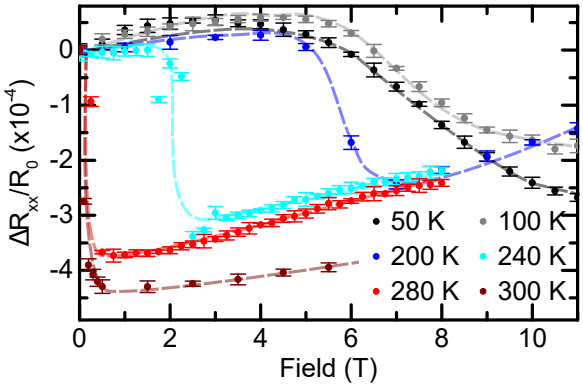

Figure 5.14: Normalised longitudinal spin Hall magnetoresistance for Hall bars aligned parallel to the in-plane projection of the crystallographic c-axis for different temperatures. The dashed lines are guides for the eye and the temperature range spans both the easy-axis ($T < 260$ K) and easy-plane ($T > 260$ K) phases. Figure adapted from Ref. [r10].

occurs is visible as a decrease in the relative resistance, allowing us to identify the critical spin flop field $H_{cr}\,(33°)$ as a function of temperature, where $\chi = 33°$ enters due to the inclined nature of the easy-axis. At lower temperatures, e.g. 50 K shown in black in Fig. 5.14, the minimum in the resistance occurs at larger magnetic fields than closer to the Morin transition temperature, e.g. 240 K shown in cyan in Fig. 5.14. Above T_M in the easy-plane phase (red and brown curves in Fig. 5.14), the SMR signal still presents features consistent with a spin flop condition at low magnetic fields. Such a feature has also been observed in antiferromagnetic resonance measurements [241, 302]. It may also originate from the inclined nature of the easy-axis and the $\boldsymbol{x}$ direction leading to a

component of $\boldsymbol{H}$ within the easy-plane. This then leads to a reorientation of $\boldsymbol{n}$ to a new equilibrium position, as discussed in Sec. 5.1.6, once the easy-plane projection of $\boldsymbol{H}$ exceeds the magnetic field required for reorientation [r1]. Alternatively, it may come from a remnant interfacial magnetism at the hematite surface [303].

From the curves exemplified in Fig. 5.14, the value of $H_{cr}\,(33^\circ)$ can be extracted as a function of temperature. This magnetic field can then be used to calculate the effective anisotropy field H_{an}^{eff}. The temperature dependence of $H_{cr}\,(33^\circ)$ is depicted in

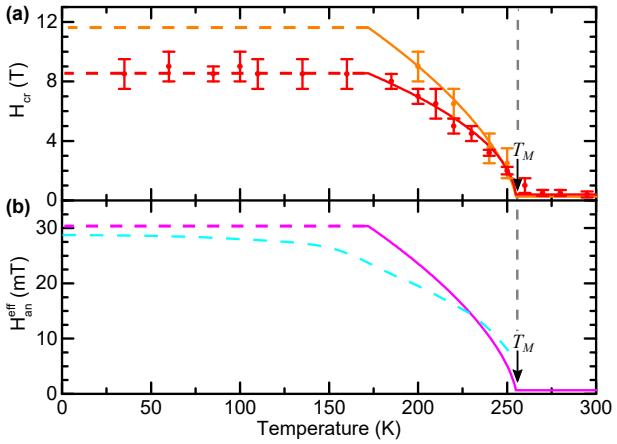

Figure 5.15: Top: Temperature dependence of $H_{cr}(\chi)$ for a magnetic field parallel ($\chi = 33^\circ$, red points) and perpendicular ($\chi = 90^\circ$, orange points) to the in-plane projection of the crystallographic c-axis. The solid lines represent fits based on second-order Landau phase transitions, scaling as $H_{cr} \propto \sqrt{T_M - T}$. The dashed lines indicate the point of constant magnetic field. Bottom: Temperature dependence of the effective anisotropy field H_{an}^{eff} calculated from the values in the top panel for H_{cr}. The Morin transition temperature T_M is indicated. The cyan curve indicates the magnetic anisotropy extracted for bulk hematite in Ref. [241]. Figure adapted from data published in Ref. [r10].

Fig. 5.15a in red. At low temperatures, $H_{cr}\,(33^\circ)$ remains fairly constant, consistent with previous investigations of the spin flop [53, 239, 241, 264]. Beginning around $T = 165$ K, $H_{cr}\,(33^\circ)$ begins to decrease towards the Morin transition temperature. The red solid line in Fig. 5.15a represents a fit to $H_{cr}\,(33^\circ)$ based on second-order phase transitions described by Landau theory and has been previously seen [239, 245]. The functional form of the fit follows $H_{cr} \propto \sqrt{T_M - T}$, giving a value of T_M ~255 K, remarkably close to the value measured by SQUID magnetometry in Fig. 5.3. If $\boldsymbol{H}$ is rotated be 90° within the sample plane, it will now lie parallel to $\boldsymbol{y}$ and thus in the basal plane perpendicular to the c-axis, i.e. perpendicular to $\boldsymbol{n}$ when $T < T_M$. Fig. 5.15a shows in orange the value of $H_{cr}(90^\circ)$ alongside a fit based on the same functional form as before, resulting in the same estimation for the value of T_M of 255 K. By assuming a temperature independent effective DMI field H_D of 2.72 T [29, 53], the effective anisotropy field can be calculated. This is shown in Fig. 5.15b. The value of H_{an}^{eff} is 0 mT at the Morin transition temperature, and it increases up to around 30 mT at low temperatures. Comparing these values with those from resonance measurements (shown in cyan), we find that the effective anisotropy field obtained from the surface sensitive measurements here represents well the internal anisotropy of the bulk [29, 239]. It is worth noting that the cyan curve of Fig.5.15b represented the sum of the two key anisotropies H_{K_1} and H_{K_2} whilst here H_{an}^{eff} represents the net effective uniaxial anisotropy field, that also includes a contribution from H_D (see Sec. 5.1.1).

5.1.8 Conclusion

This section has presented a measurements of the magnetic anisotropies of a bulk hematite crystal orientated as $(1\bar{1}02)$, also known as r-plane by making use of the spin Hall magnetoresistance. This orientation introduces a 33° angle between the crystallographic c-axis and the surface plane. Below the Morin transition temperature, this means that the antiferromagnetic easy-axis is likewise inclined whilst the easy-plane above the Morin transition temperature (and above the spin flop of the easy-axis phase) is the plane perpendicular to the c-axis. The magnetic anisotropies were investigated below the Morin transition temperature T_M for two Pt Hall bar geometries, one with the probing current parallel to the in-plane component of the easy-axis and one with the probing current perpendicular to the easy-axis in-plane component. In both configurations, the reorientation of the Néel vector that takes place was visible by a change in the relative resistance, allowing the extraction of the critical field H_{cr} for this reorientation as a function of the angle χ between the field and the easy-axis.

Using a simple model of hematite, the values of H_{cr} for an arbitrary angle between the field and Néel vector can be used to calculate the strength of the internal effective field produced by the antisymmetric Dzyaloshinskii-Moriya interaction H_D and the effective anisotropy field H_{an}^{eff} produced by the competing anisotropies that determine the Morin transition temperature. The calculated values from the surface sensitive SMR technique agree well with the previously measured values obtained from volume based techniques like antiferromagnetic resonance and neutron scattering demonstrating that SMR is a powerful tool for the investigation of antiferromagnetic anisotropies. By measuring the SMR across the Morin transition, the differences in the response of the easy-axis and easy-plane phases were discussed and the contribution from the canted moment $\boldsymbol{m}$ to the SMR was seen to be negligible in this system. The next section will focus on applying the spin Hall magnetoresistance to investigate the antiferromagnetic anisotropies of thin film hematite, where, for example, the small antiferromagnetic resonance response cannot be detected.

5.2 Using Spin Hall Magnetoresistance to Probe the Magnetostatic Properties of Thin Film Hematite

In this section, the results of Sec. 5.1 will be employed to study thin films of α-Fe_2O_3. Sec. 5.1 has demonstrated that the magnetic anisotropies of a bulk antiferromagnet could be extracted by surface sensitive measurements. Given that other common techniques used to investigate antiferromagnetic anisotropies (e.g. antiferromagnetic resonance [46, 47, 91, 94, 159, 239, 241, 242, 264, 270, 304]) are not easily applicable to thin film AFMs, the surface sensitive nature of the spin Hall magnetoresistance (SMR) offers an attractive alternative method. This section will focus on probing the antiferromagnetic anisotropies and magnetostatic properties of thin films of α-Fe_2O_3 by making use of SMR. Whilst previously, we discussed SMR for $(1\bar{1}02)$ orientated r-plane α-Fe_2O_3, this section is centred around (0001) orientated thin films, i.e. c-plane, α-Fe_2O_3. This means that the (0001) basal plane of the hematite structure is the sample plane, and therefore the frame of reference for the electrical measurements will be the same as the magnetic frame of reference, i.e. the easy-axis will be coincident with the geometric $\boldsymbol{z}$ direction rather than making a finite angle to it. In this orientation, the affect of the spin flop and

the DMI reorientation for $\boldsymbol{H} \| EA$ and $\boldsymbol{H} \perp EA$ can be investigated, with the spin accumulation now lying in the basal plane. This then allows for an in-plane easy-plane AFM above the Morin transition temperature and an easy-axis AFM with the easy-axis out-of-plane below T_M and therefore drastically different behaviour can be expected above and below the transition. As will be shown in this section, however, additional signals appear in the SMR response that cannot be accounted for if one considers the EA to be perfectly out-of-plane. Instead, this can be explained by a finite angle between the geometric out-of-plane z-axis, which is coincident with the (0001) substrate axis, and the film (0001) axis, confirmed by magnetic imaging (see Sec. 4.2.6).

Some of the work in this section is published as a research article in Ref. [r14], where the explanation of the spurious signal was developed with Dr. C. Ulloa of Utrecht University in the Netherlands. The α-Fe_2O_3 thin films investigated were obtained through collaboration with the group of Prof. Avner Rothschild at the Technion University of Technology in Haifa, Israel grown by Dr. D. A. Grave and Mr A. Kay. These films were grown on sapphire (Al_2O_3) substrates by pulsed laser deposition (PLD). A detailed description of the growth can be found elsewhere [263, 283, 305], but briefly, they were deposited from a stoichiometric Fe_2O_3 target at an atmospheric oxygen pressure of 10 mTorr at a temperature of 800 ℃ with a laser fluence of 1.1 Jcm^{-1}. Details of other contributions to this work can be found in the appendix.

For the electrical measurements, Pt Hall bars were defined by electron beam lithography and sputter deposition of 7 nm Pt in an Ar atmosphere. Electrical contacts were made by a second lithographic step and the deposition of Ti/Au contact pads. Making use of a Keithley 6221A sourcemeter and Keithley 2182A nanovoltmeter in combination in so-called Delta Mode, the longitudinal resistance of the Hall bar can be captured. Further measurement details can be found in Sec. 4.2.5.

5.2.1 Characterisation of (0001) Orientated Hematite Films

The first part of this section will focus on the structural and magnetic characterisation of 100 nm (0001) orientated hematite films. Structural measurements reveal a disparity in the alignment of the film and substrate axes, but the impact of this on the magnetic properties appears to be minimal from the measurements here. The crystallographic quality of the thin films can be assessed through XRD (c.f. Sec. 4.2.2) by making both 2θ-ω measurements of the (0006) peak and subsequent rocking curves across this peak. The results of these measurements are shown in Fig. 5.16. The hematite peak in Fig. 5.16a can be fit with a simple Gaussian with the fitting parameters of interest, that is to say the peak position and the FWHM, listed in Tab. 5.2. This Gaussian fit, shown in

Measurement	Peak Angle (°)	FWHM (°)
2θ	(39.34±0.08)°	(0.632±0.022)°
Rocking Curve	(19.670±0.047)°	(0.10±0.005)°

Table 5.2: Gaussian fit parameters for XRD measurements on (0001) orientated hematite thin films.

red in Fig. 5.16a, leads to a peak angle at 2θ = 39.34±0.08° This can then directly be translated into a value for the length of the c-axis via the Bragg equation (refer back to Sec. 4.2.2), resulting in a value of (13.726±0.001) Å, in other words ∼0.2% smaller than

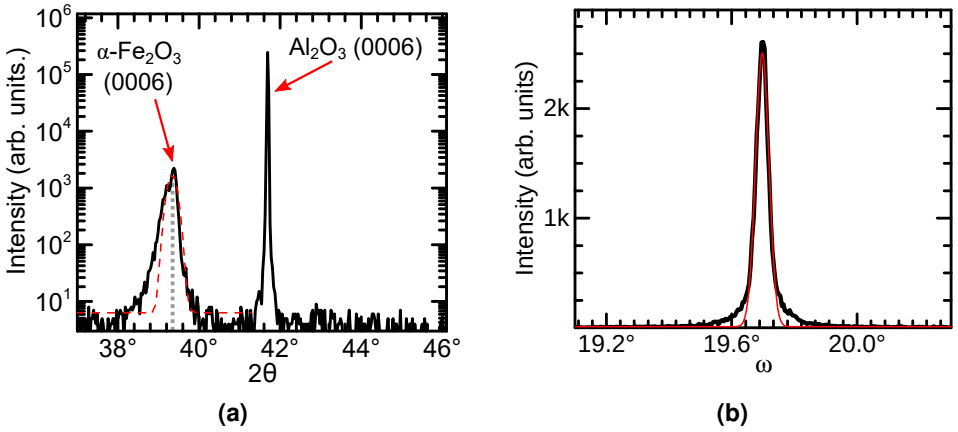

Figure 5.16: X-ray diffraction characterisation of 100 nm thick α-Fe_2O_3. a) 2θ-ω scan over the (0006) peak of α-Fe_2O_3/Al_2O_3, labelled for the respective components. The red fit represents a Gaussian fit to the α-Fe_2O_3 (0006) peak. b) Rocking curve of the (0006) peak of α-Fe_2O_3 for a fixed angle of θ taken from fitting the peak in a). Figures adapted from Ref [r14]. Copyright American Physical Society.

the bulk value of 13.749 Å [29]. Hematite and sapphire have different lattice constants in the sample plane (a-axis [α-Fe_2O_3] = 5.046 Å, a-axis [α-Al_2O_3] = 4.785 Å) resulting in a lattice mismatch of 5.02%. This then leads to compressive strain within the sample plane[5], which one would expect to result in an expansion along the c-axis according to Poisson's ratio [306]. This would then indicate that the films may suffer from some oxygen deficiency in order to allow compression along both axes. Closer inspection of the α-Fe_2O_3 (0006) peak also leads to the observation that the peak is quite broad and the Gaussian does not replicate the full shape of the peak (the Gaussian fit in Fig. 5.16a itself has an R^2 of 0.898). There is also a shoulder to the left of the main peak. This cannot be attributed to a second wavelength of the incident x-rays given that the measurements were performed with a monochromator situated between the x-ray source and the sample. Instead, such a feature would originate from a portion of the film having a larger c-axis, and thus a diffraction peak appearing at smaller values of 2θ The alignment of the film can be investigated further by fixing the incident x-rays at $2\theta = 39.34°$, i.e. the peak angle in Fig. 5.16a. The angle of the detector is then scanned around the expected value of ω for further indication of the structural quality along the out-of-plane axis, shown in Fig. 5.16b. The resulting peak can again be fit by a Gaussian and the key parameters are again shown in Tab. 5.2. The angle at which the majority of the film is aligned along, i.e. the peak of Fig. 5.16b, occurs at ω=19.70$\pm$0.047, as expected from the value of the 2θ peak.

5.2.1.1 Magnetic Characterisation of (0001) Orientated Hematite Films

In addition to the crystallographic structure, the magnetic properties can be investigated. Normally, the low net magnetisation of AFMs make it challenging to access the bulk magnetic properties by making use of SQUID magnetometry (c.f. Sec. 4.2.1), where the substrates will give rise to a large background. The main feature of interest for such films is whether there exists a Morin transition or not, identified by whether the

[5] Inspection of the a-axis finds a film lattice constant of 5.027Å, only slightly smaller than bulk, indicating that the in-plane compression is not as significant as one would expect from the lattice mismatch

canted moment is detectable ($T > T_M$) or not ($T < T_M$). We first investigate the magnetic properties at a fixed temperature as a function of magnetic field $\boldsymbol{H}$ applied within the basal plane. Above T_M, a parallel alignment of the canted moment $\boldsymbol{m}$ and $\boldsymbol{H}$ should occur once the field is strong enough to overcome the saturation field. Fig. 5.17a shows these measurements with a linear background subtracted to account for the diamagnetic sapphire substrate at 300 K (red) and 10 K (cyan). As can be seen, both temperatures present a magnetic hysteresis consistent with the presence of ferromagnetic components. One could associate both of these hystereses to the canted moment which would lead to the (incorrect) assumption that there is no Morin transition down to 10 K.

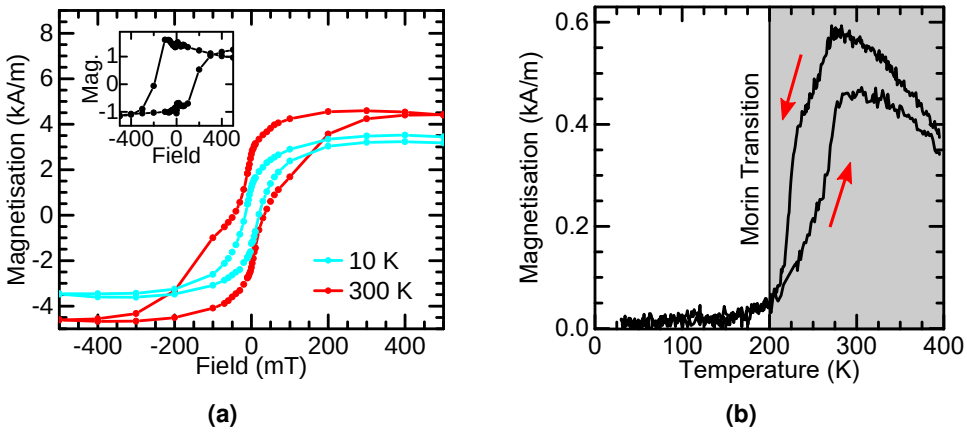

Figure 5.17: a) Magnetisation of 100 nm thick, (0001) orientated hematite films as a function of the in-plane applied field at 10 K (cyan) and 300 K (red). Inset: The difference between the two curves gives a rough idea of the hematite response. b) Temperature dependence of the magnetisation of the same films for a magnetic field applied within the basal plane. Adapted with permission from Ref. [r15]. Copyright 2020 American Chemical Society.

Instead of sweeping the magnetic field, one may keep $\boldsymbol{H}$ fixed and continuously change the temperature. At the Morin transition, the measured magnetisation should reduce due to the disappearance of the α-Fe_2O_3 moment, leaving behind only the substrate contributions. The temperature dependent magnetisation of a typical film is shown in Fig. 5.17b. This measurement was performed by first warming to 400 K and applying an in-plane magnetic field of 3 T to saturate the canted moment. The field was then reduced to a probing field of 50 mT and the temperature was lowered at a continuous rate of 1 Kmin^{-1}. After reaching 10 K, the temperature was warmed back to 400 K. After removing a temperature independent background to account for the diamagnetic substrate, the resulting curve in Fig. 5.17b shows a clear drop in the measured magnetisation indicative of a Morin transition, with $T_M \approx 200$ K. Unlike in the bulk crystal (Fig. 5.3), the transition here takes place over 50 K and shows a thermal hysteresis of $\sim$20 K although the start and end temperatures of the transition are the same. Both of these features have been reported for thin films and nanoparticles in the literature [29, 262, 263, 280, 282, 307]. The broadness of the transition comes from the additional strain in the film from the growth process leading to variable transition temperatures throughout, whilst the thermal hysteresis originates from local variations of the anisotropy hindering the nucleation of the easy-axis phase when cooling [69, 307, 308]. The growth introduces strain, which accentuates the magnetostrictive behaviour of α-Fe_2O_3, increasing the impact of this normally small anisotropy [238, 239, 309, 310].

The visible Morin transition in Fig. 5.17b indicates that the hysteresis in Fig. 5.17a

might originate from additional components in the sample rather than just the expected sapphire (a diamagnet) and hematite. Thickness dependent studies on α-Fe_2O_3 films have demonstrated that parasitic phases of iron oxide can occur, specifically γ–Fe_2O_3 (the mineral maghemite) [311]. This phase of iron oxide is a ferrimagnet rather than an antiferromagnet and thus would give rise to a hysteresis. Whilst it may initially seem that this additional phase is a problem for the studies conducted in this thesis, the work in Ref. [311] shows that this γ–Fe_2O_3 layer only persists for the first few nm of growth[6] whilst the films used here are 100 nm in thickness. Given that the hysteresis at 10 K can then be attributed to γ–Fe_2O_3, it can be removed as a background from the curve in Fig. 5.17a at 300 K, resulting in the square loop shown in the inset of the figure. This square loop indicates that there are indeed these two contributions.

5.2.2 Probing the Magnetic Anisotropies of the Easy-Plane Phase of (0001) Orientated Hematite Thin Films

The magnetic measurements in Fig. 5.17 demonstrated that the 100 nm (0001) thin films of hematite utilised here display a Morin transition. This means that the magnetic anisotropies of these films can be investigated in both the higher temperature, easy-plane phase and the lower temperature easy-axis phase. This section will focus the magnetic anisotropies of (0001) orientated thin films of hematite for temperatures $T > T_M$ by making use of the spin Hall magnetoresistance (SMR). In the course of this thesis, other works have investigated the SMR in thin film α-Fe_2O_3 [16, 17], but the films used were too thin to display a Morin transition. This means that these studies were confined to the easy-plane phase, where the behaviour was found to be very similar to the easy-plane antiferromagnet NiO [r1, 14, 15]. In other words, the Néel vector $\boldsymbol{n}$ aligns perpendicular to the applied magnetic field once a critical threshold H_{MD} to produce a rotation of $\boldsymbol{n}$ is reached.

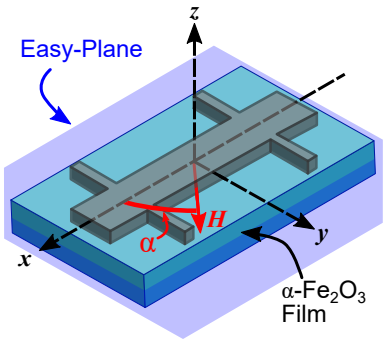

Figure 5.18: Schematic of a Hall bar on (0001) orientated hematite in the easy-plane phase above the Morin transition temperature. The easy-plane is coincident with the geometric xy-plane and indicated in light blue. The charge current is passed parallel to $\boldsymbol{x}$ as a voltage is captured.

Fig. 5.18 shows a schematic for the Hall bars used in this section, alongside the coordinate system. The direction of the charge current $\boldsymbol{j}_c$ is parallel to $\boldsymbol{x}$, whilst the xy-plane represents the magnetic easy-plane. The z-axis meanwhile is the magnetic

[6] Considering the saturation magnetisation of γ–Fe_2O_3, the thickness of this layer would need to be 3.9 nm to produce the observed magnetisation assuming that it is the sole contributor to the hysteresis at 10 K in Fig. 5.17a.

hard-axis. The longitudinal voltage measured parallel to $\boldsymbol{j}_c$ allows one to define the longitudinal SMR ratio ΔR_{xx} as the change in resistance with respect to the zero-field resistance R_0, normalised by R_0.

5.2.2.1 Probing Magnetic Anisotropies Using a Magnetic Field within the Easy-Plane

The application of a magnetic field $\boldsymbol{H}$ along either $\boldsymbol{x}$, parallel to $\boldsymbol{j}_c$, or $\boldsymbol{y}$, perpendicular to $\boldsymbol{j}_c$, will place $\boldsymbol{H}$ within the antiferromagnetic easy-plane (Fig. 5.18). The passing charge current $\boldsymbol{j}_c$ will lead to a spin accumulation $\boldsymbol{\mu}_s$, polarised along $\boldsymbol{y}$, at the Pt/α-Fe_2O_3 interface due to the spin Hall effect [7, 100]. As discussed in Sec. 5.1.1, the change in the longitudinal resistance of the Pt Hall bar originating from purely the spin Hall magnetoresistance effect should depend on the component of the Néel vector parallel to the spin accumulation (Eqn. 5.1). An increase (decrease) in the projection $\boldsymbol{n} \cdot \boldsymbol{\mu}_s$ will experimentally lead to a decrease (increase) in the measured longitudinal resistance. As $\boldsymbol{H}$ is then applied along either $\boldsymbol{x}$ or $\boldsymbol{y}$, the new equilibrium position of $\boldsymbol{n}$ will lie along either $\boldsymbol{y}$ or $\boldsymbol{x}$ respectively. By identifying the applied field required to induce this complete rotation, the underlying effective anisotropy in the easy-plane can be determined. In the case of $\boldsymbol{H} \| \boldsymbol{x}$, shown in Fig. 5.19a, the SMR response shows a sustained decrease with $\boldsymbol{H}$, consistent with the rotation of $\boldsymbol{n}$ within the easy-plane. ΔR_{xx} reaches a minimum at $\mu_0 H_{MD}$ = 2.5 T, which we can ascribe to the complete rotation of $\boldsymbol{n}$ across multiple domains [r1]. Unlike in the previous section (Fig. 5.10), where the application of a magnetic field parallel to the magnetic anisotropy axis led to an abrupt reorientation, the decrease of ΔR_{xx} here is more gradual, taking place across a range of magnetic fields. In a single domain sample, one would expect that once the magnetic field overcomes the in-plane crystalline anisotropy, the Néel vector would abruptly reorientate to a new equilibrium position. The gradual decrease here is related to the antiferromagnetic domain structure, where each domain has varying degrees of anisotropy and thus values for the critical magnetic field for the in-plane *spin flop* and the magnetic field induces domain redistribution [r1, 15]. Once the average orientation of $\boldsymbol{n}$ lies perpendicular to $\boldsymbol{H}$, further changes to the longitudinal resistance should then not have a magnetic origin. In Fig. 5.19a, ΔR_{xx} increases again above H_{MD}. Given that $\boldsymbol{H}$ is perpendicular to $\boldsymbol{n}$, this will lead to a sustained canting of $\boldsymbol{n}$ in the direction of $\boldsymbol{H}$ and an emergent moment $\boldsymbol{m}$.[7] The increasing value of $\boldsymbol{m}$ with $\boldsymbol{H}$ above H_{MD} reduces the value of $\boldsymbol{n}$ parallel to $\boldsymbol{y}$, and thus the $\boldsymbol{n} \cdot \boldsymbol{\mu}_s$ projection.[8]

When the magnetic field is now applied perpendicular to $\boldsymbol{j}_c$, along $\boldsymbol{y}$, the inverse is expected. The rotation of the average orientation of $\boldsymbol{n}$ across multiple domains will lead to a net increase of $\boldsymbol{n} \cdot \boldsymbol{\mu}_s$ across the dimensions of the Hall bar[9] and thus an increase of ΔR_{xx}, an expectation reflected by the experimental data in Fig. 5.19b. The increase of ΔR_{xx} with field reaches a plateau at the same value of $\boldsymbol{H}$ as for $\boldsymbol{H} \| \boldsymbol{x}$ in Fig. 5.19a demonstrating that the anisotropy along these two directions is similar. However, unlike in Fig. 5.19a, there is no suppression of the response at higher magnetic fields due to

[7] It could also be related to the Hanle magnetoresistance [312–314] perturbing the spin accumulation however, the absence of the effect at lower temperatures would indicate that any contribution is small for this geometry.

[8] This reduction of $\boldsymbol{n}$ at the expense of $\boldsymbol{m}$ originates from the relations between the two; $\boldsymbol{n} \cdot \boldsymbol{m} = 0$ and $\boldsymbol{n}^2 + \boldsymbol{m}^2 = 1$.

[9] 80 µm long x 20 µm wide

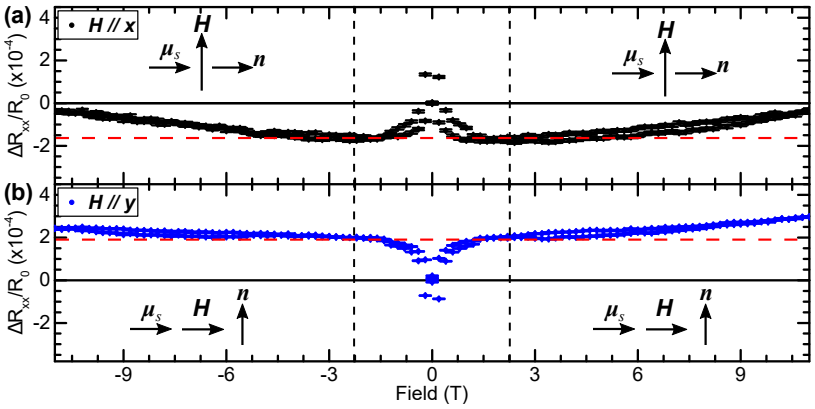

Figure 5.19: Longitudinal spin Hall magnetoresistance for (0001) orientated hematite films at 300 K and a magnetic field $\boldsymbol{H}$ applied along a) $\boldsymbol{x}$, parallel to the charge current, and b) $\boldsymbol{y}$, perpendicular to the charge current. The black dashed lines indicate the field required to create a monodomain state H_{MD} for the easy-plane, the red dashed lines indicate the saturation value and the relationship between the spin accumulation $\boldsymbol{\mu}_s$ and the Néel vector above H_{MD} is sketched. ΔR_{xx} is the change in the resistance with respect to the zero-field resistance R_0. Figure adapted from Ref. [r14]. Copyright American Physical Society.

a field induced canting. This absence could be because the signal is compensated by other, non-magnetic magnetoresistance effect contributing with an opposite sign, such as the ordinary magnetoresistance (OMR) [r1, 147].

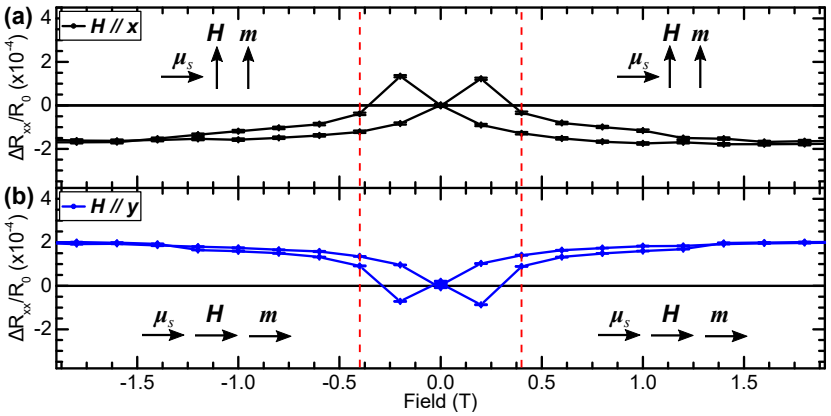

Figure 5.20: Spin Hall magnetoresistance for $\boldsymbol{H}$ along $\boldsymbol{x}$ and $\boldsymbol{y}$ on (0001) orientated hematite films around 0 T at 300 K. The red dashed lines indicate the saturation field of the canted moment measured by SQUID (Fig. 5.17a) and the behaviour of the canted moment $\boldsymbol{m}$ with field and with respect to the interfacial spin accumulation $\boldsymbol{\mu}_s$ is shown.

Looking closer at Fig. 5.19, ΔR_{xx} for both $\boldsymbol{H}\|\boldsymbol{x}$ and $\boldsymbol{H}\|\boldsymbol{y}$ shows a change of sign around 0 T. A zoomed in region of Fig. 5.19 is shown in Fig. 5.20, where it is more obvious that ΔRxx experiences a *peak* just above 0 T, before becoming dominated by the behaviour of the Néel vector. Such behaviour would be consistent with the SMR being sensitive to a ferromagnetic moment, i.e. the canted moment caused by the DMI (c.f. Sec. 4.1). The vertical dashed lines in Fig. 5.20 indicate the saturation field from SQUID (Fig. 5.17a). From these measurements, it would appear that ΔR_{xx} is, at very low fields, dominated by the orientation of $\boldsymbol{m}$ before becoming dominated by $\boldsymbol{n}$ once domain redistribution starts to occur.

From the measurements performed thus far, we can extract information on the mag-

netic anisotropies within the basal plane of these α-Fe_2O_3 films from the saturation field of ΔR_{xx} in Fig. 5.19. This value H_{MD} represents the field to produce a monodomain whereby the Néel vector aligns perpendicular to the magnetic field and can provide an indication of the effective in-plane, basal plane anisotropy. The origin of this could be related to the magnetic field required to overcome the local pinning potential and enable domain wall motion or the magnetic field required to overcome the magnetic anisotropy of a single domain and cause a rotation of the Néel vector within the domain. In the simplest approximation, this would represent only the crystalline anisotropy however, it is more correct to consider it as an effective field $H_{an}^{\perp}$ that encompasses also the effective pinning potential [15, 17]. Assuming an exchange field of $H_E = 900$ T [17, 29], $\mu_0 H_{an}^{\perp} = \mu_0 H_{MD}^2 / 4H_E \approx 1.74$ mT.[10] This value is more than 20 times smaller than $H_{an}^{\perp}$ found in NiO (46 mT) [15], likely due to the larger magnetostriction found in NiO. Note that $H_{an}^{\perp}$ differs from $H_{an}^{\perp}$ in the previous section, where the single domain nature allowed us to extract the basal plane anisotropy due to the crystalline nature, however, here the $H_{an}^{\perp}$ is dominated by other effects such as the effective pinning potential created by defects and the magnetoelastic interaction of hematite.

If the magnitude of $\boldsymbol{H}$ is fixed, then the modulation of ΔR_{xx} as a function of the angle α between $\boldsymbol{H}$ and $\boldsymbol{j}_c$ can be investigated. As discussed in Sec. 5.1, if the SMR response is dominated by the Néel vector, then this modulation should follow a $\sin^2 \alpha$ functional form for an easy-plane antiferromagnet if $\boldsymbol{n}$ is free to rotate with $\boldsymbol{H}$ [r1]. However, if $H_{an}^{\perp}$ has a significant contribution from the crystalline anisotropy related to the crystal structure, this would enter as an additional modulation of the signal. Fig. 5.21 shows

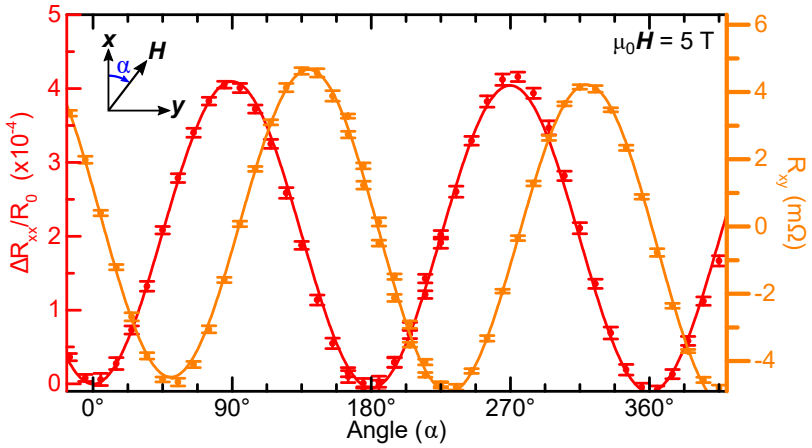

Figure 5.21: Longitudinal (ΔR_{xx}, orange) and transverse (ΔR_{xy}, red) spin Hall magnetoresistance for a magnetic field ($\mu_0 \boldsymbol{H} = 5$ T) rotated in the xy-plane of (0001) orientated α-Fe_2O_3 thin films at 300 K. Here, ΔR represents the change in resistance from the resistance at $\alpha = 0°$, i.e. $\boldsymbol{H} \| \boldsymbol{x}$, normalised with respect to the zero-field resistance R_0. α is defined as the angle between the field and the charge current. Figure adapted from Ref. [r14]. Copyright American Physical Society.

the modulation of both ΔR_{xx} and the transverse response ΔR_{xy} with α for an in-plane magnetic field $\mu_0 \boldsymbol{H} = 5$ T. Unlike in the measurements at a fixed angle in the preceding sections, where ΔR_{xx} was taken with respect to the zero-field resistance R_0, the rotation

[10] In the case of a single domain easy-plane antiferromagnet, the magnetic field required for a coherent rotation of $\boldsymbol{n}$ is instead $H_{sf} = (H_{an} H_E)$ for an in-plane anisotropy H_{an}. Here, the addition of a multi-domain state leads to a larger magnetic field required to produce a mono-domain state due to the effective pinning potential [15].

measurements here are with respect to the longitudinal resistance at $\alpha = 0°$, i.e. $R_{\alpha=0°}$. A minimum in ΔR_{xx} occurs for $\alpha = 0°$ with a maximum 90° later, consistent with the behaviour of SMR dominated by $\boldsymbol{n}$ rather than the canted moment $\boldsymbol{m}$ [r1, r9, r10, r19, 15, 17, 142]. This is further confirmed by the behaviour of R_{xy}, shown in red in Fig. 5.21, where the dependence follows n_{xy}. Whilst some of the signal in Fig. 5.21 may originate from OMR, which will have a similar sign as the AFM-SMR [r1], the signal is dominated by the signal due to the magnetic order parameters.

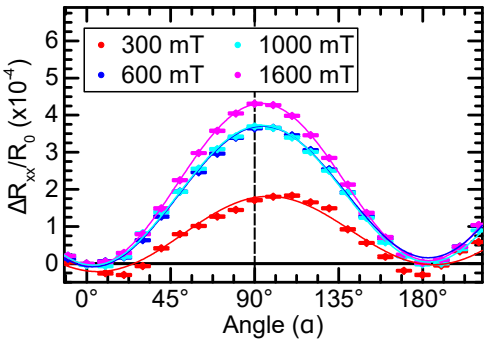

Figure 5.22: Longitudinal spin Hall magnetoresistance ΔR_{xx} for a magnetic field rotated in the xy-plane of (0001) orientated α-Fe_2O_3 thin films at 300 K for several magnetic fields. The solid lines are fits to a $\sin^2 \alpha$ function.

The dominant magnetic signal can be seen by varying the magnetic field applied within the xy-plane. Fig. 5.22 shows ΔR_{xx} for several magnetic fields below the saturation field H_{MD} in Fig. 5.19. Around the switching field of the canted moment (Fig. 5.17a), i.e. $\mu_0 \boldsymbol{H} = 300$ mT, the modulated signal is phase shifted from higher fields indicating that both the canted moment and the Néel vector are contributing at these low fields, however, once the moment is saturated, the Néel vector dominates the signal. The smooth modulation of the signal for all magnetic fields also indicates that the $H_{an}^{\perp}$ within this plane is comparable in all directions, indicating that the intrinsic crystalline anisotropy is not a significant contributor in these films even when $\boldsymbol{m}$ is dominating the response.

5.2.2.2 A Magnetic Field Perpendicular to the Easy-Plane

The application of a magnetic field within the easy-plane leads to the expected observable response for the SMR based on a dominant contribution from the Néel vector. If a magnetic field is instead applied out of the sample plane along $\boldsymbol{z}$ (Fig. 5.18), $\boldsymbol{H}$ is now parallel to the magnetic hard-axis. This should lead to no reorientation of $\boldsymbol{n}$ given that $\boldsymbol{H}$ is already perpendicular to the equilibrium orientation of $\boldsymbol{n}$, even in the presence of a degenerate domain structure. Fig. 5.23 shows ΔR_{xx} for a magnetic field $\mu_0 \boldsymbol{H} = 7$ T rotated in the xz-plane through an angle γ, where $\gamma = 0°$ occurs at $\boldsymbol{H} \| \boldsymbol{z}$. Once $\boldsymbol{H}$ is no longer parallel to $\boldsymbol{z}$, the SMR response drops as the finite in-plane component of $\boldsymbol{H}$ induces a reorientation of $\boldsymbol{n}$ once the in-plane effective anisotropy is overcome. This is also evident when $\mu_0 \boldsymbol{H} = 8$ T is rotated in the yz-plane through an angle β, where β is the angle from the y-axis. This is shown in Fig. 5.23 for the magenta axis/curve.

If the magnetic field is fixed along the $\boldsymbol{z}$ direction rather than being rotated, the field dependence of ΔR_{xx} can be investigated. Due to the relative alignment of $\boldsymbol{H}$ and $\boldsymbol{n}$, the immediate expectation is that there will be no change in the resistance due to the magnetic state of the underlying hematite films. Fig. 5.24 plots ΔR_{xx} for both positive

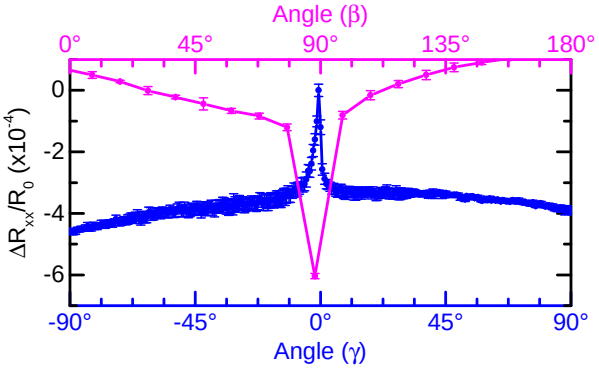

Figure 5.23: Longitudinal spin Hall magnetoresistance as a function of angle for a magnetic field rotated in the xz-plane (blue points/axis), through an angle γ where $\gamma = 0°$ occurs for $\boldsymbol{H} \| \boldsymbol{z}$. The magenta points/axis show ΔR_{xx} for a magnetic field rotated in the yz-plane through an angle β where $\beta = 0°$ arises for $\boldsymbol{H} \| \boldsymbol{y}$. Here ΔR_{xx} is the change in resistance from β (γ) = 0°.

and negative fields. As is immediately obvious, the signal displays a strong parabolic behaviour. Although $\boldsymbol{H} \| \boldsymbol{z}$ may lead to a canting of $\boldsymbol{n}$ out of the sample plane, reducing the average projection $\boldsymbol{n} \cdot \boldsymbol{\mu}_s$, the strong anisotropy confining $\boldsymbol{n}$ to the easy-plane means that this canting will be negligible for the magnetic fields used here. A likely contributor

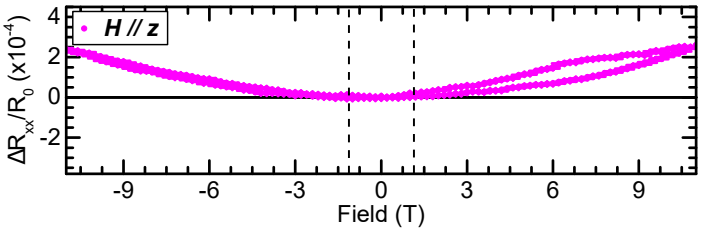

Figure 5.24: Longitudinal spin Hall magnetoresistance ΔR_{xx} for a magnetic field parallel to the hard-axis of (0001) orientated hematite at 300 K. The dashed lines indicate the field necessary to produce a monodomain state obtained from Fig. 5.19. Figure adapted from Ref. [r14]. Copyright American Physical Society.

to this out-of-plane parabolic behaviour is the ordinary magnetoresistance of the Pt [r1, 16, 147, 315] and is unrelated to the magnetic behaviour of the α-Fe_2O_3.[11] Although this measurement does not enable the determination of the in-plane anisotropy field, it does demonstrate that the hard-axis anisotropy is far larger than $H_{an}^{\perp}$.

5.2.3 Probing the Magnetic Anisotropies of the Easy-Axis Phase of (0001) Orientated Hematite Thin Films

Until this point, the SMR has been discussed in (0001) orientated hematite films at temperatures above the Morin transition temperature, where the antiferromagnetic state is that of an easy-plane AFM. The measurements of the longitudinal SMR are consistent with an easy-plane AFM, based on the reorientation of the Néel vector within individual

[11] Alternatively, this may arise from Hanle magnetoresistance (HMR), but then it should appear for $\boldsymbol{H} \| \boldsymbol{x}$ as well [312, 313]. Although $\boldsymbol{H} \| \boldsymbol{x}$ does display some parabolic behaviour at 300 K (Fig. 5.19a), the absence of such behaviour at lower temperatures (e.g. 175 K, Fig. 5.26a) is contrary to the expected behaviour for HMR [313].

domains due to degenerate states within the easy-plane and the strength of the effective basal plane anisotropy field $H_{an}^{\perp}$ was resolved. The application of a magnetic field along the hard-axis confirmed that indeed, $\boldsymbol{n}$ is confined to the easy-plane. As these films exhibit a Morin transition at $T \sim 200$ K, the effect of the antiferromagnetic symmetry can be investigated in a single sample by changing the temperature. This is a critical situation, given that comparing easy-plane and easy-axis (EA) antiferromagnets can prove challenging, for example comparing the easy-plane NiO [r1, 14, 15] with the easy-axis Cr_2O_3 [141, 316, 317]. Differences in interfacial quality and chemical terminations can confuse the role of the antiferromagnetic symmetries. This section will discuss the spin Hall magnetoresistance in the same Pt/α-Fe_2O_3 films, but rather than $T = 300$ K, the samples are cooled below T_M to 175 K and the Néel vector now lies along [0001]. When the magnetic field is applied along this axis, the classical spin flop will occur at a critical magnetic field $H_c^{\parallel}$, where $\boldsymbol{n}$ will reorientate from parallel to [0001] to lie within the (0001) plane. Meanwhile, the magnetic field perpendicular to the EA will also introduce a spin-reorientation due to the antisymmetric DMI at a critical magnetic field $H_c^{\perp}$. The detection of these two transitions can be used to determine the strength of the effective uniaxial anisotropy field of the easy-axis phase and the strength of the effective antisymmetric exchange field

5.2.3.1 Probing the Effective Uniaxial Anisotropy Field of (0001) Orientated Hematite Thin Films

The discussion will first focus on a magnetic field parallel to [0001], which should be then parallel to the geometric z-axis of Fig. 5.18. For a magnetic field $\boldsymbol{H}$ above the spin flop field $H_c^{\parallel}$, $\boldsymbol{n}$ will reorientate from $\boldsymbol{z}$ to lie in the geometric xy-plane where the value of $H_c^{\parallel}$ provides information on the strength of the effective uniaxial anisotropy field directed along the c-axis. The orientation of $\boldsymbol{n}$ within this plane will be one of several degenerate orientations, however, whichever orientation $\boldsymbol{n}$ adopts, it will lead to an increase in n_y with respect to the zero-field equilibrium position, enabling detection of this transition. ΔR_{xx} for $\boldsymbol{H} \| \boldsymbol{z}$ as a function of $\boldsymbol{H}$ is shown in Fig. 5.25a) at $T = 175$ K, i.e. just below T_M. Just as for $T = 300$ K (Fig. 5.24), the signal for $\boldsymbol{H} \| \boldsymbol{z}$ at $T = 175$ K is dominated by a parabolic background, possibly due to the ordinary magnetoresistance due to the large magnetic field perturbing the charge current [315]. Fig. 5.25 also shows a sustained decrease from 0 T before the parabolic background dominates. If one considers a spin flop of $\boldsymbol{n}$, then ΔR_{xx} should decrease at $H_c^{\parallel}$ due to the purely SMR contribution, before saturating. However, the spin flop field is not very obvious behind the parabolic background, although there is a *bump* in the signal around $\mu_0 \boldsymbol{H} = 5.5$ T. By assuming that the parabolic signal is unrelated to the magnetic nature of the films, alongside the simplistic assumption that it is not strongly temperature dependent in the temperature range so far investigated, the spin flop can be made more visible by removing the parabolic background from Fig. 5.25a. This is achieved by subtracting the curve in Fig. 5.24 from Fig. 5.25a, with result shown in Fig. 5.25b. This also allows one to assign the value to the spin flop field $\mu_0 H_c^{\parallel} = 5.5$ T for an increasing magnetic field indicated by an arrow in Fig. 5.25b. When the magnetic field is lowered, a hysteresis appears, where the transition field back to the EA is delayed until $\mu_0 \boldsymbol{H} = 4$ T.[12] For $\boldsymbol{H} > H_c^{\parallel}$, α-Fe_2O_3 has an easy-

[12] It should be emphasised that the subtraction made here is based on several, possibly unfounded, assumptions on the nature of the background and so should be approached with caution. It has been used here to emphasise the hysteretic behaviour of the spin flop. An ideal response would arise as an abrupt drop in the resistance from the zero-field value. There may also be contributions from domain

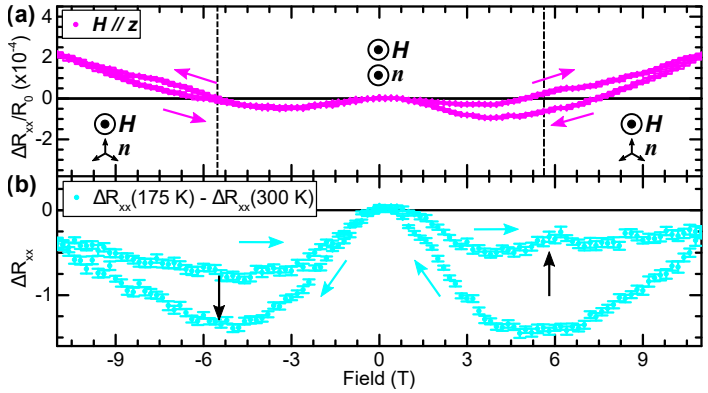

Figure 5.25: a) Longitudinal spin Hall magnetoresistance response ΔR_{xx} for (0001) orientated thin films and a magnetic field parallel to the easy-axis below the Morin transition temperature. ΔR_{xx} is the change in resistance from the zero-field resistance R_0. The relative orientation of the field $\boldsymbol{H}$ and the Néel vector $\boldsymbol{n}$ are indicated at low fields, where $\boldsymbol{n}$ and $\boldsymbol{H}$ are parallel and out-of-plane, and high fields, where $\boldsymbol{n}$ lies in the spin flop state in the plane perpendicular to $\boldsymbol{H}$. Figure adapted from Ref. [r14]. Copyright American Physical Society. b) Difference between a) and the curve in Fig. 5.24.

plane phase and the magnetic state is energetically similar to that seen above T_M (Sec. 5.2.2) [68, 69]. The additional pinning potential determined in Sec. 5.2.2 then also plays a role in stabilising the spin flop state, meaning that a lower magnetic field induces the transition back to the EA phase. When $\boldsymbol{H}$ is swept towards negative magnetic fields, similar behaviour is observed at the same magnetic fields, however there is an asymmetry in the qualitative shape of the signal. This may be an artefact from the subtraction process but an asymmetry is also visible in the raw data (Fig. 5.25a). This asymmetry could be due to the asymmetry in the magneto-elastic interaction of α-Fe_2O_3 that can arise for positive and negatives fields if a finite angle exists between the EA and $\boldsymbol{H}$, which later will be shown to be true [310].

Although the subtraction of the background qualitatively allows one to see the spin flop clearer, it does not provide robust, quantitative information on the magnitude of the SMR effect for $\boldsymbol{H}\|\boldsymbol{z}$, which is quite small in this case due to the degeneracy of $\boldsymbol{n}$ in the xy-plane reducing the overall average of $\boldsymbol{n}\cdot\boldsymbol{\mu}_s$. However, we can use the value of $H_c^{\|}$ to calculate the effective anisotropy field H_{an}^{eff} assuming a bulk value of the exchange field $H_E = 900$ T (c.f. Sec. 5.1.1) From $H_c^{\|} = \sqrt{H_{an}^{eff} H_E}$, this provides an estimate at $T = 175$ K of $H_{an}^{eff} \approx 33.6$ mT, comparable to the effective anisotropy field of bulk hematite (Fig. 5.15b). Meanwhile, the difference in the spin flop field for an increasing and decreasing field can be used to calculate the change in the anisotropy field that generates a pinning potential and delays the transition from the easy-plane to easy-axis states of $H_{ME} \approx 8.4$ mT. The pinning potential can then be calculated to be 8×10^2 J/m^3, a value that agrees with that provided in literature from measurements on bulk hematite [r15, 310]. Both H_{ME} (for $T < T_M$ and $H > H_c^{\|}$)) and $H_{an}^{\perp}$ (for $T > T_M$) act to prevent the reorientation of $\boldsymbol{n}$ in the easy-plane phase, although they are different transitions; one acts for a transition from easy-plane to easy-axis and the other plays a

redistribution above the spin flop as well as distributions in the strength of H_{an}^{eff} leading to a similar distribution in the value of $H_c^{\|}$. One could possibly make use of the transverse response, but for $\boldsymbol{H}\|\boldsymbol{z}$, the ordinary Hall effect (OHE) would be a dominant signal.

role in the reorientation of $\boldsymbol{n}$ within the easy-plane. However, the similar values extracted here (8.4 mT vs 1.74 mT) would seem to indicate that they have a similar origin in the effective pinning strength in the easy-plane.

5.2.3.2 Probing the Effective Antisymmetric Exchange Field from a Magnetic Field Perpendicular to the Easy-Axis

As already discussed, the application of the magnetic field perpendicular to the easy-axis of α-Fe_2O_3 will induce $\boldsymbol{n}$ to reorientate to lie within the (0001) plane, perpendicular to both the EA and $\boldsymbol{H}$. In the case of $\boldsymbol{H}\|\boldsymbol{x}$, $\boldsymbol{n}$ will then reorientate from parallel to $\boldsymbol{z}$ to lying parallel to $\boldsymbol{y}$, increasing n_y and decreasing the longitudinal SMR response in line with Eqn. 5.1. By detecting this transition, the strength of the effective field generated by the antisymmetric exchange interaction (DMI) directed along the c-axis can be determined given knowledge of $H_c^{\parallel}$ (c.f. Sec. 5.1.1). Fig. 5.26a, shows a decrease of ΔR_{xx} from the zero-field resistance value before reaching a minimum at $\mu_0\boldsymbol{H}$ = 2.6 T for $\boldsymbol{H}\|\boldsymbol{x}$. This magnetic field can then be attributed to be the critical magnetic field for the DMI induced spin-reorientation $H_c^{\perp}$ at 175 K. The same reorientation for $\boldsymbol{H}\|\boldsymbol{y}$ should lead to $\boldsymbol{n}$ being confined mostly to the xz-plane, i.e. n_y would remain low, around zero. Similar to the blue curve in Fig. 5.4 for bulk α-Fe_2O_3, this should then lead to no significant response in ΔR_{xx} for $\boldsymbol{H}\|\boldsymbol{y}$. However, this is not what is observed. Fig. 5.26b shows ΔR_{xx} as a

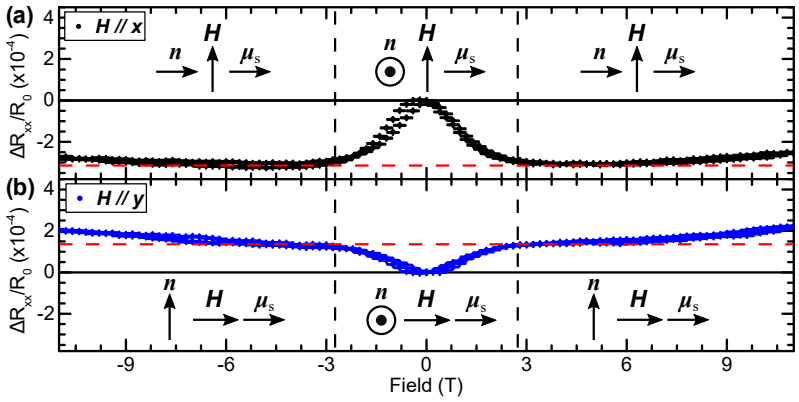

Figure 5.26: Longitudinal spin Hall magnetoresistance in (0001) orientated hematite films at 175 K for a) a magnetic field parallel to the charge current ($\boldsymbol{H}\|\boldsymbol{x}$) and b) a magnetic field perpendicular to the charge current ($\boldsymbol{H}\perp\boldsymbol{y}$). The balck dashed lines indicate the DMI spin-reorientation field $H_c^{\perp}$ and the red dashed line indicates the value of ΔR_{xx} at $H_c^{\perp}$. The behaviour of the Néel vector $\boldsymbol{n}$ with field is indicated with respect to the interfacial spin accumulation $\boldsymbol{\mu_s}$.

function of the magnetic field applied parallel to $\boldsymbol{y}$ where there is a clear increase with $\boldsymbol{H}$ from the zero-field longitudinal resistance. This then plateaus at the same magnetic field as for $\boldsymbol{H}\|\boldsymbol{x}$. Given that other effects like the OMR and HMR are related to the Pt, the saturation at the same magnetic field for $\boldsymbol{H}\|\boldsymbol{x}$ indicates that the signal must be related to the magnetic structure of the α-Fe_2O_3 films, i.e. the spin reorientation for $\boldsymbol{H}\perp EA$ that occurs for both $\boldsymbol{H}\|\boldsymbol{x}$ and $\boldsymbol{H}\|\boldsymbol{y}$. This then raises the question of what is causing this observed signal and, crucially, whether the magnetic structure of the hematite thin films differs from that expected.

5.2.3.3 Effect of a Misaligned Easy-Axis on the Spin Hall Magnetoresistance

An analytical two-spin model was develop alongside Dr C. Ulloa of Utrecht University in the Netherlands to describe the spin Hall magnetoresistance of (0001) orientated thin film hematite in order to try an explain the unexpected signal for $\boldsymbol{H}\|\boldsymbol{y}$ in Fig. 5.26b. The full details of the employed model can be found in the supplementary information of Ref. [r14]. Until now, the transport measurements presented have relied on the antiferromagnetic easy-axis being coincident with the $\boldsymbol{z}$ direction of the laboratory frame of reference, but this is a false assumption. This misalignment can be quantified in spherical coordinates by writing the easy-axis direction as $\boldsymbol{e} = (\sin\theta\cos\phi, \sin\theta\sin\phi, \cos\theta)$ such that the misalignment can be quantified by the azimuthal angle θ in both the xz and yz-planes of the laboratory frame of reference. This misalignment enters the two-spin Hamiltonian, given by,

$$\mathcal{H} = \mathcal{J}\boldsymbol{S}_1 \cdot \boldsymbol{S}_2 - \boldsymbol{\mathcal{D}} \cdot \boldsymbol{S}_1 \times \boldsymbol{S}_2 - \frac{K_z}{2}\left[(\boldsymbol{S}_1 \cdot \boldsymbol{e})^2 + (\boldsymbol{S}_2 \cdot \boldsymbol{e})^2\right] - \boldsymbol{H} \cdot (\boldsymbol{S}_1 + \boldsymbol{S}_2)\,, \quad (5.5)$$

where $\mathcal{J}$ quantifies the exchange interaction, $\boldsymbol{\mathcal{D}} = \mathcal{D}\vec{z}$ is the DMI interaction, K_z is the uniaxial interaction directed along the easy-axis $\boldsymbol{e}$ and $\boldsymbol{S}_1(\boldsymbol{S}_2)$ represents each spin on opposing antiferromagnetically aligned sublattices. For different values of θ, the spin dynamics of the system were investigated as a function of the applied magnetic field, numerically solving the Landau-Lifschitz-Gilbert equation to investigate the impact of the misalignment on the resistivity tensor. The results of these numerical calculations are shown in Fig. 5.27 for several values of θ.

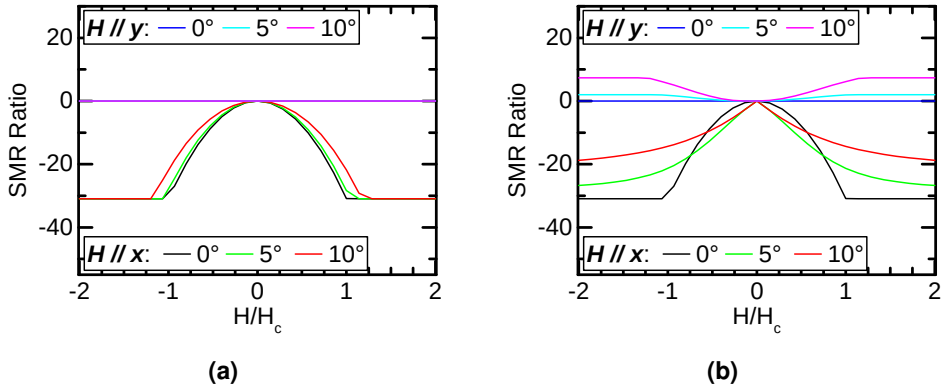

Figure 5.27: a) Calculated longitudinal spin Hall magnetoresistance as a function of magnetic field parallel to $\boldsymbol{x}$ and $\boldsymbol{y}$ for the easy-axis misaligned in the xz-plane of the laboratory frame-of-reference. b) Calculated longitudinal spin Hall magnetoresistance as a function of magnetic field parallel to $\boldsymbol{x}$ and $\boldsymbol{y}$ for the easy-axis misaligned in the yz-plane of the laboratory frame-of-reference. For both subfigures, $H_c = \left(2\mathcal{J}K_z^2 - \mathcal{D}\right)/\mathcal{D}$ is the critical magnetic field for the second-order transition when $\boldsymbol{H}$ is perpendicular to the easy-axis. Figures adapted from Ref. [r14]. Copyright American Physical Society.

The calculations in Fig. 5.27 where performed making use of the following physical parameters; $\mathcal{J}/\mu_B = 1000$ T, $\mathcal{D}/\mu_B = 0.65$ T, $K_z/\mu_B = 30$ mT and a magnetic damping of $\alpha = 0.001$. Here, μ_B is the Bohr magneton. The values for $\mathcal{D}$ and α were primarily chosen in order to allow the system to relax on a reasonable timescale and in order to have a reasonably low value of H_c (defined in the caption of Fig. 5.27).

Fig. 5.27 displays the effect of the misalignment of the EA for both a magnetic field parallel and perpendicular to the charge current $\boldsymbol{j}_c$ within the sample plane, i.e. $\boldsymbol{H}\|\boldsymbol{x}$ and

$\boldsymbol{H}\|\boldsymbol{y}$. In the instance of $\theta = 0°$, the calculated response to the magnetic field matches the expected behaviour in the case of no misalignment, as expected. Interestingly, when the misalignment increases, for example to 5° or 10° as shown in Fig. 5.27b, $\boldsymbol{H}\|\boldsymbol{y}$ begins to exhibit a response that is unexpected. With increasing magnetic field, the longitudinal response increases and plateaus above H_c, indicating a rotation of $\boldsymbol{n}$, just as for the experimental data. If the misalignment is in the xz-plane (Fig. 5.27a), then the longitudinal response for $\boldsymbol{H}\|\boldsymbol{y}$ would not allow this effect to be observered. These calculations qualitatively demonstrate that a misalignment of the EA from the naively assumed growth direction can lead to a spurious signal in SMR measurements that one needs to be careful of when considering the magnetic textures below.

In order to verify this model experimentally, the deviation of the c-axis should be measurable. The XRD diffraction measurements in Fig. 5.16 allow us to see that there is a distribution in the orientation of the c-axis leading to grains. From Scherrer's formula, a lower limit of 17.4 nm can be placed on the grain size. It would be reasonable to expect the c-axis would subtend a different angle within each grain. These deviations would average across the size of the Pt Hall bar[13], meaning that from the simple model presented here, the magnitude of this deviation cannot be accurately determined. However, a direct measurement of the Néel vector can be made in order to evidence the orientation of $\boldsymbol{n}$ below the Morin transition temperature. X-ray photoemission electron microscopy (XMLD-PEEM) was used to image the magnetic domain structure of these films. For more details on the technique, one can consult Sec. 4.2.6. The magnetic domain structure of these films is shown in Fig. 5.28 at $T = 100$ K, i.e. far below T_M, for two polarisations of the incident x-rays. X-rays polarised as linear vertical (LV) indicate the in-plane contrast whilst the out-of-plane contrast is dictated by linear horizontal (LH). The images were acquired at the Fe L_2 edge with $h\nu_1 = 720.4$ eV and $h\nu_2 = 721.79$ eV. The incident x-ray beams are inclined at 16° with respect to the sample plane, meaning that the LV polarisation represents purely the in-plane orientation of $\boldsymbol{n}$, whilst LH contains mostly the out-of-plane contrast, however some in-plane contrast still contributes. The XMLD was calculated as $h\nu_1 - h\nu_2/h\nu_1 + h\nu_2$. If the EA were parallel to the substrate normal, then the 180° easy-axis domains will not give rise to discernible magnetic contrast between neighbouring domains. However, as clearly seen in Fig. 5.28, both polarisations lead to a resolvable antiferromagnetic domain structure, where the contrast originates from differences in the orientation of the Néel vector changing the magnitude of the XMLD effect, i.e. two orientations of the Néel vector will produce two different contrasts. This direct measurement of the orientation of $\boldsymbol{n}$ demonstrates that $\boldsymbol{n}$ is tilted away from the surface normal, where the direction of this deviation is not confined to a single crystallographic plane. To further confirm that the deviation of $\boldsymbol{n}$ indeed results in this additional signal, films with no such deviation can be investigated. Such films orientated as $(1\bar{1}02)$ were investigated where XMLD-PEEM measurements demonstrate no deviations of $\boldsymbol{n}$ (Fig. 7.13 in Ch. 7). The spin Hall magnetoresistance was used to investigate the magnetic state of these films in order to demonstrate that no such signal is seen for the expected rotation of $\boldsymbol{n}$ in the plane parallel to the charge current. This is shown in the Appendix Sec. A.7 for the interested reader.

[13] 20 µm wide and 80 µm long

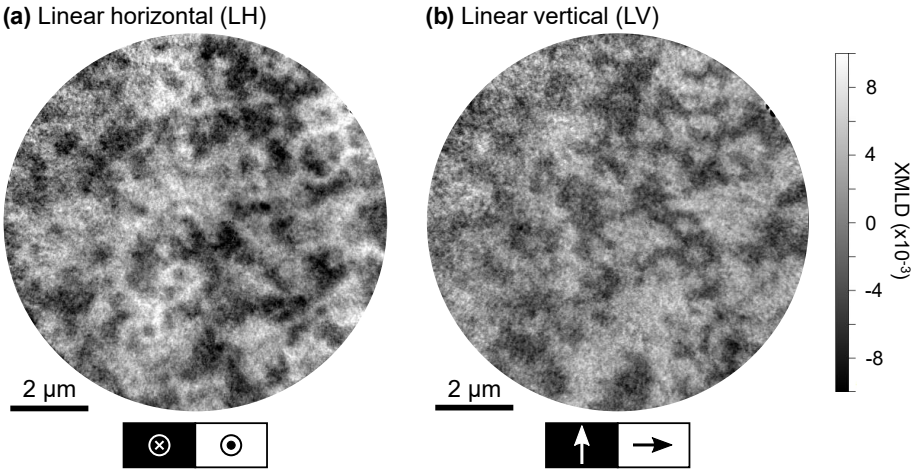

Figure 5.28: X-ray magnetic linear dichroism - photoemission electron microscopy (XMLD-PEEM) images of 100 nm thick (0001) orientated hematite thin films capped by 2 nm Pt to prevent charging effects at $T = 100$ K. The incident x-rays have either a) linear horizontal (LH) or b) linear vertical (LV) polarisation giving rise to contrast of the Néel vector in the out-of-plane or in-plane direction, as indicated below each image. The contrast arises when a finite angle exists between the orientation of $\boldsymbol{n}$ in different regions. The easy-axis anisotropy should give rise to 180° domain walls and no contrast. The deviation of $\boldsymbol{n}$ from the [0001] direction of the substrate gives rise to deviations in the orientation of $\boldsymbol{n}$ between neighbouring domains. Figure from Ref. [r14]. Copyright American Physical Society.

5.2.3.4 Determining the Magnetic Anisotropies of Thin Film Hematite

From the values of the critical magnetic fields for the spin flop (Fig. 5.25), and the DMI induced spin-reorientation (Fig. 5.26), the strength of the internal magnetic anisotropies can be determined for $T = 175$ K. The strength of the effective anisotropy field was calculated earlier in this section to be ≈ 33.6 mT, although it does depend on the value of the exchange constant present in the films [29, 240]. The strength of the internal DMI field H_D can also be calculated from $H_c^{\perp} = {H_c^{\parallel}}^2 / H_D$ (Sec. 5.1.1) From Fig. 5.26, $H_c^{\perp} = 2.6$ T, whilst $H_c^{\parallel} = 5.5$ T. Alongside a reasonable value for the exchange field used throughout this section ($H_E = 900$ T) [17, 29, 240], this gives an estimate of $H_D = 11.6$ T. This is much larger than the calculated value for bulk α-Fe_2O_3 where $H_D = 2.72$ T (Tab. 5.1), however not unexpected given that $H_c^{\parallel} > H_c^{\perp}$ in these thin films.[14] The DMI field represents the antisymmetry of the crystal structure along the c-axis between Fe atoms. As demonstrated throughout this chapter, the c-axis of these films is distorted across the film, which will correspondingly distort the unit cell altering the key anisotropies of hematite (c.f. Sec. 4.1) and ultimately leading to an increase in the DMI [53]. This leads to not only a reduction in the Morin transition temperature T_M (Fig. 5.17b), but also the observed increase in the effective anisotropy H_{an}^{eff}.

The magnetic anisotropies, and other properties, for the (0001) orientated α-Fe_2O_3 thin films used in the course of this thesis are summarised in Tab. 5.3 for the measured fields $H_c^{\parallel}$ and $H_c^{\perp}$ and the calculated values. The canting angle is also listed in Tab. 5.3 calculated from the magnetisation above the Morin transition temperature, measured by SQUID, where $\delta/2$ is just under half that found in bulk hematite (1.1 mrad [29]). However,

[14] The used value of the exchange may change slightly the value of the anisotropies but not significantly enough to alter the main conclusions on their relative strengths.

the large DMI found below T_M should lead to a larger canting angle in thin film hematite than in bulk hematite, at odds with the calculated value here. The differences may arise due to, for example impurities and defects in the hematite films [53], alternatively the 0 K sublattice magnetisation used may differ between bulk and thin film hematite (although unlikely). As shown later, the DMI has a significant temperature dependence (Fig. 5.32), so it may be that there is an abrupt decrease across the Morin transition that has not been investigated in depth here and could merit further, dedicated investigations.

Field	*Value*
$H_c^{\parallel}$	5.5 T
$H_c^{\perp}$	2.6 T
H_D	11.6 T
H_{an}^{eff}	33.6 mT
H_{ME}	8.4 mT
$H_{an}^{\perp}$ (300 K)	1.73 mT
T_M (SQUID)	200 K
T_M (SMR, c.f. Sec. 5.2.3.5)	205 K – 230 K
ΔT_M	50 K
Canting Angle[a] $\delta/2$	0.5 mrad

Table 5.3: Values for magnetic anisotropies and other properties of 100 nm (0001) orientated hematite grown on (0001) Al_2O_3 at 175 K. $H_c^{\parallel}$: Spin flop field for $\boldsymbol{H} \| EA$, $H_c^{\perp}$: Spin reorientation field for $\boldsymbol{H} \perp EA$, H_D: Effective field created by the DMI, H_{an}^{eff}: Effective anisotropy field parallel to the c-axis, H_{ME}: Effective field stabilising the spin flop state, $H_{an}^{\perp}$: Effective field in the basal plane.

[a]The canting angle is calculated as $\frac{\delta}{2} = \sin^{-1}\frac{m/2}{M}$ where m is the magnetisation for $T > T_M$ and M is taken as the 0 K sublattice magnetisation of bulk hematite.

5.2.3.5 Temperature Dependence of the Magnetic Anisotropies of (0001) Orientated Hematite Probed by Spin Hall Magnetoresistance

As discussed in Sec. 5.1.7 (and also in the introduction to hematite in Sec. 4.1), the effective uniaxial anisotropy field responsible for the spin flop is strongly temperature dependent, given that it must fall to zero at the Morin transition temperature. This means that the temperature dependence of $H_c^{\parallel}$ and $H_c^{\perp}$ can be used to not only give an insight into the internal magnetic anisotropies of these α-Fe_2O_3 thin films, but also to investigate the Morin transition temperature. Although the films utilised here resulted in a strong enough signal to noise to detect the Morin transition via magnetometry measurements (Fig. 5.17), this is not always the case. It may be that a film has a Morin transition, or conceivable another antiferromagnetic transition [r19, 254, 316], but magnetometry measurements are not sensitive enough. However, if the surface sensitive spin Hall magnetoresistance can detect such a transition, it means that such effects can be investigated theoretically down to monolayers. The recorded response ΔR_{xx} for $\boldsymbol{H} \| \boldsymbol{x}$ is

shown in Fig. 5.29 for a range of temperature both above and below the Morin transition temperature $T_M \sim 200$ K. The critical magnetic field for the spin reorientation when $\boldsymbol{H}$ is

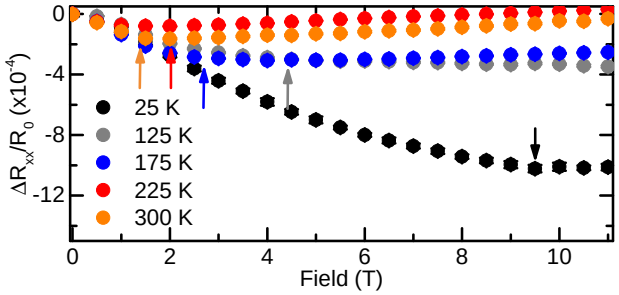

Figure 5.29: Longitudinal spin Hall magnetoresistance ΔR_{xx} for (0001) orientated hematite thin films for a magnetic field $\boldsymbol{H}$ parallel to the charge current $\boldsymbol{j}_c$ as a function of temperature. The arrows indicate the critical magnetic field $H_c^{\perp}$ for a rotation of the Néel vector $\boldsymbol{n}$ away from the easy-axis. Where visible, the error bars denote the standard deviation of the data point. Figure from Ref. [r14]. Copyright American Physical Society.

parallel to $\boldsymbol{x}$, $H_c^{\perp}$, is indicated for each temperature in Fig. 5.29. As T is reduced below the Morin transition temperature T_M, $H_c^{\perp}$ moves to higher magnetic fields, as expected [r10, 29, 241], demonstrating that the feature seen here is indeed related to the magnetic structure of the hematite film below the Pt Hall bar rather than some proximity-induced magnetism in the Pt. The increase in $H_c^{\perp}$ is accompanied by an increase in ΔR_{xx} at low temperatures. Fig. 5.30 shows the temperature dependence of ΔR_{xx}, taken at $H_c^{\perp}$ for both a magnetic field applied along $\boldsymbol{x}$ (black points) and along $\boldsymbol{y}$ (blue points). The shaded area indicates the region above T_M as measured by SQUID magnetometry (Fig. 5.17). Above T_M, ΔR_{xx} for both $\boldsymbol{H}\|\boldsymbol{x}$ and $\boldsymbol{H}\|\boldsymbol{y}$ are comparable in absolute magni-

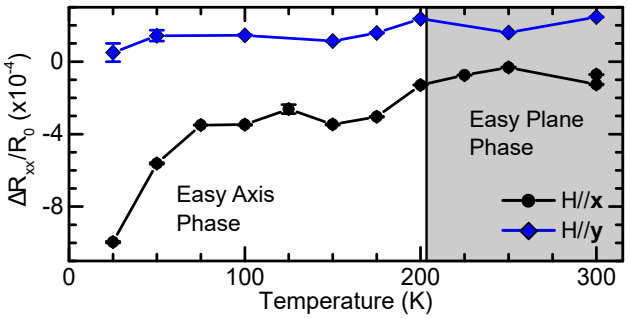

Figure 5.30: Temperature dependence of ΔR_{xx} in (0001) orientated hematite films for $\boldsymbol{H}\|\boldsymbol{x}$ (black) and $\boldsymbol{H}\|\boldsymbol{y}$ (blue). The shaded region indicates the easy-plane phase above the Morin transition temperature T_M. Figure adapted from Ref. [r14]. Copyright American Physical Society.

tude. However, below the Morin transition temperature, ΔR_{xx} increases for $\boldsymbol{H}\|\boldsymbol{x}$ with decreasing temperature whilst no such dependence is seen for $\boldsymbol{H}\|\boldsymbol{y}$. The effective spin mixing conductance that quantifies the efficiency of the spin transfer across the interface can be calculated across the Morin transition, where, although there is some slight variation, it is fairly independent for a large temperature range, indicating that both the temperature dependent SMR measurements used to extract the magnetostatic properties and also the spin transport in the subsequent chapters can be compared without significant renormalisation being required (c.f. Sec. A.5 in Appendix).

As well as extracting the temperature dependence of ΔR_{xx}, which demonstrated that the electrical response represents the magnetic state, the curves in Fig. 5.29 also

allows for the identification of the critical magnetic field $H_c^{\perp}$ for the spin reorientation $\boldsymbol{H} \perp \boldsymbol{n}$. This then allows for the temperature dependence of $H_c^{\perp}$ to be recorded, shown in Fig. 5.31. The same can be said for ΔR_{xx} when $\boldsymbol{H} \| \boldsymbol{z}$, however the determination of $H_c^{\parallel}$ is harder than for $H_c^{\perp}$ given the parabolic background (Fig. 5.25). The temperature dependence of $H_c^{\parallel}$ is shown alongside $H_c^{\perp}$ in Fig. 5.31. The experimental data points of both critical fields are accompanied by fits with the functional form $H_c^{\perp} \propto \sqrt{T - T_M}$, in keeping with a second-order phase transition within Landau's theory [r10, 53, 239]. This allows an estimate for T_M to be made from the surface sensitive nature of the spin Hall magnetoresistance of $T_M \sim 205\,\mathrm{K} - 230\,\mathrm{K}$. Comparing this value to magnetometry measurements of the canted moment as a function of temperature, where the Morin transition was found to take place over $\sim$50 K and was completed by 200 K, this shows good agreement between the two measurements.

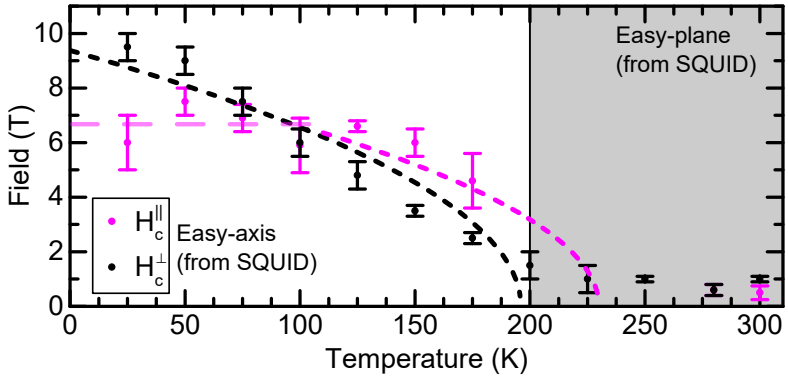

Figure 5.31: Temperature dependence of the critical magnetic fields for (0001) orientated hematite thin films extracted from longitudinal spin Hall magnetoresistance measurements. The (bold) dashed lines represent a functional fit $\propto \sqrt{T - T_M}$ giving an estimate for T_M of 205–230 K. The translucent magenta line indicates a constant value at lower temperatures. Figure adapted from Ref. [r14]. Copyright American Physical Society.

Comparing the temperature dependence of the critical fields in thin film α-Fe_2O_3 (Fig. 5.31) to that of a bulk crystal (Fig. 5.15a) also presents several key differences. First is that at low temperatures, both critical fields of bulk α-Fe_2O_3 remain constant [239, 241]. However, this saturation is not present in these thin films of α-Fe_2O_3, where $H_c^{\perp}$ continues to increase down to 25 K. Meanwhile, $H_c^{\parallel}$ increases with decreasing temperature below T_M before saturating for some finite temperature range. In the case of a bulk crystal, the magnetic anisotropies were combined into an effective anisotropy field H_{an}^{eff} that was considered temperature dependent whilst the Dzyaloshinskii-Moriya field H_D was considered temperature independent (see Sec. 5.1.7). Based on these assumptions, the two predominant anisotropies of α-Fe_2O_3, H_{K_1} and H_{K_2}, dictate the temperature dependence of both critical fields shown here. However, the differences between Fig. 5.15a and Fig. 5.31 indicate that H_D is likely temperature dependent, at least in these thin films (based on the behaviour of $H_c^{\perp}$). Fig. 5.32 shows the temperature dependence of the effective DMI field H_D below T_M based on the values of $H_c^{\parallel}$ and $H_c^{\perp}$, where it decreases linearly with temperature. One possible explanation could be the thermal expansion of the films, whereby the films and the Al_2O_3 substrates expand at different rates with changing temperature. This would then lead to changes in the distortion of the film unit cell, as H_D is related to the asymmetry in the exchange field between neighbouring Fe atoms along the c-axis (c.f. Sec. 4.1). However the origin of this decrease is not known at this point in time and merits further investigation. In general, H_D will

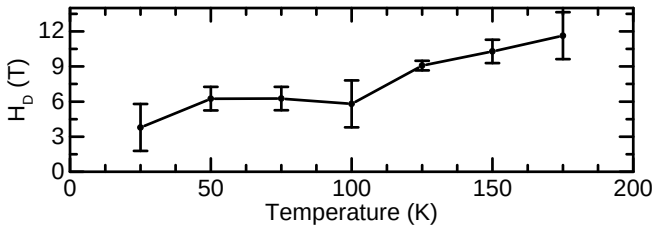

Figure 5.32: Temperature dependence of the DMI field H_D in (0001) orientated thin film hematite below the Morin transition temperature based on measurements of the critical fields.

affect the value of $H_c^{\perp}$, however, it also enters into the value of $H_c^{\parallel}$ (c.f. Sec. 5.1.1) and, by extension, the anisotropies responsible for the Morin transition [29]. Meanwhile the temperature dependence of $H_c^{\parallel}$, especially at low temperatures, is more complex in the thin film than in bulk α-Fe_2O_3, possibly due to higher order terms in the magnetic free energy[15] becoming important at low temperatures.

5.3 Conclusions

This chapter has utilised spin Hall magnetoresistance measurements of Pt/α-Fe_2O_3 bilayers to investigate the magnetic anisotropies, equilibrium orientation of the Néel vector, and field-induced and temperature-induced spin reorientation transitions of bulk crystals and thin films of this ubiquitous antiferromagnetic insulator. From the field dependence of the spin Hall magnetoresistance, the strengths of the effective anisotropy field, effective anisotropy field in the basal plane and the Dzyaloshinskii-Moriya field were extracted for a bulk crystal of hematite and found to be comparable to the anisotropies extracted by other methods. The surface sensitive nature of this technique allows access to the volume anisotropies of antiferromagnets, making it well-suited for the investigation of thin film antiferromagnets where other techniques are either not possible, or require large scale facilities. By measuring the spin Hall magnetoresistance in bilayers of Pt and thin film α-Fe_2O_3 orientated at (0001), the effective anisotropy directed along the c-axis was found to be comparable to a bulk sample, whilst the Dzyaloshinskii-Moriya effective field originating from the antisymmetric exchange interaction was four times larger. The effective field within the basal plane was found to be two orders of magnitude larger than in a bulk crystal and was determined to be dominated by an effective pinning potential, likely due to defects and strain introduced by the thin film growth process. Finally, SMR-based measurements have revealed that the thin film growth led to a finite angle between the antiferromagnetic easy-axis and the film normal, leading to spurious signals that need to be carefully considered when investigating thin film antiferromagnets to ensure accurate interpretation of results.

[15] For example the anisotropic exchange which is normally ignored [29].

6

Magnon Propagation in Bulk Single Crystalline Hematite

This chapter will look at the transport of magnons through the insulating antiferromagnet hematite (α-Fe_2O_3), described in detail in Sec. 4.1, a ubiquitous antiferromagnet with low magnetic damping [r13, 19]). In order to functionalise antiferromagnetic insulators for information transfer and processing, the information carried by propagating magnons needs to be sustained over sufficient distances to enable operations to occur. As detailed previously in Tab 3.2, spin diffusion lengths in metallic and insulating antiferromagnets have been found not to exceed $\sim$10 nm when the magnons are excited either monochromatically [97, 196, 198] or using broadband excitations [r2, 164, 318] of a ferromagnetic layer adjacent to the AFM (c.f. Sec. 3.3.2). However, theoretical works on AFMs anticipate that, even excluding the exotic spin superfluidity phase [20–23, 208], some AFMs with a low anisotropy (in order to have accessible critical magnetic fields) and low magnetic damping could be as efficient as FMs in the transport of spin angular momentum [20, 21, 205, 207].

In this chapter, long distance transport of spin angular momentum will be demonstrated in an antiferromagnetic system without ferromagnetic components. The conditions for the efficient transport of angular momentum will be demonstrated in the chosen system, the easy-axis phase of bulk hematite. Through carefully chosen geometries, magnon transport with the absence of a magnetic field can be realised. The results of this chapter have been published as a research article [r3] and an overview of the different measurements performed can be found in Appendix Sec. A.8. Unlike previous reports of transport in AFMs [r2, 97, 164, 196, 198, 318], a bulk crystal was used here rather than a thin film. Thin film AFMs suffer from the presence of multiple domains due to defects in the growth [r1, r4, 73, 295, 297, 319] and the magnetic fields required for generating a single domain state can be far larger than those used in typical transport experiments [223]. Conversely, the domains of bulk antiferromagnets, including hematite, are typically far larger than the transport lengths investigated here [60, 74, 77, 320–323]. Indeed, the AFM domains of the bulk crystals employed here have domains spanning hundreds of µm, deduced by measuring the magneto-optical Kerr effect due to the canted moment at temperatures above the Morin transition temperature, Fig. 6.1a. The domain size of hematite is also maintained across the Morin transition [322, 323]. These

large domains, alongside the low magnetic damping of hematite [r13, 19, 240], make it an ideal candidate for magnon transport. Examples of the antiferromagnetic domains of a bulk hematite crystal and a thin film are shown in Fig. 6.1. These principles for AFM

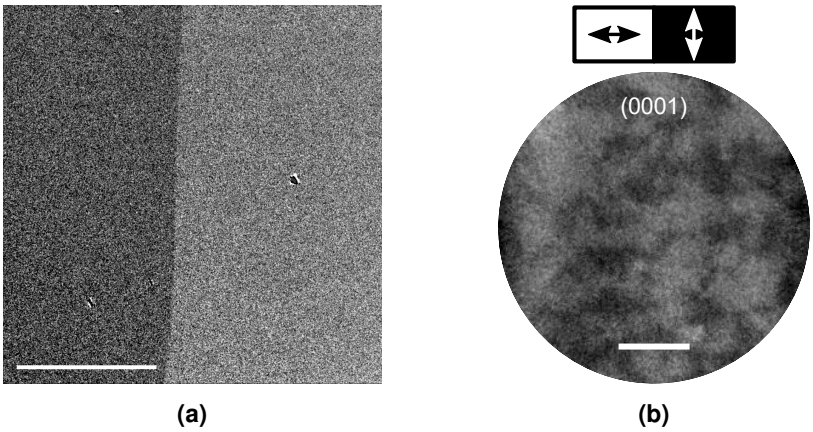

Figure 6.1: a) Antiferromagnetic domain structure of a bulk hematite crystal at room temperature measured by the magnetic optical Kerr effect, sensitive to the canted moment $\boldsymbol{m}$. The white scale bar represents 50 µm and the contrast indicates the rotation of the reflected light that is directly proportional to the orientation of the canted moment. b) Antiferromagnetic domain structure of a (0001) orientated, 100 nm thick film of hematite at 300 K measured by XMLD-PEEM. The scale bar represents 2 µm and the black (white) arrows above indicate the orientation of the Néel vector. Adapted with permission from Ref. [r15]. Copyright 2020 American Chemical Society.

transport are then extended to the thin film regime in the next chapter where results on transport experiments in the easy-axis phase of differently orientated films of hematite will be shown.

In order to have long distance, detectable transport of angular momentum, the polarisation of the magnons being excited can reasonably be expected to be circular rather than linear. As discussed in Sec. 2.4, circularly polarised $k = 0$ magnons can be excited in easy-axis AFMs. In the easy-axis phase of α-Fe_2O_3, the two $k = 0$ magnon modes are degenerate with the same frequency ω_0 in the absence of a magnetic field (c.f. Sec. 4.1 for more details on the magnon modes of α-Fe_2O_3). Each mode has either a left or right circular polarisation and thus they carry a finite but opposite angular momenta. At thermal equilibrium, these two modes cannot be populated separately. Instead, they have the same occupation and so no net transport is observed. However, a magnon imbalance and a breaking of the degeneracy can be created in a few ways including the application of a magnetic field [88], a thermal gradient across an AFM/NM interface [324, 325], an uncompensated antiferromagnetic interface [205] or the excitation of magnons through a neighbouring spin accumulation [205, 207].

By placing a heavy metal (HM) such as Pt in contact with the antiferromagnetic insulator, a charge current passing through the HM leads to a spin accumulation $\boldsymbol{\mu}_s$ building up at the interface due to the spin Hall effect (c.f. Sec. 3.1.1). The Pt/α-Fe_2O_3 interface presents a dissipation channel for $\boldsymbol{\mu}_s$ due to the "spin-bias" and subsequent spin flow across the interface [170, 171] (c.f. Sec. 3.3). This results in the excitation of spin-polarised magnons, depending on the relative alignment of the magnetic order parameter and $\boldsymbol{\mu}_s$ (Fig. 6.2a). In the case of an AFM, this magnetic order parameter could be either the Néel vector $\boldsymbol{n}$ or the field induced magnetisation $\boldsymbol{m}$ (or the canted moment in

the case of hematite) [170, 325, 326]. The excitation of magnons modifies the magnon chemical potential for the two magnon modes in proportion to $\boldsymbol{\mu}_s$ [185, 187]. Alongside this spin-biasing from the HM, the Joule heating of the passing charge current leads to thermally excited magnons by means of the spin Seebeck effect (c.f. Sec. 3.2, Fig. 6.2b). These can propagate in the presence of a net magnetic moment $\boldsymbol{m}$, which can generated for example by an applied magnetic field, that breaks the symmetry between the two modes [158, 197]. The resulting non-equilibrium magnon density that builds up in the α-Fe_2O_3 due to both effects diffuses away from the injector [161, 183, 185]. Two parameters can be introduced to describe the magnon transport properties of the antiferromagnetic material between the injector and detector. The spin-bias signal is related to the spin conductance G of the antiferromagnetic material between the wires, that is to say the "resistance" of a magnetic material to transport magnons [161, 205, 207]. Meanwhile, the efficiency of the thermally generated spin current (c.f. Sec. 3.2) is governed by the spin Seebeck conductance S [158, 205, 325]. As the magnon transport could be carried by both the Néel vector $\boldsymbol{n}$ and the field induced magnetisation $\boldsymbol{m}$, this results in four possible coefficients describing the transport properties of the hematite crystal representing the possible permutations of the magnetic orders and conductances $G_{\boldsymbol{n}}$, $G_{\boldsymbol{m}}$, $S_{\boldsymbol{n}}$, and $S_{\boldsymbol{m}}$. The measurements presented in this chapter will resolve the relative contributions of these four coefficients in order to determine the dominant transport mechanisms of magnons in antiferromagnetic insulators.

The flowing magnon current can be probed by making use of a non-local Pt detector where the non-equilibrium magnon chemical potential in the hematite leads to a spin flow across the Pt/α-Fe_2O_3 interface into the Pt. This spin flow is converted to a measurable voltage by means of the inverse SHE [7, 100] allowing the magnon current to be detected and probed. The spin current is measured as a voltage in the detector wire and will contain contributions from both effects, which can then be disentangled by reversing the polarity of the charge current, as detailed previously in Sec. 4.2.5.2. $R_{el} = \left(V^+ - V^-\right)/2I$ represents the non-local resistance caused by the magnons excited by the spin-bias and $R_{th} = \left(V^+ + V^-\right)/2I^2$ is proportional to the thermally excited magnon population, where $V^+\,(V^-)$ is the non-local voltage in response to a current I in the injector with positive (negative) polarity. The measured non-local resis-

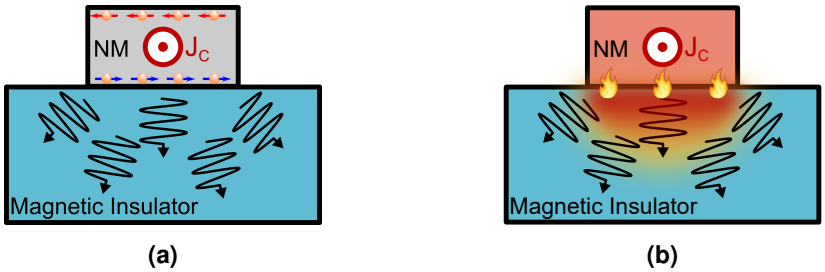

Figure 6.2: Schematic of non-local magnon excitation in a magnetic insulator. A charge current passing through a normal metal injector leads to an excitation of magnons a) that diffuse away from the injector. This occurs due to either the interfacial spin accumulation from the SHE and also via b) Joule heating and the thermally induced SSE.

tances can then be expressed in terms of the four conductance coefficients by making use of a two-channel phenomenological method [r3],

$$R_{el} = G_{\boldsymbol{n}} \left(\boldsymbol{n} \cdot \boldsymbol{e}_\perp\right)^2 + G_{\boldsymbol{m}} \left(\boldsymbol{m} \cdot \boldsymbol{e}_\perp\right)^2, \tag{6.1a}$$

$$R_{th} = S_{\boldsymbol{n}} \left(\boldsymbol{n} \cdot \boldsymbol{e}_{\perp} \right) + S_{\boldsymbol{m}} \left(\boldsymbol{m} \cdot \boldsymbol{e}_{\perp} \right), \tag{6.1b}$$

where $\boldsymbol{e}_{\perp}$ is the unit vector parallel to the interfacial $\boldsymbol{\mu}_s$. The values of $G_{\boldsymbol{n}}$ and $G_{\boldsymbol{m}}$ can be obtained by direct measurements of the spin-bias signal which is directly related to the spin conductance of the hematite crystal [161] and will be addressed in the subsequent sections.

6.1 Experimental Details

The magnon transport in bulk α-Fe_2O_3 was investigated in a commercially obtained single crystal from SurfaceNet GmbH orientated with the [$1\bar{1}02$] direction out of the sample plane, i.e. the sample plane is the r-plane. This orientation results in a chemically stable surface [300] (see Sec. A.9) as well as benefits from an in-plane projection of the antiferromagnetic easy-axis (EA). This means that a magnetic field applied within the sample plane subtends a finite angle with the easy-axis, breaking the degeneracy of the spin flop phase. This crystal was characterised via SQUID magnetometry measurements in order to determine the temperature of the Morin transition to be $T_M \sim 257$ K (see Fig. 5.3). In order to investigate the magnon propagation, this crystal was patterned via EBL into a non-local geometry including three Pt wires (c.f. Sec. 4.2.5.2), with wires separated by centre-to-centre distances of between 450 nm and 80 µm. For wires with separations up to 1 µm, the length of the detector wires was 80 µm but for the larger separations the length of the wires were doubled in order to reduce the geometric impact on the signal and maintain an approximation where the wire length is a lot larger than the transport length scale [161]. Furthermore, the current density in the injector was doubled to increase the signal to noise ratio for these large distances where the signal is reduced, however still remaining in the linear regime (see later, Fig. 6.13). The non-local devices were patterned such that there were wires both parallel and perpendicular to the in-plane component of the EA, which is itself inclined at 33° to the surface plane for this growth orientation. This then means that the interfacial spin accumulation $\boldsymbol{\mu}_s$ will be polarised perpendicular or parallel to the easy-axis respectively. The in-plane component is termed the geometric $\boldsymbol{x}$-axis in the later discussions and the geometries are shown in Fig. 6.3. The measurements presented in this chapter were all made at 200 K so as to

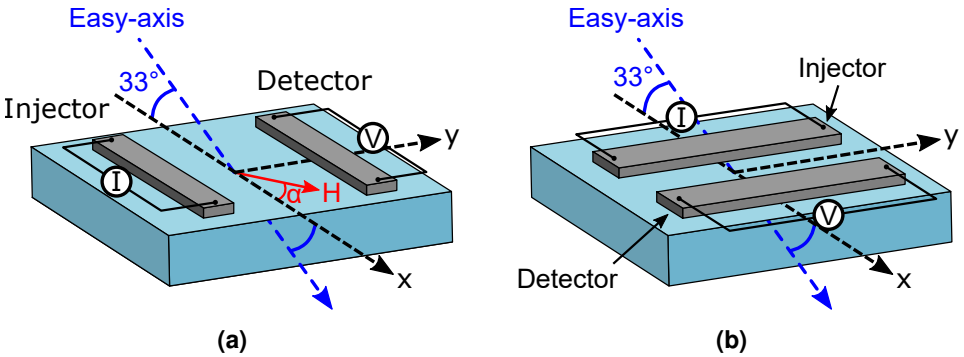

Figure 6.3: a) Coordinate system for r-plane hematite and a non-local geometry parallel to the in-plane component of the easy-axis. b) Coordinate system for r-plane hematite and a non-local geometry perpendicular to the in-plane component of the easy-axis. The easy-axis (blue) is inclined at 33° to the sample plane.

stabilise the easy-axis phase below T_M.

Details of the individual contributions to the results shown here can be found in Appendix Sec. A.1. The focus here will mostly be on the experimental results, although a brief overview of the theoretical understanding developed through collaboration with Dr. A. Qaiumzadeh from the group of Prof. Arne Brataas at NTNU and Dr. S. Bender from the group of Prof. Rembert Duine at Utrecht University will be covered. For a complete discussion of the theoretical model, the extensive methods section of Ref. [r3] can be consulted.

6.2 Non-local Magnon Transport for Wires Parallel to the Easy-Axis

In this section, the long distance magnon propagation in hematite will be investigated for a non-local geometry aligned such that the wire, and hence the charge current, are parallel to the in-plane component of the easy-axis $\boldsymbol{x}$, schematically shown in Fig. 6.3a, in order to determine the roles of the spin and spin Seebeck conductances. The spin accumulation $\boldsymbol{\mu}_s$ at the Pt/α-Fe_2O_3 interface then lies along the $\boldsymbol{y}$ direction, coincident with the transport direction for this geometry. When $\boldsymbol{H}$ is applied parallel to the wires, and thus the easy-axis, the classical spin flop is expected to occur [264]. It is worth pointing out that $\boldsymbol{H}\|\boldsymbol{x}$ will yield the aforementioned 33° angle between the EA and $\boldsymbol{H}$. Normally in a uniaxial antiferromagnet, such as for example Cr_2O_3, when a magnetic field is applied at a finite angle to the EA, the critical field required for a spin flop increases exponentially and above a certain angle a spin flop is not possible due to the fields required [46]. For very large angles between the field and EA, the Néel vector instead cants in the direction of the field rather than "flops". As discussed previously, hematite is special in that there is a spin reorientation for a magnetic field applied at any angle to the easy-axis, the critical field for which transitions smoothly between the values of $H_c^{\parallel}$ and $H_c^{\perp}$ [r10, r14, 241, 269], as discussed in Ch. 5. There is then still a smooth transition, even though there is the finite angle between the EA and field.

The measured signals for a magnetic field applied parallel ($\boldsymbol{H}\|\boldsymbol{x}$) and perpendicular to the wire ($\boldsymbol{H}\|\boldsymbol{y}$) for are shown in Figs 6.4 and 6.5 for R_{el} and R_{th}, respectively. Looking first at the spin-bias signal R_{el} for $\boldsymbol{H}\|\boldsymbol{x}$ (Fig. 6.4a), in the absence of a magnetic field there is no net spin transport and $\boldsymbol{n}$ lies perpendicular to $\boldsymbol{\mu}_s$. With increasing magnetic field, $\boldsymbol{n}$ begins to smoothly rotate until the critical field for the spin flop is reached and $\boldsymbol{n}$ rotates to lie perpendicular to $\boldsymbol{H}$, placing it parallel to $\boldsymbol{\mu}_s$ [r10]. Noticeable at this field ($\mu_0\boldsymbol{H}$ = 6.5 T), the spin transport experiences a sharp increase, due to an increase in the spin conductance G at the spin flop [205, 207], before falling away just as sharply. Above the spin flop, despite the value of R_{el} falling sharply, there remains a persistent signal for all magnetic fields presented even though the magnetic state is that of an easy-plane, where the magnon modes are linearly polarised [r13, 327]. This feature will be discussed more in Sec. 6.3.1.

Fig. 6.4b shows R_{el} for $\boldsymbol{H}$ perpendicular to the wire, i.e. $\boldsymbol{H}\|\boldsymbol{y}$, where no spin transport is observed. In the well studied case of ferromagnetic insulators, a magnetic field applied in this manner leads to a maximum in the observed values of R_{el} [r5, r6, 161, 165]. This occurs because the magnetic moment of the FMI aligns with $\boldsymbol{H}$ and hence with the polarisation of $\boldsymbol{\mu}_s$. This then leads to the excitation or depletion of ferromagnetic magnons depending on the sign of $\boldsymbol{\mu}_s$ [183, 187], (c.f. Sec. 3.3.1). In the case of an

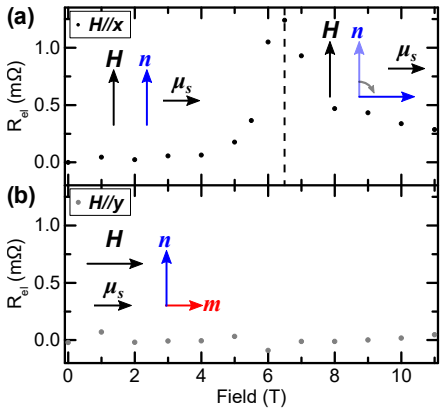

Figure 6.4: Non-local spin-bias signal R_{el} for wires along $\boldsymbol{x}$ and magnetic field a) $\boldsymbol{H}\|\boldsymbol{x}$ (black) and b) $\boldsymbol{H}\|\boldsymbol{y}$ (grey). The dashed line indicates the spin flop field. The arrows indicate the behaviour of the Néel vector under the applied magnetic field. In a), the Néel vector and magnetic field are parallel. Above the spin flop field, $\boldsymbol{n}$ rotates to lie perpendicular to the field. In b) the field is now perpendicular to the field and a field induced magnetisation appears. Figure adapted from Ref. [r3].

AFM, the orientation of $\boldsymbol{n}$ means that $\boldsymbol{H}\|\boldsymbol{y}$ leads to the emergence of a field induced magnetic moment $\boldsymbol{m} \perp \boldsymbol{n}$ ($\boldsymbol{m}^2 + \boldsymbol{n}^2 = 1$). However, the maximum applied magnetic field of 12 T is insignificant as compared to the exchange field of $H_E \sim 1000$ T. A simple trigonometric calculation leads to an estimate for the canting of the magnetic moments away from the easy-axis of ~ 12 mrad[1]. The presence of $\boldsymbol{m}$ should still facilitate the excitation of magnons that can then be transported given that $\boldsymbol{m}$ in AFMs has been shown to support excitations [29, 277, 328] and a magnon condensate [211] has even been reported in canted antiferromagnets [84]. Very recent spin pumping experiments of an EA AFM have also shown magnons excited and transported by $\boldsymbol{m}$ in the spin flop phase, albeit, these are *local* rather than *non-local* measurements [159, 304]. This does not completely rule out the possibility of magnons being carried by $\boldsymbol{m}$ and it is unlikely that there is *no* magnon transport carried by $\boldsymbol{m}$. However, it is not possible to detect any spin-bias transport carried by $\boldsymbol{m}$ within the experimental resolution because the signal is expected to be small.

It is worth recalling (c.f. Sec. 4.1 or Ch. 5) that hematite has a continuous spin reorientation for any angle between the magnetic field and the easy-axis due to the additional DMI term [r10, 29]. The final state for this transition places the Néel vector in a new equilibrium position within the (0001) plane, as close to perpendicular to both the field direction and the easy-axis direction as possible. The two extremes in the magnitude of the critical field of the spin reorientation occur for a field parallel ($H_c^{\parallel}$) and perpendicular ($H_c^{\perp}$) to the easy-axis [r10]. This means that, as $\boldsymbol{H}\|\boldsymbol{y}$ will place the field perpendicular to the easy-axis, the DMI spin reorientation should be visible. For this crystal, the critical field for this reorientation occurs at $\mu_0 H_c^{\perp} \sim 10$ T [r10] (c.f. Ch. 5, Sec. 5.1.5). However, $\boldsymbol{n}$ reorientates in the plane perpendicular to the direction of the magnetic field and the projection of $\boldsymbol{n}$ along $\boldsymbol{y}$ does not change. This also means that the projection of $\boldsymbol{n}$ on $\boldsymbol{\mu}_s$ also does not change. The result of this is that, regardless of the magnetic field applied, there is no discernible evidence of magnon transport for

[1] Considering the perpendicular nature of the exchange and applied fields, one can use $\tan \boldsymbol{H}/H_E$ to provide a rough estimate for the canting angle.

$\boldsymbol{H}\|\boldsymbol{y}$ in Fig. 6.4b due to either $\boldsymbol{n}$ or $\boldsymbol{m}$.

In terms of the spin conductances ($G_{\boldsymbol{n}}$ and $G_{\boldsymbol{m}}$) in Eqn. 6.1a, the two field orientations presented in Fig. 6.4 demonstrate that $G_{\boldsymbol{n}}$ dominates the transport mechanisms so far investigated. Meanwhile, at least within the experimental resolution of the measurements performed, $G_{\boldsymbol{m}}$ is effectively zero. This allows a first key conclusion to be drawn: the relative alignment of the Néel vector $\boldsymbol{n}$ and the spin accumulation $\boldsymbol{\mu}_s$ is important for the transport of magnons in antiferromagnets excited by an interfacial spin-bias.

6.2.1 Transport of Thermally Excited Magnons in Hematite for Wires Parallel to the Easy-Axis

The measurements of the spin current originating from thermally excited magnons can be investigated simultaneously alongside the electrical spin-bias. Fig. 6.5 shows the non-local resistance due to the propagation of thermally excited magnons R_{th} for the two field directions of parallel or perpendicular to the Pt wires. Below the spin flop field for $\boldsymbol{H}\|\boldsymbol{x}$, there is no projection of either $\boldsymbol{n}$ or $\boldsymbol{m}$ along the transport direction $\boldsymbol{y}$ as seen in Fig. 6.5a. Even though the application of $\boldsymbol{H}$ breaks the degeneracy between the two magnon modes, there is no obvious evidence of magnon transport[2]. In the vicinity of the spin flop, R_{th} demonstrates a small deviation around zero, certainly due to the reorientation of the Néel vector, compensation of magnetic anisotropy and the change in the magnon modes available. Above the spin flop field, the absence of R_{th} allows for the conclusion that the Néel spin Seebeck conductance $S_{\boldsymbol{n}}$ is inevitably small.

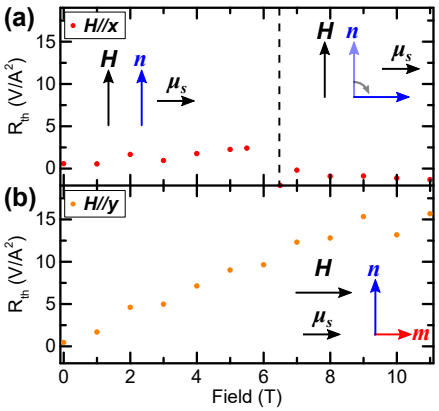

Figure 6.5: Non-local thermal signal R_{th} for wires along $\boldsymbol{x}$ and magnetic field a) $\boldsymbol{H}\|\boldsymbol{x}$ (red) and b) $\boldsymbol{H}\|\boldsymbol{y}$ (orange). In a), the parallel alignment of the field and Néel vector leads to a spin flop (indicated by the dashed line) but no net magnetisation along the transport direction. In b) a net magnetisation $\boldsymbol{m}$ appears parallel to the transport direction and linear in the applied magnetic field. Although the excitation mechanism is thermal, $\boldsymbol{\mu}_s$ indicates the transport direction of the geometry. Figure adapted from data published in Ref. [r3].

When $\boldsymbol{H}$ is now rotated perpendicular to the Pt wires (i.e. parallel to $\boldsymbol{y}$), R_{th} increases linearly with increasing field and consequently with increasing $\boldsymbol{m}$ (Fig. 6.5b). This leads to the conclusion that $S_{\boldsymbol{m}}$ is dominant in the R_{th} signal. This observation for

[2]This broken degeneracy increases linearly to a maximum at the spin flop field where the energy difference between the two modes will be twice the zero-field energy gap of hematite [29]. Based on measured values for the spin flop at different frequencies, one can extrapolate a value for ω_0 of 200 – 215 GHz at 200 K [241]. This then leads to a maximum energy difference of $\sim$ 1.6 meV at the spin flop.

the non-local spin Seebeck measurements here is congruent with local, bulk measurements on other AFMs, where a signal only appears in the presence of a significant field induced moment such as above the spin flop [158, 159, 197, 304].

6.2.2 Angular Dependence of the Spin-Bias and Thermal Magnon Transport in Hematite

The symmetry of the signals and the roles of the spin ($G_{\boldsymbol{n}}$ and $G_{\boldsymbol{m}}$) and spin Seebeck ($S_{\boldsymbol{n}}$ and $S_{\boldsymbol{m}}$) conductances can be confirmed by maintaining a constant magnetic field and rotating the angle α between $\boldsymbol{H}$ and the wire geometry, whilst measuring R_{el} and R_{th}. These non-local resistances are shown in Fig. 6.6. Focussing first on R_{el}, at

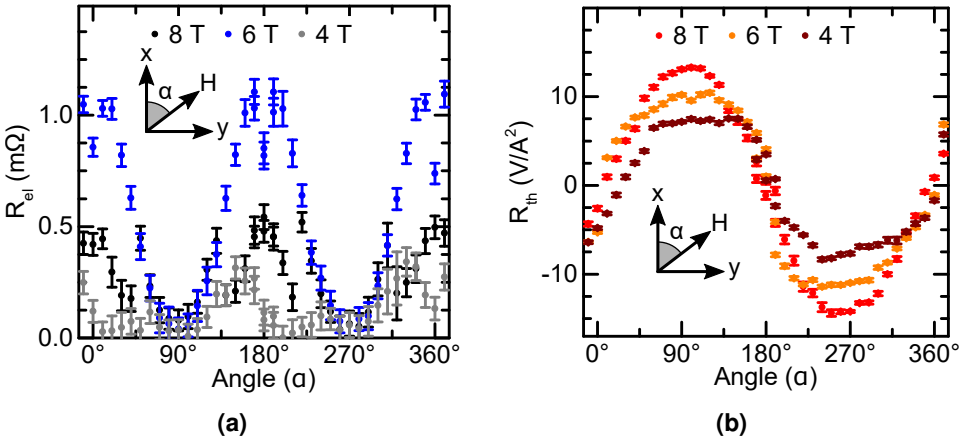

Figure 6.6: a) Angular dependence of R_{el} for wires along $\boldsymbol{x}$. b) Angular dependence of R_{th} for wires along $\boldsymbol{x}$ through an angle α between the field and the wire direction. The symmetry with α highlights the generation and detection mechanisms depend on the spin Hall effect.

low magnetic fields ($\mu_0\boldsymbol{H} = 4$ T, grey points in Fig. 6.6a), the rotation of $\boldsymbol{H}$ leads to little modulation of R_{el} given that the magnitude of the field is too small to lead to any significant deviation of $\boldsymbol{n}$ from the easy-axis, consistent with the measurements of the field applied along a single direction. In the vicinity of the spin flop ($\mu_0\boldsymbol{H} = 6$ T, blue points in Fig. 6.6a), there is a distinct, smooth modulation of R_{el} as $\boldsymbol{H}$ is rotated. At $\alpha = 0°$ ($\alpha = 90°$), $\boldsymbol{H}$ is parallel (perpendicular) to the easy-axis and thus $\boldsymbol{n}$ is parallel (perpendicular) to $\boldsymbol{\mu}_s$ and R_{el} is maximum (minimum). Above the spin flop ($\mu_0\boldsymbol{H} = 8$ T, black points in Fig. 6.6a), this smooth modulation persists but, as expected, occurs at a reduced magnitude as compared to measurements at the spin flop field.

Meanwhile, the angular dependence of R_{th} follows a $\cos\alpha$ dependence, with a maximum (minimum) for a magnetic field parallel (antiparallel) to the transport direction that increases linearly with increasing magnetic field (Fig. 6.6b). This then confirms that it is indeed the canted moment and thus $S_{\boldsymbol{m}}$ dominating the transport of thermally excited magnons. Given that the detection mechanism introduces a cosine dependence to the signal, it also demonstrates that the excitation mechanism is the spin Seebeck effect. The relative phase between R_{el} and R_{th} of 90° highlights the differences to the FM case. The similar symmetry of R_{th} is owed to the similar transport mechanism to ferromagnets through $\boldsymbol{m}$, whilst R_{el} is dominated by the Néel spin conductance $G_{\boldsymbol{n}}$ and only present when $\boldsymbol{n}$ and $\boldsymbol{\mu}_s$ are coincident.

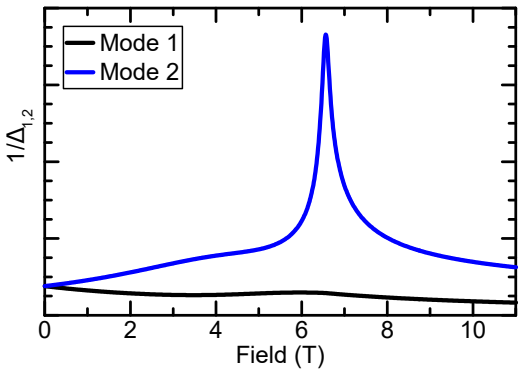

Figure 6.7: Calculations of the inverse of the magnon gap $1/\Delta_i$ (where $i = 1,2$) for the two magnon modes as a function of magnetic field. Figure adapted from Ref. [r3].

6.3 Modelling the Spin Transport in Hematite

The theoretical understanding of the magnon transport in AFMs, as mentioned previously, was developed through collaboration with Dr. S. Bender from the group of Prof. R. Duine and Dr. A. Qaiumzadeh from the group of Prof. A. Brataas. The full model can be found in the methods section of Ref. [r3] and here an overview will be provided so as to enhance the understanding of the experimental results. The two earlier given equations (Eqn. 6.1a and Eqn. 6.1b) represent a minimal model for two channel transport making use of both $\boldsymbol{n}$ and $\boldsymbol{m}$. The factors of $\boldsymbol{n} \cdot \boldsymbol{e}_\perp$ and $\boldsymbol{m} \cdot \boldsymbol{e}_\perp$ arise for both the injection and detection mechanisms, hence the square of these being present in Eqn. 6.1a and linear terms in Eqn. 6.1b. The four coefficients $G_{\boldsymbol{n}}$, $G_{\boldsymbol{m}}$, $S_{\boldsymbol{n}}$, and $S_{\boldsymbol{m}}$ depend generally on both $\boldsymbol{n}$ and $\boldsymbol{m}$ and the sublattice symmetry of the AFM order implies inversion symmetry. The spin conductance G is predicted to be significantly enhanced as the magnon gap for the lowest magnon branch closes [205, 207]. The low energy behaviour of G can be approximated in terms of the magnon gap under an applied magnetic field,

$$G \sim G_0 \frac{\boldsymbol{H}}{\Delta_{min}}, \tag{6.2}$$

where G_0 is a constant to be determined and Δ_{min} is the smaller magnon gap of the two lowest magnon branches under an external field $\boldsymbol{H}$. For a given $\boldsymbol{H}$, the value of Δ_{min} can be calculated through the equilibrium positions of $\boldsymbol{n}$ and $\boldsymbol{m}$ alongside excitations of the two sublattices around these equilibrium positions (c.f. Sec. 2.4.2). Fig. 6.7 plots the inverse of the magnon gap as a function of the applied magnetic field. At finite field, the expectation of R_{el} is determined by $1/\Delta_{min}$ and the projection $\boldsymbol{\mu}_s\,(\boldsymbol{y} \cdot \boldsymbol{n})$. Providing that the magnetic spin conductance $G_{\boldsymbol{m}} = 0$ ($G \sim G_{\boldsymbol{n}}$), as inferred from the electrical measurements Fig. 6.4, this anticipation qualitatively reproduces the measured behaviour of R_{el}, indicated by the fits in Fig. 6.8a-b and Fig. 6.11 of the next section. In this simplified model, the constant of proportionality G_0 is assumed to be independent of field, an assumption motivated by the dominant contribution to the spin current being symmetric with field.

Since the minimal model derived in Ref. [r3] was published, other theoretical works have directly focussed on the mechanisms of spin transport through antiferromagnetic insulators in response to experimental works. For example, the divergence of the spin conductance in the vicinity of the spin flop from Ref. [205] is adjusted in Ref. [207] for the

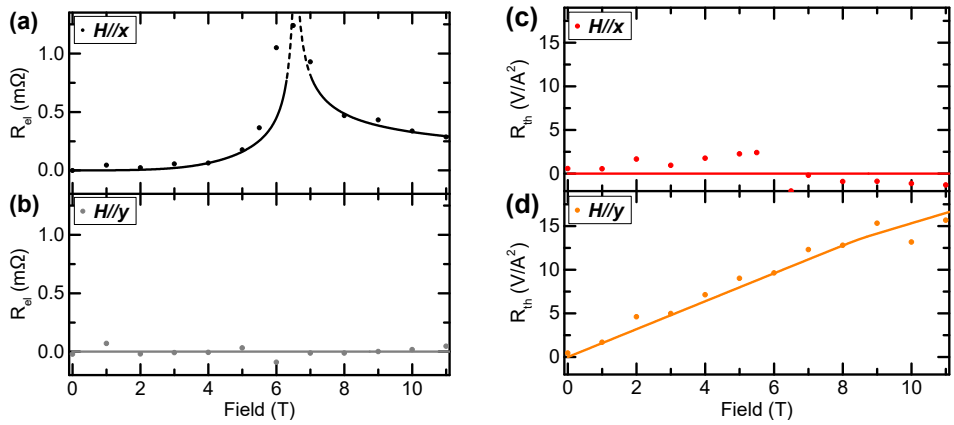

Figure 6.8: Reproduction of experimental data from Fig. 6.4 a)-b) R_{el} and Fig. 6.5 c)-d) R_{th} for wires along $\boldsymbol{x}$. The solid lines in each panel represent fits based on Eqn. 6.1, Eqn. 6.2 and a simple model for hematite given in a previous chapter by Eqn. 4.1. Fitting yields values of $G_0 \sim 0.17\,\mathrm{m\Omega}$ and $S_0 \sim 60.6\,\mathrm{V\,A^{-2}}$. Figure adapted from Ref. [r3].

thick limit of the AFM. Although the spin diffusion length and spin conductance increase in the vicinity of the spin flop, the non-local signal is limited by the interfacial magnon conductance of the AFM/HM interface [207], which is to say the the ability for magnons to transmit across the interface. In order to verify whether the spin conductance G of the AFM or the interfacial magnon conductance dominates the transport, one would need to vary the thickness of the AFM whilst maintaining high quality interfaces. As one transitions from the thin film limit (the thickness d is a lot less than the equilibration length l of a magnon gas) to a thick film limit ($d \gg l$), one would notice a *bottle-necking* effect caused by the interfaces. The transport driven by the spin Hall effect in similar geometries to that used here, rather than in a 1D linear geometry, is also investigated in, for example, Ref. [326]. In Ref. [326] the authors do not consider a conventional spin current picture but instead follow a linear response theory centred around treating the exchange interaction between spins in the AFM and the HM electrode perturbatively. There then exists a spin correlation function of the AFM order that vanishes for a spin direction perpendicular to the Néel vector and decays exponentially with distance from the point of perturbation. A spin current can then only propagate parallel to the direction of $\boldsymbol{n}$, identical to the conclusions drawn from experiment and the simple model above. Within the formulation of Ref. [326], perturbations to the Néel vector give rise to a two component magnon field, corresponding to the two magnon polarisations of an easy-axis antiferromagnet. The long range behaviour of the correlation function is then dominated by magnons with a small wavenumber $\boldsymbol{k}$. At finite magnetic field, the transport is mediated by the mixing of the two magnon branches, a feature that has recently been experimentally investigated for easy-plane antiferromagnets [r13, 327, 329], and is then suppressed by an increase of the magnon gap of the upper mode. This differs from the above case, where the magnon gap of the lower magnon branch was considered. However, the reality is that the difference between the two branches is more important so the increase of Δ_2 is congruent to a decrease of Δ_1. The model presented in Ref. [326] captures many of the experimental features seen here and specifically discusses the dominant behaviour of low $\boldsymbol{k}$ magnons. However, in order to probe the roles of high and low $\boldsymbol{k}$ magnons, one would need to utilise a more frequency specific excitation mechanism than the one employed here.

Given that the experimental data in Fig. 6.5 is consistent with $S_{\boldsymbol{m}} \gg S_{\boldsymbol{n}}$, it is then reasonable to only focus on $S_{\boldsymbol{m}}$. Unlike $G_{\boldsymbol{n}}$, $S_{\boldsymbol{n}}$ is known to have a continuous dependence on the applied magnetic field given that the net spin current is the difference between the thermal populations of the two magnon modes. It is also dependent on the frequency of the two modes, which are linear with applied magnetic field [158, 205, 325]. It is then also a reasonable assumption that $S_{\boldsymbol{m}}$ also displays a continuous dependence on $\boldsymbol{H}$. Given that the field dependence of R_{th} enters Eqn. 6.1b through the term $\boldsymbol{m} \cdot \boldsymbol{e}_{\perp}$, the lowest order, field independent term can be used to model $S_{\boldsymbol{m}} \sim S_0$. These assertions are used to produce the fits to Fig. 6.8c-d and, in the next section, Fig. 6.12. Furthermore, although the thermal heating caused by the spin Seebeck effect modifies the magnon population of each mode, the thermal gradient has no impact, in a simple model, on the net population change responsible for the spin-bias signal [330].

6.3.1 Persistence of a Magnon Current Above the Spin Flop

It should be clarified that the polarisation of the magnon modes does not abruptly transition as expected from theory, but is a more gradual transition with increasing ellipticity caused by both the distribution of critical fields, increased anisotropy in thin films antiferromagnets and the additional DMI term [42, 88]. Nevertheless, it is also still possible to have magnon transport in the easy-plane phase close to the spin flop through a superposition of magnon modes which has very recently been demonstrated [r13, 327] As discussed in an earlier chapter (Sec. 2.4.2), easy-plane antiferromagnets can have two magnon modes with a linear polarisation at $k = 0$, resulting in the dispersion relation plotted in the same chapter in Fig. 2.14. Fig. 6.9a shows the k dependence of the two lowest magnon modes for a generic easy-plane antiferromagnet. For a given excitation frequency ω, the two magnon modes will be excited with a wavenumber of k_1 and k_2 respectively. This will then create a superposition of the two modes, where each mode has a group velocity $v_g = d\omega/dk$. Although the individual modes will be linearly po-

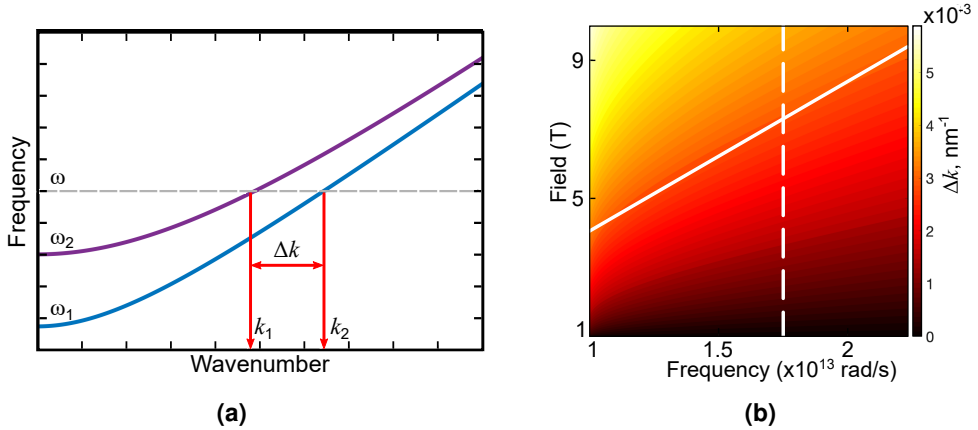

Figure 6.9: a) Frequency dependence of the wavenumber of magnon modes in an easy-plane antiferromagnet. For an excitation frequency ω, the two modes have wavenumbers k_1 and k_2 and are linearly polarised. b) Phase diagram of Δk (and equivalently the inverse of the propagation length) as a function of the applied magnetic field and frequency. The dashed line indicates the upper limit of the magnon frequency set by the temperature and the angled solid line indicates the spin flop field. Both figures courtesy of Prof. O. Gomonay of JGU Mainz.

larised, the superposition can have a circular polarisation component. As the two modes

propagate, they will begin to dephase. This then results in a propagation length,

$$\ell \propto \frac{1}{\Delta k}, \tag{6.3}$$

where $\Delta k = k_1 - k_2$ is the difference between the wavenumbers of the two modes at a frequency ω. From Equ. 6.3, if Δk is large, then the propagation length before the two modes dephase is very small. As Δk is determined by ω, it then also must depend on the magnitude of the applied field. This allows one to create a phase diagram of the propagation length from Eqn. 6.3 as a function of the applied magnetic field and frequency above the spin flop field for hematite. This is shown in Fig. 6.9b. The dashed line indicates the upper limit of the frequency determined by the temperature, and thus the thermal magnon population. Meanwhile, the solid, angled line indicates the spin flop field which is inherently frequency dependent when the full spectrum of wavenumbers is considered rather than just the $k = 0$ mode. As seen from Fig. 6.9b, the propagation length decreases above the spin flop field as the modes dephase, but it is not the abrupt suppression one would expect with a naive assumption of a strictly circular mode below $H_c^{\parallel}$ and a linear one above.

Very recently, experimental investigations on magnon transport in the easy-plane phase of bulk [r13] and thin film [327] hematite have been reported. Both of these works find persistent magnon transport without the need for an easy-axis antiferromagnet and utilise two similar explanations about the mixing of two linearly polarised magnon modes to create a superposition. These results will be briefly discussed later Sec. 7.4.

6.4 Non-local Magnon Transport for Wires Perpendicular to the Easy-Axis

The previous geometry in Sec. 6.2 demonstrated that efficient spin transport in AFMs requires the key condition of $\boldsymbol{n} \| \boldsymbol{\mu}_s$ to be satisfied. Alongside this there are additional contributions of the closing of the magnon gap, the reduction of magnetic anisotropy that occurs at the spin flop and the magnon polarisation seem to play a role given the reduced, but finite value of R_{el} above the spin flop. For the previous geometry, $\boldsymbol{n} \| \boldsymbol{\mu}_s$ was only achievable at and above the spin flop. However, it does not allow the separation of the role of the orientation of $\boldsymbol{n}$ as compared to the closing of the magnon gap. It is important to notice that the crystallographic orientation of the used crystal has an in-plane component of $\boldsymbol{n}$ within the sample plane. This means that if the wires are placed perpendicular to the easy-axis, then the in-plane component of $\boldsymbol{n}$ is parallel to $\boldsymbol{\mu}_s$ in the absence of a magnetic field. If $\boldsymbol{H}$ is then applied parallel to the easy-axis, the rotation of $\boldsymbol{n}$ at the spin flop should then suppress any spin transport allowing us to probe whether the closing of the magnon gap is critical for spin transport or if zero-field magnon transport is possible even in the presence of a significant magnon gap.

To investigate this, wires were patterned along the geometric y-axis, resulting in the adapted geometry shown in Fig. 6.3b and reproduced here for reference (Fig. 6.10). The charge current now flows along $\boldsymbol{y}$ resulting in the interfacial spin accumulation $\boldsymbol{\mu}_s$ polarised along the $\boldsymbol{x}$ direction, i.e. the in-plane projection of the easy-axis. A magnetic field $\boldsymbol{H} \| EA$ is then coincident with the transport direction, also along $\boldsymbol{x}$.

The spin-bias signal for a magnetic field both parallel (Fig. 6.11a) and perpendicular

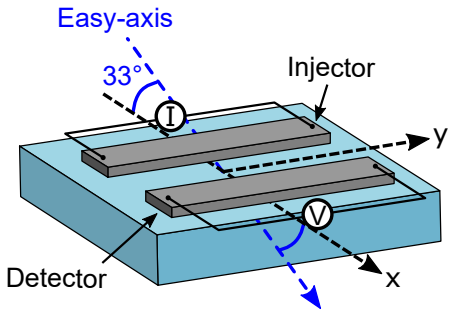

Figure 6.10: Non-local geometry for r-plane hematite, with Pt wires perpendicular to the in-plane component of the easy-axis.

(Fig. 6.11b) to the EA is shown in Fig. 6.11. A significant value of R_{el} appears at zero

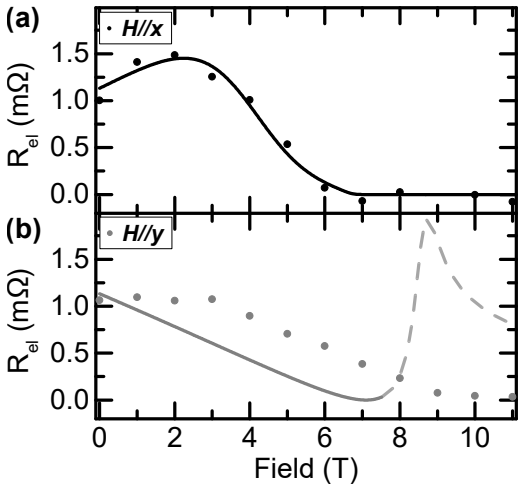

Figure 6.11: R_{el} for wires perpendicular to the easy-axis and with a magnetic field applied a) parallel (black) and b) perpendicular (grey) to the easy-axis. For this geometry, the spin accumulation is polarised along $\boldsymbol{x}$. Solid lines represent theoretical fits. Figure adapted from data published in Ref. [r3].

magnetic field for both field orientations. Given the earlier statements about the degeneracy of the magnon modes preventing spin transport, this finite signal in the absence of $\boldsymbol{H}$ demonstrates the theoretical expectations of the breaking of the mode degeneracy in the presence of an interfacial spin-bias [205]. As $\boldsymbol{H}$ increases along either in-plane axis, $\boldsymbol{n}$ begins to smoothly rotate due to the additional DMI field of hematite [r10, 29]. For $\boldsymbol{H}||\boldsymbol{x}$, i.e. along the easy-axis and shown in Fig. 6.11a, the signal increases slightly at low magnetic fields as $\boldsymbol{n}$ begins its smooth rotation and $\boldsymbol{\mu}_s(\boldsymbol{x}\cdot\boldsymbol{n})$ slightly increases. As the spin flop field is approached, $\boldsymbol{\mu}_s(\boldsymbol{x}\cdot\boldsymbol{n})$ substantially reduces until, at the spin flop field, it falls to zero. Correspondingly, R_{el} falls to zero at the same magnetic field. Meanwhile, when $\boldsymbol{H}$ is along the geometric y-axis (Fig. 6.11b), $\boldsymbol{n}$ smoothly rotates as the DMI spin reorientation is approached and $\boldsymbol{n}$ rotates completely to lie within the crystallographic basal plane. This then leads to a sustained decrease of $\boldsymbol{\mu}_s(\boldsymbol{x}\cdot\boldsymbol{n})$ with increasing magnetic field until the rotation occurs at high magnetic fields. The solid lines in Fig. 6.11 represent fits based on the same assumptions as before and given in Sec. 6.3; that the transport is dominated by the size of the magnon gap for the lowest energy modes and the projection $\boldsymbol{\mu}_s(\boldsymbol{x}\cdot\boldsymbol{n})$. These curves represent the behaviour of R_{el} well except in the vicinity of the DMI spin reorientation where the theoretical expectations would be a divergence of R_{el} at $\sim 8\,\mathrm{T}$, indicated by the dashed line in Fig. 6.11b. How-

ever, the experimental DMI reorientation happens at $H_c^{\perp} \sim 10\,\mathrm{T}$ (c.f. Sec. 5.1.5) [r10] and no increase of R_{el} is seen. The model used for the theoretical calculation makes use of three parameters, the exchange, the magnetic anisotropy along the easy-axis and the strength of the DMI. However, high order anisotropy terms could play a role in the experimental observations as well as the magnon modes which are not considered in the theoretical calculations and changes in the mode polarisation for $\boldsymbol{H} \perp EA$ leading to less efficient magnon transport, dephasing effects or reduced transport lengths [r13, 42, 88, 327].

The measurements shown here for the two geometries with respect to the magnetic anisotropy axis then provides some key information in the interpretation of the magnon transport in AFMs. From the first geometry, the importance of the relative orientation of $\boldsymbol{n}$ was evident but the role that the magnon gap plays was less clear, i.e. whether the reduction of the magnetic anisotropy at the spin flop, combined with the closure of the magnon gap and the associated increase in the excitable frequencies, was key for efficient transport or not. Through these measurements of R_{el}, whilst the magnon gap surely plays a role, it is indeed the orientation of $\boldsymbol{n}$ that dictates the efficiency of the magnon transport. Meanwhile the decrease of the efficiency above the spin flop in Fig. 6.4, even though $\boldsymbol{n}$ is parallel to the spin accumulation, is due to the change in the mode polarisation that occurs at the spin flop field [42, 88]. There was also the question raised in the previous section about the role of $\boldsymbol{m}$ above the spin flop in the magnon transport. Whilst for the previous geometry, a field larger than the spin flop field ($\boldsymbol{H} > H_c^{\parallel}$) leads to a field induced moment which may have contributed to the finite, persistent value of R_{el} at higher fields, the complete absence of R_{el} for $\boldsymbol{H} \| EA$ (Fig. 6.11a) above the spin flop in this second geometry indicates that, within the experimental resolution, $\boldsymbol{m}$ does not carry a magnon current from electrically excited magnons.

6.4.1 Transport of Thermally Excited Magnons in Hematite for Wires Perpendicular to the Easy-Axis

Having discussed the behaviour of R_{el}, we can now turn our attention to the behaviour of R_{th} for this geometry (Fig. 6.12). For $\boldsymbol{H} \| \boldsymbol{x}$ (Fig. 6.12a), a field induced moment only emerges as $\boldsymbol{n}$ rotates to lie perpendicular to $\boldsymbol{H}$. This is reflected in the experimental data where a significant, linear, component of R_{th} only appears above the spin flop field. Meanwhile, $\boldsymbol{H} \| \boldsymbol{y}$ in Fig. 6.12b places $\boldsymbol{H}$ parallel to the wire. Under no conditions can $\boldsymbol{m}$ appear directed along the transport direction and R_{th} thus remains low for all magnetic fields. These behaviours are reproduced by the theoretical fits to both field orientations (solid lines in Fig.6.12). Given that the curve for $\boldsymbol{H} \| \boldsymbol{y}$ provides no information on the significance of either $\boldsymbol{n}$ or $\boldsymbol{m}$ with regard to the transport of thermally excited magnons, one needs to consider the other field orientation to draw conclusions for R_{th}. The linear contribution of R_{th} above the spin flop supports the previous conclusion that $S_{\boldsymbol{m}}$ dominates the thermal transport whilst $S_{\boldsymbol{n}}$ is far smaller.

More recent measurements of the thermal transport in hematite for magnon propagation parallel and perpendicular to the easy-axis show a slightly different picture to the one discussed in this thesis, where transport is present in the absence of a field-induced moment along the transport direction. In general, the picture is more complicated and not fully understood and a more in depth discussion is the focus of a future work. Nevertheless, for the measurements presented here and in Sec. 6.2.1, the main conclusions

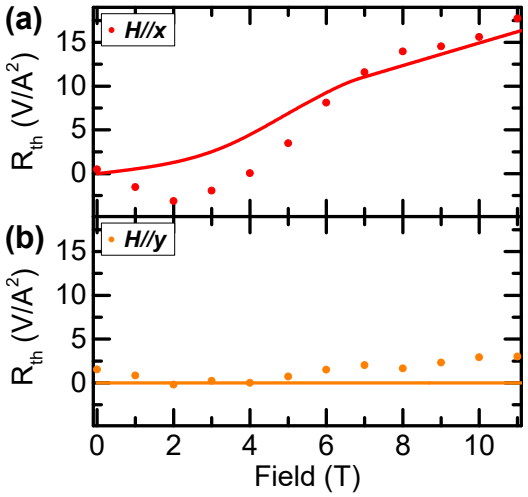

Figure 6.12: R_{th} for wires perpendicular to the easy-axis and with a magnetic field a) parallel (red) or b) perpendicular (orange) to the easy-axis. Solid lines represent theoretical fits. Figure adapted from in Ref. [r3].

drawn of $S_{\boldsymbol{m}} \gg S_{\boldsymbol{n}}$ and the importance of the canted moment remain valid.

6.5 Determination of the Magnon Propagation Regime in Bulk Hematite

The observation of magnon transport for the devices in Sec. 6.2 and Sec. 6.4 demonstrates that AFMs are capable of hosting a magnonic spin current without ferromagnetic components. The next question is about the transport regime in which such a magnonic spin current propagates within the AFM. Theoretical studies on the transport of magnonic spin currents in antiferromagnets have proposed quasi-ballistic [205], diffusive [191] and spin superfluid regimes [20, 21]. Each regime is expected to display different characteristics. The ballistic regime exists for transport occurring over distances far smaller than the mean free path of the propagating magnons such that there is minimal impact of magnon scattering. Although the magnon mean free path of YIG has been reported to be up to micrometres for thermally excited magnons [161, 181], it shows a strong temperature dependence [181] and the precise determination of the magnon mean free path, and which magnons are contributing, is challenging [180]. The other regimes to consider are a diffusive (or some other exponential) regime and spin superfluidity. Spin superfluidity (Sec. 3.3.2.1) is anticipated to demonstrate a power law decay with distance from the point of excitation [20, 21] and also, for a real system where anisotropy exists, a critical spin current required to induce transport [21]. Such theoretical works have focussed on easy-plane antiferromagnets. A similar magnetic state can appear at the spin flop [21]. This section will determine the magnon transport regime for the easy-axis phase of α-Fe_2O_3 at 200 K by probing both the behaviour of the electrical spin-bias signal with injection current and also as a function of distance between the injector and detector.

6.5.1 Determination of the Transport Regime from Current Dependent Measurements

To investigate the possibility of a threshold current required to overcome the magnetic anisotropy, the spin-bias signal R_{el} was investigated as a function of the electrical current density applied to the injector. As seen in Fig. 6.13, there is no obvious threshold for transport for either orientation of wires when the magnetic field is fixed at 6 T (in the case of wires parallel to the easy-axis) or 2 T (in the case of wires perpendicular to the easy-axis). Across a large range of current densities, both orientations display a linear relationship between the current density and the recorded voltage, however, there is some deviation from this linear behaviour at large current densities. The linear regime directly highlights that the magnon excitation here is related to the magnon chemical potential of α-Fe_2O_3 [183, 185, 187]. The non-linearity meanwhile can be attributed to a breakdown of the insulating behaviour of the hematite, where the applied charge current leads to a leakage current across the short distances investigated here [221, 225]. Alongside this, the increased current density deposits additional heat into the hematite, altering the magnetic anisotropy which is known to be strongly temperature dependent [239]. Finally, there is the possibility of the high density of the spin accumulation leading to auto-oscillations of the antiferromagnetic order beneath the injector at these high limits [169, 226, 227]. The difference between the two orientations with respect to this non-linearity may come from the differences in the electron distribution of hematite when measured parallel or perpendicular to the crystallographic c-axis [331], as well as differences in the interfacial quality between devices. Despite these non-linearities, all transport measurements were conducted at the current density indicated in Fig. 6.13 for wires with a separation d <1 µm and twice this value for separations larger that 1 µm, so the possibility of a breakdown in insulating behaviour and other non-linear effects play no role here.

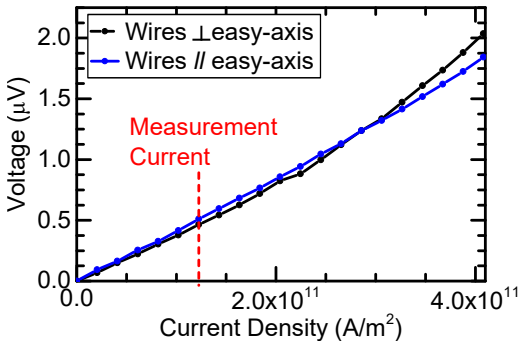

Figure 6.13: Current dependence of the non-local voltage for wires parallel (black) and perpendicular (blue) to the easy-axis of bulk hematite. The dashed red line indicates the current density for non-local measurements. Figure adapted from Ref. [r3].

With regard to a possible threshold, a current density of $(6.89\pm3.27)\times10^9\,\mathrm{A\,m^{-2}}$ arises from extrapolating to zero voltage, a value that is close to the lowest current density investigated where a voltage of 33 nV±15 nV was recorded. Given that this value is almost the noise floor of the system, it is difficult to assert whether there is a very low threshold or not. The presence of a threshold is still an interesting concept and should depend on the temperature and magnetic anisotropy. However, for the system shown here, an obvious threshold is not observed within the measurement accuracy.

6.5.2 Determination of the Magnon Propagation Length in Hematite

Given the lack of a threshold current density, the real test to determine the transport regime here instead comes from the functional form of the signal decay with distance, which should be exponential in the case of diffusive transport [161] or following some other power law for other transport regimes [20, 21, 208]. Fig. 6.14 plots the distance dependence of R_{el} for both geometries; parallel to the easy-axis at the spin flop and perpendicular to the easy-axis at a finite field. For both geometries, $\boldsymbol{H}$ is parallel to the easy-axis, i.e. the signals shown in Figs 6.4a and 6.11a. The reasons a finite field is chosen for the second geometry are two-fold. First, there have been reports of interfacial pinning caused by frustration at the interface between a magnetic insulator and the electrodes in a non-local geometry [178, 332]. The application of a finite field overcomes this. Secondly, the application of a magnetic field serves to break the degeneracy of the magnon modes. Even though the applied spin-bias from the Pt already breaks this degeneracy, evident from the finite value of R_{el} even in the absence of $\boldsymbol{H}$ (Fig. 6.11), the additional field serves to further break this symmetry. As seen in Fig. 6.14, the

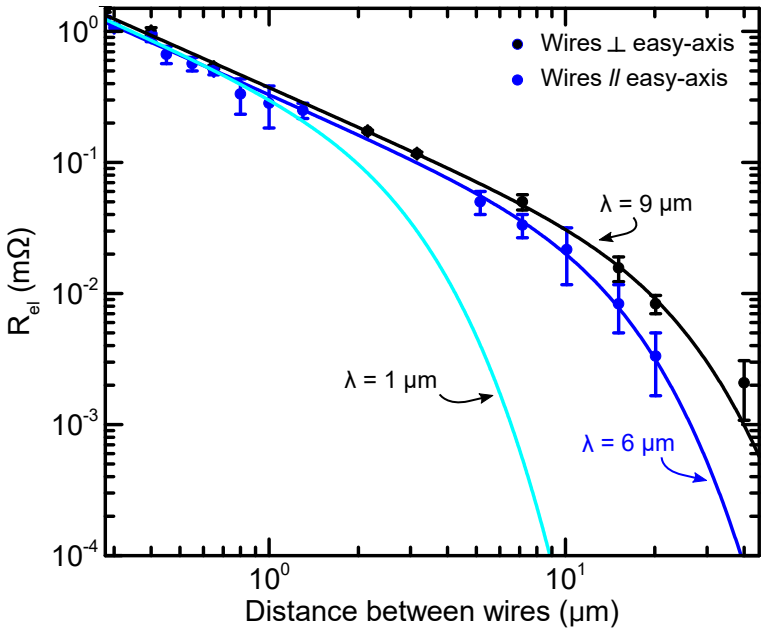

Figure 6.14: Evolution of R_{el} with increasing distance between the Pt wires for a geometry parallel (blue) and perpendicular (black) to the easy-axis. Solid lines represent fits to Eqn. 6.4 with spin diffusion lengths of $\lambda = 1$ μm (cyan), $\lambda = 6$ μm (black), and $\lambda = 9$ μm (blue). Figure adapted from Ref. [r3].

magnon spin current persists across micrometers for both geometries. The decay at low distances follows a $1/d$ power law, reminiscent of spin superfluidity. This behaviour is characteristic of diffusive transport below the diffusion length, where the transport is not dominated by scattering and the non-equilibrium magnons move along the gradient of the magnon chemical potential away from the injector [185, 187]. A one dimensional diffusion equation for magnons can be written as $d^2 n_m/dx^2 = n_m/D\tau$ where n_m is the non-equilibrium magnon density, D is the magnon diffusion constant and τ is the magnon relaxation time [161]. Assuming that the magnon velocity is constant, this is then proportional to the inverse of the distance. However, at large distances, the transport exponentially drops off as scattering dominates and the magnons relax. This, along with the absence of a threshold in current (see Fig. 6.13) and the elevated temperature

that these measurements were performed at (200 K), therefore indicate that the transport regime is in fact diffusive.

In order to describe the non-local magnon transport in ferrimagnetic YIG, the authors of Ref. [161] derived an equation based on one dimensional spin diffusion consisting of two regimes; the low distance diffusion regime characterised by a $1/d$ behaviour and a large distance exponential regime dominated by magnon relaxation. A single model can be applied to both regimes by adapting the one dimensional spin diffusion equation to magnon transport based on the non-equilibrium magnon density, magnon relaxation time, diffusion constant and diffusion length. The resulting equation is given by [161],

$$R_{el} = \frac{C}{\lambda} \frac{\exp(d/\lambda)}{1 - \exp(2d/\lambda)}, \tag{6.4}$$

where the distance independent parameters of the system are combined into a single constant C, λ is the spin diffusion length and d is the distance traversed by the spin current. This equation is plotted in Fig. 6.14 for a spin diffusion length of $\lambda = 1\,\mu m$, an optimistic value as compared to previous investigations of the magnon diffusion in AFMs, represented by the cyan line. This value of λ is obviously too low to represent the decay of the magnon transport measured here for both geometries. Instead, values of $\lambda = 6\,\mu m$ for the geometry parallel to $\boldsymbol{x}$ (blue) and $\lambda = 9\,\mu m$ for the geometry parallel to $\boldsymbol{y}$ (black) represent the data better, orders of magnitude larger than the 10s of nm previously evaluated for antiferromagnets. Although the exact values of λ for the two geometries differ, they share the common feature of micrometre spin diffusion lengths, orders of magnitude larger than previous reports and comparable to the largest reported for the current best magnon conduit, the ferrimagnetic material YIG [161]. This one dimensional approach relies on the thickness of the magnetic material being smaller than the lateral distance travelled by the magnons and the wire length being much larger than both. Here, the wire length is indeed much larger than the separation of the wires, however the thickness of the hematite crystal is larger than the propagation length of the excited magnons. When the sample is thicker than the propagation length, spin loss can occur, reducing the effective spin diffusion length evaluated by this model and the transport becomes dominated by the magnon relaxation [220]. The diffusion lengths evaluated here are therefore lower limits on the magnon propagation lengths for hematite.

It is worth clarifying at this point that one publication has put forward observations of long distance (thermally excited) spin transport in thin films of the antiferromagnetic insulator Cr_2O_3, published around the same time as our work discussed above [214]. A discussion of this work can be found in Sec. 3.3.2.1.

6.6 Spin Conductivity of Hematite

The ease of spin transmission can be quantified through the spin conductance of the magnetic insulator, represented in Eqn. 6.1a by $G_{\boldsymbol{n}}$ and $G_{\boldsymbol{m}}$. Given that $G_{\boldsymbol{m}} \ll G_{\boldsymbol{n}}$, we can than provide a quantitative estimate of the spin conductance of hematite from the non-local measurements. The spin conductance of a magnetic insulator can be estimated by making use of a spin resistor circuit model [161, 170, 216],

$$\frac{R_{nl}}{R_{SMR}} = \frac{R^S_{Pt}}{2R^S_{Pt} + 2R^S_I - 2R^S_{\alpha-Fe_2O_3}}, \tag{6.5}$$

where R_{nl} is the non-local resistance, R_{SMR} is the change in the resistance due to SMR, $R^S_{Pt(I)}$ are the spin resistance of the Pt wires (interface) and $R^S_{\alpha-Fe_2O_3}$ is the spin resistance of hematite. This is the value that we would like to calculate and compare to ferromagnetic insulators. For the shortest distance measured here, R_{nl}/R_{SMR} ∼1/1000. From calculations of the spin conductance of the Pt wires ($1.3\times10^{15}\,\Omega^{-1}\,m^{-2}$), interfacial area ($1.75\times10^{-11}\,m^2$) and the effective spin mixing conductance across the interface ($\sim10^{13}\,\Omega^{-1}\,m^{-2}$), the spin conductivity can be estimated. It however relies on making some assumptions with regard to the thickness of the spin channel. Here, the thickness of the crystal (500 µm) is much larger than the evaluated spin diffusion lengths, something that does not prove such a problem in thin films. By assuming that the thickness of the spin channel is comparable to the spin diffusion length, the model assumes that no spins are lost into the bulk of the crystal. However, this is something that is not true for ferromagnets [154, 220], and could lead to deviations from diffusive behaviour close to the injector [330]. Nevertheless, with this basic assumption, the spin conductivity of hematite calculated here is on the order of $10^5\,S\,m^{-1}$. This lower limit is then comparable to the ferromagnetic case [161].

6.7 Open Questions

The result presented in this chapter have demonstrated efficient, diffusive magnon transport in antiferromagnetic hematite. There are, however, many open questions remaining, such as the role the antisymmetric exchange interaction (DMI) plays in the magnon transport given that it allows for a smooth rotation of $\boldsymbol{n}$ in hematite as compared to a simple uniaxial AFM where the field induced behaviour is more rigidly fixed by the angle between the field and $\boldsymbol{n}$. The role of the magnon wavevector is also not clear. There is a clear contribution from low k magnons given the stark correlation between the behaviour of the $k = 0$ mode and the closure of the magnon gap at the spin flop and the experimental observations. However, their importance, and the role of other magnons is not completely understood. There is a distribution of $\boldsymbol{k}$, and therefore frequency, of the two magnon modes within the Brillouin zone [240]. In hematite, the two modes are degenerate in the absence of a magnetic field and their frequencies range from ∼500 GHz in the centre of the Brillouin zone to ∼24 THz at the edge [240], although spin waves at the edge of the Brillouin zone are standing waves and thus do not transfer angular momentum. There is also a large density of spin wave states around ∼22 THz [240]. To what extent these higher frequency modes play a role is not clear, but they should not be ignored. For example, in the SSE in YIG/Pt at 300 K, it was found that magnons with a normalised wavenumber in the range of 0.3 – 0.5 (frequencies of 1 THz – 3 THz) were integral to the understanding [154, 325]. Although the spin flop is related to the lower magnon branch at $k = 0$, the spin flop influences all the possible spin waves present. However it was found that the Morin transition[3] has no impact on spin waves with a frequency above 19.3 THz [240]. There is also the matter of the difference in decay length scales and maximum transport efficiency between the two geometries. This may arise due to differences in the interfacial quality between the two geometries that occurred during patterning or indicative of something else. Furthermore, the closure of the magnon gap at $H_c^{\parallel}$ may come with additional dissipation channels for the propagating magnons that have yet to be explored [87] alongside the larger magnetic field possibly altering the

[3] Given the energetic equivalence between the Morin transition and the spin flop, the lack of an impact of the Morin transition likely implies a small impact at the spin flop.

magnon diffusion length[207, 325, 333–335]. Finally, differences in the spin wave velocity parallel and perpendicular to the easy-axis may also contribute to this difference in the propagation length scales [240]. Given the anisotropic spin wave velocity, it is likely that the magnetic damping would also be anisotropic. There would then be a difference in the scattering experienced by magnons propagating along each direction, contributing to differences in the propagation lengths.

6.8 Conclusions

By making use of a bulk single crystal of antiferromagnetic hematite in the easy-axis phase, the first (to our knowledge) observation of long distance magnon transport in antiferromagnets was reported. With ultra-low damping and large antiferromagnet domains, this material proves as good as the "gold standard" for ferromagnetic based magnonic devices, YIG, at transporting a magnon current. Without relying on ferromagnetic components for the excitation of the magnonic current, the spin Hall effect was used to produce a spin-bias across the interface of the hematite crystal and Pt wires. Such a spin-bias led to the excitation of polarised magnons that propagated along the Néel order across micrometers. The key requirement for such transport was revealed by modifying the relative orientation of the spin polarisation of the interfacial spin-bias to the Néel vector. A parallel alignment of $\boldsymbol{\mu}_s$ and $\boldsymbol{n}$ is required for transport, even in the presence of a significant magnon gap providing a route for zero-field antiferromagnetic magnonic devices. Meanwhile, the transport of magnons produced by the spin Seebeck effect in the hematite relies on an emerging field induced magnetisation along the desired transport direction. Unlike in ferromagnetic materials, the two distinct transport mechanisms allow for the separation of R_{el} and R_{th} through the consideration of the antiferromagnetic symmetries relative to the applied magnetic field, enabling efficient, electrical control of the magnon transport without parasitic contributions originating from Joule heating. The next chapter will build on these observations to unravel the complex transport mechanisms in antiferromagnetic insulators by probing thin films of hematite of various orientations.

7

Magnon Transport in Thin Film Hematite

In the previous chapter, the long distance transport of magnons in a bulk crystal of hematite (α-Fe_2O_3) was discussed. However, such crystals are 500 µm thick and are therefore not practical for utilisation in most real device applications which would prefer to employ thin films of the materials in order to save space as well as gain potential faster information processing capabilities. When scaling down to the thin film regime, materials can take on new properties that were not present in the bulk. Conversely, the properties that one wants can disappear. For the particular case of ferromagnetic materials, this can lead to an increase in the magnetic damping [336] and a decrease in the magnon propagation length [154]. One clear example of this, of obvious relevance here, is the Morin transition. If the α-Fe_2O_3 films become too thin, the Morin transition is suppressed and the easy-axis phase is inaccessible [280]. Although very recent results have demonstrated magnon transport in α-Fe_2O_3 without the need for an easy-axis phase through mode mixing of linear polarised magnons [r13, r16, 327, 329], the conventional understanding of magnon modes is that the circular polarisation present in the easy-axis phase is critical for the efficient transport of angular momentum over long distances. If there is no Morin transition, or the temperature of T_M is very low, then there is no possibility within this understanding for efficient magnon transport.

In this chapter, results on the investigation of magnon transport in thin films of hematite of different orientations will be discussed, an overview of which can be found in Appendix Sec. A.8. Starting first with films of hematite orientated such that the sample plane is the (0001) orientated (in order to have the easy-axis of the antiferromagnetic order below T_M out of the sample plane) the spin transport will be presented and discussed. Whilst sharing similar features to the measurements presented in Ch. 6, there are distinct differences in the transport properties for a magnetic field applied parallel and perpendicular to the easy-axis and the efficiency of the transport can be trained by repeated exposure to a magnetic field. Alongside measurements of R_{el}, the signal of thermal origins R_{th} is also present. Due to the crystallographic orientation (0001), the easy-axis normal to the sample plane does not allow for field free transport. For this, we turn again to $(1\bar{1}02)$ r-plane hematite with its in-plane projection of the Néel vector. The magnetic anisotropy of these films is much higher than the (0001) orientated samples, possibly due to strain along the c-axis due to the growth process, and the spin flop field is almost unattainable in the laboratory setting available here, so the main focus will be on measurements of the

zero field transport. An understanding of the diffusion properties in these films is investigated through a combination of domain imaging and theoretical modelling where the domain structure is found to correlate with the observed transport lengths. Finally, the temperature dependence of the magnon transport in thin film α-Fe_2O_3 will be discussed. Some of these results are published in Ref. [r15].

The experimental results presented in this chapter were obtained on devices fabricated by the author from thin film hematite grown by the research group of Prof. Avner Rothschild from the Technion University of Technology in Haifa, Israel. The magnetic imaging was performed by Drs R. Lebrun and L. Baldrati of JGU with the assistance of Dr. F. Kronast at the BESSY[1] II synchrotron in Berlin. The theoretical understanding of the decay of R_{el} for the different films was obtained through collaboration with Prof. O. Gomonay from JGU, Dr. A. Qaiumzadeh from NTNU and Dr. C. Ulloa at Utrecht University.

7.1 Magnon Transport in Thin Film (0001) Hematite

The discussion of magnon transport in thin film antiferromagnets will commence with results for the (0001) orientated thin films of α-Fe_2O_3 grown by pulsed laser deposition. The crystalline and magnetic characterisation can be found in a previous chapter (c.f. Sec. 5.2.1). The key point to note is the presence of a Morin transition with a value of $T_M \sim 200$ K, indicating the presence of an easy-axis phase below this temperature. Due to being a thin film, the value of T_M is suppressed as compared to a bulk crystal due to changes in the magnetic anisotropies responsible for the Morin transition (Sec. 4.1.1). All measurements of the magnon transport in these (0001) films presented in this section were performed at $T = 175$ K, i.e. just below T_M. For this orientation of hematite, the easy-axis (EA) lies out of the sample plane when below T_M (parallel to the geometric $\boldsymbol{z}$-axis in Fig. 7.1), and thus the magnon transport can be investigated for a magnetic field applied parallel or perpendicular to the EA, rather than making an oblique angle to it as for the case of the bulk r-plane crystal used previously (Sec. 6.2).

The non-local structures were defined as in the previous chapter by EBL with subsequent DC sputtering of 7 nm Pt with electrical contacts of Cr/Au (more details can be found in Sec. 4.2.5.2). As before, DC measurements were made, with the current inverted for successive measurements in order to extract $R_{el} = \left(V^+ - V^-\right)/2I$ and $R_{th} = \left(V^+ + V^-\right)/2I^2$. The geometry of these films is shown in Fig. 7.1, demonstrating the direction of $\boldsymbol{n}$ in the easy-axis (Fig. 7.1b) or spin flop (Fig. 7.1c) phases relative to the non-local structure and the coordinate system that is adopted for this section. Note that in the previous chapter, the x-axis was defined as the easy-axis and other directions were defined relative to this. Here, however, the x-axis is defined as parallel to the non-local geometry and thus parallel to the charge current. The interfacial spin accumulation $\boldsymbol{\mu}_s$ is then polarised along the geometric y-axis and the easy-axis lies along $\boldsymbol{z}$.

7.1.1 Magnetic Field Parallel to the Easy-Axis

In the previous chapter (Ch. 6), it was revealed that efficient magnon transport in antiferromagnets relies on $G_{\boldsymbol{n}}$. Experimentally, this is probed through setting the relative orientation of the Néel vector and the spin accumulation, i.e. $\boldsymbol{n} \| \boldsymbol{\mu}_s$. For these films,

[1] Berliner Elektronenspeicherring-Gesellschaft für Synchrotronstrahlung m. b. H.

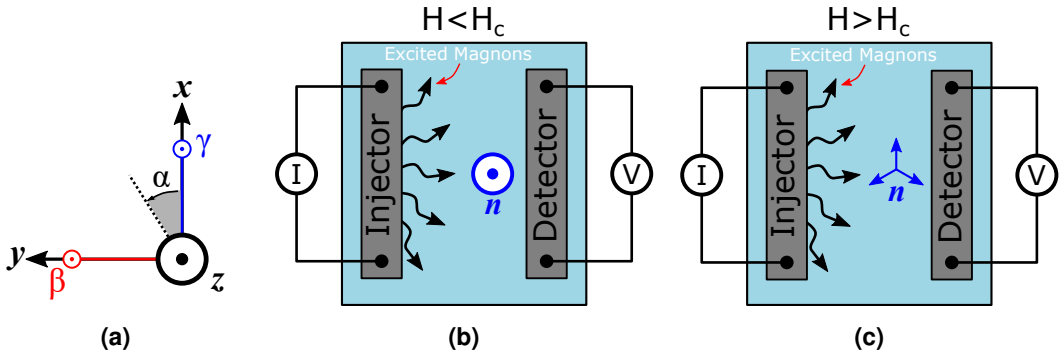

Figure 7.1: a) Overview of the coordinate system employed in the later discussions. b)-c) Schematic for the non-local geometry of Pt wires (grey) atop a (0001) oriented hematite thin film (turquoise) viewed from above. A charge current in the injector excites magnons in the hematite that diffuse away from the electrode. b) The Néel vector lies out of the sample plane at zero field and for magnetic fields below the critical fields for the spin transitions, shown in blue. c) Above the critical field for the spin flop, $\boldsymbol{n}$ lies in the sample plane with a three-fold degeneracy.

this condition can be satisfied above the classical spin flop field $H_c^{\parallel}$ for a magnetic field applied along the easy-axis. This promotes $\boldsymbol{n}$ to lie within the xy-plane (see Fig. 7.1c), the same plane as the polarisation of $\boldsymbol{\mu}_s$. The magnon transport was thus investigated for $\boldsymbol{H}\|EA$ ($\boldsymbol{z}$) as shown in Fig. 7.2. For an increasing magnetic field, the signal begins to increase up to a maximum at some magnetic field $H_c^{\parallel}$. This behaviour is similar to that shown in a bulk crystal in Sec. 6.2 where, at the spin flop field, the Néel vector $\boldsymbol{n}$ rotates to lie in the sample plane. This rotation satisfies the aforementioned key requirement for antiferromagnetic magnon transport of $\boldsymbol{n}\|\boldsymbol{\mu}_s$ accompanied by the closure of the magnon gap that occurs at the spin flop (c.f. Sec. 6.3). Above $H_c^{\parallel}$, the spin transport is suppressed as the magnetic anisotropy increases, reopening the magnon gap and the magnon modes adopt an increasingly more elliptical polarisation [88]. However, whilst the magnon transport in the bulk crystal peaked sharply at $H_c^{\parallel}$, before falling away equally sharply, the peak seen here is more gradual and broad. It instead takes place across a larger range of field values than one would expect.

The broad peak in R_{el} can be explained by a distribution of the critical fields required to induce the spin flop as a result of a distribution of growth crystallites, as discussed in the section on film characterisation in the previous chapter, Sec. 5.2.1. Each crystallite then has a slight variation in the anisotropy, along with a slightly different angle relative to the external magnetic field, and thus a distribution in the value of $H_c^{\parallel}$ develops across the film. When lowering the magnetic field, a feature not seen in the bulk crystal appears: a hysteresis, where the signal peaks at some other magnetic field depending on whether the transport is investigated for a field swept down from high fields or up from zero.

7.1.2 Origin of the Magnetic Hysteresis for a Magnetic Field Parallel to the Easy-Axis

To understand the emergence of this hysteresis-like signal of R_{el} in Fig. 7.2, the behaviour of $\boldsymbol{n}$ at and above the spin flop for $\boldsymbol{H}\|\boldsymbol{z}$ needs to be considered. In the spin flop phase, the inherent in-plane anisotropies of hematite act to produce a three-fold degen-

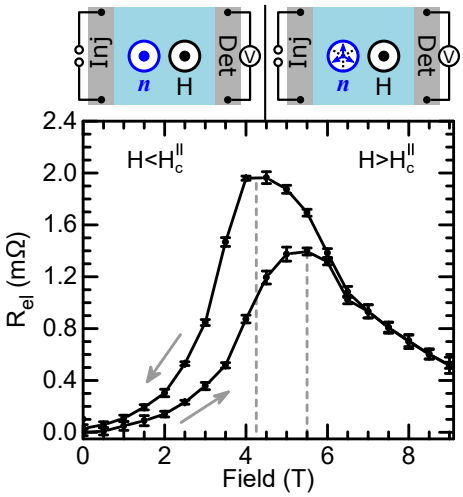

Figure 7.2: Non-local resistance for (0001) plane hematite for a magnetic field applied along the easy-axis. The arrows indicate the direction of the magnetic field sweep and the dashed lines indicate the maximum for an increasing and decreasing field branch. The behaviour of the Néel vector $\boldsymbol{n}$ is shown in the sketches above. Below the spin flop field, the Néel vector lies along th easy-axis out of the sample plane. Above the spin flop, $\boldsymbol{n}$ rotates to lie in-plane with three degenerate directions, forming a multi-domain state. Adapted with permission from Ref. [r15]. Copyright 2020 American Chemical Society.

eracy of $\boldsymbol{n}$. This then leads to the formation of domains where $\boldsymbol{n}$ is rotated by 60° due to this degeneracy. Such a degeneracy and domain formation only appear due to the fact that the magnetic field is along the EA. As soon as a finite angle appears between $\boldsymbol{H}$ and the EA, this degeneracy is broken. However, the pure nature of having degenerate domains does not explain the presence of the hysteresis, only that the antiferromagnetic structure above the spin flop may show a multi-domain state, where the domains nucleate from defects or existing domain walls [50, 73]. Instead, the appearance of a hysteresis can be explained by the additional magnetostrictive anisotropy that plays a role above $H_c^{\parallel}$, stabilising the easy-plane phase [68, 69, 309, 310]. Due to the strained nature of thin film growth, it is reasonable to assume that this additional anisotropy can play a significant role in these films (Sec. 5.2). This anisotropy is key for the stabilisation of domains in easy-plane antiferromagnets where $\boldsymbol{n}$ rotated across 60° domain walls, whilst in the easy-axis phase this anisotropy plays no role [308]. When lowering the magnetic field, the additional anisotropy acts to stabilise the easy-plane phase over the easy-axis phase and thus the return of the Néel vector to lie along $\boldsymbol{z}$ is delayed.

As the magnetostriction interaction is responsible for the antiferromagnetic domain structure above $H_c^{\parallel}$, as well as above T_M [309, 310], this also means that in the spin flop phase a magnetic field will exert a force on and influence the domain walls. This can then result in motion of the domain walls in response to the applied magnetic field, depending on the relative orientation of the applied magnetic field and the rotation of $\boldsymbol{n}$ across the domain walls [r1, 15]. The manipulation of domain walls by magnetic field has been shown in other easy-plane antiferromagnets [60]. These studies on bulk crystals, where there are few defects, show domain walls freely moving with increasing magnetic field, with domains of certain orientations of $\boldsymbol{n}$ growing at the expense of neighbouring domains. The domain wall continues to move under a given field, until it encounters a pinning site where an increase of $\boldsymbol{H}$ is required to overcome the pinning effect and

induce further movement of the domain wall. This free movement is not seen in thin film antiferromagnets, where the density of defects is generally much higher resulting in pinning of the domain structure [337]. The movement of domains then requires large torques [r4, 295, 296] or magnetic fields much larger than those used on bulk, easy-plane AFMs [223].

This then raises the question of whether the domain structure is influencing the transport efficiency and if the efficiency can be modified by exposure to large magnetic fields altering the domain structure. To test this, the magnetic field was cycled repeatedly whilst R_{el} was measured. Fig. 7.3 shows the effect on the efficiency of the magnon transport for multiple magnetic field sweeps along z. The curves are labelled in the order that

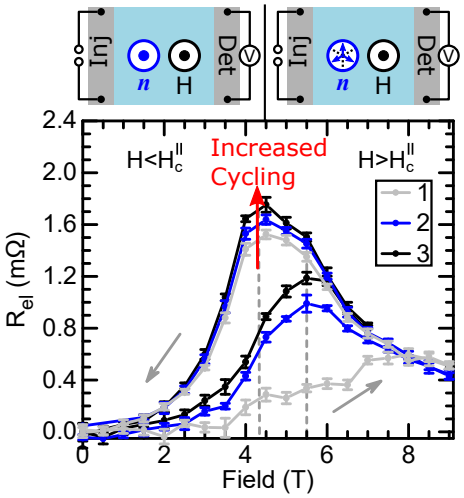

Figure 7.3: Multiple sweeps of the magnetic field applied along the easy-axis showing a training effect of the non-local resistance. The arrows indicate the increasing or decreasing field branch. The peak magnetic fields remain unchanged between successive cycles of the magnetic field. The sketches above show the behaviour of the Néel vector with field, where above the spin flop, it adopts a multi-domain state. Adapted with permission from Ref. [r15]. Copyright 2020 American Chemical Society.

they were measured and it is obvious that the repeated application of the magnetic field leads to a modification of the magnon transport, enhancing it for both an increasing and decreasing magnetic field. Despite the increase in the transport efficiency, the critical magnetic fields for both sweep directions remain unchanged, as indicated by the dashed grey lines.

The magnetic state of the film under investigation can be returned to a "default" state in two ways. The first is by warming above the Morin transition and then cooling again without a magnetic field. This then leads to the nucleation of the easy-axis phase based on defects in the crystal structure and thus should be random [73]. The second way to return to the initial state is to apply a magnetic field perpendicular to the easy-axis. This then induces the DMI spin reorientation at $H_c^{\perp}$ that is explained in Sec. 4.1 [241, 270] and discussed in detail in Ch. 5. After going through this transition, the Néel vector falls into a preferred domain orientation where $\boldsymbol{n}$ is perpendicular to both the magnetic field and the easy-axis. As the magnetic field is then lowered to zero, $\boldsymbol{n}$ returns to lie along z and the magnetic landscape then returns to that which exhibits the training effect.

From the width of the hysteresis in Fig. 7.2 ($\sim$ 1.5 T) as well as the value of the critical field, the strength of both the uniaxial anisotropy field and the magnetostrictive field for

these films can be calculated[2]. These values are ∼30 mT and ∼8 mT respectively (c.f. Sec. 5.2).

The increase of R_{el} in both Figs. 7.2 and 7.3 at $H_c^{\parallel}$ can be explained through the strong softening that happens to one of the modes of hematite at the spin flop and the increasing magnon population that occurs at fixed temperature as the frequency of the mode lowers. Combined with an increasing projection of $\boldsymbol{n}$ on $\boldsymbol{\mu}_s$ as the Néel vector smoothly rotates, the magnon transport is enhanced, whilst the suppression above $H_c^{\parallel}$ can be attributed to the opening of the magnon gap, the corresponding reduction of the thermal magnon population and the transition of the magnon polarisation from circular ($\boldsymbol{H} < H_c^{\parallel}$) to elliptical, with increasing ellipticity with increasing field ($\boldsymbol{H} > H_c^{\parallel}$) [88]. This behaviour is then similar to that observed in Sec. 6.2 on bulk hematite, confirming that the Néel spin conductance $G_{\boldsymbol{n}}$ dominates the transport mechanism.

7.1.3 Magnetic Field Misaligned to the Easy-Axis

At the spin flop field, the Néel vector falls into degenerate directions however, this degeneracy can be broken by introducing a finite angle between the easy-axis and the magnetic field. This section will investigate the effect on the spin transport in the case of a broken degeneracy above the spin flop field. Fig. 7.4a shows the measured curves over multiple cyclings, where an angle of 2° exists between the EA and $\boldsymbol{H}$. The signal

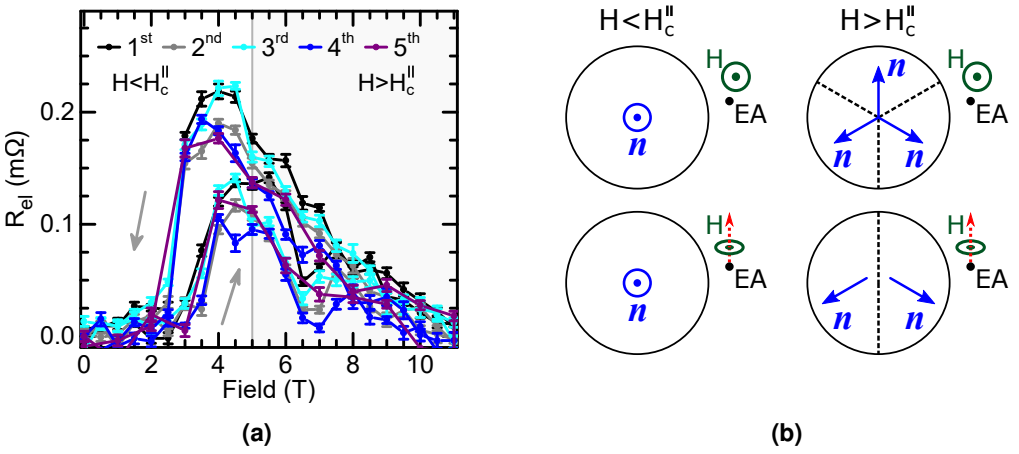

Figure 7.4: a) Non-local resistance of (0001) orientated hematite for a magnetic field applied at a finite angle to the easy-axis at 175 K. The arrows indicate the increasing and decreasing magnetic field branches. b) Schematic sketch of the three-fold degenerate domain structure of the easy-plane with respect to an applied magnetic field. The top panels show the case of the spin flop for a magnetic field parallel to the easy-axis. Above the spin flop field, the Néel vector falls into three degenerate states. The bottom panels shows the case when a finite angle exists between the easy-axis and the magnetic field. Above the spin flop field, the degeneracy is broken and some domains are preferred over others.

displays similar characteristics to before; the signal increases up to some critical field $H_c^{\parallel}$, above this field the signal decreases and finally, when lowering the magnetic field,

[2]For the effective uniaxial anisotropy field, one can make use of the formulation given in Ch. 5 where $H_c^{\parallel} = \sqrt{\left(H_{an}^{eff} H_E\right)}$ and the exchange field is assumed close to the bulk value. The value of the spin flop field is then that for an increasing field branch. The strength of the magnetostrictive field is then the change in H_{an}^{eff} one would need in order to produce a change of $H_c^{\parallel}$ of 1.5 T.

a hysteresis emerges stabilising the spin flop phase over the easy-axis. There are, however, a couple of clear differences between Fig. 7.3 and Fig. 7.4a, despite the misalignment of the field being small. The first and most striking is the sharpness of the transition back to the easy-axis phase when the magnetic field is lowered. The second is the lack of a clear training effect across the five field cycles shown, along with a lower absolute value for the efficiency of the magnon transport.

The easier of the two effects to explain is the second, the lack of a training effect and lower absolute value of the magnon spin transport. By having a finite angle between $\boldsymbol{H}$ and the EA, the degeneracy of the easy-plane phase is broken and thus, in the spin flop phase, $\boldsymbol{n}$ will preferentially adopt some orientations over others. As the magnetic field is cycled, there is no reason for a training effect as $\boldsymbol{n}$ will always fall into the preferred domains and thus there will be no domain walls that move with repeated cyclings. This is also seen in bulk NiO for example, where multiple domains can be stabilised for a given field direction and repeated exposure to a magnetic field does little to the domain configurations [74]. With regard to the reduced magnitude of the magnon transport, this can be explained by considering the in-plane component of $\boldsymbol{H}$ with respect to both $\boldsymbol{n}$ and $\boldsymbol{\mu}_s$. As can be seen in the top frame of Fig. 7.4b, if the field is perfectly along the easy-axis, then $\boldsymbol{n}$ will show a three fold degeneracy. However, with the small misalignment of $\boldsymbol{H}$ with respect to the EA, some domain orientations will be preferred over others while not necessarily favouring a monodomain state. This is shown in the bottom frame of Fig. 7.4b. This would then lead to several orientations of $\boldsymbol{n}$ above the spin flop. Given that R_{el} depends on the projection $\boldsymbol{n} \cdot \boldsymbol{\mu}_s$, having several different contributing orientations may give rise to cancellation effects and thus a lower value of R_{el}. For the remainder of this section, we will only consider the more instructional case of $\boldsymbol{H} \| \boldsymbol{z}$ rather than this more complex case.

7.1.4 Magnetic Field Perpendicular to the Easy-Axis

Next, the spin transport was investigated for a magnetic field within the sample plane, either $\|\boldsymbol{x}$ or $\|\boldsymbol{y}$, i.e. either parallel or perpendicular to the charge current in the Pt wires. This places the field perpendicular to the easy-axis and thus the DMI induced spin reorientation at $H_c^{\perp}$ will ultimately place $\boldsymbol{n}$ within the sample plane, just like at $H_c^{\parallel}$. However, unlike for the classical spin flop, which results in the three degenerate directions, the spin reorientation at $H_c^{\perp}$ will result in a clearly defined direction of $\boldsymbol{n}$ perpendicular to both $\boldsymbol{H}$ and the effective magnetic field H_D created by the DMI along the easy-axis. This should result in magnon transport that is more controllable than in the previous orientation.

Starting first with $\boldsymbol{H} \| \boldsymbol{x}$, $\boldsymbol{n}$ will reorientate parallel to $\boldsymbol{y}$ and one would expect a controllable enhancement of the spin transport at the transition. The non-local resistance for $\boldsymbol{H} \| \boldsymbol{x}$ is shown in Fig. 7.5. Starting from an absence of a signal at zero applied magnetic field, just as for the previous orientation of $\boldsymbol{H}$ in Fig. 7.2, R_{el} increases up to a peak at $\mu_0 H_c^{\perp} \sim 2.6\,\mathrm{T}$ before decreasing back to zero at high magnetic fields. Just as a field parallel to the easy-axis of a simple uniaxial AFM leads to a closing of the magnon gap for one of the two lowest $k = 0$ magnon modes at $H_c^{\parallel}$, so too does a field perpendicular to the EA of an AFM with DMI parallel to the easy-axis [270]. The magnon dispersion for the $k = 0$ mode in an increasing magnetic field was shown previously in Fig. 4.5a. The lower branch drops to zero at $H_c^{\perp}$ whilst the other exponentially increases, an effect experimentally observed previously [241, 270]. This then allows us to utilise the simple

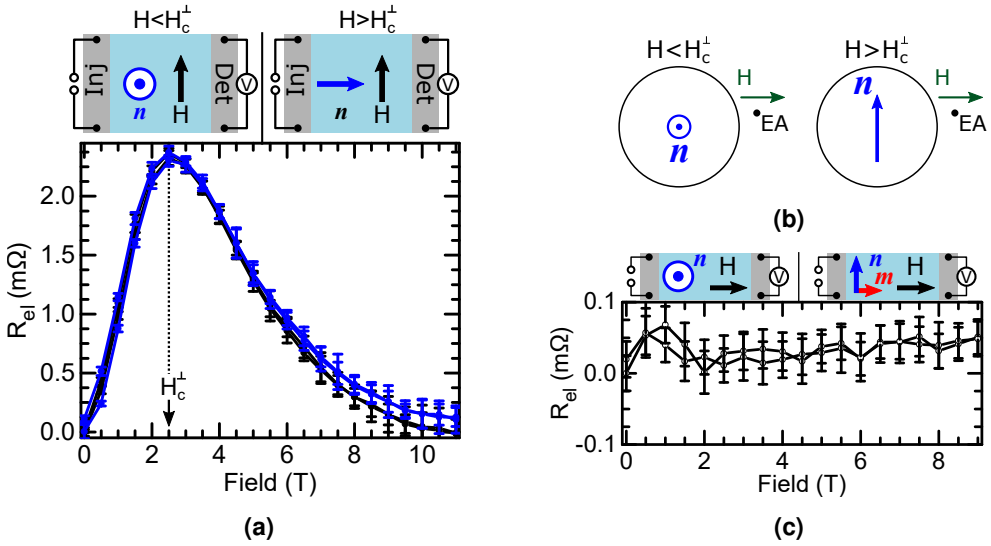

Figure 7.5: a) Non-local resistance for (0001) orientated hematite films for a magnetic field applied perpendicular to the easy-axis in the plane of the sample parallel to the wires for two successive measurements. No training effect or hysteresis is observed. The sketches above show the reorientation of the Néel vector $\boldsymbol{n}$ to lie perpendicular to the field and the easy-axis direction above some critical field. Adapted with permission from Ref. [r15]. Copyright 2020 American Chemical Society. b) Schematic of the domain structure for a magnetic field perpendicular to the easy-axis for a magnetic field below and above $H_c^\perp$. c) R_{el} for a magnetic field parallel to $\boldsymbol{y}$, perpendicular to the non-local structure and the easy-axis. Although $\boldsymbol{n}$ reorientates at some critical field, no transport is seen. A field induced magnetisation appears along the transport direction, but no evidence of this moment transporting magnons is seen.

model given in Sec. 6.3 to explain the magnon transport of this orientation. The spin reorientation at $H_c^\perp$ leads to an increase in $\boldsymbol{n}\cdot\boldsymbol{\mu}_s$ whilst the magnetic anisotropy is reduced by the magnetic field, leading to an increase in the spin conductivity [205, 207].

Despite the similarities between the transport shown in Fig. 7.5 and Fig. 7.2, there are also several differences. When $\boldsymbol{H}$ is lowered back to 0 T from $>$11 T, no hysteresis appears in the electrical response shown in Fig. 7.5. Furthermore, contrary to $\boldsymbol{H}\|\boldsymbol{z}$, for this orientation of the magnetic field the repeated application of the magnetic field leads to no discernible training effect of the magnon transport, as demonstrated through the two curves shown in Fig. 7.5a overlapping for all fields.

Whilst at $H_c^\parallel$ for $\boldsymbol{H}\|\boldsymbol{z}$ a three-fold degeneracy emerges, paving the way for field training of the domain structure through repeated field exposure, the domain structure at $H_c^\perp$ for $\boldsymbol{H}\|\boldsymbol{x}$ does not have this same degeneracy. Just as a finite angle between $\boldsymbol{H}$ and $\boldsymbol{z}$ led to no training effect in Fig. 7.4a, so too is there no training effect when the finite angle is 90° rather than the 2° of Fig. 7.4a. Due to the additional effective field from the DMI directed along the easy-axis, $\boldsymbol{n}$ is forced to lie along $\boldsymbol{y}$ so that it is perpendicular to both the external and effective internal fields present in the system. Furthermore, neighbouring domains with an antiparallel alignment of the Néel vector will be delimited by domain walls where $\boldsymbol{n}$ rotates by 180°. The magnetostrictive interaction previously responsible for the stabilisation of the magnetic landscape at $\boldsymbol{H} > H_c^\parallel$ is then not present for $\boldsymbol{H} > H_c^\perp$ [69]. This lack of additional anisotropy above the spin reorientation field

then means that the critical field for the transition of $\boldsymbol{n}$ back to along the c-axis occurs at the same magnetic field as for the increasing field branch, $H_c^{\perp}$, and thus no hysteresis appears for this orientation.

From the values of $H_c^{\parallel}$, $H_c^{\perp}$ and the estimation for the effective anisotropy, i.e. H_{an}^{eff}, the values for the strength of the effective DMI field H_D can be estimated as discussed in Sec. 5.2). This places an estimate of $H_D \sim 11.6$ T, which is more than four times as large as the value found in bulk hematite [r10, 29]. Given that the DMI field originates from a broken inversion symmetry, an increase in the asymmetry of the crystal structure along the c-axis will correspondingly increase H_D. As discussed in Sec. 5.2.1, the c-axis of these films suffers from distortion introduced by the growth process and the large lattice mismatch between the film and substrate (∼5.02%), thus increasing H_D.

The final orientation of $\boldsymbol{H}$ and $\boldsymbol{n}$ that can be investigated would be to apply $\boldsymbol{H}\|\boldsymbol{y}$. This will induce a spin reorientation of $\boldsymbol{n}$ at $H_c^{\perp}$, just as in the case of $\boldsymbol{H}\|\boldsymbol{x}$ as directly evidenced in the previous chapter, however this time the final state of $\boldsymbol{n}$ will be parallel to the wire and thus perpendicular to $\boldsymbol{\mu}_s$. In this instance, no magnon transport should be expected as a function of the applied magnetic field if the magnetic spin conductance $G_{\boldsymbol{m}}$ is negligible, and indeed no magnon transport due to the excitation of magnons at the Pt/α-Fe_2O_3 interface is experimentally observed either below, at or above $H_c^{\perp}$ as can be seen in Fig. 7.5c where the scale differs from that of $\boldsymbol{H}\|\boldsymbol{x}$ in order to show the lack of a signal above the noise level. The device this curve was measured on had the smallest electrode separation available and thus offered the best chance to observe transport of electrically excited magnons carried by the canted moment. It is immediately clear that, within the experimental resolution, no significant magnon transport is seen. As mentioned in the previous chapter (Sec. 6.2.1), this does not rule out the possibility of $\boldsymbol{m}$ facilitating the transport of magnons excited by the interfacial spin-bias, just that we are unable to resolve a signal above the noise, showing that this is not a significant contribution here.

7.1.5 Angular Dependence of Magnon Transport in (0001) Orientated Thin Film Hematite

The field dependences previously discussed are further exemplified through measurements for rotations of $\boldsymbol{H}$ in the xy, yz and xz-planes shown in Fig. 7.6. The symmetry of R_{el} for magnetic rotations in the xy-plane is shown in Fig. 7.6a for four different field strengths. Increasing the magnitude of $\boldsymbol{H}$ results in an increase of the in-plane projection of $\boldsymbol{n}$, whilst rotating through α alters the orientation of this projection relative to $\boldsymbol{\mu}_s$. As a function of the angle between $\boldsymbol{H}$ and the direction of the charge current $\boldsymbol{x}$, denoted by the angle α, R_{el} displays a $\sin^2\alpha$ dependence. There is a minimum for $\boldsymbol{H}\|\boldsymbol{y}$ at $\alpha = 90°$ where there is no spin transport and the signal increases smoothly up to a maximum at $\alpha = 0°/180°$. The amplitude of modulation in Fig. 7.6a with increase field is consistent with the uniaxial measurements of both $\boldsymbol{H}\|\boldsymbol{x}$ and $\boldsymbol{H}\|\boldsymbol{y}$ whereby R_{el} increases with increasing field up to a maximum at $H_c^{\perp}$ before decreasing.

For a magnetic field rotated instead within the yz-plane, the expected behaviour would be to transition between the uniaxial scan of $\boldsymbol{H}\|\boldsymbol{z}$ (Fig. 7.2) and the absence of magnon transport for $\boldsymbol{H}\|\boldsymbol{y}$ (Fig. 7.5c). When $\boldsymbol{H}$ is rotated through this plane, it will inevitably result in both a parallel and perpendicular alignment of $\boldsymbol{H}$ and the easy-axis.

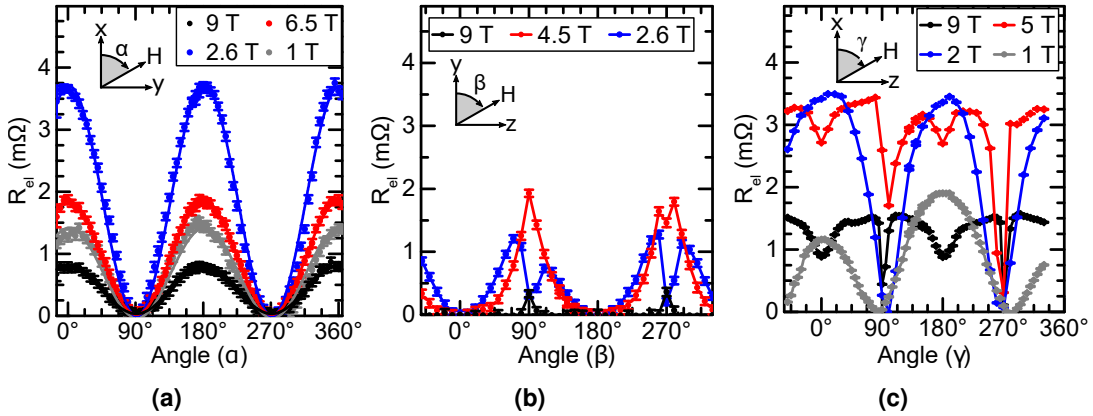

Figure 7.6: Non-local resistance at 175 K for a device rotated in a static magnetic field through the a) xy-plane, b) yz-plane and c) xz-plane where the field subtends an angle α, β and γ respectively. a) and b) adapted with permission from Ref. [r15]. Copyright 2020 American Chemical Society.

The conditions for both the traditional spin flop and the DMI spin reorientation will then both be satisfied, albeit at different magnitudes of the applied field. However, the spin reorientation at $H_c^{\perp}$ is not observable in this plane[3]. Indeed, by looking at Fig. 7.6b, the measured response shows a smooth transition when the field is rotated around $\beta = 0°$ and the projection of $\boldsymbol{n}$ on $\boldsymbol{\mu}_s$ smoothly changes. However, as it approaches a parallel alignment with the easy-axis, $\boldsymbol{H} > H_c^{\parallel}$ the signal diverges as the Néel vector undergoes the spin flop and the signal increases. This behaviour is consistent with the previous investigations on the spin transitions in hematite, showing that the spin flop is a first order transition and thus the signal diverges, whilst a field at any other angle produces a second order spin transition with a smooth rotation of $\boldsymbol{n}$.

The final plane of rotation, shown in Fig. 7.6c, places the field in a plane that allows for an enhancement of the magnon transport at both $H_c^{\parallel}$ ($\boldsymbol{H} \| \boldsymbol{z}$) and $H_c^{\perp}$ ($\boldsymbol{H} \| \boldsymbol{x}$). However, as evidenced by the uniaxial scans (Figs 7.2 and 7.5), $H_c^{\parallel} \neq H_c^{\perp}$ and thus the rotational dependence shows a similar disparity for the magnon transport. There are enhancements and suppressions of R_{el} as $\boldsymbol{H}$ approaches 0° and 90° and the net response is a combination of the signals seen in the other two planes. At low magnetic fields, the rotation is smooth between zero for $\boldsymbol{H} \| EA$ and a maximum when perpendicular with a magnitude that increases up to $H_c^{\perp}$. In the vicinity of $H_c^{\parallel}$, there are suppressions of R_{el} when the field is perpendicular to the easy-axis and also when a small but finite angle exists between field and the EA (consistent with Fig. 7.4a)). At magnetic fields higher than both critical fields, the electrical response is suppressed, consistent with the uniaxial measurements along both axes. However, there still persists a significant value of R_{el} when $\boldsymbol{H}$ is neither parallel nor perpendicular to the easy-axis, indicating that this intermediate angle between $\boldsymbol{H}$ and the two geometric orientations may lead to a more robust spin transport as a function of the magnetic field. This, however, is not currently understood and merits a more detailed study of the transport mechanisms.

[3]Given that this plane involves $\boldsymbol{H} \| \boldsymbol{y}$ where no transport is visible (Fig. 7.5c).

7.1.6 Transport of Thermally Excited Magnons in (0001) Orientated Thin Film Hematite

Alongside the signal directly originating from the current in the heavy metal, the transport of magnons excited thermally through the SSE is simultaneously captured during the electrical measurements. Based on measurements of the non-local SSE in bulk hematite where $S_{\boldsymbol{m}} \gg S_{\boldsymbol{n}}$ (Sec. 6.2.1 and Sec. 6.4.1), a maximum in R_{th} is expected for a parallel alignment of the direction of transport $\boldsymbol{y}$ and the field induced canted moment $\boldsymbol{m}$, i.e. 90° offset from R_{el}. This behaviour is confirmed through measurements of the thermal transport R_{th} for both $\boldsymbol{H}\|\boldsymbol{x}$ and $\boldsymbol{H}\|\boldsymbol{y}$, as shown in Fig. 7.7a through measurements where $\boldsymbol{H}$ was rotated within the xy-plane as shown in Fig. 7.7b. For $\boldsymbol{H}\|\boldsymbol{x}$, there is no evidence of transport either below, at, or above $H_c^{\perp}$ from thermally excited magnons. This is not surprising as $\boldsymbol{m}$ is directed along $\boldsymbol{x}$ for all values of $\boldsymbol{H}$. However, when the symmetry breaking field induced magnetisation is directed along the direction of transport, such as when $\boldsymbol{H}\|\boldsymbol{y}$, a linearly increasing signal is observed. There is no evidence of the spin reorientation that takes place from the value of R_{th} (Fig. 7.7a), further confirming that the orientation of $\boldsymbol{n}$ relative to either $\boldsymbol{\mu}_s$ or the transport direction has no direct impact on R_{th}, and it is only the orientation and magnitude of $\boldsymbol{m}$ that is important. By rotating the magnetic field within the sample plane through an angle α, a $\cos\alpha$ dependence of the signal is found, which originates from the detection mechanism via the inverse SHE. There is a maximum (minimum) of the signal for a parallel (antiparallel) alignment of $\boldsymbol{m}$ and $\boldsymbol{\mu}_s$ as shown in Fig. 7.7b. The magnitude of R_{th} recorded here is an order of magnitude smaller than found in bulk hematite (Fig. 6.5). This may be to do with a smaller value of the field induced magnetisation in these films or, alternatively, the antiferromagnetic domain structure is acting to attenuate the signal. As will be shown later (Sec. 7.3.1), the antiferromagnetic domain structure can lead to significant magnon scattering for low frequency magnons. However, whether this is responsible for the lower magnitude seen here is not known and a more detailed study focusing on the non-local spin Seebeck effect in insulating antiferromagnets with varying domain sizes would need to be made.

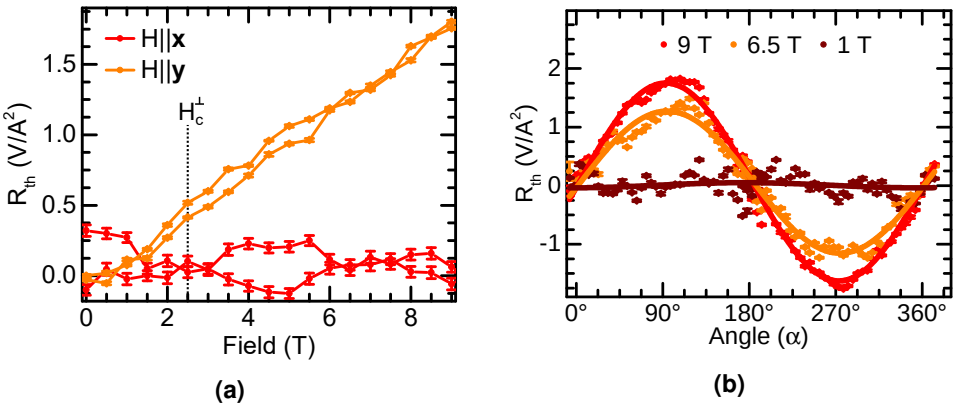

Figure 7.7: R_{th} for 100 nm (0001) orientated α-Fe_2O_3 films for a) a magnetic field directed along $\boldsymbol{x}$ (red circles) and $\boldsymbol{y}$ (orange circles). The critical field for the DMI spin reorientation is indicated but no signature of this reorientation is seen in the data. b) R_{th} for a static magnetic field rotated in the xy-plane. The solid lines represent fits of $\cos\alpha$ to the weighted data. The error bars in both figures represent the standard deviation of the data points.

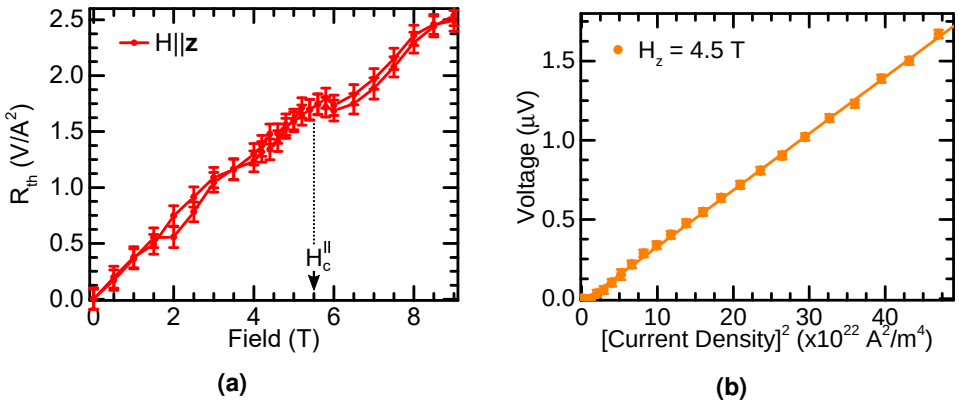

Figure 7.8: a) R_{th} for (0001) orientated hematite and $\boldsymbol{H} \| \boldsymbol{z}$. The spin flop field $H_c^{\|}$ is indicated. b) Dependence of the signal shown in a) at $\mu_0 \boldsymbol{H} = 4.5\,\mathrm{T}$ as a function of the square of the current density. Error bars where visible represent standard deviations of the data points.

7.1.6.1 Transport of Thermally Excited Magnons for a Field Along the Easy-Axis

As well as investigating thermal effects for a magnetic field applied within the sample plane, R_{th} can also be investigated for $\boldsymbol{H}$ out of the sample plane along $\boldsymbol{z}$. This then places the field parallel to the easy-axis so there will be no field induced moment at low magnetic fields $\boldsymbol{H} < H_c^{\|}$[4]. Above $H_c^{\|}$, there is now the possibility of an emergent value of $\boldsymbol{m}$ due to the field induced canting of $\boldsymbol{n}$, where $\boldsymbol{m} \| \boldsymbol{z}$. There will then be a contribution of $\boldsymbol{m}$ in the sample plane from the DMI induced canting, but the major component of $\boldsymbol{m}$ will align with $\boldsymbol{H}$. Thus the expectation for the non-local SSE signal for $\boldsymbol{H} \| \boldsymbol{z}$ would be a complete absence of a signal below $H_c^{\|}$, followed by a small increase in the signal as the spin flop occurs when a small component of $\boldsymbol{m}$ appears within the xy-plane. At higher fields this would then be expected to be suppressed with $\boldsymbol{H}$. Given that the component of $\boldsymbol{m}$ in the plane of the sample would be small, no significant magnon transport is expected either above or below $H_c^{\|}$.

In contrast to these possible expectations, as shown in Fig. 7.8a the reality is very different. It is observed that there is an increasing linear signal with increasing field that starts from zero. Given that the plotted quantity is derived from $R_{th} = \left(V^+ + V^-\right)/2I^2$, i.e. it removes current polarity effects, the presence of a signal implies a thermal origin, as does the linear behaviour with magnetic field (Fig. 7.8a) and quadratic behaviour with current (see Fig. 7.8b where R_{th} is plotted against the square of the current density).

This raises the question of whether this signal is related to the thermal excitation of magnons by the injector or not. One could argue that perhaps it is the Néel vector that facilitates the transport of the thermally activated magnons with the applied field breaking the degeneracy between the two magnon branches [88, 205, 207, 324, 325]. An estimate of $\sim 1.6\,\mathrm{meV}$ can be made for the maximum energy difference caused by this degeneracy breaking (see Footnote 2 in Ch. 6), i.e. $\sim$10% of the thermal energy available at 175 K (15.1 meV). However, if the broken degeneracy between the magnon modes led to significant magnon transport, the observed signal should display a marked change at $H_c^{\|}$. Furthermore, there is no evidence of thermally activated magnon trans-

[4] This occurs due to the parallel alignment of $\boldsymbol{H}$ and $\boldsymbol{n}$.

port facilitated by the Néel vector for other configurations of the magnetic field (Fig. 7.7a). Thus one can conclude that $\boldsymbol{n}$ leads to negligible transport of thermally excited magnons in these films for the field strengths used. Additionally there is insufficient $\boldsymbol{m}$ across the field range investigated to account for the observed signal. Thus the signal must be related to something other than the magnetic state of the hematite film below the detector.

Before continuing the discussion of the origin of this strongly linear signal with field (Fig. 7.8a), it is worth noting that in the vicinity of the spin flop field there is a small feature present. If a linear fit is made, the difference (ΔR_{th}) results in no noticeable deviations from the fit until $H_c^{\parallel}$ is reached. At this field, ΔR_{th} deviates by $\sim$0.3±0.15 V A^{-2} before regaining its linear behaviour. This behaviour, without the linear contribution, is reminiscent of the previously described expectation for the signal based on expectation of $S_{\boldsymbol{m}}$. However as mentioned before this does not account for the linear background.

To explain this, we consider that below the detector, there will be a thermal gradient created by the nearby injector which leads to the non-local SSE [161, 176, 178, 220, 221]. This thermal gradient then generates a perpendicular thermal gradient across the Pt/α-Fe_2O_3 interface of the detector. A thermal gradient in a metal induces a charge current by means of the ordinary Seebeck effect [148]. The additional application of a magnetic field leads to a deflection of this charge current due to the Lorentz force acting on the electrons, resulting in a transverse charge current. Alongside this, the application of a magnetic field perpendicular to the thermal gradient between the wires also leads to a transverse component of a thermal gradient along the length of the detector, known as the thermal Hall effect (aka the Righi-Leduc effect) [221]. In this case, the thermal gradient between the injector and detector lies along $\boldsymbol{y}$, with the field along $\boldsymbol{z}$ leading to a transverse thermal gradient along $\boldsymbol{x}$. This transverse thermal gradient then acts along the length of the detector, producing a Seebeck voltage (also along $\boldsymbol{x}$) that scales linearly with the applied magnetic field and has been observed for an out-of-plane magnetic field in YIG based non-local devices [221]. For the magnetic field out of the sample plane, there is then a significant parasitic contribution to the signal that is not related to the magnetic structure of the hematite or the transport of magnons. When measuring thermal signals in (antiferro-)magnetic insulators, care then needs to be taken in the interpretation of the results [214].

Summarising the uniaxial measurements and the angular dependence, the electrically excited magnon transport in these (0001) orientated α-Fe_2O_3 films shows no evidence of the field induced moment or canted moment, whilst the thermal transport is unaffected by the orientation of $\boldsymbol{n}$. However, the electrically excited magnon transport is only significant in close proximity to the two critical fields, with zero transport in the absence of a magnetic field and also at large values of $\boldsymbol{H}$. As mentioned before, the application of large magnetic fields is not of practical use for the future development of antiferromagnetic spintronic devices and zero field transport would be preferred. Whilst the previous measurements were performed with the easy-axis out the the sample plane, there is a growth orientation that places the easy-axis completely in-plane and thus should lead to the greatest magnon transport in the absence of an applied field and a complete suppression at and above $H_c^{\parallel}$. This is the so called a-plane or the crystallographic orientation defined by (11$\bar{2}$0). However, this orientation of hematite suffers from an unstable surface termination and proved challenging to structure into devices for electrical measurements. Additionally, the 100 nm films of this orientation failed to

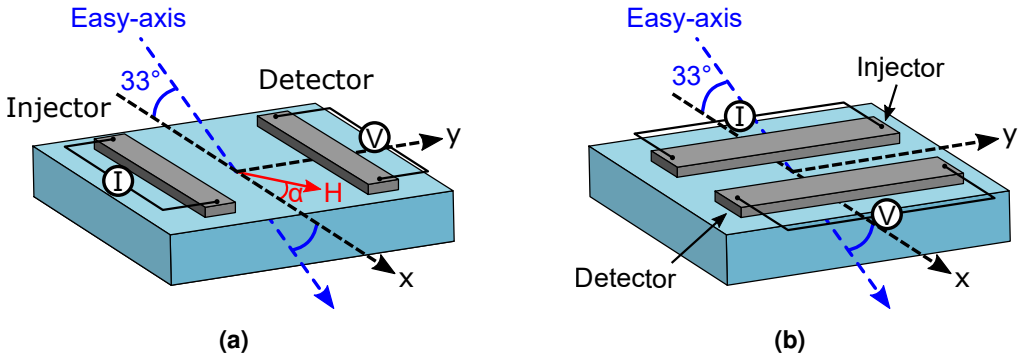

Figure 7.9: a) Coordinate system for r-plane hematite films and a non-local geometry parallel to the in-plane projection of the easy-axis. b) Coordinate system for r-plane hematite films and a non-local geometry perpendicular to the in-plane projection of the easy-axis.

show a Morin transition and so the magnon transport in the easy-axis phase could not be investigated.

7.2 Magnon Transport in (1$\bar{1}$02) Orientated Hematite Thin Films

500 nm thick hematite films orientated with the sample plane as the (1$\bar{1}$02) plane were grown by PLD on likewise orientated sapphire substrates [263, 283]. These films show a Morin transition, with a value of T_M~200 K, as measured by SQUID magnetometry (details of film characterisation in Appendix Sec. A.6), and the c-axis aligns parallel to the c-axis of the sapphire substrate (refer to Fig. A.4a in the appendix). Films of this orientation benefit from the same advantages as the bulk crystals in Ch. 6, Sec. 6.1, not least the stable surface termination [300] (see Appendix Sec. A.9). Non-local devices were patterned such that there were wires and thus the associated charge current both parallel (Fig. 7.9a) and perpendicular (Fig. 7.9b) to the in-plane component of $\boldsymbol{n}$. Sec. 7.1 made use of the wire direction to define the geometric coordinate system but this proves confusing when discussing the two orientations here. Instead, the discussion will revert to the coordinate system employed in Ch. 6 where the field is applied relative to the magnetic easy-axis, termed $\boldsymbol{x}$. This was shown previously for parallel wires in Fig. 6.3a and perpendicular wires in Fig. 6.3b. To save the reader having to refer back to these figures, they are reproduced here in Fig. 7.9.

7.2.1 Magnon Transport for Wires Parallel to the Easy-Axis

First, wires parallel to the easy-axis investigated given the pronounced signal observed in the bulk crystal at the spin flop field when $\boldsymbol{H}$ is applied parallel to $\boldsymbol{x}$ (Fig. 6.4). Although the signal is likely not to be as sharp as in the bulk based on the broad peak at $H_c^{\parallel}$ observed in the measurements of the (0001) orientated films already investigated (Fig. 7.2), an enhancement is nevertheless expected at the transition. Furthermore, due to the finite angle between $\boldsymbol{H}$ and the EA, no hysteresis is expected in measurements of R_{el}, again based on the previous findings for the (0001) films. Alongside this, expectations for R_{th} would be similar to those of the bulk crystal shown in Fig. 6.5, that is to say $S_{\boldsymbol{n}}$ is expected to play a minimal role and $S_{\boldsymbol{m}}$ is expected to dominate the non-local

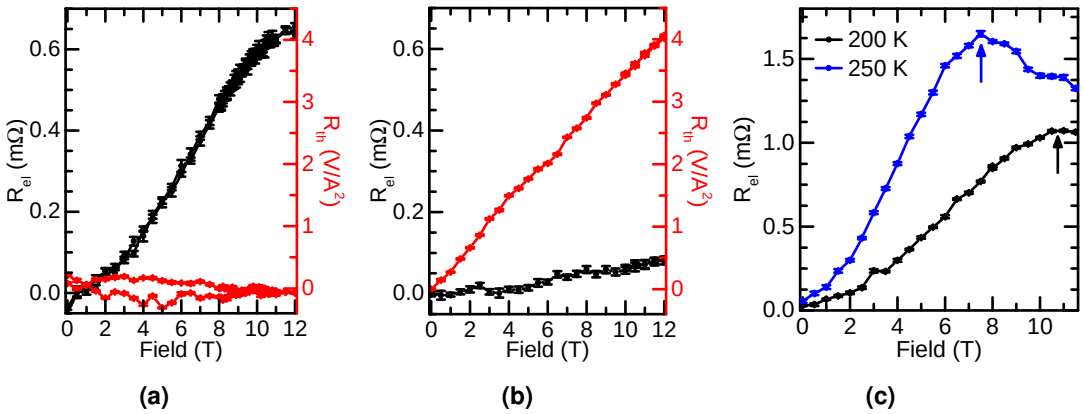

Figure 7.10: R_{el} (black) and R_{th} (red) for 500 nm, $(1\bar{1}02)$ plane hematite films for Pt wires parallel to the easy-axis and a magnetic field applied a) parallel ($\boldsymbol{H}\|\boldsymbol{x}$) or b) perpendicular ($\boldsymbol{H}\|\boldsymbol{y}$) to the easy-axis. Measurements performed at 175 K, just below T_M. c) R_{el} for a magnetic field parallel to the non-local structure at 200 K and 250 K.

SSE, emerging only for $\boldsymbol{H}\|\boldsymbol{y}$.

The measured values of R_{el} and R_{th} are presented in Figs 7.10a and 7.10b for $\boldsymbol{H}\|\boldsymbol{x}$ and $\|\boldsymbol{y}$ respectively. Noting first the behaviour of R_{th}, the red curves in Fig. 7.10, a magnetic field parallel to the wires (Fig. 7.10a) does not lead to a significant spin transport due to the non-local SSE, as expected. Meanwhile the magnetic field perpendicular to the wires (Fig. 7.10b) leads to a field induced canting of the Néel vector $\boldsymbol{n}$ and thus a linearly increasing value for R_{th}. These observations therefore agree with the previous measurements and support the conclusions on the impact of the magnetic ($S_{\boldsymbol{m}}$) and Néel ($S_{\boldsymbol{n}}$) Seebeck conductances provided in Sec. 6.2.1 and 7.1.6.

Moving onto the signal that is of more interest from an applications point of view, R_{el} increases with magnetic field as expected when $\boldsymbol{H}$ is directed along the easy-axis component (Fig. 7.10a, black curve) whilst $\boldsymbol{H}$ perpendicular to the EA (Fig. 7.10b, black curve) does not yield a measurable signal. Unlike in the bulk case in Sec. 6.2, R_{el} does not show a true peak with a turning point and subsequent reduction, however this can be attributed to the limits of the magnetic fields obtainable in the experimental setup available during this thesis. Given the 33° angle of the easy-axis, the maximum field of the experimental setup corresponds to a field along the easy-axis itself of $\boldsymbol{H}$ ~10 T. Despite not seeing a decrease of R_{el} which would allow us to estimate the value of $H_c^{\|}$, this maximum field can be considered a lower limit for the spin flop field. Assuming that the exchange in such a thick films is equivalent to that of bulk hematite, this sets a lower limit on the uniaxial anisotropy field (the net effective field directed along the easy-axis regardless of underlying anisotropy) of $H_{an}^{eff} > 105$ mT, nearly four times higher than that extracted for the c-plane films (~30 mT, Sec. 5.2) and the bulk r-plane crystal (23.8 mT, Sec. 5.1) at similar temperatures.

The value of H_{an}^{eff} calculated here at 175 K should also display a temperature dependence [r10, r14, 241] and decrease closer to the Morin transition. The value of T_M in these films is 200 K (see Fig. A.4b in the appendix), where the films begin to transition to the easy-plane phase. By moving to temperatures closer to, or even within, the transition, H_{an}^{eff} can be reduced given that H_{an}^{eff} must fall to zero by the end of the transition,

which should lead to a reduction in the value of $H_c^{\parallel}$. This is shown in Fig. 7.10c for 2 additional temperatures; 200 K in black and 250 K in blue. The arrows in Fig. 7.10c show the point where the value of R_{el} plateaus in the case of the black curve and displays a turning point in the case of the blue curve[5]. As expected, the value of $H_c^{\parallel}$ moves to lower magnetic fields with increasing temperature. Nevertheless, at 200 K there is still no significant decrease of R_{el}, so it is difficult to ascertain the exact value of $H_c^{\parallel}$ as it is right at the edge of the field range available. Meanwhile, the turning point for R_{el}, and thus $H_c^{\parallel}$, at 250 K clearly occurs at $\sim$7 T. This confirms the expectation of the temperature dependent H_{an}^{eff}, however, the temperature of 250 K places the film firmly within the Morin transition of these films, resulting in a mixture of the easy-axis and easy-plane phases. This mixture of phases, whilst resulting in a definite value of $H_c^{\parallel}$, means that transport is not occurring in the purely easy-axis phase. Furthermore, the maximum value of R_{el} obtained in the measured field range here is far smaller than the bulk (Sec. 6.2) and (0001) film (Sec. 7.1.1 and 7.1.4) measurements of R_{el}. Given that this orientation of wire in these films proves less efficient than the second geometry investigated (Fig. 7.9b), as well as the large anisotropy field of H_{an}^{eff} = 105 mT, further measurements of these devices are not pursued or discussed. Instead the focus will be on the second geometry with wires perpendicular to the easy-axis (Fig. 7.9b).

7.2.2 Magnon Transport for Wires Perpendicular to the Easy-Axis

For the geometry shown in Fig. 7.9b, the charge current is passed along the geometric y-axis and $\boldsymbol{\mu}_s$ is parallel to $\boldsymbol{n}$ at zero field. Significant magnon transport would be expected in the absence of $\boldsymbol{H}$ where $\boldsymbol{\mu}_s$ acts to break the zero field degeneracy of the magnon modes as shown for bulk crystals of the same orientation in Sec. 6.4. From the first geometry investigated on these films in the previous section, the steadily increasing value of R_{el} indicates that $\boldsymbol{n}$ begins to rotate due to the finite angle between the easy-axis and $\boldsymbol{H}$ inducing a smooth, continuous rotation as opposed to the abrupt first order transition of the pure spin flop [29]. Furthermore, the large value of H_{an}^{eff} directed along the easy-axis, that limited the expected enhancement in the signal, plays a minimal role here in the expected zero-field transport. R_{el} is shown for this geometry for both configurations of $\boldsymbol{H}$ relative to the direction of the charge current in Fig. 7.11. For both orientations of the magnetic field, there exists a significant signal at 0 T that is suppressed at higher magnetic fields. As the magnetic field increases, $\boldsymbol{n}$ begins to rotate given the finite angle between it and $\boldsymbol{H}$. Alongside this smooth rotation of $\boldsymbol{n}$ with increasing field, the increasing magnetic field also acts to overcome interfacial pinning that may be present [178, 332] and further break the degeneracy of the magnon modes. The net result is that for both field directions, there is a slight increase of the transport efficiency just above 0 T before the suppression that occurs with increased rotation of $\boldsymbol{n}$ reducing the projection on $\boldsymbol{\mu}_s$. For $\boldsymbol{H} \| EA$ (Fig 7.11a), the transport begins to suppress at 4 T, similar to the bulk crystal in the previous chapter. However, in the bulk crystal, the signal was suppressed by the spin flop at $\sim$6 T. For the thin films, the signal is suppressed around 8 T even though the complete rotation of $\boldsymbol{n}$ due to the spin flop occurs above this (Fig. 7.10). As for $\boldsymbol{H} \perp EA$, the signal in the bulk crystal for the same geometry was suppressed at 10 T by the reorientation of $\boldsymbol{n}$. Meanwhile for the thin films (Fig 7.11b), the signal is suppressed by a similar magnetic field, however it displays a peak at

[5] It is worth noting the measurements in Fig. 7.10a and Fig. 7.10c were conducted on devices with different electrode separations, hence the differences in the magnitude of R_{el}.

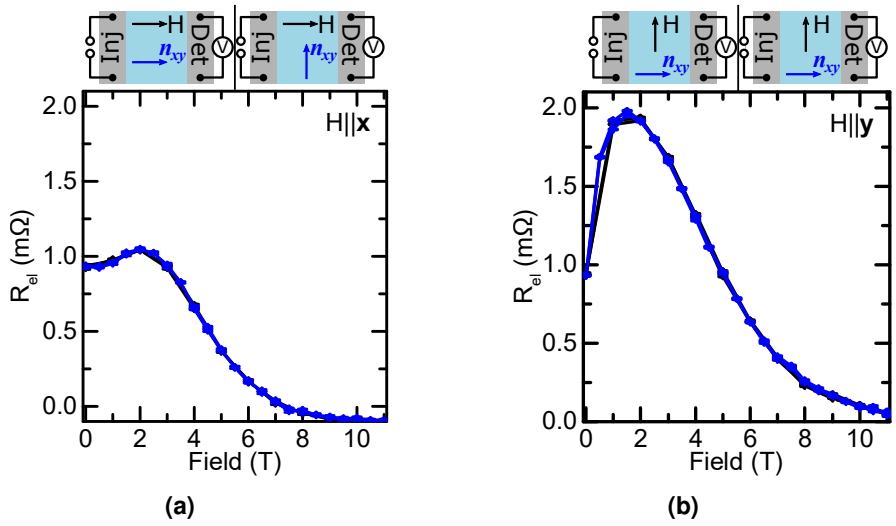

Figure 7.11: Non-local spin-bias signal R_{el} for 500 nm thick α-Fe_2O_3 films orientated with [1$\bar{1}$02] out-of-the-plane and wires perpendicular to the easy-axis for a) $\boldsymbol{H}\|\boldsymbol{x}$ and b) $\boldsymbol{H}\|\boldsymbol{y}$ for two cycles of the applied field (blue and black). No hysteresis is visible. The sketches above each figure indicate the behaviour of the Néel vector $\boldsymbol{n}$ with applied magnetic field, whereby $\boldsymbol{n}$ begins to rotate under the applied magnetic field. Adapted with permission from Ref. [r15]. Copyright 2020 American Chemical Society.

low fields that was not seen for the bulk crystal in Fig. 6.11b. One possible explanation of this peak could be evidence of the DMI spin flop that was not seen in the bulk crystal, although the theoretical calculation did anticipate this. This could be occurring at lower magnetic fields than the calculated bulk value due to a larger value of the DMI field in these films, similar to the (0001) orientated films in Sec. 7.1. Unlike for the magnon transport for $\boldsymbol{H}\|\boldsymbol{z}$ in the (0001) orientated films (Sec. 7.1.1), there also exists no training effect between successive field cycles or hysteresis when lowering the magnetic field back through the critical fields. This behaviour is not surprising considering that the magnetic field makes a finite angle with the easy-axis and thus there is no degeneracy in the domain structure above the critical fields. Even though the magnetic structure is that of the easy-plane phase, the domain walls delimiting neighbouring domains will feature a 180° rotation of $\boldsymbol{n}$ and the magnetostrictive interaction will have no effect on stabilising the state with lowering magnetic fields.

7.2.3 Angular Dependence for Wires Perpendicular to the Easy-Axis

Given the larger value of H_{an}^{eff} that exists in these films as compared to the bulk crystals, investigations of R_{el} as a function of the angle between the magnetic field and direction of the charge current can shed light on the role of this stronger anisotropy. Fig. 7.12a shows measurements of R_{el} for three magnitudes of the applied magnetic field; 2 T shown in grey, 5 T in blue and 8 T in black. The curves shown in Fig. 7.12a represent transitions between the two curves in Fig. 7.11. Starting first with $\boldsymbol{H} = 2$ T (grey points in Fig. 7.12a), R_{el} smoothly transitions between a maximum and minimum. However, contrary to naive expectations drawn from earlier discussions in Sec. 7.1.5, both the maximum and minimum occur for $\boldsymbol{H} \perp EA$ whilst the value for both instances of $\boldsymbol{H}\|EA$ (i.e. $\alpha = 0°$ and $\alpha = 180°$) remains constant. This means that for this low

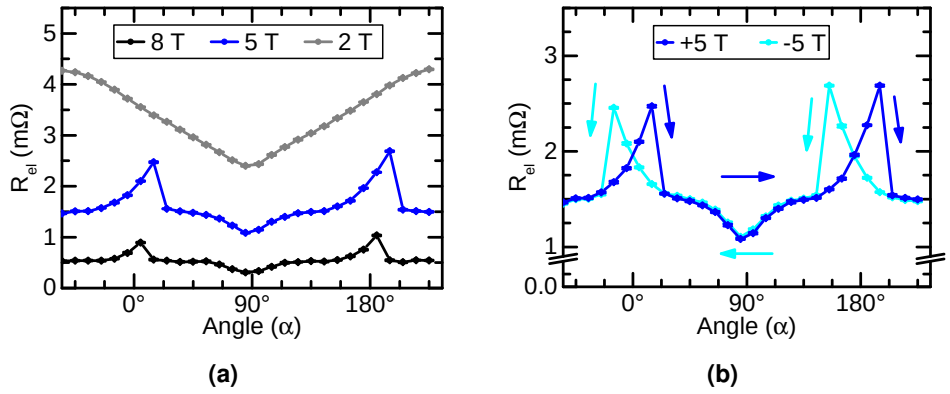

Figure 7.12: Non-local resistance for wires perpendicular to the easy-axis in $(1\bar{1}02)$ plane thin film hematite and a magnetic field rotated in-plane. a) R_{el} as a function of the angle between the wire direction and $\boldsymbol{H}$. $\alpha = 0°$ (180°) corresponds to a field (anti-)parallel to the easy-axis direction. b) R_{el} for $\boldsymbol{H} = \pm 5$ T and the same rotation angles. The two curves fail to overlap in the vicinity of $\boldsymbol{H}$ parallel to the easy-axis. This hysteresis decreases with larger fields

field[6], a magnetic field parallel and antiparallel to the (constant) direction of the charge current gives rise to a large change in the measured value of R_{el}. Whilst the magnetic field (anti-) perpendicular to the charge current result in the same magnitude of R_{el}, as one would expect from Fig. 7.6 and symmetry. The anisotropy responsible for the antiferromagnetic order is considered to be uniaxial, not unidirectional, however, the curve shown here seems to indicate that at lower magnetic fields, there is a unidirectional behaviour occurring. As the spin transport depends on $\boldsymbol{n} \cdot \boldsymbol{\mu}_s$, it may be that the transition that occurs for a magnetic field parallel to the charge current leads to a different sense of rotation as when $\boldsymbol{H}$ is antiparallel to the charge current. This may arise if there exists strain, which is unidirectional, within the film perpendicular to the easy-axis projection.

The behaviour at large fields, is more reminiscent of what one would expect. As $\boldsymbol{H}$ is aligned close to either parallel or perpendicular to the easy-axis, R_{el} exhibits peaks and dips, respectively. The dips come from $\boldsymbol{H}$ canting $\boldsymbol{n}$ in the direction of $\boldsymbol{H}$ when perpendicular to the easy-axis, thereby reducing the projection of $\boldsymbol{n}$ on $\boldsymbol{\mu}_s$ and thus leading to a small suppression of the transport. Meanwhile when $\boldsymbol{H}$ is parallel to the easy-axis, there is a smooth rotation of $\boldsymbol{n}$ away from the EA due to the finite angle between $\boldsymbol{H}$ and the EA and the projection of $\boldsymbol{n}$ on $\boldsymbol{\mu}_s$ correspondingly increases slightly. These features are more noticeable at 5 T (blue points) than at 8 T (black points) given that the higher field leads to a larger decrease of the projection $\boldsymbol{n} \cdot \boldsymbol{\mu}_s$. A feature that appears in these two higher field rotations is the abrupt jump in R_{el} in the vicinity of the easy-axis. However, this jump does not occur perfectly at $\boldsymbol{H} \| EA$ but rather at $\sim$+15° at 5 T and $\sim$+6° at 8 T, indicating that there may be an additional anisotropy leading to $\boldsymbol{n}$ abruptly reorientating after $\boldsymbol{H}$ has passed the EA that is compensated by the increasing magnetic field. This effect is highlighted further in Fig. 7.12b which depicts the rotation through +α with $\boldsymbol{H}$ = 5 T (blue) and a rotation through -α with $\boldsymbol{H}$ = -5 T (cyan). On the assumption of a uniaxial anisotropy, these two curves should overlap each other at all angles, but clearly this does not apply in the vicinity of $\boldsymbol{H} \| EA$. This highlights the conclusion from the rotation at $\mu_0 \boldsymbol{H}$ = 2 T in Fig. 7.12a of additional contributions present

[6]This field was chosen because the maximum value of R_{el} in Fig. 7.11 occurs at 2 T.

in these films than the simple uniaxial field along the easy-axis.

The origin of this hysteresis lies in the DMI parallel to the easy-axis. The application of a magnetic field not parallel to the easy-axis creates a net moment parallel to the field and the Néel vector can be made to rotate. The DMI term then leads to a net moment within the basal plane that competes with the field induced moment. Depending on whether the magnetic field is parallel or anti-parallel to the DMI vector will then lead to different equilibrium positions of the net moment and thus the Néel vector. If one rotates under a parallel or anti-parallel magnetic field, one will then end up with a hysteresis in the recorded response that is present until the magnetic field overcomes the DMI term.[7] The energy terms of interest for determining the equilibrium positions of $\boldsymbol{n}$ can be written analytically as,

$$\text{DMI Term} : \frac{{H_c^{\parallel}}^2}{H_c^{\perp}} \sin\theta \left(H_Y \cos\phi - H_X \sin\phi\right), \tag{7.1a}$$

$$\text{Zeeman Term} : \frac{1}{2}\left(H_X^2 \cos^2\phi + H_Y^2 \sin^2\phi\right) \sin^2\theta, \tag{7.1b}$$

where ϕ and θ are the position of the Néel vector in spherical coordinates assuming X and Y are in the plane perpendicular to the easy-axis along Z. Assuming no other terms are contributing, the DMI term is proportional to the component of the field in the XY-plane whilst the Zeeman energy is proportional to the square of the same. The determination of which term dominates comes from the prefactor in Eqn.7.1a, ${H_c^{\parallel}}^2/H_c^{\perp}$. Once this is overcome, the Zeeman energy dominates and the hysteresis disappears. The real situation will be slightly more complicated with the magneto-elastic anisotropy likely playing a role as well but this provides some insight into the presence of a rotational hysteresis in uniaxial AFMs with DMI parallel to the easy-axis. This also explains the strange behaviour at low fields, where the Zeeman energy is insufficient to even induce a hysteresis.

7.3 Magnon Propagation Length in Hematite Thin Films in the Easy-Axis Phase

Having established that long distance magnon transport is not limited to a bulk antiferromagnet but is also possible in thin films of α-Fe_2O_3, the question that naturally arises is how far can these excited magnons can be transported. Considering that the spin transport at $H_c^{\parallel}$ in the (0001) films was heavily influenced by field cycling, this appears to indicate that the AFM domain structure influences the magnon transport across a finite distance. The simple model behind the spin diffusion equation for magnons derived in Ref. [161], and used in Sec. 6.5, fails to take into account the magnetic domain structure. This same assumption of a single domain was also applied in the case of the bulk hematite measurements made in Ch. 6. This is a reasonable assumption in the case of a ferromagnet where the magnon transport is measured above the saturation field and the ferromagnet shows a monodomain state. However, this criterion is unlikely to be fulfilled in an AFM thin film, even with a large applied magnetic field. For example, the repeated exposure to a field over the spin flop fails to produce a monodomain state in the metallic AFM Mn_2Au [222, 223]. Nevertheless, the domain size can be increased through careful growth optimisation of the films [r17, 222, 223, 338]. It is then reasonable

[7] Private discussion with Prof. O. Gomonay of JGU Mainz.

to expect that the AFM domain structure should play a role in determining the magnon diffusion lengths scales.

To accurately analyse the propagation lengths in thin AFMs, we can consider two contributing factors; (i) the intrinsic decay of magnons due to magnetic damping, that results in a material dependent attenuation, and is independent of the spin structure and (ii) the interaction between the magnons and the magnetic domain walls. This second contribution is motivated by theoretical interest in the action of magnons on domain walls as a method for manipulating a magnetic state for memory devices. Studies of the interaction of magnons with domain walls have predicted changes to the magnon polarisation to occur [339–341], as well as incident magnons to impart angular momentum to the domain wall [341–344]. The ferromagnetic analogue of domain wall motion being assisted by spin waves has been shown [345]. Thus, considering that there should be an action of magnons on domain walls, it is to be expected that the reciprocal process must also be present, i.e. the scattering of magnons from a pinned domain wall. This assumption has since been supported by additional theoretical works showing that, in the presence of a magnetic field, magnons are expected to scatter from a domain wall [346].

This section will briefly introduce the expectations for the impact that the AFM domain structure will have on magnon transport. This will then be compared to the experimental observation of the decay the magnon transport signal R_{el} with increasing separation between the electrodes of the non-local devices and direct observations of the AFM domain structure in the different films.

7.3.1 Theoretical Expectations of Magnon Propagation in Thin Film Antiferromagnets

As mentioned at the beginning of this chapter, theoretical calculations were performed by Prof. O. Gomonay, Dr. A. Qaiumzadeh and Dr. C. Ulloa of JGU, NTNU and Utrecht respectively. The details of the model can be found in the supporting information of Ref. [r15]. Here, an outline of the model and the ramifications of the predicted magnon scattering will be given. The propagating magnons are excited with a broad distribution of energies and wavevectors $\boldsymbol{k}$ with an upper limit set by the available thermal energy $k_B T$. There are then two contributions to their transport and dissipation. The intra-domain transport is dominated by diffusion which is governed by the intrinsic magnetic damping, whilst the interaction of the magnons with the domain walls introduces additional channels for dissipation via spin dependent scattering. Experimentally, this would be evident through an increased attenuation of the signal in the presence of a domain wall and a reduction of the magnon propagation lengths. Whilst the Néel vector rotation in a 60° domain wall, such as present for fields above $H_c^{\parallel}$ and temperatures above T_M, would lead to a scattering of the incident magnons, the interaction between magnons and 180° domain walls is less clear [347]. For the circularly polarised magnons found in the easy-axis phase of hematite, a toy model was developed to describe the scattering process at a pinned 180° domain wall with a width x_{DW}. The dynamics of the Néel vector in an AFM texture can be described within the Lagrange formalism [308, 348] which allows the derivation of an expression for the pinned domain wall in the presence of a uniaxial anisotropy. Magnons can then be considered as a perturbation to the static Néel texture and the domain wall leads to a reflection of the incident magnons with a reflection

coefficient given by,

$$\mathcal{R} = \frac{4\left(E_{pin}/E_{DW}\right)^2}{4\left(E_{pin}/E_{DW}\right)^2 + \boldsymbol{k}^2 x_{DW}^2}, \tag{7.2}$$

where E_{pin} and E_{DW} are respectively the pinning and domain wall energies. If the wavevector $\boldsymbol{k} \leq \boldsymbol{k}_{crit}$, significant reflection then occurs, where the upper limit is given by,

$$\boldsymbol{k}_{crit} = \frac{4E_{pin}}{E_{DW}} \frac{1}{x_{DW}}, \tag{7.3}$$

in other words a ratio of the pinning and domain wall energies. Eqn. 7.2 is valid for $\boldsymbol{H} < H_{sf}$, the spin flop field, even though it was derived under the assumption of no applied magnetic field. The energy of the domain wall is, however, modified by the magnetic field as $E_{DW} \Rightarrow E_{DW}\sqrt{1 - H^2/H_{sf}^2}$ and the reflection of magnons from the domain wall increases substantially in the vicinity of the spin flop as $\boldsymbol{k}_{crit} \gg 1/x_{DW}$. The scattering of magnons from the pinned domain wall is then significant up to this critical value of the wave vector $\boldsymbol{k}_{crit}$, which is proportional to the pinning field obtained from the experimental data. Thus, for a large pinning, all types of antiferromagnetic magnons are expected to scatter from domain walls and the magnon propagation length scale would then be dominated by the domain size and the distance between successive domain walls.

The additional dissipation mechanism of the domain wall scattering can be included by a set of diffusion equations,

$$D_k \Delta \rho_k - \frac{1}{\tau}\rho_k = 0, \tag{7.4}$$

where the diffusion coefficients D_k depend on the magnon wavenumber $\boldsymbol{k}$, ρ_k is the number of magnons with a given wavenumber per unit volume and τ is the relaxation time which can be considered as independent of $\boldsymbol{k}$. The domain walls are effectively transparent for magnons with a wavevector $\boldsymbol{k} > \boldsymbol{k}_{crit}$ and the diffusion coefficient for these magnons correspondingly is equivalent to that of a single domain sample $D_k = D_0$. If $\boldsymbol{k} < \boldsymbol{k}_{crit}$ then the scattering from the domain walls will greatly reduce the effective diffusion length. For simplicity, all magnons that satisfy this condition can be assumed to have the same diffusion constant $D_k \sim D_1$. With this simple assumption in place, the measured non-local resistance at a distance x is then proportional to the total magnon flux,

$$\begin{aligned} R_{el}(x) &\propto \sum_k \rho_k'(x) \\ &\simeq \rho_0 \left(\frac{f}{\lambda_1} \exp\left(-\frac{x}{\lambda_1}\right) + \frac{1-f}{\lambda_0} \exp\left(-\frac{x}{\lambda_0}\right) \right), \end{aligned} \tag{7.5}$$

where ρ_0 is the total number of magnons excited due to $\boldsymbol{\mu}_s$ below the injector, f is the fraction of the magnons satisfying the condition $\boldsymbol{k} < \boldsymbol{k}_{crit}$ and $\lambda_{0,1} = \sqrt{D_{0,1}\tau}$ is the diffusion lengths for the magnons with either $\boldsymbol{k} < \boldsymbol{k}_{crit}$ or $\boldsymbol{k} > \boldsymbol{k}_{crit}$. In samples with large domains, the magnon transport should be dominated by the intrinsic material dependent diffusion properties and Eqn. 7.5 relies only on λ_1. In other words, the simple 1D spin diffusion model of Ref. [161] that results in Eqn. 6.4 can be applied. However, in samples with multiple domains, these additional dissipation mechanisms open and Eqn. 7.5

is required. The intrinsic length scale in hematite can reasonably be expected to be large given the transport length scales discussed in Ch. 6 as well as measurements demonstrating an ultra-low magnetic damping [r13]. Such a low magnetic damping should lead to low attenuation of the propagating magnon current and the magnetic damping in thin films can also be considered to be low, albeit not as low as in a bulk crystal [336].

7.3.2 Antiferromagnetic Domain Structure of Thin Film Hematite

In order to establish whether the magnetic domain structure, and thus a spin structure dependent propagation length, is indeed contributing to the magnon diffusion, we need to determine the AFM domain structure of the films under investigation. It would be expected that diffusion lengths would be larger in samples with larger domains. XMLD-PEEM imaging (c.f. Sec. 4.2.6) at the Fe L_2 edge was performed at the BESSY II beamline in Berlin on (0001), 100 nm and $(1\bar{1}02)$, 500 nm hematite films identical to those used for the transport measurements, capped by 2 nm Pt to prevent charging.

First, the domain structure of the $(1\bar{1}02)$ plane films below T_M will be shown since the zero field magnetic structure is easy to access with this technique. This then replicates the domain structure encountered by the magnonic current in the transport measurements of Sec. 7.2.2. As shown in Fig. 7.13, large single domain areas separated by clear 180° domain walls are easily observed indicating that a flowing magnon current will encounter few domain walls on the length scales probed in the transport measurements. The in-plane component of the Néel vector, (Fig. 7.13b) and the out-of-plane component (Fig. 7.13a) show no correlation, indicating that the Néel vector rotates out-of-plane between neighbouring domains. A feature of interest in these images occurs in the upper

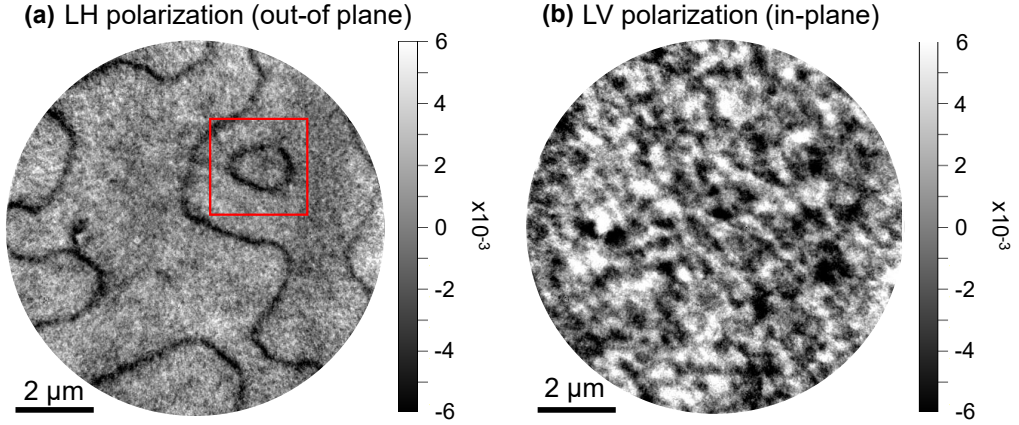

Figure 7.13: XMLD-PEEM images of $(1\bar{1}02)$ orientated hematite thin films capped by 2 nm Pt at 100 K. The incident x-rays have either a) a linear horizontal polarization or b) a linear vertical polarization. The clear, dark domain walls for a) and the absence of contrast for the domain walls in b) indicate that the Néel vector rotates out of the plane between neighbouring domains. The red box indicates a closed domain wall with a central core that may be an *antiferromagnetic anti-skyrmion* but further studies are required. Figures adapted from Ref. [r14]. Copyright American Physical Society.

right quadrant of Fig. 7.13a, a closed domain wall with a central core and shown in more detail in Fig. 7.14. This is reminiscent of an *antiferromagnetic anti-skyrmion* and is an interesting feature for the wider spintronics community and merits further research into similar domain structures in α-Fe_2O_3 films.

Although 60° [349] and 90° [350] AFM domain walls have been observed by XMLD-

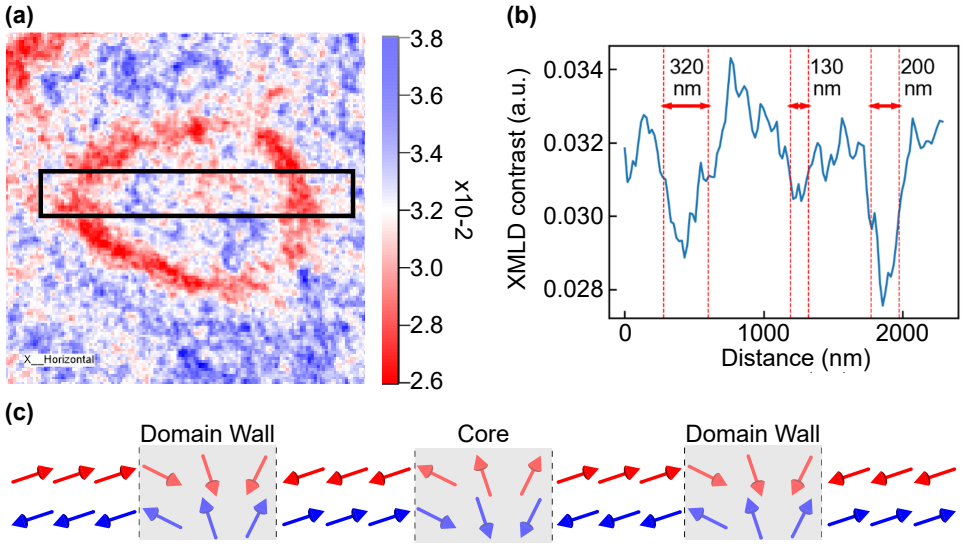

Figure 7.14: a) Zoom in of the red highlighted area in Fig. 7.13a. The black box indicates a line scan, the intensity of which is shown in b) showing two domain walls and a central core. c) Schematic of how the antiferromagnetic structure rotates through the spin structure. Figures adapted from Ref. [r14]. Copyright American Physical Society.

PEEM previously, this is, to the author's knowledge, the first direct observation of a 180° domain wall in an antiferromagnet. 180° domains have been inferred from other measurements [319, 351], but explicit imaging of such a domain wall by XMLD-PEEM has so far not been reported. Given the inclined nature of the easy-axis, the broad transition visible in Fig. 7.13 does not represent the true width of the domain wall but rather the projection of out-of-plane component of $\boldsymbol{n}$ that is imaged by the polarised x-rays convoluted with the imaging optics. The true width is then ∼84% of the observed width (a factor of $\cos 33°$).

Although the domain structure of the $(1\bar{1}02)$ films at zero-field can be imaged directly, the domain structure in the (0001) films at either $H_c^{\parallel}$ or $H_c^{\perp}$ cannot be imaged in this manner due to the need for high magnetic fields that cannot be applied during PEEM imaging. This is a fundamental limitation due to the detection mechanism of XMLD-PEEM relying on electron emission, where the magnetic field interferes with the emitted electrons due to the Lorentz force. Although XMLD itself can be carried out in high magnetic fields,[8] XMLD-PEEM is limited to fields of a few mT. However, we can make use of the temperature-field equivalence of the Morin transition [29] to gain a qualitative insight into the domain structure at the spin flop. Above T_M, the magnetic state is that of an easy-plane AFM, with a small in-plane canting in the absence of a magnetic field. Meanwhile, below T_M and above $H_c^{\parallel}$ in the spin flop state, the magnetic configuration is also that of a canted easy-plane AFM. Given this equivalence, a qualitative understanding of the AFM domain structure of the (0001) films at $H_c^{\parallel}$ can be gained through temperature dependent XMLD-PEEM measurements in the absence of a magnetic field (Fig. 7.15). A multidomain pattern is observed in these (0001) films at 300 K, shown in Fig. 7.15c. The contrast indicates a differing in-plane orientation of $\boldsymbol{n}$ relative to the incoming x-rays, where regions of similar contrast indicate regions where $\boldsymbol{n}$ is (anti-)parallel. The strong

[8] An example of high field XMLD is the XTREME beamline of PSI which allows for 7 T along the beam direction

contrast indicates that there are multiple orientations of $\boldsymbol{n}$ above T_M and by extension at $H_c^{\parallel}$, as expected from the in-plane degeneracy observed in bulk hematite [29] (Sec. 4.1). These easy-plane domains with dimensions of a few hundred nanometres are then separated by 60° rotations of $\boldsymbol{n}$ given the threefold crystalline anisotropy of hematite. As the temperature is lowered, the spin structure changes strongly across the Morin transition to the easy-axis state where surprisingly, contrast is still visible (Fig. 7.15a). The ex-

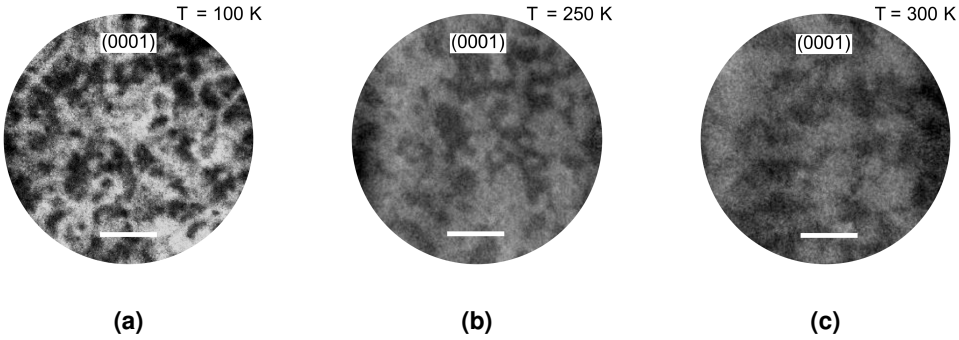

Figure 7.15: Antiferromagnetic domain structure of 100 nm (0001) orientated hematite capped by 2 nm Pt, imaged by XMLD-PEEM at a) 100 K, b) 250 K, and c) 300 K. The scale bar (white) represents 2 µm in each case. Adapted with permission from Ref. [r15]. Copyright 2020 American Chemical Society.

pected 180° domain walls of the easy-axis phase should lead to no visible contrast due to the identical dichroic contrast of the neighbouring domains as seen previously in Fig. 7.13. The origin of the observed contrast can be attributed to the distribution of growth crystallites that was evident in the rocking curve of the hematite films (see Sec. 5.2.1). However, the presence of 180° domains walls can be inferred from the clearer observation in the $(1\bar{1}02)$ films. Thus as expected, the transition from the easy-axis phase to the easy-plane phase that occurs at $H_c^{\parallel}$ leads to a transition from 180° to 60° domain walls.

Despite using the field-temperature equivalence to infer information at $H_c^{\parallel}$, there is no equivalent transition for the domain structure at $H_c^{\perp}$. However, some assumptions can be made based on energetic arguments. Given that at $H_c^{\perp}$, $\boldsymbol{n}$ reorientates to lie perpendicular to both $\boldsymbol{H}$ and the EA, it is reasonable to say that the domains would be similarly sized to those at $H_c^{\parallel}$, but lacking the degeneracy. This is supported by the lack of a hysteretic behaviour for a field applied perpendicular to the easy-axis in the transport measurements on the (0001) films (Fig. 7.5a). The character of the domain wall would then be a 180° rotation of $\boldsymbol{n}$ rather than 60°.

7.3.3 Fitting the Distance Dependence

Having established a model to describe the influence of the magnetic domain structure on the magnon transport and directly imaged the domain structure encountered by a magnon current across a finite distance, attention can now be turned to understanding the evolution of R_{el} for the different hematite orientations and geometries as the distance between the wires is increased. The centre-to-centre separation of the non-local devices was varied from 425 nm to over 5 µm on both the (0001) and $(1\bar{1}02)$ hematite films. The measured values of R_{el} at 175 K for the two films are shown in Fig. 7.16 for the available distances where a significant signal was recorded. R_{el} at $H_c^{\perp}$ (blue) (Sec. 7.1.4) and $H_c^{\parallel}$ (magenta) (Sec. 7.1.1) for an increasing magnetic field are chosen for the

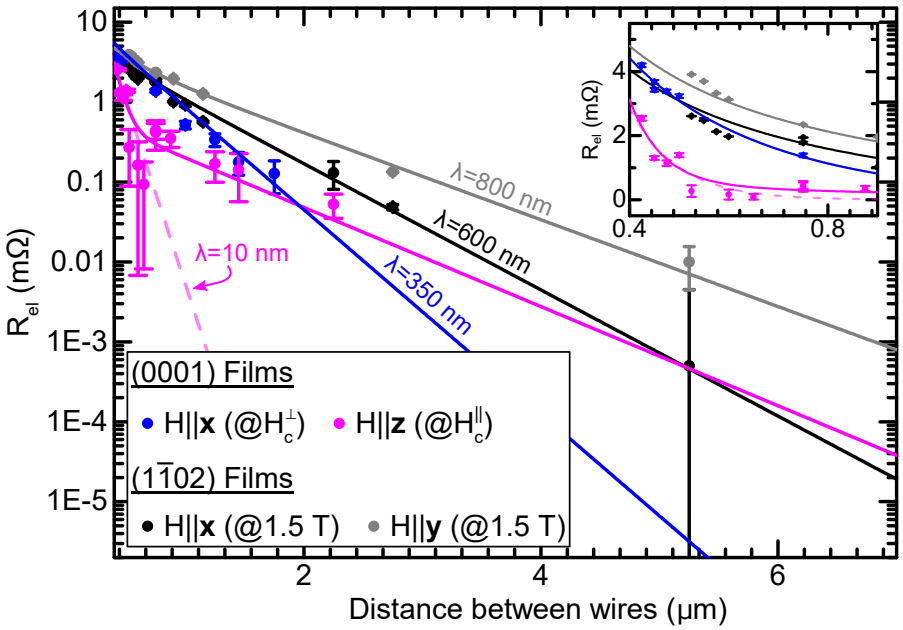

Figure 7.16: Distance dependence of maximum magnon transport in thin films of hematite oriented as (0001) and (1$\bar{1}$02) for different field geometries. The thick lines represent fits to the experimental data and the error bars show the standard deviation of the data points. Fit lines indicate either the 1D spin diffusion equation of Eqn. 6.4 (black, grey, blue and dash magenta) or a fit to Eqn. 7.5 (solid magenta). Adapted with permission from Ref. [r15]. Copyright 2020 American Chemical Society.

(0001) orientated films. For the (1$\bar{1}$02) plane films, R_{el} at $\mu_0 \boldsymbol{H} = 1.5$ T was taken for the geometry discussed in Sec. 7.2.2 where the wires are perpendicular to the easy-axis. A finite field is chosen for these (1$\bar{1}$02) plane films rather than taking the signal at zero field because the application of a magnetic field breaks the symmetry of the interface, reduces interfacial pinning and prompts the initiation of the smooth rotation of $\boldsymbol{n}$.

As can be seen from the data presented in Fig. 7.16, a significant value of R_{el} persists over several micrometres, however it falls far short of the transport visible over tens of micrometres in Sec. 6.5. The exponential decrease of signal with distance alongside the measurement temperature of 175 K again indicates a dominating diffusive transport rather than spin superfluid regime as concluded in Sec. 6.5. First, a one dimensional spin relaxation equation (Eqn. 6.4) is applied in order to extract the spin diffusion length of the flowing magnonic spin current for the different geometries [161]. This equation fits the data in Fig. 7.16 for the decay of the magnon transport in the (1$\bar{1}$02) films for both a magnetic field parallel (black points) and perpendicular (grey points) to the easy-axis. The spin diffusion lengths for these films and $\boldsymbol{H} \| \boldsymbol{x}$ and $\boldsymbol{H} \| \boldsymbol{y}$ can then be estimated as $\lambda_{r,\boldsymbol{x}} = 600$ nm (represented by the black line) and $\lambda_{r,\boldsymbol{y}} = 800$ nm (represented by the grey line) respectively. These values of the spin diffusion length are smaller than the domain sizes observed in these films (Fig. 7.13) and it is then expected that the intrinsic intra-domain diffusion dominates over possible domain wall scattering and Eqn. 6.4 remains valid. These values are then representative of the intrinsic spin diffusion lengths of hematite films and remain orders of magnitude larger than evaluated spin diffusion lengths reported for other thin film antiferromagnets (see examples provided previously in Tab. 3.2 in Ch. 3).

The measured value of R_{el} in the (0001) orientated films at the DMI induced spin reorientation at $H_c^{\perp}$ (Sec. 7.1.4) also matches the 1D spin diffusion equation with a spin diffusion length of $\lambda_{c,DMI}^{\perp}$ = 350 nm, as indicated by the blue line. However, this simple picture fails for the spin transport at $H_c^{\parallel}$ and the fitting by such a simple model does not accurately describe the observed behaviour, resulting in a spin diffusion length of $\lambda \sim$10 nm as indicated in Fig. 7.16 by the translucent dashed magenta line. This evaluated spin diffusion length which ignores the domain structure is very comparable with the maximum spin diffusion lengths evaluated in previous reports, e.g. [188, 198]. More appropriately, this dataset can be fit by Eqn. 7.5, as derived above, to take into account the more complicated domain structure alongside the previously mentioned adaptation of the domain wall energy when approaching the spin flop field $H_c^{\parallel}$. Making use of this equation yields λ_0 = 67 nm and λ_1 = 700 nm for R_{el} at $H_c^{\parallel}$ in the (0001) films. Thus, magnons with a high wavenumber, i.e. the high frequency magnons that one would hope to utilise for logic operations in antiferromagnetic spintronic devices, diffuse with characteristic length scales of the same order of magnitude as the other geometries discussed for the thin films here. Meanwhile, the lower frequency magnons diffuse with a secondary length scale (λ_0) that is qualitatively governed by the domain structure and the distances between domain walls and thus scattering sites.

A summary of the different transport lengths, alongside the domain sizes extracted from the XMLD-PEEM images in Fig. 7.13 and Fig. 7.15, is given in Tab 7.1. Fig. 7.17 details example profiles of the intensities extracted from the earlier PEEM images. The domain walls and domains are indicated for the two crystal orientations. The domain wall widths were defined by the point where the intensity reached 25% and 75% of the difference between domains for the (0001) orientated films in the easy-plane phase and at 25% intensity for the $(1\bar{1}02)$ plane films. One can notice from this figure and table that the scattering length dominates the magnon decay only when the average size of the antiferromagnetic domain walls is smaller that the intrinsic diffusion length of the magnons. The domain structure in antiferromagnets thus acts as a spin filter on

Film Orientation	Domain Size (nm)	Domain Wall Width (nm)	λ_0, λ_1 (nm)
$(1\bar{1}02)$	2230±930	147±23	700±100, $\gg \lambda_0$
(0001) ($T > T_M$)	485±225	79±32	67±10, 700±50
(0001) ($T < T_M$)	460±205	105±25	350±30, $\gg \lambda_0$

Table 7.1: Comparison of evaluated spin transport lengths and domain sizes in hematite thin films of two orientations used for transport measurements. For (0001) orientated hematite, there is information on the easy-plane phase ($T > T_M$, $\boldsymbol{H} > H_c^{\parallel}$) and the easy-axis phase ($T < T_M$, $\boldsymbol{H} < H_c^{\perp}$). The error bars, represent the standard deviation of the average sizes. However, they are limited by the lack of statistics arising from the size of the XMLD-PEEM images. Data published in Ref. [r15].

the propagating magnonic current. The small domains frequently observed in thin film antiferromagnets therefore hinder the transport of spin information across a long distance if the magnons being transported are lower in frequency. This then helps to explain the short spin diffusion lengths presented earlier in Tab. 3.2. In those experiments, the

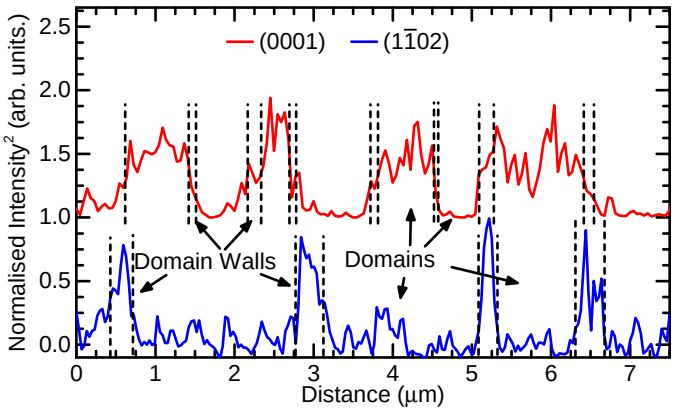

Figure 7.17: Intensity profiles of XMLD-PEEM images of (0001) and (1$\bar{1}$02) plane hematite films. The (0001) intensity profile is from the easy-plane phase whilst the (1$\bar{1}$02) was taken in the easy-axis phase. Adapted with permission from Ref. [r15]. Copyright 2020 American Chemical Society.

spin current was produced either monochromatically via FMR on a FM layer [97, 188, 194–196, 198] or a broadband excitation via SMR [r8, 193, 352] or SSE [r2, 164, 190] but again was dominated by lower frequency excitations of the FM layer. These lower frequency magnons would then scatter at the domain walls of the AFM layer and this would lead to an evaluated spin diffusion length for the AFM of a comparable size to the AFM domains.

7.3.4 Conclusion

In Ch. 6, the conditions for efficient magnon transport in antiferromagnets were revealed in a bulk crystal of α-Fe_2O_3. Through a parallel alignment of an interfacial spin-bias $\boldsymbol{\mu}_s$ and the antiferromagnetic Néel vector $\boldsymbol{n}$, magnon transport was found to be possible across micrometres. In the pursuit of device applications, this section has built on the methods developed in Ch. 6 to demonstrate efficient transport of a magnon current in thin film hematite. The magnon efficiency has been shown to not only depend on the applied magnetic field, but also the crystalline orientation, relative orientation of $\boldsymbol{n}$ and the AFM domain structure. With intrinsic diffusion lengths of hundreds of nanometers, hematite has proved capable of efficient long distance magnon transport even in the thin film regime. However, as demonstrated, the presence of a multi domain magnetic state proves to be detrimental to the passage of a magnon current. In order to functionalise thin AFMs for magnonic devices, large, single domain samples are required. This work has been performed at a point in time where most reports on thin film hematite focus on growth with the aim of photovoltaic cells rather than spintronic aims. Hopefully, with the demonstration shown here, future work can be made to optimise the growth and promote higher values of T_M, through doping or strain engineering, and larger domains such as by making use of single domain γ-Fe_2O_3 underlayers [311]. Previously, such a focus on the growth of the garnet YIG has led to ever increasing records for the lowest magnetic damping observed with consistently high film quality being achieved in numerous research groups across the scientific community, something that is currently absent for hematite and other antiferromagnetic insulating compounds.

It is also worth commenting here that at the time of writing, the transport of spin

across large distances was reported in films of hematite that do not show a Morin transition and thus remain in the easy-plane phase [327, 329]. Whilst this does not invalidate the need for studies pursuing higher quality growth, it does mean that the presence of a Morin transition is not required for antiferromagnetic magnonics. The transport in the easy-plane phase is dictated by different spin dynamics to the easy-axis phase, where a superposition of the linearly polarised modes [r13, 327] or mode coupling [329] has been suggested for allowing the transfer of spin angular momentum. The length scales involved then include the coherence and dephasing lengths of the involved magnon modes, offering further routes for improving the efficiency of magnon transport.

7.4 Temperature Dependence of Magnon Transport in Thin Film Hematite

The magnon transport in the previous section was investigated at 175 K, $\sim$25 K below T_M for both film orientations discussed. This section will cover the behaviour of the magnon transport for (0001) orientated hematite films with decreasing temperature below the Morin transition for a magnetic field parallel to both $\boldsymbol{x}$ and to $\boldsymbol{z}$. Given that the value of $H_c^{\parallel}$ in the (1$\bar{1}$02) plane films is too large to reach below T_M (see Sec. 7.2.1 and Fig. 7.10c), further investigation of the temperature dependence is not warranted. Meanwhile, the zero field transport for this orientation will represent just a measure of the magnon population at any given temperature so this is also not as interesting as for the (0001) orientated films.

With decreasing temperature, the available energy for thermal magnons will decrease, and thus the frequency of the available magnon modes that can be populated will decrease. Alongside this, the magnon propagation length has been shown to increase with decreasing temperature [180, 353]. This increase of the magnon population length comes from increasing contributions of lower energy magnons [180, 325, 334], however Sec. 7.3 showed that the lower energy magnons in AFMs can be hindered by the presence of domain walls (quantified by Eqn. 7.5). Depending on the direction of the applied field, the frequencies of the magnon modes that propagate can then be tuned. Based on the information learned in the previous section, the following expectations can be stated. Given that for $\boldsymbol{H}\|\boldsymbol{x}$, the behaviour is reminiscent of diffusive transport with no impact of the domain structure, the temperature dependence of the maximum value of R_{el} below T_M should follow the decrease of total magnon population as in a ferromagnet [216]. Alongside this decrease of R_{el} due to the reduced thermal magnon population, the value of $H_c^{\perp}$ should increase with decreasing temperature [r10, 239, 241]. In ferromagnetic YIG, larger magnetic fields introduce additional dissipation channels for the propagating magnons [333] so the increase of $H_c^{\perp}$ at low temperatures may similarly suppress the magnon transport on top of the decrease of R_{el} with temperature. With higher temperatures than shown previously, as the film goes through the transition to the easy-plane, one would reasonably expect the transport to decrease as the easy-axis phase disappears. Meanwhile, for $\boldsymbol{H}\|\boldsymbol{z}$, the decrease of the "upper" limit of available thermal magnons will be far more noticeable as the low frequency magnons that play a role at lower temperatures are unavailable due to scattering at domain walls. The reduction for a fixed distance would then be far quicker than for $\boldsymbol{H}\|\boldsymbol{x}$.

7.4.1 Temperature Dependence of Magnon Transport in (0001) Orientated Hematite Films Below the Morin Transition

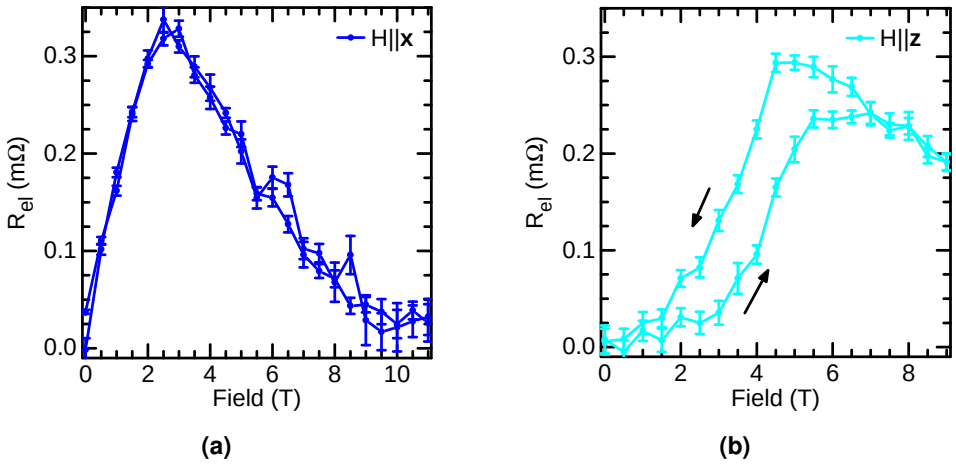

Figure 7.18: R_{el} for (0001) orientated hematite at 100 K for a magnetic field parallel to a) $\boldsymbol{x}$ with a centre-to-centre separation of 650 nm, as in Fig. 7.5a. b) R_{el} for a field parallel to $\boldsymbol{z}$. This device has a smaller centre-to-centre separation than that shown previously as no signal was resolvable on the previous device. Adapted with permission from Ref. [r15]. Copyright 2020 American Chemical Society.

The magnetic field dependence of R_{el} is shown in Fig. 7.18 for an environment temperature of 100 K. Looking first at a magnetic field applied perpendicular to the easy-axis and parallel to the device geometry, i.e. $\boldsymbol{H}\|\boldsymbol{x}$ (Fig. 7.18a), the same basic characteristics as seen at 175 K occur; starting from no observable transport in the absence of a magnetic field, R_{el} increases up to a maximum at $H_c^{\perp}$ before decreasing at higher magnetic fields. When $\boldsymbol{H}$ is lowered back to zero, R_{el} demonstrates no hysteresis. This behaviour confirms the observations made just below T_M sec. 7.1.4, whilst the increased value of $H_c^{\perp}$ (from 2.6 T to 3 T) and the reduction of R_{el} from 2.4 mΩ to 0.32 mΩ is in line with the expectations made at the beginning of this section related to the decreasing magnon population. However, the increase of $H_c^{\perp}$ is smaller than that seen from comparable temperatures in the local measurements of the previous chapter (see Fig. 5.31) on similar films where the value of $H_c^{\perp}$ at 100 K is in the region of 8 T. This indicates that the local measurements of the magnetic state, which are probing only length scales on the order of the exchange length across the interface between the electrons of the Pt and the hematite, may represent a different configuration to the non-local measurements [r16, 165, 303]. Given that the SMR is giving a good representation of the magnetic state in the bulk, as demonstrated in Ch. 5, this difference may be related to something outside the orientation of $\boldsymbol{n}$ and possibly hints that the individual available magnon modes and the magnon gap may be significant. However, a dedicated study comparing these measurements is needed to investigate this difference.

Although a measurable value of R_{el} was present for the same device at both 175 K and 100 K when $\boldsymbol{H}$ was applied along $\boldsymbol{x}$, the same cannot be said for $\boldsymbol{H}$ along the easy-axis (i.e. along $\boldsymbol{z}$). Fig. 7.18b shows R_{el} for this field orientation, but on a device with a smaller centre-to-centre separation of the electrodes than the exemplary curves of Fig. 7.2. This initial observation follows the above discussion whereby the decreasing magnon population will be more evident for this field orientation. Despite this, just as for $\boldsymbol{H}\|\boldsymbol{x}$, the qualitative similarities between R_{el} at 100 K and 175 K indicate that the

transport is dominated by the same mechanism at both temperatures.

The temperature dependence of R_{el} for $\boldsymbol{H}\|\boldsymbol{x}$ and $\boldsymbol{H}\|\boldsymbol{z}$ is shown in Fig. 7.19 for a single device. Each point is taken to be the value of R_{el} at $H_c^{\perp}$ or $H_c^{\parallel}$, and thus represents R_{el} at different applied magnetic fields. Despite the difference in the magnetic field magnitude, the magnetic states with respect to the Néel vector orientation are similar as well as having a similar sized magnon gap. As expected, R_{el} increases with increasing temperature, up to a point just below were the Morin transition begins ($\sim$200 K), after which it then falls. The shaded part of Fig. 7.19 indicates the temperature range where the Morin transition takes place and a purely easy-axis phase cannot be expected. The decrease of R_{el} then at $T = 225$ K stems from the mixture of phases between the easy-axis and easy-plane phases. The fit lines of Fig. 7.19 represent exponential decays of R_{el} with decreasing temperature, motivated by the decrease in the magnon population with temperature. The value of R_{el} falls faster for $\boldsymbol{H}\|\boldsymbol{z}$ than for $\boldsymbol{H}\|\boldsymbol{x}$. This is not surprising given that this signal is far more sensitive to the domain structure, as already mentioned above.

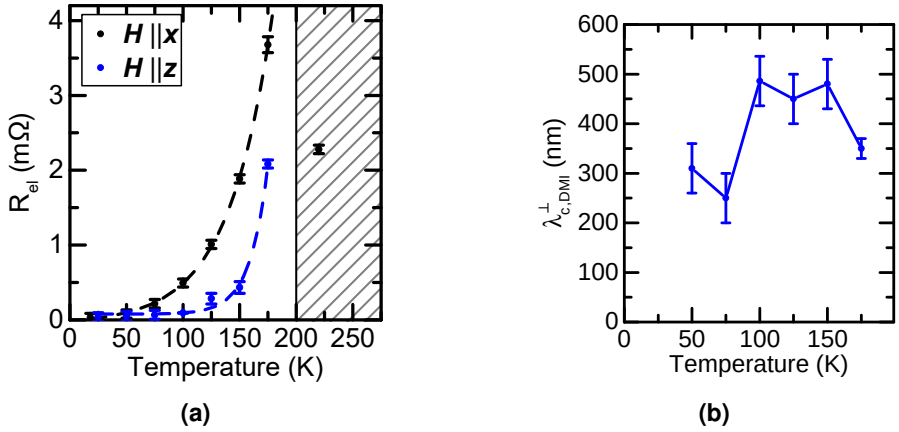

Figure 7.19: a) R_{el} for a magnetic field applied along $\boldsymbol{x}$ for (0001) orientated hematite thin films as a function of temperature. The solid line represents an exponential fit to the data and the Morin transition region is indicated by the shading. b) Temperature dependence of the spin diffusion length for a magnetic field applied along $\boldsymbol{x}$, parallel to the non-local device. There are insufficient data points at $T <$25 K to allow for a fit to the 1D spin diffusion equation.

Extracting the spin transport length scales at $H_c^{\parallel}$ is difficult due to the rapid drop in the signal intensity at lower temperatures, resulting in too few data points to enable a fit with Eqn. 7.5. However, R_{el} at $H_c^{\parallel}$ can be sufficiently recorded as a function of distance down to 50 K, from which values of $\lambda_{c,DMI}$ can be evaluated. Initially, with decreasing temperature, the spin diffusion length increases slightly from 350$\pm$19 nm up to a maximum of 489$\pm$58 nm at around 100 K. Below this temperature, there is then a sharp decrease in the evaluated spin diffusion length. This is likely due to the reduction of the thermal magnon populations. The decreasing temperature will lead to a decreasing magnon population. There should then be less magnon-magnon scattering and a larger transport length scale [r13]. However the available magnon modes at lower temperatures will have a lower maximum frequency and thus should be subject to increased scattering from domain walls as discussed in Sec. 7.3.1. Additionally, the distance to which a reliable value of R_{el} can be extracted reduces which means that the value of $\lambda_{c,DMI}$ becomes less defined without the distances being far larger than the diffusion length.

The values extracted for $\lambda_{c,DMI}$ below 100 K should then be approached with caution.

7.4.2 Magnon Transport in (0001) Plane Hematite Thin Films Above the Morin Transition

The temperature range in the previous section and shown in Fig. 7.19 covered temperatures up to the Morin temperature at ∼200 K. Data points above 225 K were not shown in Fig. 7.19 as the insulating nature of the films changes and the conductivity increases. This then leads to a large leakage current as the temperature moves through the Morin transition, where the zero field offset changes from the noise of the system in the nanovolt regime to several microvolts (Fig. 7.20a and Fig. 7.20b). It then becomes increasingly harder to ascertain what constitutes magnon transport and what is purely charge transport through the surface layers of the hematite films. Fig. 7.20 presents measurements performed at 290 K for a magnetic field along a single direction, as well as for a magnetic field rotated in the xz-plane. As immediately obvious, the value of R_{el}

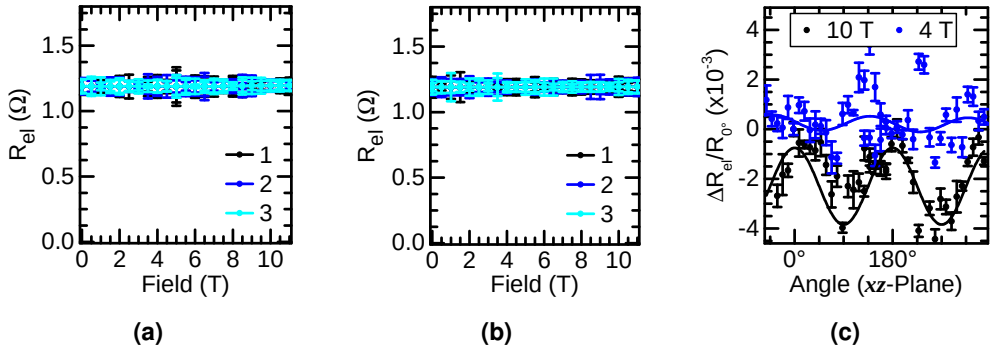

Figure 7.20: R_{el} for (0001) orientated hematite at 290 K for a) a magnetic field parallel to $\boldsymbol{x}$ and b) for a field parallel to $\boldsymbol{z}$. A large offset of $\sim 1\,\Omega$ is present due an increase of the film conductivity above T_M. c) R_{el} for a magnetic field rotated in the xz-plane. Given the easy-plane nature of these films, this plane represents a magnetic field rotating from within the easy-plane to perpendicular to it. Multiple field cycles are shown for the uniaxial curves. Adapted with permission from Ref. [r15]. Copyright 2020 American Chemical Society.

is three orders of magnitude larger than in the easy-axis phase (Fig. 7.19a), representing not so much the *non-local* resistance but rather the actual electrical resistance of the hematite film which is not sufficiently large to allow for the investigation of pure magnon transport. Fig. 7.21 shows the same data but with the value of R_{el} at 0 T subtracted as a constant offset for the magnetic field applied along the two directions. For a magnetic field within the easy-plane, Fig. 7.21a, there is no noticeable change in the measured value of R_{el} from zero field to around $\mu_0 \boldsymbol{H} \sim 8$ T, whereupon an increase occurs. From local magnetoresistance measurements (Sec. 5.2.2 and Ref. [r14]), the orientation of $\boldsymbol{n}$ within the easy-plane occurs at a magnetic field of ∼2 T at this temperature, however there is no evidence of this alignment in the non-local signal. This immediately makes sense because here is an easy-plane AFM and the linear polarisation of the magnon modes should prohibit the transport of angular momentum, although recent measurements have shown a superposition of magnons can lead to significant magnon transport [r13, r16, 327, 329]. However, this should obviously lead to no transport across the entire field range investigated. Given the large offset in the raw data of this signal, it is not immediately clear if this signal is at all related to magnon transport rather than, for example, a Hall effect in the hematite itself [354, 355]. On the assumption that this is in-

deed magnon transport, one would need to establish a reasonable explanation for it that would be consistent also with R_{el} for $\boldsymbol{H}\|\boldsymbol{z}$ (Fig. 7.21b) where it appears that there is a constantly increasing signal with field. This is currently outside of the scope of the work performed in this thesis and warrants further, dedicated investigations of this transport regime, such as was performed in Ref. [327] during the writing of this thesis. It could be related to spin canting leading to a finite transfer of angular momentum via high energy magnons [88], or a less exotic explanation involving the anomalous Hall effect due to the surface magnetism could also be put forward [303]. In order to investigate the magnon

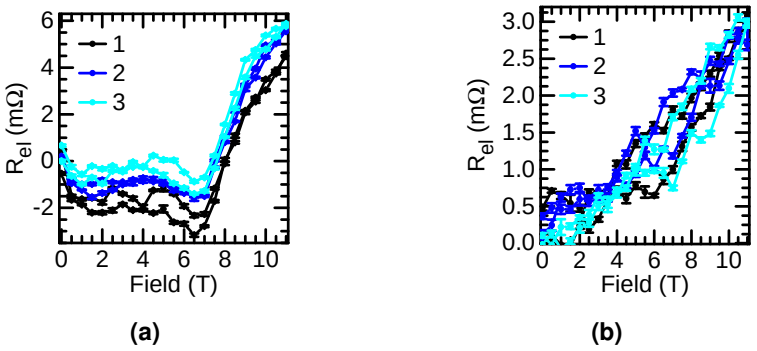

Figure 7.21: R_{el} for (0001) orientated hematite at 290 K for a magnetic field parallel to a) $\boldsymbol{x}$ and b) for a field parallel to $\boldsymbol{z}$. The large offset seen in Fig. 7.20 has been subtracted. Multiple field cycles are shown.

transport in the higher temperature regime, films that retain their insulating properties in the temperature regime of interest are required, however here it is only the easy-axis phase that is of interest for the present discussion.

7.4.3 Magnon Transport in Bulk Hematite in the Weak Ferromagnetic Phase

As mentioned briefly previously (Sec. 6.3.1), recent experimental evidence has been provided for magnon transport in the easy-plane phase of hematite [r13, 327, 329]. Whilst Ref. [327] focusses on thin films of hematite, as discussed in the previous section, the thin films used in the course of this thesis become slightly conductive above the Morin transition temperature (c.f. Sec. 7.4). Ref. [r13] meanwhile focusses on a bulk crystal of hematite, as discussed in Ch. 6. This crystal is orientated as $(1\bar{1}02)$ with a non-local geometry aligned parallel to the in-plane component of the easy-axis. This geometry is shown in Fig. 7.22. The non-local voltage V_{el} for a magnetic field applied parallel to the non-local structure is shown in Fig. 7.23a. As expected from measurements of the critical magnetic field $H_c^{\parallel}$ [r10] (c.f. Sec. 5.1.7) the peak in the magnon transport moves to higher magnetic fields with decreasing temperature. This indicates that behaviour discussed in Sec. 7.4 (Fig. 7.18) may have additional contributions. The maximum value for V_{el} taken at $H_c^{\parallel}$ as a function of temperature is shown in Fig. 7.23b. With decreasing temperature the spin-bias signal decreases, with a maximum occurring at 200 K. The absence of detectable signal below 75 K indicates a diffusive transport process dominated by thermal magnons and no dominating spin superfluidity From 200 K until the Morin transition temperature, there is a slight decrease of R_{el} that can be attributed to increases of fluctuations of the Néel vector in the vicinity of the Morin transition. However, surprisingly, V_{el} is continuous across the Morin transition, decreasing with increasing temperature. This is counter to the statements made before

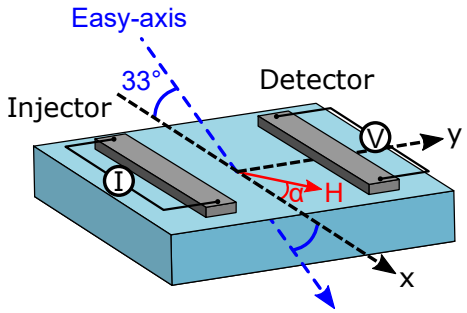

Figure 7.22: Coordinate system for r-plane hematite films and a non-local geometry parallel to the in-plane component of the easy-axis.

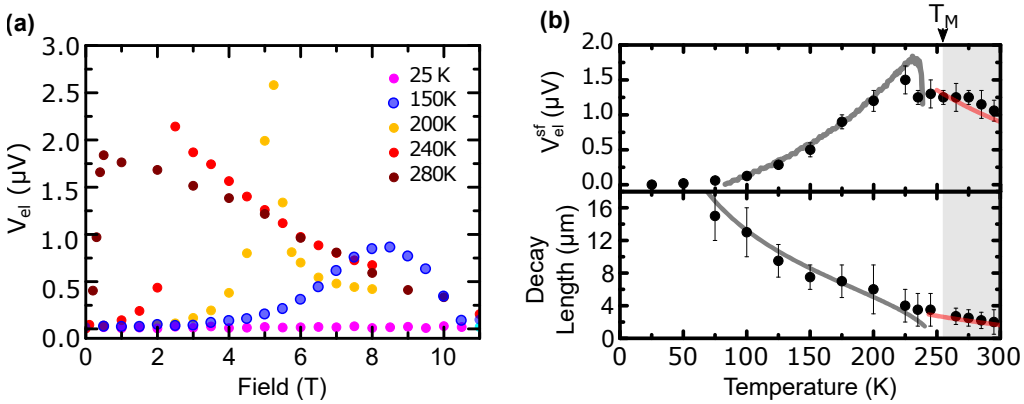

Figure 7.23: a) Temperature dependence of R_{el} for a magnetic field applied parallel to the in-plane projection of the easy-axis in bulk hematite. b) Top: V_{el} measured at the spin flop (sf) field. The signal and approaches zero at low temperature, indicating a diffusive regime. Bottom: Spin-diffusion length as a function of temperature at the spin flop field. (Gray and red lines respectively correspond to fits with a magnon transport in the easy-axis phase and on pairs of linearly polarized spin-waves in the easy-plane phase. For modelling, the exchange field $H_E = 1040\,\mathrm{T}$, $H_D = 2.72\,\mathrm{T}$ and $H_\perp = 24\,\mu\mathrm{T}$ [r10]. Figures adapted from Ref. [r13].

concerning how easy-axis antiferromagnets are required to transport angular momentum given the need for circularly polarised magnon modes [42, 88]. Below the critical magnetic field for transport, both above and below the Morin transition temperature, the magnon modes are polarised parallel or antiparallel to the equilibrium orientation of the Néel vector. The presence of magnon transport can be explained through a superposition of different magnon modes [326], as discussed in Sec. 6.3.1. However, instead of being a superposition of modes above the spin flop, it is a superposition of linearly polarised modes in the easy-plane phase. If the two modes satisfy the energy conservation relation $\omega_1^2 + c^2\boldsymbol{k}_1^2 = \omega_2^2 + c^2\boldsymbol{k}_2^2$, they can lead to a net non-equilibrium magnon accumulation and lead to a transfer of angular momentum. The dephasing-induced attenuation of the signal above the Morin transition temperature relies on a characteristic length scale $\propto 1/\boldsymbol{k}_1 - \boldsymbol{k}_2$. Close to the Morin transition, this splitting between the magnon modes is small and thus the transport length scale is relatively large however as this splitting increases, either by applying a magnetic field or the temperature is increased far above the Morin transition, the frequency splitting is so large that the dephasing length is below the experimental resolution.

The magnon spin-diffusion length can be probed by varying the distance between the injector and detector, shown in Fig. 7.23b, and decreases as the temperature increases. This decrease is in contrast to the increase with temperature observed in ferrimagnetic YIG. The presence of V_{el} for distances larger than 500 nm between the injector and the detector up to 320 K demonstrates that the transport length scales even above room temperature are still in the range of µm. Fits to both V_{el} and the magnon diffusion length are shown in Fig. 7.23b based on circularly polarised magnons below T_M and on a superposition of linearly polarised modes above T_M.

A similar explanation based around a birefringence-type effect between linearly polarised modes is made in Ref. [327] that was published just after the work in Ref. [r13] was submitted.

7.5 Conclusions

This chapter has presented experimental investigations of magnon transport through thin films of antiferromagnetic iron oxide (α-Fe_2O_3) known as hematite. By stabilising the easy-axis anisotropy below the Morin transition temperature, the long distance propagation of magnons with a circular polarisation was realised in thin films of this material with different orientations. Distinct from ferromagnetic materials, the magnons excited by an interfacial spin-bias with heavy metal platinum were found to propagate providing the key requirement that $\boldsymbol{\mu}_s \cdot \boldsymbol{n}$ was non-zero. The propagation reached a maximum for a parallel alignment. This condition enabled long distance spin transport even in the absence of a magnetic field, where the interfacial spin-bias alone provided sufficient breaking of the magnon mode degeneracy to facilitate a net spin current. The previous chapter demonstrated diffusion lengths of up to 9 µm for bulk crystals, whilst thin films, with their increased magnetic damping, exhibited more modest diffusion lengths of hundreds of nm but still orders of magnitude larger than previously extracted spin diffusion lengths for antiferromagnets. The domain structure of the thin films proved critical to developing a full understanding of the antiferromagnetic transport properties. The effects of domain walls on the transmission of magnonic spin currents were investigated and found to play a key role when the size of the antiferromagnetic domains were smaller than the intrinsic diffusion lengths of the hematite films, leading to significant scattering of magnons below a frequency threshold related to the domain wall. Despite the efficient transport of spin shown here, it still requires cryogenic temperature in order to stabilise the easy-axis phase, a feature that is undesirable for possible antiferromagnetic magnonic devices. The temperature dependence of the magnon transport was investigated for (0001) orientated thin film hematite below the Morin transition temperature, where the transport efficiency is modulated not only by the decreasing magnon population but increasingly by the antiferromagnetic domain structure as the intrinsic length scale exceeds the distance between domain walls, which act as scattering sites for lower frequency magnons. Finally, the possibility of room temperature transport was briefly introduced for the easy-plane phase of hematite, explained through a superposition of linearly polarised magnon modes.

8

Conclusion and Outlook

Conclusion

In this thesis, fundamental aspects that are key for future insulating antiferromagnetic spintronics have been investigated. Although Louis Néel relegated antiferromagnetic materials to merely a theoretical curiosity [10], several decades later they are at the forefront of spintronics research which seeks to functionalise their high frequency spin dynamics, resilience to external magnetic fields and absence of stray fields. In the course of this thesis, the spin Hall magnetoresistance was used to probe the key anisotropies in both bulk and thin films of the insulating antiferromagnetic iron oxide (α-Fe_2O_3), known as the mineral hematite, the main component of rust. Accessing information about the underlying antiferromagnetic anisotropies in order to engineer them is a challenging endeavour, where the few established available techniques are only applicable to bulk antiferromagnets. However, this simple, surface sensitive resistance measurement provides an easy method to probe the underlying anisotropies of antiferromagnets, even in thin films, a key requirement for future device development such as as non-volatile memory components where the equilibrium position of the magnetic order parameter, the Néel vector, is used to encode information. These anisotropies, which include not only the intrinsic crystalline anisotropies, but also anisotropies introduced by the growth process in thin films, dictate how the Néel vector will respond to, for example, a magnetic field or applied spin-orbit torques. For real memory devices, the resultant anisotropy needs to be strong enough to maintain the equilibrium position of the Néel vector in the presence of external perturbations but also low enough that controlled switching events can occur. The material of interest in this thesis, hematite, is an ubiquitous antiferromagnet and an attractive prospect for antiferromagnetic spintronics with a high Néel temperature, a low magnetic damping and a controllable magnetic structure. Below the Néel temperature, the Néel vector is confined to the ab-plane, termed an easy-plane anisotropy. Meanwhile, an antisymmetric effective exchange field parallel to the crystallographic c-axis, known as the Dzyaloshinskii-Moriya field, leads to a canting of the Néel vector within the easy-plane. The equilibrium position of the Néel vector within this plane is further determined by an effective basal plane anisotropy field that encompasses the effects of the intrinsic crystalline anisotropy in this plane but also other effects such as strain or defect induced pinning. At around 260 K, the magnetic structure undergoes a reorientation where the magnetic order rotates a full 90° to lie parallel to the c-axis, known as the

Morin transition. The parallel alignment of the Dzyaloshinskii-Moriya field and the Néel vector removes the canting that was present above the Morin transition and the magnetic state is now that of an easy-axis antiferromagnet. This transition originates from the antiferromagnetic anisotropy directed along the c-axis changing sign at the transition temperature. The strength of this anisotropy was extracted for bulk hematite and thin film hematite by detecting the reorientation of the Néel vector under an applied field, detected by spin Hall magnetoresistance measurements, where it was found to be comparable for the two regimes. By comparing the magnitude of the field parallel and perpendicular to the Néel vector required to elicit this reorientation, the strength of the effective Dzyaloshinskii-Moriya field was calculated and it was shown that the value extracted from surface sensitive measurements for bulk hematite is comparable to that extracted previously from antiferromagnetic resonance. However, in thin film hematite, the effective Dzyaloshinskii-Moriya field was shown to not only be four times larger than in bulk, but also adopt a strong temperature dependence, something not reported for bulk hematite. Given that this effective field arises due to an asymmetry in the exchange interaction between Fe atoms along the c-axis, the larger value for this anisotropy field likely originates from an increased distortion of the unit cell caused by the thin film growth. As for the temperature dependence, this possibly originates from the differing thermal expansion of hematite and the substrate material Al_2O_3, leading to differences in the unit cell distortion with temperature. By measuring above the Morin transition, it was shown that the effective anisotropy in the basal plane of bulk hematite was dominated by the small intrinsic crystalline anisotropy, something expected given the high quality nature of the crystals with few defects and large antiferromagnetic domains. However, in thin film hematite, the strained growth on Al_2O_3 substrates alongside an increase in defects means that the effective basal plane anisotropy field is three orders of magnitude larger than in bulk crystals. The smooth modulation of the spin Hall magnetoresistance of thin film hematite/Pt bilayers in the easy-plane phase, demonstrated that the basal plane is dominated by an effective pinning potential with no evidence of the crystalline anisotropy. This same pinning potential also contributes to the stabilisation of the easy-plane phase in these thin films that emerges above the spin flop, delaying the return to the easy-axis phase, leading to an emerging hysteresis in the signal. Finally, it was shown that, although additional contributions may enter the spin Hall magnetoresistance response due to, for example a distribution of the antiferromagnetic anisotropy axis, the value of the magnetic field required to induce spin reorientation transitions can be used to effectively extract the underlying antiferromagnetic anisotropies.

Having developed an understanding of the antiferromagnetic anisotropies and realised control over the magnetic state in antiferromagnetic hematite, the later part of this thesis focussed on the transport of angular momentum mediated by magnons. As well as utilising antiferromagnets for non-volatile memory components, devices based around the low-power efficient transport of magnons in magnetic insulators would enable the processing and transport of information with a reduction in the associated Joule heating. Prior to the work conducted in this thesis, the spin diffusion lengths of numerous antiferromagnets had been evaluated to be only a few nanometers. To make use of antiferromagnetic magnons, these nanometer length scales are insufficient to allow for logic operations or wave-based computing to occur. In this thesis, the long distance transport of magnons in bulk and thin film hematite has been shown, with spin diffusion lengths orders of magnitude larger than previously reported. One of the key results of this thesis demonstrates that a parallel component of the Néel vector along the transport

direction is required to facilitate the transport of electrically excited magnons. Meanwhile, the thermal excitation of magnons via the spin Seebeck effect can elicit transport in the presence of a net magnetisation in the transport direction, whilst the Néel spin Seebeck conductance is far smaller. This distinction between thermally generated and electrically generated magnons does not exist in ferromagnets, allowing for selective transport. The parallel alignment of the Néel vector and interfacial spin accumulation can be achieved through a magnetic field and driving a spin-flop, which is accompanied by the strong softening of the lowest energy magnon branch. Alternatively, geometrical choices can be made that allows for a parallel alignment in the absence of a magnetic field, enabling zero-field transport of magnons in antiferromagnets. This zero-field transport however is not accompanied by a closing of the magnon gap such as at the spin-flop, raising a key question about whether this closure is important for magnon transport. In bulk hematite, where the antiferromagnetic domains are large and the spin-flop is abrupt, the transport of magnons was detected in excess of 40 µm leading to spin diffusion lengths of up to 9 µm. Moving to thin films of hematite, the magnon transport displayed more modest transport length scales of 100's of nanometers. Nevertheless, the long diffusion lengths indicate that the magnetic damping in thin film hematite is low, just as in bulk hematite [r13]. The propagation of magnons in thin film hematite was observed to be enhanced with successive field cycling, indicating that the antiferromagnetic domain structure influences the transport properties. Through direct magnetic imaging and a theoretical toy model of magnon scattering at antiferromagnetic domain walls, two length scales can be attributed to the antiferromagnetic magnon transport, separated by a threshold frequency. Magnons with a frequency below this threshold experience strong scattering at domain walls, visible as a sharp attenuation of the electrical signal and a length scale indicative of the distance between scattering sites. Meanwhile, magnons with a frequency above this threshold are unaffected by the presence of domain walls and decay with a length scale indicative of the intrinsic decay of the hematite thin films. In previous reports, the magnons were excited by ferromagnetic layers before being passed through thin film antiferromagnets, which likely were in multi-domain states. The insights gained in this thesis then suggest one cause of the low evaluated spin diffusion lengths previously reported comes from magnon scattering from domain walls in the antiferromagnetic layer.

Outlook

Although the work presented in this thesis contributes to the development and advancement of antiferromagnetic (magnon) spintronics, various challenges still exist that need to be overcome to accomplish the ultimate aim of fully integrated antiferromagnetic components functioning as magnetic memory, logic, and information conduits.

As discussed in this thesis, a thorough understanding of thin film antiferromagnetic anisotropies is required, where currently only a few materials have been well studied. In application settings, polycrystalline antiferromagnets would be easier to grow in a variety of environments to allow for easier integration. Very recently, the detection of the average Néel vector in polycrystalline NiO has been observed [r18] so the principles established here can conceivably be transferred. The introduction of polycrystalline order not only makes it easier to fabricate films, but they can also be produced atop more functional layers such as piezoelectrics for direct, low power control and detection of the magnetic state.

In terms of information transport, one could improve the efficiency of the magnon transport by confining the magnon transport channel in order to increase the magnon density. By interfacing such *channels*, interference effects could be studied in order to generate boolean logic devices. Unlike in ferromagnets, antiferromagnetic magnons have a "handed-ness" which would allow for additional outcomes from logic operations based not only on constructive and destructive interference but also on the handed-ness of the resultant signal. There is also the possibility for active manipulation of the transport by using intermediate wires to alter the local magnon density or locally changing the magnetic anisotropies from heating between the injector and detector [r5].

This thesis has focussed primarily on the material hematite, however other antiferromagnetic materials should also be capable of hosting magnon currents. Recent results on magnon transport have demonstrated that the easy-plane phase of hematite can also host a magnon current though a superposition of magnon modes [r13, 327, 329], or even magnon transport in systems with a low magnetic symmetry [r16], opening up antiferromagnets without a uniaxial anisotropy to future investigations. Meanwhile, there are numerous rare earth (R) orthoferrites with the chemical formula $RFeO_3$. These materials have the same crystal structure as hematite and have various antiferromagnetic structures but some possible candidates to investigate would be $YFeO_3$ which has a canted easy-axis, an accessible spin-flop field and no spin-reorientation transition or $TmFeO_3$ which also has a canted easy-axis but a low temperature spin-reorientation of the easy-axis. These canted orthoferrites can not only act as magnon conduits, but also as sources for monochromatic, THz magnons and radiation though excited auto-oscillations [356].

Own and Contributed Works

r1. Baldrati, L., Ross, A., Niizeki, T., Schneider, C., Ramos, R., Cramer, J., Gomonay, O., Filianina, M., Savchenko, T., Heinze, D., Kleibert, A., Saitoh, E., Sinova, J. & Kläui, M. Full angular dependence of the spin Hall and ordinary magnetoresistance in epitaxial antiferromagnetic NiO(001)/Pt thin films. *Phys. Rev. B* **98,** 024422 (2018).

r2. Baldrati, L., Schneider, C., Niizeki, T., Ramos, R., Cramer, J., Ross, A., Saitoh, E. & Kläui, M. Spin transport in multilayer systems with fully epitaxial NiO thin films. *Phys. Rev. B* **98,** 014409 (2018).

r3. Lebrun, R.*, Ross, A.*, Bender, S., Qaiumzadeh, A., Baldrati, L., Cramer, J., Brataas, A., Duine, R. A. & Kläui, M. Tunable long-distance spin transport through a crystalline antiferromagnetic insulator. *Nature* **561,** 222–225 (2018). [*shared first authorship].

r4. Baldrati, L., Gomonay, O., Ross, A., Filianina, M., Lebrun, R., Ramos, R., Leveille, C., Fuhrmann, F., Forrest, T. R., Maccherozzi, F., Valencia, S., Kronast, F., Saitoh, E., Sinova, J. & Kläui, M. Mechanism of Néel order switching in antiferromagnetic thin films revealed by magnetotransport and direct imaging. *Phys. Rev. Lett.* **123,** 177201 (2019).

r5. Cramer, J., Baldrati, L., Ross, A., Vafaee, M., Lebrun, R. & Kläui, M. Impact of electromagnetic fields and heat on spin transport signals in $Y_3Fe_5O_{12}$. *Phys. Rev. B* **100,** 094439 (2019).

r6. Cramer, J., Ross, A., Jaiswal, S., Baldrati, L., Lebrun, R. & Kläui, M. Orientation-dependent direct and inverse spin Hall effects in $Co_{60}Fe_{20}B_{20}$. *Phys. Rev. B* **99,** 104414 (2019).

r7. Ding, S., Ross, A., Lebrun, R., Becker, S., Lee, K., Boventer, I., Das, S., Kurokawa, Y., Gupta, S., Yang, J., Jakob, G. & Kläui, M. Interfacial Dzyaloshinskii-Moriya interaction and chiral magnetic textures in a ferrimagnetic insulator. *Phys. Rev. B* **100,** 100406 (2019).

r8. Dong, B.-W., Baldrati, L., Schneider, C., Niizeki, T., Ramos, R., Ross, A., Cramer, J., Saitoh, E. & Kläui, M. Antiferromagnetic NiO thickness dependent sign of the spin Hall magnetoresistance in γ-Fe_2O_3/NiO/Pt epitaxial stacks. *Appl. Phys. Lett.* **114,** 102405 (2019).

r9. Hajiri, T., Baldrati, L., Lebrun, R., Filianina, M., Ross, A., Tanahashi, N., Kuroda, M., Gan, W. L., Menteş, T. O., Genuzio, F., Locatelli, A., Asano, H. & Kläui, M. Spin structure and spin Hall magnetoresistance of epitaxial thin films of the insulating non-collinear antiferromagnet $SmFeO_3$. *J. Phys. D: Condens. Matter* **31,** 445804 (2019).

r10. Lebrun, R., Ross, A., Gomonay, O., Bender, S. A., Baldrati, L., Kronast, F., Qaiumzadeh, A., Sinova, J., Brataas, A., Duine, R. A. & Kläui, M. Anisotropies and magnetic phase transitions in insulating antiferromagnets determined by a spin-Hall magnetoresistance probe. *Comms. Phys.* **2,** 50 (2019).

r11. Ding, S., Ross, A., Go, D., Ren, Z., Freimuth, F., Becker, S., Kammerbauer, F., Yang, J., Jakob, G., Mokrousov, Y. & Kläui, M. Harnessing non-local orbital-to-spin conversion of interfacial orbital currents for efficient spin-orbit torques. *Phys. Rev. Lett.* **125,** 177201 (2020).

r12. Ding, S., Baldrati, L., Ross, A., Ren, Z., Wu, R., Becker, S., Yang, J., Jakob, G., Brataas, A. & Kläui, M. Identifying the origin of the nonmonotonic thickness dependence of spin-orbit torque and interfacial Dzyaloshinskii-Moriya interaction in a ferrimagnetic insulator heterostructure. *Phys. Rev. B* **102,** 054425 (2020).

r13. Lebrun, R., Ross, A., Gomonay, O., Baltz, V., Ebels, U., Barra, A. L., Qaiumzadeh, A., Brataas, A., Sinova, J. & Kläui, M. Long-distance spin-transport across the Morin phase transition up to room temperature in the ultra-low damping α-Fe_2O_3 antiferromagnet. *Nat. Commun.* **11,** 6332 (2020).

r14. Ross, A., Lebrun, R., Ulloa, C., Grave, D., Kay, A., Baldrati, L., Kronast, F., Valencia, S., Rothschild, A. & Kläui, M. Structural sensitivity of the spin Hall magnetoresistance in antiferromagnetic thin films. *Phys. Rev. B* **102,** 094415 (2020).

r15. Ross, A.*, Lebrun, R.*, Gomonay, O., Grave, D. A., Kay, A., Baldrati, L., Becker, S., Qaiumzadeh, A., Ulloa, C., Jakob, G., Kronast, F., Sinova, J., Duine, R., Brataas, A., Rothschild, A. & Kläui, M. Propagation length of antiferromagnetic magnons governed by domain configurations. *Nano Lett.* **20,** 306–313 (2020). [*shared first authorship].

r16. Ross, A., Lebrun, R., Baldrati, L., Kamra, A., Ding, S., Schreiber, F., Backes, D., Maccherozzi, F., Grave, D., Rothschild, A., Sinova, J. & Kläui, M. An insulating doped antiferromagnet with low magnetic symmetry as a room temperature spin conduit. *Appl. Phys. Lett.* **117,** 242405 (2020).

r17. Schmitt, C., Baldrati, L., Sanchez-Tejerina, L., Schreiber, F., Ross, A., Filianina, M., Ding, S., Fuhrmann, F., Ramos, R., Maccherozzi, F., Backes, D., Saitoh, E., Finocchio, G. & Kläui, M. Identification of Néel vector orientation in antiferromagnetic domains switched by currents in NiO/Pt thin films. arXiv: 2008.08507 (2020). [Accepted for publication by Phys. Rev. Appl.]

r18. Barra, A., Ross, A., Gomonay, O., Baldrati, L., Lebrun, R., Chavez, A., Schneider, J. D., Wang, Q., Shirazi, P., Carmen, G. & Kläui, M. Effective strain manipulation of the antiferromagnetic state of polycrystalline NiO. *Submitted to Appl. Phys. Lett.* (2021).

r19. Becker, S., Ross, A., Lebrun, R., Baldrai, L., Ding, S., Schreiber, F., Maccherozzi, F., Backes, D., Kläui, M. & Jakob, G. Electrical detection of the spin reorientation transition in $TmFeO_3$ thin films by spin Hall magnetoresistance. *Phys. Rev. B* **103,** 024423 (2021).

Bibliography

1. Dayarathna, M. *et al.* Data center energy consumption modelling: A survey. *IEEE Commun. Surv. Tutorials* **18,** 732–794 (2016).
2. Pop, E. *et al.* Heat generation and transport in nanometerscale transistors. *Proc. IEEE* **94,** 1587–1601 (2006).
3. Wolf, S. *et al.* Spintronics: a spin-based electronics vision for the future. *Science.* **294,** 323–410 (2001).
4. Baibich, M. *et al.* Giant magnetoresistance of (001)Fe/(001)Cr magnetic superlattices. *Phys. Rev. Lett.* **61,** 2472 (1988).
5. Binasch, G. *et al.* Enhanced magnetoresistance in layered magnetic structures with antiferromagnetic interlayer exchange. *Phys. Rev. B* **38,** 4828(R) (1989).
6. Slonczewski, J. Current-driven excitation of magnetic multilayers. *J. Magn. Magn. Mater* **159,** L1–L7 (1996).
7. Sinova, J. *et al.* Spin Hall effects. *Rev. Mod. Phys.* **87,** 1213–1260 (2015).
8. Kruglyak, V. V. *et al.* Magnonics. *J. Phys. D: Appl. Phys.* **43,** 264001 (2010).
9. Chumak, A. V. *et al.* Magnon spintronics. *Nat. Phys.* **11,** 453–461 (2015).
10. Néel, L. Magnetism and the Local Molecular Field. *Nobel Lectures* (1970).
11. Baltz, V. *et al.* Antiferromagnetic spintronics. *Rev. Mod. Phys.* **90,** 015005 (2018).
12. Chen, X. Z. *et al.* Antidamping-torque-induced switching in biaxial antiferromagnetic insulators. *Phys. Rev. Lett.* **120,** 207204 (2018).
13. Nakayama, H. *et al.* Spin Hall magnetoresistance induced by a nonequilibrium proximity effect. *Phys. Rev. Lett.* **110** (2013).
14. Hoogeboom, G. R. *et al.* Negative spin Hall magnetoresistance of Pt on the bulk easy-plane antiferromagnet NiO. *Appl. Phys. Lett.* **111,** 052409 (2017).
15. Fischer, J. *et al.* Spin Hall magnetoresistance in antiferromagnet/heavy-metal heterostructures. *Phys. Rev. B* **97,** 014417 (2018).
16. Cheng, Y. *et al.* Anisotropic magnetoresistance and nontrivial spin Hall magnetoresistance in Pt/α-Fe_2O_3. *Phys. Rev. B* **100,** 220408 (2019).
17. Fischer, J. *et al.* Large spin Hall magnetoresistance in antiferromagnetic α-Fe_2O_3/Pt heterostructures. *Phys. Rev. Appl.* **13,** 014019 (2020).
18. Fink, H. J. & Shaltiel, D. High-Frequency Resonance of A Weak Ferromagnet: $MnCO_3$. *Phys. Rev.* **130,** 627–631 (1963).
19. Fink, H. J. Resonance line shapes of weak ferromagnets of the α-Fe_2O_3 and NiF_2 type. *Phys. Rev.* **133,** A1322–A1326 (1964).
20. Takei, S. *et al.* Superfluid spin transport through antiferromagnetic insulators. *Phys. Rev. B* **90,** 094408 (2014).
21. Qaiumzadeh, A. *et al.* Spin superfluidity in biaxial antiferromagnetic insulators. *Phys. Rev. Lett.* **118,** 137201 (2017).

22. Sonin, E. Spin currents and spin superfluidity. *Adv. Phys.* **59,** 181–255 (2010).

23. Sonin, E. B. Superfluid spin transport in ferro- and antiferromagnets. *Phys. Rev. B* **99,** 104423 (2019).

24. Coey, J. M. D. *Magnetism and magnetic materials* (Cambridge University Press, 2010).

25. Blundell, S. *Magnetism in condensed matter (Oxford master series in condensed matter physics)* (Oxford University Press, 2001).

26. Anderson, P. W. Antiferromagnetism. Theory of superexchange interaction. *Phys. Rev.* **79,** 350–356 (1950).

27. Anderson, P. W. Theory of magnetic exchange interactions: Exchange in insulators and semiconductors. *Solid State Phys.* **14,** 99–214 (1963).

28. Bruno, P. Tight-binding approach to the orbital magnetic moment and magnetocrystalline anisotropy of transition-metal monolayers. *Phys. Rev. B* **39,** 865–868 (1989).

29. Morrish, A. H. *Canted antiferromagnetism: Hematite* 1st ed. (World Scientific, Singapore, 1995).

30. Landau, L. A possible explanation of the field dependence of the susceptibility at low temperatures. *Phys. Z. Sowjet* **4,** 675 (1933).

31. Néel, L. Influence des fluctuations des champs moléculaires sur les propriétés magnétiques des corps. *Ann. de Phys.* **17,** 5–105 (1932).

32. Néel, L. Propriétés magnétiques de l'état magnétique et énergie d'interaction entre atomes magnétiques. *Ann. de Phys.* **5,** 232–279 (1936).

33. Néel, L. Théorie du paramagnétisme constant; application au manganése. *C. R. Acad. Sci.* **203,** 304–306 (1936).

34. Shull, C. & Smart, J. Detection of antiferromagnetism by neutron diffraction. *Phys. Rev.* **76,** 1256–1257 (1949).

35. Tsukada, I. *et al.* Two-stage spin-flop transitions in the S =1/2 antiferromagnetic spin chain $BaCu_2Si_2O_7$. *Phys. Rev. Lett.* **87,** 127203 (2001).

36. Taniguchi, H. *et al.* Fabrication of thin films of two-dimensional triangular antiferromagnet Ag_2CrO_2 and their transport properties. *AIP Adv.* **8,** 025010 (2018).

37. Xing, W. *et al.* Magnon transport in quasi-two-dimensional van der Waals antiferromagnets. *Phys. Rev. X* **9,** 011026 (2019).

38. Doki, H. *et al.* Spin thermal Hall conductivity of a Kagome antiferromagnet. *Phys. Rev. Lett.* **121,** 097203 (2018).

39. Kohn, A. *et al.* The antiferromagnetic structures of $IrMn_3$ and their influence on exchange-bias. *Sci. Rep.* **3,** 2412 (2013).

40. Weiss, P. La variation du ferromagnetisme avec la temperature. *Comptes Rendus* **143,** 1136 (1906).

41. Weiss, P. L'hypothése du champ moléculaire et la propriété ferromagnétique. *J. Phys. Théor. App.* **6,** 661–690 (1907).

42. Gurevich, A. & Melkov, G. *Magnetization oscillations and waves* (CRC Press, 1996).

43. Nikotin, O. *et al.* Magnon dispersion relation and exchange interactions in MnF_2. *J. Phys. C: Solid State Phys.* **2,** 1168–1173 (1969).

44. Poulis, N. *et al.* On antiferromagnetism in a single crystal. *Phys. Rev.* **82,** 552 (1951).

45. Gorter, C. & Haantjes, J. Anti-ferromagnetism at the absolute zero of temperature in the case of rhombic symmetry. *Physica* **18,** 285–294 (1952).

46. Foner, S. High-field antiferromagnetic resonance in Cr_2O_3. *Phys. Rev.* **130,** 183–197 (1963).

47. Anderson, P. W. *et al.* Magnetic resonance in α-Fe_2O_3. *Phys. Rev.* **93,** 717–718 (1954).

48. Johnson, F. & Nethercot, A. Antiferromagnetic resonance in MnF_2. *Phys. Rev.* **114,** 705–716 (1959).

49. Néel, L. Some new results on antiferromagnetism and ferromagnetism. *Rev. Mod. Phys.* **25,** 58 (1953).

50. Li, Y.-Y. Domain walls in antiferromagnets and the weak ferromagnetism of α-Fe_2O_3. *Phys. Rev.* **101,** 1450–1454 (1956).

51. Dzyaloshinsky, I. A thermodynamic theory of "weak" ferromagnetism of antiferromagnetics. *J. Phys. Chem. Solids* **4,** 241–255 (1958).

52. Moriya, T. Anisotropic superexchange interaction and weak ferromagnetism. *Phys. Rev.* **120,** 91–98 (1960).

53. Foner, S. & Williamson, S. J. Low-temperature antiferromagnetic resonance in α-Fe_2O_3. *J. Appl. Phys.* **36,** 1154–1156 (1965).

54. Elliston, P. R. & Troup, G. J. Some antiferromagnetic resonance measurements in α-Fe_2O_3. *J. Phys. C (Proc. Phys. Soc). 2* **1** (1968).

55. Finocchio, G. *et al.* Magnetic skyrmions: From fundamental to applications. *J. Phys. D: Appl. Phys.* **49,** 423001 (2016).

56. Jiang, W. *et al.* Blowing magnetic skymion bubbles. *Science* **349,** 283–286 (2015).

57. Garst, M. *et al.* Collective spin excitations of helices and magnetic skyrmions: Review and perspectives of magnonics in non-centrosymmetric magnets. *J. Phys. D: Appl. Phys.* **50,** 293002 (2017).

58. Avci, C. O. *et al.* Interface-driven chiral magnetism and current-driven domain walls in insulating magnetic garnets. *Nat. Nanotechnol.* **4,** 561–566 (2019).

59. Néel, L. *Proc. Kyoto Conf. Theor. Phys. (Science Council of Japan),* 701 (1954).

60. Roth, W. Neutron and optical studies of domains in NiO. *J. Appl. Phys.* **31,** 2000–2011 (1960).

61. Náfrádi, B. *et al.* Magnetostriction and magnetostructural domains in antiferromagnetic YBa. *Phys. Rev. Lett.* **116,** 047001 (2016).

62. Scholl, A. *et al.* Observation of antiferromagnetic domains in epitaxial thin films. *Science* **287,** 1014–1016 (2000).

63. Incr, W. J. & Platzker, A. Antiferromagnetic domains in $RbMnF_3$. *Phys. Rev.* **175,** 650–653 (1968).

64. Goltsev, A. V. *et al.* Structure and interaction of antiferromagnetic domain walls in hexagonal $YMnO_3$. *Phys. Rev. Lett.* **90,** 177204 (2003).

65. Spooner, F. D. & Vernon, M. W. Growth, perfection and antiferromagnetic domain structure of epitaxial cobalt oxide. *J. Mater. Sci.* **4,** 734–742 (1969).

66. Zimmermann, A. S. *et al.* Anisotropy of antiferromagnetic 180° domains in magnetoelectric $LiMPO_4$ (M = Fe, Co, Ni). *Eur. Phys. J. B* **71,** 355–360 (2009).

67. Brown, W. F. *Magnetoelastic Interactions* (Springer Berlin Heidelberg, 1966).

68. Gomonaj, E. V. On the theory of equilibrium magnetoelastic domain structure in easy-plane antiferromagnet. *Low Temp. Phys.* **25,** 520–526 (1999).

69. Gomonay, H. & Loktev, V. M. Magnetostriction and magnetoelastic domains in antiferromagnets. *J. Phys. Condens. Matter* **14,** 3959–3971 (2002).

70. Gomonay, O. *et al.* Antiferromagnetic spin textures and dynamics. *Nat. Phys.* **14,** 213–216 (2018).

71. Rado, G. & Folen, V. Observation of the magnetically induced magnetoelectric effect and evidence for antiferromagnetic domains. *Phys. Rev. Lett.* **7,** 310–311 (1961).

72. Mitsek, A. *et al.* Domain structure of uniaxial antiferromagnets. The problem of nucleation. *Phys. Status Solidi B* **38,** 69–79 (1970).

73. Appel, P. *et al.* Nanomagnetism of magnetoelectric granular thin-film antiferromagnets. *Nano Lett.* **19,** 1682–1687 (2019).

74. Slack, G. A. Crystallography and domain walls in antiferromagnetic NiO crystals. *J. Appl. Phys.* **31,** 1571–1582 (1960).

75. Xu, J. *et al.* Imaging antiferromagnetic domains in nickel oxide thin films by optical birefringence effect. *Phys. Rev. B* **100,** 134413 (2019).

76. Safa, M. & Tanner, B. Antiferromagnetic domain wall motion in $KNiF_3$ and $KCoF_3$ observed by X-ray synchrotron topography. *Philos. Mag. B* **37,** 739–750 (1978).

77. Tanner, B. K. Antiferromagnetic domains. *Contemp. Phys.* **20,** 187–210 (1979).

78. Grzybowski, M. J. *et al.* Imaging current-induced switching of antiferromagnetic domains in CuMnAs. *Phys. Rev. Lett.* **118,** 057701 (2017).

79. Bloch, F. Zur Theorie des Ferromagnetismus. *Zeitsch. für Physik* **61,** 206–219 (1930).

80. Holstein, T. & Primakoff, H. Field dependence of the intrinsic domain magnetization of a ferromagnet. *Phys. Rev.* **58,** 1098–1113 (1940).

81. Dyson, F. J. General theory of spin-wave interactions. *Phys. Rev.* **102,** 1217–1230 (1956).

82. Lenk, B. *et al.* The building blocks of magnonics. *Phys. Rep.* **507,** 107–136 (2011).

83. Prozorova, L. & Kotyuzhanskii, B. Direct observation of the propagation of spin waves in an antiferromagnet. *Physica B+C* **86-88,** 1061–1065 (1977).

84. Alakshin, E. M. *et al.* Magnon Bose-Einstein condensation in $CsMnF_3$ and $MnCO_3$. *J. Phys.: Conf. Ser.* **324,** 012006 (2011).

85. Khatamian, D. & Collins, M. F. Spin-waves in $CsMnF_3$. *Can. J. Phys.* **55,** 773–778 (1976).

86. Des Cloizeaux, J. & Pearson, J. J. Spin-wave spectrum of the antiferromagnetic linear chain. *Phys. Rev.* **128,** 2131–2135 (1962).

87. Rezende S. M. and White, R. Multimagnon theory of antiferromagnetic resonance relaxation. *Phys. Rev. B* **14,** 2939–2955 (1976).

88. Rezende, S. *et al.* Introduction to antiferromagnetic magnons. *J. Appl. Phys.* **126,** 151101 (2019).

89. Keffer, F. *"Spin waves" in Handbuch der Physik* (Springer-Verlag Berlin-Heidelberg, 1966).

90. Milano, J. *et al.* Effect of dipolar interaction on the antiferromagnetic resonance spectra of NiO. *Phys. Rev. Lett.* **93,** 077601 (2004).

91. Kittel, C. Theory of antiferromagnetic resonance. *Phys. Rev.* **82,** 565–565 (1951).

92. Maxwell, L. & McGuire, T. Antiferromagnetic resonance. *Rev. Mod. Phys.* **25,** 279–284 (1953).

93. Nagamiya, T. Theory of antiferromagnetism and antiferromagnetic resonance absorption, II. *Prog. Theor. Phys.* **6,** 350–355 (1951).

94. Keffer, F. & Kittel, C. Theory of antiferromagnetic resonance. *Phys. Rev.* **85,** 329–337 (1952).

95. Trounson, E. P. *et al.* Magnetic resonance in antiferromagnetic materials near the Curie temperature. *Phys. Rev.* **79,** 542–543 (1950).

96. Maxwell, L. Microwave resonance absorption in antiferromagnetic materials. *Am. J. Phys.* **20,** 80–85 (1952).

97. Cramer, J. *et al.* Magnon detection using a ferroic collinear multilayer spin valve. *Nat. Commun.* **9,** 1089 (2018).

98. Hall, E. XVIII. On the "rotational coefficient" in nickel and cobalt. *Lond. Edinb. Dubl. Phil. Mag. J. Sci.* **12,** 157–172 (1881).

99. Nagaosa, N. *et al.* Anomalous Hall effect. *Rev. Mod. Phys* **82,** 1539–1592 (2010).

100. Niimi, Y. & Otani, Y. Reciprocal spin Hall effects in conductors with strong spin–orbit coupling: A review. *Rep. Prog. Phys.* **78,** 124501 (2015).

101. D'yakonov, M. & Perel', V. I. Possibility of orienting electron spins with current. *J. Exp. Theor. Phys. Lett.* **13,** 467 (1971). [ZhETF Pis. Red. **13**, 657-660 (1971)].

102. Hirsch, J. E. Spin Hall Effect. *Phys. Rev. Lett.* **83,** 1834–1837 (1999).

103. Zhang, S. Spin Hall effect in the presence of spin diffusion. *Phys. Rev. Lett.* **85,** 393–396 (2000).

104. Murakami, S. *et al.* Dissipationless quantum spin current at room temperature. *Science* **301,** 1348–1351 (2003).

105. Sinova, J. *et al.* Universal intrinsic spin Hall effect. *Phys. Rev. Lett.* **92,** 126603 (2004).

106. Kato, Y. *et al.* Observation of the spin Hall Effect in semiconductors. *Science* **306,** 1910–1913 (2004).

107. Wunderlich, J. *et al.* Experimental observation of the spin-Hall effect in a two-dimensional spin-orbit coupled semiconductor system. *Phys. Rev. Lett.* **94,** 047204 (2005).

108. Saitoh, E. *et al.* Conversion of spin current into charge current at room temperature: Inverse spin-Hall effect. *App. Phys. Lett.* **88,** 182509 (2006).

109. Kontani, H. *et al.* Giant intrinsic spin and orbital Hall effects in Sr_2MO_4 (M=Ru, Rh, Mo). *Phys. Rev. Lett.* **100,** 096601 (2008).

110. Tanaka, T. *et al.* Intrinsic spin Hall effect and orbital Hall effect in $4d$ and $5d$ transition metals. *Phys. Rev. B* **77,** 165117 (2008).

111. Hoffmann, A. Spin Hall effects in metals. *IEEE Trans. Magn.* **49,** 5172–5193 (2013).

112. Morota, M. *et al.* Indication of intrinsic spin Hall effect in 4d and 5d transition metals. *Phys. Rev. B* **83,** 174405 (2011).

113. Tian, Y. *et al.* Proper Scaling of the Anomalous Hall Effect. *Phys. Rev. Lett.* **103,** 087206 (2009).

114. Sagasta, E. *et al.* Tuning the spin Hall effect of Pt from the moderately dirty to the superclean regime. *Phys. Rev. B* **94,** 060412 (2016).

115. Sagasta, E. *et al.* Unveiling the mechanisms of the spin Hall effect in Ta. *Phys. Rev. B* **98,** 060410 (2018).

116. Weischenberg, J. *et al.* Ab initio theory of the scattering-independent anomalous Hall effect. *Phys. Rev. Lett.* **107,** 106601 (2011).

117. Berger, L. Side-jump mechanism for the Hall effect of ferromagnets. *Phys. Rev. B* **2,** 4559–4566 (1970).

118. Wang, H. L. *et al.* Scaling of spin Hall angle in 3d, 4d, and 5d metals from $Y_3Fe_5O_{12}$. *Phys. Rev. Lett.* **112,** 197201 (2014).

119. Cramer, J. *et al.* Complex terahertz and direct current inverse spin Hall effect in YIG/$Cu_{1-x}Ir_x$ bilayers across a wide concentration range. *Nano Letters* **18,** 1064–1069 (2018).

120. Niimi, Y. *et al.* Extrinsic spin Hall effect induced by iridium impurities in copper. *Phys. Rev. Lett.* **106,** 126601 (2011).

121. Laczkowski, P. *et al.* Experimental evidences of a large extrinsic spin Hall effect in AuW alloy. *App. Phys. Lett.* **104,** 142403 (2014).

122. Kikkawa, T. *et al.* Detection of induced paramagnetic moments in Pt on $Y_3Fe_5O_{12}$ via X-ray magnetic circular dichroism. *Phys. Rev. B* **95,** 214416 (2017).

123. Huang, S. Y. *et al.* Transport magnetic proximity effects in platinum. *Phys. Rev. Lett.* **109,** 107204 (2012).

124. Althammer, M. *et al.* Quantitative study of the magnetoresistance in ferromagnetic insulator/normal metal hybrids. *Phys. Rev. B* **87,** 224401 (2013).

125. Geprägs, S. *et al.* Investigation of induced Pt magnetic polarization in Pt/$Y_3Fe_5O_{12}$ bilayers. *App. Phys. Lett.* **101** (2012).

126. Hahn, C. *et al.* Comparative measurements of inverse spin Hall effects and magnetoresistance in YIG/Pt and YIG/Ta. *Phys. Rev. B* **87,** 174417 (2013).

127. Kobs, A. *et al.* Anisotropic interface magnetoresistance in Pt/Co/Pt sandwiches. *Phys. Rev. Lett.* **106,** 217207 (2011).

128. Vlietstra, N. *et al.* Exchange magnetic field torques in YIG/Pt bilayers observed by the spin-Hall magnetoresistance. *Appl. Phys. Letters* **103,** 032401 (2013).

129. Chen, Y.-T. *et al.* Theory of spin Hall magnetoresistance. *Phys. Rev. B* **87,** 144411 (2013).

130. Ganzhorn, K. *et al.* Spin Hall magnetoresistance in a canted ferrimagnet. *Phys. Rev. B* **94,** 094401 (2016).

131. Marmion, S. *et al.* Temperature dependence of spin Hall magnetoresistance in thin YIG/Pt films. *Phys. Rev. B* **89,** 220404 (2014).

132. Meyer, S. *et al.* Temperature dependent spin transport properties of platinum inferred from spin Hall magnetoresistance measurements. *Appl. Phys. Lett.* **104,** 242411 (2014).

133. Yang, Y. *et al.* Thickness dependence of spin Hall magnetoresistance in FeMn/Pt bilayers. *AIP Adv.* **6,** 065203 (2016).

134. Kim, J. *et al.* Spin Hall magnetoresistance in metallic bilayers. *Phys. Rev. Lett.* **116,** 097201 (2016).

135. He, C. *et al.* Spin-torque ferromagnetic measurements utilizing spin Hall magnetoresistance in W/$Co_{40}Fe_{40}B_{20}$/MgO structures. *App. Phys. Lett.* **109,** 202404 (2016).

136. Kobs, A. & Oepen, H. P. Disentangling interface and bulk contributions to the anisotropic magnetoresistance in Pt/Co/Pt sandwiches. *Phys. Rev. B* **93,** 014426 (2016).

137. Avci, C. O. *et al.* Unidirectional spin Hall magnetoresistance in ferromagnet/normal metal bilayers. *Nat. Phys.* **11,** 570–575 (2015).

138. Avci, C. O. *et al.* Origins of the unidirectional spin Hall magnetoresistance in metallic bilayers. *Phys. Rev. Lett.* **121,** 087207 (2018).

139. Lidig, C. *et al.* Unidirectional spin Hall magnetoresistance as a tool for probing the interfacial spin polarization of Co_2MnSi. *Phys. Rev. Appl.* **10,** 44039 (2019).

140. Zhang, S. S.-L. *et al.* Theory of unidirectional spin Hall magnetoresistance in heavy-metal/ferromagnetic-metal bilayers. *Phys. Rev. B* **94,** 140411 (2016).

141. Ji, Y. *et al.* Spin Hall magnetoresistance in an antiferromagnetic magnetoelectric Cr_2O_3/ heavy-metal W heterostructure. *App. Phys. Lett.* **110,** 262401 (2017).

142. Han, J. H. *et al.* Antiferromagnet-controlled spin current transport in $SrMnO_3$/Pt hybrids. *Phys. Rev. B* **90,** 144431 (2014).

143. Manchon, A. Spin Hall magnetoresistance in antiferromagnet/normal metal bilayers. *Phys. Status Solidi RRL* **11,** 1600409 (2017).

144. Brataas, A. *et al.* Finite-element theory of transport in ferromagnet-normal metal systems. *Phys. Rev. lett.* **84,** 2481 (2000).

145. Brataas, A. *et al.* Spin-transport in multi-terminal normal metal-ferromagnet systems with non-collinear magnetizations. *Eur. Phys. J. B* **22,** 99–110 (2001).

146. Wang, S. *et al.* Spin Seebeck effect and spin Hall magnetoresistance at high temperatures for a Pt/yttrium iron garnet hybrid structure. *Nanoscale* **7,** 17812–17819 (2015).

147. Isasa, M. *et al.* Spin Hall magnetoresistance as a probe for surface magnetization in Pt/$CoFe_2O_4$. *Phys. Rev. Appl.* **6,** 034007 (2016).

148. Seebeck, T. Magnetische Polarisation der Metalle und Erze durch Temperatur-Differenz. *Abhandlungen der Königlichen Akademie der Wissenschaften zu Berlin,* 265–373 (1821).

149. Peltier, J. Nouvelles expériences sur la caloricité des courants électrique. *Ann. Chim. Phys.* **56,** 371–386 (1834).

150. Uchida, K. *et al.* Observation of the spin Seebeck effect. *Nature* **455,** 778–781 (2008).

151. Flipse, J. *et al.* Observation of the spin Peltier effect for magnetic insulators. *Phys. Rev. Lett.* **113,** 027601 (2014).

152. Avery, A. D. *et al.* Observation of the planar Nernst effect in permalloy and nickel thin films with in-plane thermal gradients. *Phys. Rev. Lett.* **109,** 196602 (2012).

153. Meier, D. *et al.* Longitudinal spin Seebeck effect contribution in transverse spin Seebeck effect experiments in Pt/YIG and Pt/NFO. *Nat. Commun.* **6,** 8211 (2015).

154. Kehlberger, A. *et al.* Length scale of the spin Seebeck effect. *Phys. Rev. Lett.* **115,** 096602 (2015).

155. Geprägs, S. *et al.* Origin of the spin Seebeck effect in compensated ferrimagnets. *Nat. Commun.* **7,** 1–6 (2016).

156. Meier, D. *et al.* Thermally driven spin and charge currents in thin $NiFe_2O_4$/Pt films. *Phys. Rev. B* **87,** 54421 (2013).

157. Wu, S. *et al.* Paramagnetic spin Seebeck effect. *Phys. Rev. Lett.* **114,** 186602 (2015).

158. Wu, S. *et al.* Antiferromagnetic spin Seebeck effect. *Phys. Rev. Lett.* **116,** 097204 (2016).

159. Li, J. *et al.* Spin current from sub-terahertz-generated antiferromagnetic magnons. *Nature* **578,** 70–74 (2020).

160. Seki, S. *et al.* Thermal generation of spin current in an antiferromagnet. *Phys. Rev. Lett.* **115,** 266601 (2015).

161. Cornelissen, L. J. *et al.* Long-distance transport of magnon spin information in a magnetic insulator at room temperature. *Nat. Phys.* **11,** 1022–1026 (2015).

162. Goennenwein, S. T. B. *et al.* Non-local magnetoresistance in YIG/Pt nanostructures. *App. Phys. Lett.* **107,** 172405 (2015).

163. Brataas, A. *et al.* Spin battery operated by ferromagnetic resonance. *Phys. Rev. B* **66,** 060404 (2002).

164. Cramer, J. *et al.* Spin transport across antiferromagnets induced by the spin Seebeck effect. *J. Phys. D: Appl. Phys.* **51,** 144004 (2018).

165. Shan, J. *et al.* Nonlocal magnon spin transport in $NiFe_2O_4$ thin films. *Appl. Phys. Lett.* **110,** 132406 (2017).

166. Ganzhorn, K. *et al.* Non-local magnon transport in the compensated ferrimagnet GdIG. arXiv: 1705.02871 (2017).

167. Cornelissen, L. J. *et al.* Spin-current-controlled modulation of the magnon spin conductance in a three-terminal magnon transistor. *Phys. Rev. Lett.* **120,** 0977020 (2018).

168. Ganzhorn, K. *et al.* Magnon-based logic in a multi-terminal YIG/Pt nanostructure. *Appl. Phys. Lett.* **109,** 022405 (2016).

169. Wimmer, T. *et al.* Spin transport in a magnetic insulator with zero effective damping. *Phys. Rev. Lett.* **123,** 257201 (2019).

170. Zhang, S. S.-L. & Zhang, S. Spin convertance at magnetic interfaces. *Phys. Rev. B* **86,** 214424 (2012).

171. Zhang, S. & Zhang, S. Magnon mediated electric current drag across a ferromagnetic insulator layer. *Phys. Rev. Lett.* **109,** 096603 (2012).

172. Kajiwara, Y. *et al.* Transmission of electrical signals by spin-wave interconversion in a magnetic insulator. *Nature* **464,** 262–266 (2010).

173. Gramila, T. J. *et al.* Mutual friction between parallel two-dimensional electron systems. *Phys. Rev. Lett.* **66,** 1216–1219 (1991).

174. Wu, H. *et al.* Observation of magnon-mediated electric current drag at room temperature. *Phys. Rev. B* **93,** 060403 (2016).

175. Li, J. *et al.* Observation of magnon-mediated current drag in Pt/yttrium iron garnet/Pt(Ta) trilayers. *Nat. Commun.* **7,** 10858 (2016).

176. Ganzhorn, K. *et al.* Temperature dependence of the non-local spin Seebeck effect in YIG/Pt nanostructures. *AIP Adv.* **7,** 085102 (2017).

177. Giles, B. L. *et al.* Long-range pure magnon spin diffusion observed in a nonlocal spin-Seebeck geometry. *Phys. Rev. B* **92,** 224415 (2015).

178. Cramer, J. *Propagation, manipulation and detection of magnonic spin currents in magnetic oxides and metals* PhD thesis (Johannes Gutenberg-Universität Mainz, 2018).

179. Cramer, J. *et al.* Magnon mode selective spin transport in compensated ferrimagnets. *Nano Lett.* **17,** 3334–3340 (2017).

180. Chavez-Angel, E. *et al.* Reconstruction of an effective magnon mean free path distribution from spin Seebeck measurements in thin films. *New J. of Phys.* **19,** 013011 (2017).

181. Boona, S. R. & Heremans, J. P. Magnon thermal mean free path in yttrium iron garnet. *Phys. Rev. B* **90,** 064421 (2014).

182. Ritzmann, U. *et al.* Propagation of thermally induced magnonic spin currents. *Phys. Rev. B* **89,** 24409 (2014).

183. Cornelissen, L. J. *et al.* Magnon spin transport driven by the magnon chemical potential in a magnetic insulator. *Phys. Rev. B* **94,** 014412 (2016).

184. Fjærbu, E. L. *et al.* Electrically driven Bose-Einstein condensation of magnons in antiferromagnets. *Phys. Rev. B* **95,** 144408 (2017).

185. Flebus, B. Chemical potential of an antiferromagnetic magnon gas. *Phys. Rev. B* **100,** 064410 (2019).

186. Flebus, B. *et al.* Two-fluid theory for spin superfluidity in magnetic insulators. *Phys. Rev. Lett.* **116,** 117201 (2016).

187. Du, C. *et al.* Control and local measurement of the spin chemical potential in a magnetic insulator. *Science* **357,** 195–198 (2017).

188. Wang, H. *et al.* Spin transport in antiferromagnetic insulators mediated by magnetic correlations. *Phys. Rev. B* **91,** 220410 (2015).

189. Shang, T. *et al.* Effect of NiO inserted layer on spin-Hall magnetoresistance in Pt/NiO/YIG heterostructures. *Appl. Phys. Letters* **109,** 032410 (2016).

190. Lin, W. *et al.* Enhancement of thermally injected spin current through an antiferromagnetic insulator. *Phys. Rev. Lett.* **116,** 186601 (2016).

191. Rezende, S. *et al.* Diffusive magnonic spin transport in antiferromagnetic insulators. *Phys. Rev. B* **93,** 054412 (2016).

192. Khymyn, R. *et al.* Transformation of spin current by antiferromagnetic insulators. *Phys. Rev. B* **93,** 224421 (2016).

193. Hung, Y.-M. *et al.* Spin transport in antiferromagnetic NiO and magnetoresistance in $Y_3Fe_5O_{12}$/ NiO/ Pt structures. *AIP Adv.* **7,** 055903 (2017).

194. Zhang, W. *et al.* Spin Hall effects in metallic antiferromagnets. *Phys. Rev. Lett.* **113,** 196602 (2014).

195. Merodio, P. *et al.* Penetration depth and absorption mechanisms of spin currents in $Ir_{20}Mn_{80}$ and $Fe_{50}Mn_{50}$ polycrystalline films by ferromagnetic resonance and spin pumping. *App. Phys. Lett.* **104,** 032406 (2014).

196. Saglam, H. *et al.* Spin transport through the metallic antiferromagnet FeMn. *Phys. Rev. B* **94,** 140412 (2016).

197. Prakash, A. *et al.* Spin Seebeck effect through antiferromagnetic NiO. *Phys. Rev. B* **94,** 014427 (2016).

198. Hahn, C. *et al.* Conduction of spin currents through insulating antiferromagnetic oxides. *Europhys. Lett.* **108,** 57005 (2014).

199. Frangou, L. *et al.* Enhanced spin pumping efficiency in antiferromagnetic IrMn thin films around the magnetic phase transition. *Phys. Rev. Lett.* **116,** 077203 (2016).

200. Qiu, Z. *et al.* Spin colossal magnetoresistance in an antiferromagnetic insulator. *Nature Materials* **17,** 577–580 (2018).

201. Alders, D. *et al.* Temperature and thickness dependence of magnetic moments in NiO epitaxial films. *Phys. Rev. B* **57,** 11623–11631 (1998).

202. Tang, Y. J. *et al.* Finite size effects on the moment and ordering temperature in antiferromagnetic CoO layers. *Phys. Rev. B* **67,** 054408 (2003).

203. Hou, D. *et al.* Tunable sign change of spin Hall magnetoresistance in Pt/NiO/YIG structures. *Phys. Rev. Lett.* **118,** 147202 (2017).

204. Qiu, Z. *et al.* Spin-current probe for phase transition in an insulator. *Nat. Commun.* **7** (2016).

205. Bender, S. *et al.* Enhanced spin conductance of a thin-film insulating antiferromagnet. *Phys. Rev. Lett.* **119,** 056804 (2017).

206. Brataas, A. *et al.* Heat transport between antiferromagnetic insulators and normal metals. *Phys. Rev. B* **92,** 180414(R) (2015).

207. Troncoso, R. E. *et al.* Spin transport in thick insulating antiferromagnetic films. *Phys. Rev. B* **101,** 054404 (2020).

208. Takei, S. & Tserkovnyak, Y. Superfluid spin transport through easy-plane ferromagnetic insulators. *Phys. Rev. Lett.* **112,** 227201 (2014).

209. Sonin, E. B. Spin superfluidity and spin waves in YIG films. *Phys. Rev. B* **95,** 144432 (2017).

210. Fomin, I. Spin currents in superfluid ^{3}He. *Physica B* **169,** 153–163 (1991).

211. Demokritov, S. O. *et al.* Bose–Einstein condensation of quasi-equilibrium magnons at room temperature under pumping. *Nature* **443,** 430–433 (2006).

212. Sun, C. *et al.* Bose–Einstein condensation and superfluidity of magnons in yttrium iron garnet films. *J. Phys. D: Appl. Phys.* **50,** 143002 (2017).

213. Sonin, E. Observation of spin superfluidity: YIG magnetic films and beyond. *J. Phys. Conf. Ser.* **969,** 012116 (2018).

214. Yuan, W. *et al.* Experimental signatures of spin superfluid ground state in canted antiferromagnet Cr_2O_3 via nonlocal spin transport. *Sci Adv.* **4,** eaat1098 (2018).

215. Stepanov, P. *et al.* Long-distance spin transport through a graphene quantum Hall antiferromagnet. *Nat. Phys.* **14,** 907–911 (2018).

216. Cornelissen, L. J. *et al.* Temperature dependence of the magnon spin diffusion length and magnon spin conductivity in the magnetic insulator yttrium iron garnet. *Phys. Rev. B* **94,** 180402 (2016).

217. Cornelissen, L. J. *et al.* Nonlocal magnon-polaron transport in yttrium iron garnet. *Phys. Rev. B* **96,** 104441 (2017).

218. Zhou, X. J. *et al.* Lateral transport properties of thermally excited magnons in yttrium iron garnet films. *App. Phys. Lett.* **110,** 062407 (2017).

219. Shan, J. *et al.* Criteria for accurate determination of the magnon relaxation length from the nonlocal spin Seebeck effect. *Phys. Rev. B* **96,** 184427 (2017).

220. Shan, J. *et al.* Influence of yttrium iron garnet thickness and heater opacity on the nonlocal transport of electrically and thermally excited magnons. *Phys. Rev. B* **94,** 174437 (2016).

221. Thiery, N. *et al.* Electrical properties of epitaxial yttrium iron garnet ultrathin films at high temperatures. *Phys. Rev. B* **97,** 064422 (2018).

222. Sapozhnik A. A. and Abrudan, R. *et al.* Manipulation of antiferromagnetic domain distribution in Mn_2Au by ultrahigh magnetic fields and by strain. *Phys. Status Solidi RRL* **11,** 1600438 (2017).

223. Sapozhnik, A. *et al.* Direct imaging of antiferromagnetic domains in Mn_2Au manipulated by high magnetic fields. *Phys. Rev. B* **97,** 134429 (2018).

224. Upadhyaya, P. *et al.* Magnetic domain wall floating on a spin superfluid. *Phys. Rev. Lett.* **118,** 097201 (2017).

225. Thiery, N. *et al.* Nonlinear spin conductance of yttrium iron garnet thin films driven by large spin-orbit torque. *Phys. Rev. B* **97,** 060409 (2018).

226. Collet, M. *et al.* Generation of coherent spin-wave modes in yttrium iron garnet microdiscs by spin-orbit torque. *Nat. Commun.* **7,** 1–8 (2016).

227. Evelt, M. *et al.* High-efficiency control of spin-wave propagation in ultra-thin yttrium iron garnet by the spin-orbit torque. *App. Phys. Lett.* **108,** 172406 (2016).

228. Morin, F. Magnetic susceptibility of α-Fe_2O_3 and α-Fe_2O_3 with added titanium. *Phys. Rev.* **78,** 819 (1950).

229. Van der Woude, F. Mössbauer Effect in α-Fe_2O_3. *Phys. Status Solidi B* **17,** 417–432 (1966).

230. Liu, J. Morin transition in hematite doped with iridium ions. *J. Magn. Magn Mater.* **54–57,** 901–902 (1986).

231. Novakovic, L. *et al.* Physical properties of hematite near the high-temperature magnetic phase transition. *High Temp. High Press.* **19,** 437–442 (1987).

232. Pauling, L. & Hendricks, S. The crystal structures of hematite and corundum. *J. Am. Chem. Soc.* **47,** 781–790 (1925).

233. Blake, R. L. *et al.* Refinement of the hematite structure. *Am. Mineral.,* 123–129 (1966).

234. Artman, J. O. *et al.* Determination of the nuclear quadrupole moment of Fe^{57m} from α-Fe_2O_3 data. *Phys. Rev.* **173,** 337 (1968).

235. Raymond, M. & Hafner, S. Nuclear quadrupole moment of ^{57m}Fe from α-Fe_2O_3 data. *Phys. Rev. B* **1,** 979–981 (1970).

236. Coey, J. M. D. & Sawatzky, G. A. A study of hyperfine interactions in the system $(Fe_{1-x}Rh_x)_2O_3$ using the Mössbauer effect (Bonding parameters). *J Phys. C: Solid State Phys.* **4,** 2386–2407 (1971).

237. Momma, K. & Izumi, F. VESTA 3 for three-dimensional visualization of crystal, volumetric and morphology data. *J. Appl. Crystallogr.* **44,** 1272–1276 (2011).

238. Flanders, P. J. & Remeika, J. P. Magnetic properties of hematite single crystals. *Phil. Mag.: J. Theor. Exp. Appl. Phys.* **11,** 1271–1288 (1965).

239. Besser, P. J. *et al.* Magnetocrystalline anisotropy of pure and doped hematite. *Phys. Rev.* **153,** 632–640 (1967).

240. Samuelsen, E. & Shirane, G. *Phys. Status Solidi B* **42,** 241–256 (1970).

241. Morrison, B. *et al.* High-field antiferromagnetic resonance in α-Fe_2O_3. *Phys. Stat. Sol. B* **56** (1973).

242. Ozhogin, V. & Shapiro, V. “Premature” disappearance of antiferromagnetic resonances in Hematite. *Sov. Phys. - J. Exper. Theor. Phys.* **28,** 915 (1969). [Zh. Eksp. Teor. Fiz. **55**,1737 (1968)].

243. Searle C. W. and Dean, G. Temperature and field dependence of the weak ferromagnetic moment of hematite. *Phys. Rev. B* **1,** 4337–4342 (1970).

244. Néel, L. & Pauthenet, R. Etude thermomagnitique d’un monocristal de Fe_2O_3. *Compt. Rend. Acad. Sci. (Paris)* **234,** 2172 (1952).

245. Foner, S. & Shapira, Y. Magnetic phase transition in pure α-Fe_2O_3. *Phys. Lett. A* **29,** 276–277 (1969).

246. Honda, K. & Soné, T. *Sci. Rep.. Tohoku Imp. Univ. Ser. I* **3,** 223 (1914).

247. Charlesworth, G. & Long, F. A. *Proc. Leeds. Phil. Lit. Soc., Sci. Sect.* **3,** 315 (1939).

248. Artman, J. O. *et al.* Magnetic anisotropy in antiferromagnetic corundum-type sesquioxides. *Phys. Rev.* **138,** A912–A917 (1965).

249. Levinson, L. *et al.* Microscopic model for reorientation of the easy axis of magnetization. *Phys. Rev.* **187,** 715–722 (1969).

250. Yosida, K. On the antiferromagnetism of single crystals. *Prog. of Theor. Phys.* **6,** 691–701 (1951).

251. Tachiki, M. & Nagamiya, T. Origin of the magnetic anisotropy energy of antiferromagnetic Cr_2O_3. *J. Phys. Soc. Jpn.* **13,** 452–455 (1958).

252. Allen, J. W. & Young, C. Y. Magnetic anisotropy due to spin-orbit and dipole-dipole interactions in spin-density-wave antiferromagnets. *Phys. Rev. B* **16,** 1103–1108 (1977).

253. Wynn, C. *et al.* Magnetic dipole-dipole interactions and single-ion anisotropy: Revisiting a classical approach to magnets. *Chem. Mater.* **9,** 2156–2163 (1997).

254. Belov, K. P. *et al.* Spin-reorientation transitions in rare-earth magnets. *Sov. Phys. -Uspekhi* **19,** 574–596 (1976).

255. Fabritchnyi, P. B. *et al.* Etude par effet Mössbauer de la structure hyperfine nucleaire de ^{121}Sb dans α-Fe_2O_3. *Solid State Commun.* **12,** 1031–1033 (1973).

256. Lamykin, E. V. *et al.* Effect of small Sn addition on Morin transition temperature in hematite (α-Fe_2O_3). *Sov. Phys.-Solid State, USSR* **15,** 601–605 (1973).

257. Liu, J. & Fan, C. Morin transition in the system of (1-x)Fe_2O_3-xRu_2O_3. *Phys. Lett. A* **105,** 80–82 (1984).

258. Gallon, T. E. & Blackman, M. The remanent magnetization of haematite single crystals. *Proc. R. Soc. Lond. A. Math. and Phys. Sci.* **303,** 511–524 (1968).

259. Zhetbaev, A. K. & Donbaev, K. M. Study of neutron irradiation effect on Morin transition in hematite. *Hyperfine Interact.* **28,** 623–626 (1986).

260. Zhetbaev, A. K. *et al.* Spin Reorientation in Irradiated Hematite at 7 to 60 K. *Physica Status Solidi B* **157,** K55–K59 (1990).

261. Verbeeck, A. E. *et al.* The effect of the particle morphology on the Mössbauer effect in α-Fe_2O_3. *Hyperfine Interact.* **28,** 639–642. ISSN: 0304-3843 (1986).

262. Shimomura, N. *et al.* Morin transition temperature in (0001)-oriented α-Fe_2O_3 thin film and effect of Ir doping. *J. Appl. Phys.* **117** (2015).

263. Ellis, D. S. *et al.* Magnetic states at the surface of α-Fe_2O_3 thin films doped with Ti, Zn, or Sn. *Phys. Rev. B* **96,** 094426 (2017).

264. Besser, P. J. & Morrish, A. H. Spin flopping in synthetic hematite crystals. *Phys. Lett.* **13,** 289–290 (1964).

265. Kaneko, T. & Abe, S. Field-induced transitions in the hematite crystal. *J. Phys. Soc. Jpn.* **20,** 2001–2006 (1965).

266. Voskanyan, R. A. *et al.* Magnetostriction of a hematite monocrystal in fields up to 150 kOe. *Sov. Phys.-J Exp. Theor. Phys.* **27,** 423 (1968). [Zh. Eksp. Teor. Fiz. **54**, 790-795 (1968)].

267. Blum, N. *et al.* Mössbauer studies of spin flop in antiferromagnetic hematite. *J. Appl. Phys.* **36,** 1169–1170 (1965).

268. Kaczér, J. & Shalnikova, T. A. Anomalous temperature dependence of magnetization of hematite. *Phys. Status Solidi B* **6,** K77–K80 (1964).

269. Cinader, G. & Shtrikman, S. Antiferromagnetic to weak ferromagnetic transition and the temperature dependence of the transverse susceptibility in hematite below the Morin transition. *Solid State Commun.* **4,** 459–462 (1966).

270. Ozhogin, V. & Shapiro, V. New type of antiferromagnet resonance in α-Fe_2O_3. *J. Exp. Theor. Phys. Lett.* **6,** 7 (1967). [Zh. Eksp. Teor. Fiz. Pis'ma 6, No. 1, 467-471 (1967)].

271. Cinader, G. Effect of antisymmetric exchange interaction on the magnetization and resonance in antiferromagnets. *Phys. Rev.* **155,** 453–457 (1967).

272. Cinader, G. *et al.* Magnetization and Mössbauer studies of the field dependence of the Morin transition in hematite. *Phys. Rev.* **162,** 419–422 (1967).

273. Flanders, P. J. Spin axis rotation in hematite. *J. Appl. Phys.* **40,** 1247–1248 (1969).

274. Shapira, Y. Ultrasonic behavior near the spin-flop transitions of hematite. *Phys. Rev.* **184,** 589–600 (1969).

275. Jacobs, I. *et al.* Field induced magnetic phase transitions in antiferromagnetic hematite (α-Fe_2O_3). *Int. J. Mag.* **1,** 193–202 (1971).

276. Aieksandrov, K. S. *et al.* Anomalies of high-frequency magnetic permeability of hematite at the Morin phase transition. *J. Exp. Theor. Phys.* **65,** 591 (1987). [Zh. Eksp. Teor. Fiz **92** (3), 1042 (1987)].

277. Borovik-Romanov, A. S. Investigation of weak ferromagnetism in the $MnCO_3$ single crystal. *J. Exp. Theor. Phys.* **9,** 539–549 (1959). [Zh. Eksp. Teor. Fiz **36** (3), 766 (1959)].

278. Turov, E. A. On the theory of weak ferromagnetism. *Sov. Phys J. Exp. Theor. Phys.* **9,** 890–893 (1959). [Zh. Eksp. Teor. Fiz **36** (4), 1254 (1959)].

279. Kumagai, H. *et al.* Frequency dependence of magnetic resonance in α-Fe_2O_3. *Phys. Rev.* **99,** 1116–1118 (1955).

280. Yamamoto, N. The shift of the spin flip temperature of α-Fe_2O_3 fine particles. *J. Phys. Soc. Jpn* **24,** 23–28 (1968).

281. Kündig, W. *et al.* Some properties of supported small α-Fe_2O_3 particles determined with the Mössbauer effect. *Phys. Rev.* **142,** 327–333 (1966).

282. Pati, S. P. *et al.* Control of spin-reorientation transition in (0001) oriented α-Fe_2O_3 thin film by external magnetic field and temperature. *Phys. Status Solidi RRL* **11,** 1700101 (2017).

283. Grave, D. A. *et al.* Heteroepitaxial hematite photoanodes as a model system for solar water splitting. *J. Mat. Chem. A* **4,** 3052–3060 (2016).

284. *The SQUID handbook: Fundamentals and technology of SQUIDs and SQUID systems* (eds Clarke, J. & Braginski, A. I.) (Wiley-VCH Verlag GmbH & Co. KGaA, Weinheim, FRG, 2004).

285. Drung, D. High-T_c and low-T_c DC SQUID electronics. *Supercond. Sci. Technol.* **16,** 1320–1336 (2003).

286. QuantumDesign & Note, M. *Effects of Magnetic Field Uniformity on the Measurement of Superconducting Samples* (2000).

287. Als-Nielsen, J. & McMorrow, D. *Elements of modern X-ray physics* (Wiley, 2011).

288. *Handbook of sputtering technology (second edition)* (eds Wasa, K. *et al.*) (William Andrew Publishing, Oxford, 2012).

289. *Nanotechnology and nanoelectronics* (eds Fahrner, W. R. *et al.*) (Springer-Verlag, Berlin/Heidelberg, 2005).

290. Natarajan, S. *et al. A 14nm logic technology featuring 2nd-generation FinFET, air-gapped interconnects, self-aligned double patterning and a 0.0588 μm^2 SRAM cell size* in *2014 IEEE International Electron Devices Meeting* (IEEE, 2014), 3.7.1–3.7.3.

291. Vieu, C. *et al.* Electron beam lithography: resolution limits and applications. *Appl. Surf. Sci.* **164,** 111–117 (2000).

292. Stöhr, J. & Siegmann, H. C. *Magnetism: From fundamentals to nanoscale dynamics* (Springer Berlin Heidelberg, Berlin, Heidelberg, 2006).

293. Kosub, T. *et al.* Purely antiferromagnetic magnetoelectric random access memory. *Nat. Commun.* **8,** 13985 (2017).

294. Lebeugle, D. *et al.* Electric-field-induced spin flop in $BiFeO_3$ single crystals at room temperature. *Phys. Rev. Lett.* **100,** 227602 (2008).

295. Bodnar, S. Y. *et al.* Writing and reading antiferromagnetic Mn_2Au by Néel spin-orbit torques and large anisotropic magnetoresistance. *Nat. Commun.* **9,** 348 (2018).

296. Wadley, P. *et al.* Electrical switching of an antiferromagnet. *Science* **351,** 587–90 (2016).

297. Bodnar, S. Y. *et al.* Imaging of current induced Néel vector switching in antiferromagnetic Mn_2Au. *Phys. Rev. B* **99,** 140409 (2019).

298. Wang, H. *et al.* Antiferromagnetic anisotropy determination by spin Hall magnetoresistance. *J. Appl. Phys.* **122,** 083907 (2017).

299. Isasa, M. *et al.* Spin Hall magnetoresistance at $Pt/CoFe_2O_4$ interfaces and texture effects. *Appl. Phys. Lett.* **105,** 142402 (2014).

300. Kraushofer, F. *et al.* Atomic-scale structure of the hematite α-Fe_2O_3 $(1\bar{1}02)$ "R-Cut" surface. *J. Phys. Chem. C* **122,** 1657–1669 (2018).

301. Ji, Y. *et al.* Temperature dependence of spin Hall magnetoresistance in a Cr_2O_3 film with a TaOx buffer layer. *Jpn J. Appl. Phys.* **58,** 0609110 (2019).

302. Poulis, N. *et al.* Nuclear magnetic resonance and relaxation in zero field and near the threshold field. *Physica* **24,** 280–288 (1958).

303. Krinchik, G. S. & Zubov, V. E. Surface magnetism of hematite. *J. Exp. Theor. Phys.* **42,** 359 (1976). [Zh. Eksp. Teor. Fiz. **69**, 707 (1975)].

304. Vaidya, P. *et al.* Subterahertz spin pumping from an insulating antiferromagnet. *Science* **368,** 160–165 (2020).

305. Kay, A. *et al.* Heterogeneous doping to improve the performance of thin-film hematite photoanodes for solar water splitting. *ACS Energy Lett.* **1,** 827–833 (2016).

306. Chicot, D. *et al.* Mechanical properties of magnetite (Fe_3O_4), hematite (α-Fe_2O_3) and goethite (α-FeO·OH) by instrumented indentation and molecular dynamics analysis. *Mat. Chem. Phys.* **129,** 862–870 (2011).

307. Goya, G. *et al.* Thermal hysteresis of spin reorientation at Morin transition in alkoxide derived hematite nanoparticles. *Appl. Phys. A* **80,** 1523–1526 (2005).

308. Gomonay, E. V. & Loktev, V. M. Spintronics of antiferromagnetic systems (Review article). *Low Temp. Phys.* **40,** 17–35 (2014). [Fiz. Nizk. Temp. **40**, 22-47 (2014)].

309. Urquhart, H. M. A. & Goldman, J. E. Magnetostrictive effects in an antiferromagnetic hematite crystal. *Phys. Rev.* **101,** 1443–1450 (1956).

310. Levitin, R. *et al.* Magnetoelastic properties of hematite. *J. Exp. Theor. Phys.* **29,** 669–673 (1969). [Zh. Eksp. Teor. Fiz **56**, 1242 - 1251 (1969)].

311. Bezencenet, O. *et al.* Origin and tailoring of the antiferromagnetic domain structure in α-Fe_2O_3 thin films unraveled by statistical analysis of dichroic spectromicroscopy (X-ray photoemission electron microscopy) images. *Phys. Rev. Lett.* **106,** 107201 (2011).

312. Wu, H. *et al.* Hanle magnetoresistance: The role of edge spin accumulation and interfacial spin current. *Phys. Rev. B* **94,** 174407 (2016).

313. Vélez, S. *et al.* Hanle magnetoresistance in thin metal films with strong spin-orbit coupling. *Phys. Rev. Lett.* **116,** 016603 (2016).

314. Hanle, W. *Zeitschr. für Physik* **30,** 93 (1924).

315. Meaden, G. *Electrical resistance of metals* (Springer US, 1965).

316. Schlitz, R. *et al.* Evolution of the spin hall magnetoresistance in Cr_2O_3/Pt bilayers close to the Néel temperature. *App. Phys. Lett.* **112,** 132401 (2018).

317. Ji, Y. *et al.* Negative spin Hall magnetoresistance in antiferromagnetic Cr_2O_3/Ta bilayer at low temperature region. *App. Phys. Lett.* **112,** 232404 (2018).

318. Chen, Y. *et al.* Spin transport in an insulating ferrimagnetic - antiferromagnetic - ferrimagnetic trilayer as a function of temperature. *AIP Adv.* **9,** 105319 (2019).

319. Bode, M. *et al.* Atomic spin structure of antiferromagnetic domain walls. *Nat. Mater.* **5,** 477–481 (2006).

320. Roth, W. & Slack, G. Antiferromagnetic structure and domains in single crystal NiO. *J. Appl. Phys.* **31,** S352–S353 (1960).

321. Eaton, J. A. & Morrish, A. H. Magnetic domains in hematite at and above the Morin transition. *J. Appl. Phys.* **40,** 3180–3185 (1969).

322. Eaton, J. A. & Morrish, A. H. Magnetic domain structure of hematite. *Can. J. Phys.* **49,** 2768–2777 (1971).

323. Blackman, M. & Gustard, B. Domains in Hæmatite. *Nature* **193,** 360–361 (1962).

324. Bender, S. A. & Tserkovnyak, Y. Interfacial spin and heat transfer between metals and magnetic insulators. *Phys. Rev. B* **91,** 140402 (2015).

325. Rezende, S. *et al.* Magnon diffusion theory for the spin Seebeck effect in ferromagnetic and antiferromagnetic insulators. *J. Phys. D: Appl. Phys.* **51,** 174004 (2018).

326. Tatara, G. & Pauyac, C. O. Theory of spin transport through an antiferromagnetic insulator. *Phys. Rev. B* **99,** 180405 (2019).

327. Han, J. *et al.* Birefringence-like spin transport via linearly polarized antiferromagnetic magnons. *Nat. Nanotechn.* **15,** 563–568 (2020).

328. Velikov, L. V. & Rudashevskii, E. G. Antiferromagnetic resonance in hematite in the weakly ferromagnetic state. *Sov. Phys. J. Exp. Theor. Phys.* **29,** 836 (1969). [Zh. Eksp. Teor. Fiz. **56**, 1557-1564 (May, 1969)].

329. Wimmer, T. *et al.* Observation of Antiferromagnetic Magnon Pseudospin Dynamics and the Hanle Effect. *Phys. Rev. Lett.* **125,** 247204 (2020).

330. Shen, K. Pure spin current in antiferromagnetic insulators. *Phys. Rev. B* **100,** 094423 (2019).

331. Antipin, M. Y. *et al.* Electron density distribution in hematite α-Fe_2O_3 determined by precise X-Ray diffraction data. *Sov. Phys.-Dokl.* **30,** 257 (1985).

332. Vélez, S. *et al.* Competing effects at Pt/YIG interfaces: Spin Hall magnetoresistance, magnon excitations, and magnetic frustration. *Phys. Rev. B* **94,** 174405 (2016).

333. Cornelissen, L. J. & Van Wees, B. J. Magnetic field dependence of the magnon spin diffusion length in the magnetic insulator yttrium iron garnet. *Phys. Rev. B* **93,** 20403(R) (2016).

334. Ritzmann, U. *et al.* Magnetic field control of the spin Seebeck effect. *Phys. Rev. B* **92,** 174411 (2015).

335. Kikkawa, T. *et al.* Critical suppression of spin Seebeck effect by magnetic fields. *Phys. Rev. B* **92,** 64413 (2015).

336. Jungfleisch, M. *et al.* Thickness and power dependence of the spin-pumping effect in $Y_3Fe_5O_{12}$/Pt heterostructures measured by the inverse spin Hall effect. *Phys. Rev. B* **91,** 134407 (2015).

337. Kim, J.-V. & Stamps, R. Hysteresis from antiferromagnet domain-wall processes in exchange biased systems. *J. Mag. Mag. Mat.* **286.** Proceedings of the 5th International Symposium on Metallic Multilayers, 233–237 (2005).

338. Jourdan, M. *et al.* Epitaxial Mn_2Au thin films for antiferromagnetic spintronics. *J. Phys. D: Appl. Phys.* **48,** 385001 (2015).

339. Lan, J. *et al.* Antiferromagnetic domain wall as spin wave polarizer and retarder. *Nat. Commun.* **8,** 178 (2017).

340. Yu, W. *et al.* Polarization-selective spin wave driven domain-wall motion in antiferromagnets. *Phys. Rev. B* **98,** 144422 (2018).

341. Kim, S. *et al.* Propulsion of a domain wall in an antiferromagnet by magnons. *Phys. Rev. B* **90,** 104406 (2014).

342. Tveten, E. *et al.* Antiferromagnetic domain wall motion induced by spin waves. *Phys. Rev. Lett.* **112,** 147204 (2014).

343. Qaiumzadeh, A. *et al.* Controlling chiral domain walls in antiferromagnets using spin-wave helicity. *Phys. Rev. B* **97,** 020402 (2018).

344. Selzer, S. *et al.* Inertia-free thermally driven domain-wall motion in antiferromagnets. *Phys. Rev. Lett.* **117,** 107201 (2016).

345. Woo, S. *et al.* Magnetic domain wall depinning assisted by spin wave bursts. *Nat. Phys.* **13,** 448–454 (2017).

346. Shen, P. *et al. Driving a magnetized domain wall in an antiferromagnet by magnons* 2020.

347. Paul, D. I. Interaction of antiferromagnetic spin waves with a Bloch wall. *Phys. Rev.* **126,** 78–82 (1962).

348. Kosevich, A. M. *et al.* Magnetic solitons. *Phys. Rep.* **194,** 117–238 (1990).

349. Arai, K. *et al.* Three-dimensional spin orientation in antiferromagnetic domain walls of NiO studied by x-ray magnetic linear dichroism photoemission electron microscopy. *Phys. Rev. B* **85,** 104418 (2012).

350. Wadley, P. *et al.* Current polarity-dependent manipulation of antiferromagnetic domains. *Nat. Nanotechnol.* **13,** 362–365 (2018).

351. Sass, P. *et al.* Magnetic imaging of domain walls in the antiferromagnetic topological insulator $MnBi_2Te_4$. *Nano Lett.* **20,** 2609–2614 (2020).

352. Lin, W. & Chien, C. L. Electrical detection of spin backflow from an antiferromagnetic insulator/$Y_3Fe_5O_{12}$ interface. *Phys. Rev. Lett.* **118,** 067202 (2017).

353. Guo, E.-J. *et al.* Influence of thickness and interface on the low-temperature enhancement of the spin Seebeck effect in YIG films. *Phys. Rev. X* **6,** 031012 (2016).

354. Morin, F. Electrical properties of α-Fe_2O_3 and α-Fe_2O_3 containing titanium. *Phys. Rev.* **83,** 1005–1010 (1951).

355. Morin, F. Electrical Properties of α-Fe_2O_3. *Phys. Rev.* **93,** 1195 (1954).

356. Sulymenko, O. *et al.* Terahertz-frequency spin Hall auto-oscillator based on a canted antiferromagnet. *Phys. Rev. Appl.* **8,** 064007 (2017).

357. Lad, R. J. & Henrich, V. E. Structure of α-Fe_2O_3 single crystal surfaces following Ar+ ion bombardment and annealing in O_2. *Surf. Sci.* **193,** 81–93 (1988).

358. Guo, H. & Barnard, A. S. Surface structure and environment-dependent hydroxylation of the nonpolar hematite (100) from density functional theory modeling. *J. Phys. Chem. C* **115,** 23023–23029 (2011).

A

Appendix

A.1 List of Contributors

This section will detail the contributions of the author and co-workers from Mainz and collaborating researchers to the results presented in this thesis.

A.1.1 Extraction of magnetic anisotropies in bulk hematite

i. Angular and field dependent measurements, magnetometry measurements by the author, supported by R. Lebrun (JGU Mainz at the time).

ii. Data evaluation by the author, supported by R. Lebrun (JGU Mainz at the time), O. Gomonay (JGU) and S. Bender (Utrecht University at the time).

iii. Analytical calculations performed by O. Gomonay (JGU Mainz) with S. Bender (Utrecht University at the time) and A. Qaiumzadeh (Norwegian University of Science and Technology; QuSpin).

iv. Own Contributions: See above, fabrication of measurement devices.

A.1.2 Extraction of magnetic anisotropies in thin film hematite

i. Growth of thin films by A. Kay (Technion University at the time) and D. Grave (Technion University at the time).

ii. Structural and magnetic characterisation of films by the author supported by S. Becker (JGU Mainz).

iii. Numerical calculations of the longitudinal spin Hall magnetoresistance by C. Ulloa (Utrecht University at the time).

iv. Magnetic imaging of hematite films by R. Lebrun (JGU Mainz at the time), L. Baldrati (JGU Mainz) and F. Kronast (Helmhotz Zentrum Berlin).

v. Analysis of magnetic imaging by L. Baldrati (JGU Mainz) and S. Valentina (Helmholtz Zentrum Berlin).

vi. Own contributions: See above, device fabrication, field dependent electrical measurements, angular dependent measurements, data analysis.

A.1.3 Non-local detection of magnon currents in bulk antiferromagnets

i. Electrical measurements performed by the author with support from R. Lebrun (JGU at the time), L. Baldrati (JGU) and J. Cramer (JGU at the time).

ii. Data evaluation performed by the author with support from R. Lebrun (JGU at the time) and S. Bender (Utrecht University at the time).

iii. Numerical calculations performed by S. Bender (Utrecht University at the time) with support from A. Qaiumzadeh (Norwegian University of Science and Technology; QuSpin).

iv. Own contributions: See above, device fabrication.

A.1.4 Non-local detection of magnon currents in thin film hematite

i. Growth of thin films by A. Kay (Technion University at the time) and D. Grave (Technion University at the time).

ii. Structural and magnetic characterisation of films by the author supported by S. Becker (JGU Mainz).

iii. Analytical model of magnon scattering at domain walls developed by O.Gomonay (JGU Mainz) with C. Ulloa (Utrecht University at the time) and A. Qaiumzadeh (Norwegian University of Science and Technology; QuSpin) and input from the author.

iv. Magnetic imaging of hematite films by R. Lebrun (JGU Mainz at the time), L. Baldrati (JGU Mainz) and F. Kronast (Helmhotz Zentrum Berlin).

v. Analysis of magnetic imaging by the author, supported by L. Baldrati (JGU Mainz).

vi. Electrical measurements and evaluation of data performed by the author with support from R. Lebrun (JGU at the time).

vii. Own contributions: See above, device fabrication, temperature dependent measurements.

A.2 Direct Current vs Alternating Current for Non-local Measurements

Although a DC excitation was used for the measurements in this thesis, one can also make use of an alternating current. If the excitation used is an alternating current, then the current takes the form $I = I_0 \sin\omega t$, where I_0 is the average current modulated at a frequency ω and t is the time. The non-local voltage measured due to the electrically excited magnon current is then modulated at the same frequency ω. The thermal signal

meanwhile is proportional to $\sin^2 \omega t \propto \cos 2\omega t$ and can thus be detected via the second harmonic, i.e. at a frequency of 2ω.

When separating the thermal and electrical signals, one can also consider the individual contributions from the excitation and detection mechanisms as well as the dependence on the input current. This will arise through modulation of the electrically detected signal. Only the component of $\boldsymbol{\mu}_s$ that is collinear with $\boldsymbol{m}$ (or $\boldsymbol{n}$ in the case of AFMs) contributes to the magnon creation/detection. If an external magnetic field is used to manipulate the orientation of $\boldsymbol{m}$ ($\boldsymbol{n}$) relative to $\boldsymbol{\mu}_s$, a dependence of the recorded signal on the angle α between $\boldsymbol{m}$ ($\boldsymbol{n}$) and $\boldsymbol{\mu}_s$ is anticipated. As both the creation and detection of the magnon spin current will contribute a $\cos\alpha$ ($\sin\alpha$) term to the recorded voltage, the signal is expected to be modulated as $\cos^2\alpha$ ($\sin^2\alpha$) in the case of the electrically generated magnons. For the thermally excited magnons however, they only pick up a $\cos\alpha$ ($\sin\alpha$) dependence from the detection mechanism. There are thus two ways to identify the origin of the recorded signal: (i) the angular dependence of the signal with magnetic field and (ii) the dependence on current. Both AC and DC measurements will show the same dependence on current amplitude and angle between the applied field, current and magnetic order.

The reason that the current reversal method is employed in the work of this thesis is that when an AC excitation is used, a large capacitative and inductive coupling can appear between the non-local wires due to their geometric proximity and the insulating nature of the magnetic material under investigation. Such an AC excitation was used briefly during this thesis and the parasitic coupling, which appeared $90°$ out of phase, was ignored. However, the rate of device breakage was abnormal even when the system was well grounded, with large discharges damaging neighbouring devices. With the current reversal method, the rate of breakage was heavily reduced, with devices damaged only in the case of faulty grounding or applied current densities close to the upper threshold. Many groups have had success with AC excitations, obtaining the same results as when DC measurements are performed, validating the approached used here.

A.3 Recipes for electron beam lithography

In this part of the appendix, details of the sample fabrication will be provided, performed by the author.

A.3.1 Sample Cleaning

i. Immerse sample in acetone for 60 s

ii. Immerse sample in isopropyl alcohol for 60 s

iii. Immerse sample in deionised, distilled water for 60 s

iv. Dry sample with nitrogen gas

v. Place sample on hot plate ($T > 120^\circ$) for water desorption for 60 s

vi. Allow to cool for 60 s

The sample may also be placed in an ultrasonic bath whilst immersed in solvent in the case additional cleaning is required.

A.3.2 Resist Spin-coating

For the lift-off structures in this work, the positive resist polymethyl methacrylate (PMMA) 950K was used along with the developer methyl isobutyl ketone (MIBK) diluted with iso-2-propanol (IPA) in a ratio of 1:3. The steps for spin-coating PMMA are given below, resulting in a thickness of $\approx 200\,\text{nm}$ After spin-coating, the sample is left

Step	Time	Speed	Acceleration
Prespin	2 s	500 rpm	500 rpm/s
Main	60 s	4000 rpm	4000 rpm/s

for 5 minutes before a 90 s *soft-bake* on a hot plate at 180 °C and a second pause in the process of 5 minutes. Many of the substrates used in this thesis were insulating so a second step was required to avoid charging during the lithography. This was achieved with a conductive resist, ARPC 5090, which is removed by H_2O. After spin-coating, the

Step	Time	Speed	Acceleration
Main	60 s	3000 rpm	3000 rpm/s

sample was left for 2 minutes before being soft-baked for 2 minutes at 90 °C.

A.3.3 Lithographic Process

For the lithography, acceleration voltages between $10\,\text{kV}$ and $30\,\text{kV}$ were used along with electron beam apertures between $10\,\mu\text{m}$ and $120\,\mu\text{m}$. The dose required to expose the resist is heavily dependent on the acceleration voltage used as well as consideration of the additional exposure caused by proximity effects between separated structures. In order to give an idea of some used parameters, the non-local wires for one series of samples were defined using an aperture of $10\,\mu\text{m}$, an acceleration voltage of $30\,\text{kV}$ and dosages up to $350\,\mu\text{C}/\text{cm}^2$. For the contact pads, these parameters change to $120\,\mu\text{m}$, $10\,\text{kV}$ and $110\,\mu\text{C}/\text{cm}^2$ respectively.

Following the lithographic process, the samples were developed by first immersing in deionised water to remove the conductive resist for 30 s and dried with nitrogen gas. The sample was then held on a glass slide as MIBK:IPA was dripped continuously across the surface using a pipette for 45 s. The development was stopped by immersion in pure IPA for 30 s, then deionised water for 30 s and dried with nitrogen gas. The development was checked by an optical microscope and, if needed, additional development in steps of 10 s was made.

The deposition of material was achieved by sputtering (c.f. Sec. 4.2.3) before the unwanted material was removed by lift-off. This process entails placing the sample post-deposition into a beaker of the solvent AR 300.70 and placed on a hot plate at 50 °C for at least 2 hours. Using a pipette, the warm solvent was moved across the sample surface until the unwanted material was removed. The sample was then transferred to acetone to remove trace amounts of the AR 300.70 before rinsing in IPA and deionised water for 30 s each. The lift-off was then assessed by optical microscope and later by electron microscope for small structures.

A.4 Sputtering Parameters

Following the definition of structures for non-local and local measurements by EBL, the heavy metal Pt and the contact pads (Cr/Au or Ti/Au) were deposited by magnetron sputtering. The base pressure of the used chamber was approximately 3x10^{-9} mbar. The growth parameters of Pt and Ti were evaluated by others, whilst the author evaluated the growth conditions of Cr and Au.

Material	Gas	Pressure (mbar)	Power	Distance	Growth Rate
Pt	Ar	1x10^{-2}	15 mA/278 V	10 cm	0.79 Ås^{-1}
Cr	Ar	2.6x10^{-2}	15 mA/200 V	10 cm	0.33 Ås^{-1}
Ti	Ar	2.0x10^{-2}	25 mA/215 V	10 cm	0.24 Ås^{-1}
Au	Ar	2.0x10^{-2}	15 mA/288 V	10 cm	1.92 Ås^{-1}

A.5 Spin Mixing Conductance of Thin Film Hematite

Making use of the formulation of Chen *et. al.* [129] (c.f. Sec. 3.1.2), the effective spin mixing conductance $G^{\uparrow\downarrow}$ can be calculated for the two antiferromagnetic phases. The effective spin mixing conductance is defined as,

$$\frac{\Delta\rho}{\rho} = \theta_{SH}^2 \frac{\lambda}{d_N} \frac{2\lambda G_r \tanh^2 \frac{d_N}{2\lambda}}{\sigma + 2\lambda G_r \coth \frac{d_N}{\lambda}}, \tag{A.1}$$

where $\Delta\rho/\rho$ is the SMR response for a system with a resistivity ρ, θ_{SH}, λ and σ are respectively the spin Hall angle, spin diffusion length and conductivity of the Pt. Both θ_{SH} and λ were extracted for the Pt deposited here in Ref. [r11] at room temperature, and assumed to be temperature independent. G_r is the real part of $G^{\uparrow\downarrow}$ and can be calculated for $\boldsymbol{H}\|\boldsymbol{x}$ in order to compare this system with other, similar systems as a function of temperature. The temperature dependence of the effective spin mixing conductance is shown in Fig. A.1 alongside ΔR_{xx} for $\boldsymbol{H}\|\boldsymbol{x}$ for comparison. As can be seen from this

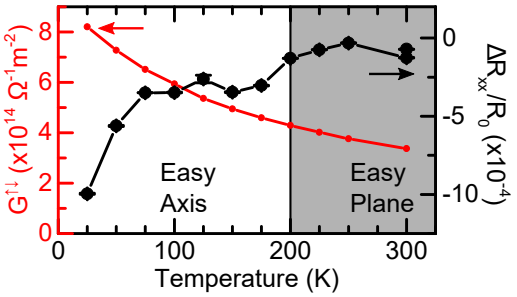

Figure A.1: Temperature dependence of the effective spin mixing conductance calculated according to Eqn. A.1 for a magnetic field applied parallel to the charge current ($\boldsymbol{H}\|\boldsymbol{x}$) for (0001) orientated α-Fe_2O_3 thin films. The right axis compares with the longitudinal SMR response ΔR_{xx} for the same configuration. The shaded region indicates the easy-plane phase above the Morin transition temperature. Figure from Ref. [r14]. Copyright American Physical Society.

figure, the increase in the absolute value of ΔR_{xx} at low temperatures leads to a similar increase in $G^{\uparrow\downarrow}$, however, whether this truly represents an increase in the effective spin mixing conductance or is just an artefact from the assumptions made in the calculation is not clear and more dedicated investigations centred around the properties of the Pt are required [131, 132, 146]. Nevertheless, $G^{\uparrow\downarrow}$ has an effective value of 3.37x10^{14} Ω m^{-1} at 300 K in the easy-plane phase and 4.60x10^{14} Ω m^{-1} below the Morin transition temperature, increasing up to 8.02x10^{14} Ω m^{-1} at 25 K. Although ΔR_{xx} shows a small change across the Morin transition which may be attributed to the change in antiferromagnetic symmetry, the effective spin mixing conductances are similar between both phases and consistent with other antiferromagnetic systems [r1, 15, 17]. This means that measurements of both the spin Hall magnetoresistance and spin transport across the Morin transition will not be significantly impacted by the spin mixing conductance and thus changes can be attributed to the antiferromagnetic material rather than the interface.

A.6 Characterisation of (1$\bar{1}$02) Orientated Hematite Thin Films

This section will focus on the structural and magnetic characterisation of 500 nm thick hematite films from on (1$\bar{1}$02) orientated Al_2O_3 sapphire substrates grown by pulsed laser deposition. These films were used for spin Hall magnetoresistance measurements in Sec. A.7 as a comparison to (0001) plane films where a finite angle between the surface normal and the crystallographic c-axis existed. Non-local measurements in these films are also shown in Sec. 7.2 Just as for the (0001) orientated films in Sec. 5.2.1, the films will take on the orientation of the Al_2O_3 substrate due to the shared corundum structure. These films were grown in collaboration with the group of Prof. Avner Rothschild from Technion University in Haifa, Israel.

The structure was assessed by making use of X-ray diffraction (XRD, c.f. Sec. 4.2.2). Starting with the out-of-plane axis, the r-axis, the resulting 2θ - ω scan across both the (1$\bar{1}$02) and (2$\bar{2}$04) peaks is shown in Fig. A.2a, where the film and substrate peaks are labelled appropriately. The (1$\bar{1}$02) peak can be fit by a Gaussian with the parameters given in Tab. A.1. Unlike the (0001) orientated films (Fig. 5.16 and Tab. 5.2), the Gaussian fit here represents the experimental data far better, with an R^2 of 0.995. Nevertheless, even though such a thick films should be completely relaxed, the out-of-plane axis of the film is not parallel to that of the substrate. This is supported by fixing the value of 2θ at the angle of the (1$\bar{1}$02) peak and performing a rocking curve, the results of which are shown in Fig. A.2b along with a Gaussian fit in red. The parameters for this fit can also be found in Tab. A.1. The peak value for ω occurs at (11.994$\pm$0.001)°, whilst Fig. A.2a indicates that ω should be 12.12° for a parallel alignment of the two axis.

Measurement	Peak Angle (°)	FWHM (°)
2θ - ω	24.241$\pm$0.002	0.0970$\pm$0.001
Rocking Curve	11.994$\pm$0.001	0.250$\pm$0.001

Table A.1: Gaussian fit parameters for XRD measurements on (1$\bar{1}$02) orientated hematite thin films.

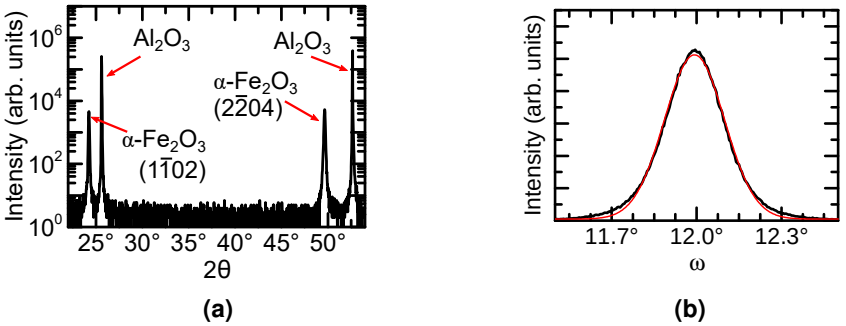

Figure A.2: a) 2θ - ω measurement of (1$\bar{1}$02) orientated hematite grown on likewise oriented sapphire. b) Rocking curve of the hematite (1$\bar{1}$02) peak with a Gaussian fit with an R^2 of 0.997. The fit parameters of interest are shown in Tab. A.1. Adapted with permission from Ref. [r15]. Copyright 2020 American Chemical Society.

The axes of interest with regard to the magnetic ordering are the c-axis along [0001] and the a-axis along [11$\bar{2}$0]. By tilting the stage that the sample is mounted to, these two axes can be investigated. However, the total intensity will be a lot lower. This method was then used to investigate both the c-axis (Fig. A.3a) and a-axis (Fig. A.3b) of the film. For both axes, the substrate and film peaks are labelled. Both peaks are visible, indicating that the film indeed displays a hexagonal crystal structure.

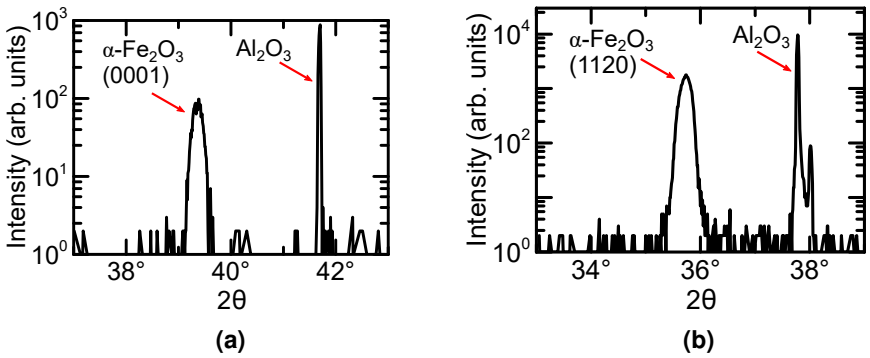

Figure A.3: XRD measurements of (1$\bar{1}$02) plane hematite films by introducing a component of the incident X-ray momentum within the sample plane. a) 2θ - ω measurement across the (0001) peak to investigate the c-axis. b) 2θ - ω measurement across the (11$\bar{2}$0) peak to investigate the a-axis.

With regard to experimental transport measurements Ch. 7 and Sec. A.7, it is crucial to understand where the c-axis of the film lies relative to the substrate as precisely as possible, given that it is the substrate edges to which transport devices and the magnetic field will be aligned. Although the XRD measurements presented already show that aligning to the substrate c-axis also shows the film peak, it doesn't tell much about the actually alignment of the two, i.e. whether the c-axis is tilted in a different plane to that which the XRD is sensitive. One can investigate the relative alignments of the two axes in three dimensional space be making a so-called reciprocal space map (RSM). The resulting RSM around the substrate c-axis is shown in Fig. A.4a. This maps the intensity around a given (hkl) coordinate of the substrate, measured by keeping h constant[1].

[1]Cubic coordinates and hexagonal coordinates are related via (hkl) = $(hk(-h-k)l)$. Although the c-axis is frequently stated in this thesis in hexagonal coordinates as (0006), in cubic coordinates this is

From Fig. A.4a, the substrate peak can be clearly seen from the narrow, high intensity band parallel to $l = 6$ and centred around $k = 0$. The high intensity point below the substrate can easily be attributed to the α-Fe_2O_3 film. From this map, we can see that the c-axis of the film is parallel to the c-axis of the substrate and centred around $k = 0$. The peak is slightly broader than the substrate and at a lower l value due to the lower thickness and different lattice constant respectively. This measurement allows us to conclude that if we apply a magnetic field parallel (perpendicular) to the substrate c-axis, this will also be parallel (perpendicular) to the film c-axis.

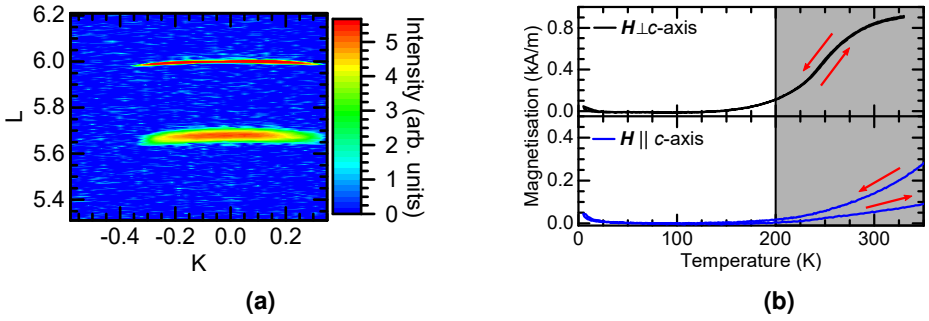

Figure A.4: a) Reciprocal space map (RSM) of the c-axis of a $(1\bar{1}02)$ orientated, 500 nm thick hematite film showing the parallel alignment of the film and substrate c-axes. Reprinted with permission from Ref. [r15]. Copyright 2020 American Chemical Society. b) SQUID measurements of $(1\bar{1}02)$ orientated hematite for a field applied perpendicular (black) and parallel (blue) to the in-plane projection of the c-axis. Figure adapted from Ref. [r14]. Copyright American Physical Society.

With the crystallographic c-axis of the film known, we can also investigate the magnetic properties of these films with SQUID magnetometry. Fig. A.4b shows the magnetisation as a function of temperature for a magnetic field applied perpendicular (top, black) or parallel (bottom, blue) to the c-axis. The measurement protocol for both is similar; upon heating to the start temperature, a large magnetic field of 5 T was applied along the respective direction. The magnetisation was then measured as the temperature was cooled at a rate of $2\,\mathrm{K\,min^{-1}}$ under a probing field of 75 mT for $\boldsymbol{H} \| c$ and 50 mT for $\boldsymbol{H} \perp c$. Upon reaching 4 K, the temperature was then warmed back to the start temperature whilst the magnetisation was again measured. The different probing fields is due to the magnetic field required to produce a significant moment at the starting temperature[2]. After measuring the curves, a temperature independent background is subtracted to account for the diamagnetic substrate.

Focussing first on $\boldsymbol{H} \perp c$ (top panel of Fig. A.4b), the magnetisation has a maximum at the start temperature. As the temperature is reduced, this magnetisation begins to decreases, indicating the Morin transition occurring in this film and the net canted moment reducing. The high temperature, easy-plane phase is indicated by the grey shading. When the temperature is then warmed back up, there is no presence of a thermal hysteresis as there was in the (0001) films (see Fig. 5.17a). Meanwhile, for $\boldsymbol{H} \| c$ (bottom panel of Fig. A.4b), the magnetic field is perpendicular to the canted moment $\boldsymbol{m}$, so the

(006).

[2]The substrate contributes a diamagnetic (negative) response to the applied field and the film contributes a positive response with field. For some value of the applied field, these two contributions will cancel one another.

recorded signal is correspondingly lower, representing the field induced magnetisation. As T is reduced, the measured magnetisation reduces, falling close to zero at the same temperature as before. When warming, the value of the magnetisation fails to recover the initial value. This reduction in the magnetisation at higher temperatures comes from the initial condition of applying 5 T introducing an small but finite additional moment that is not recovered when warming back through T_M in a small field. From these measurements, the Morin transition is clearly present in these films, with a value of $T_M \sim 200$ K. Below this temperature, a pure easy-axis phase exists. Even though these films are 500 nm thick, and should approximate bulk hematite in their magnetic properties, the Morin transition temperature is reduced from the bulk value as well as taking place over 50 K. This change from the bulk behaviour is likely due to distortions in the unit cell. Although the c-axis of the film and substrate are parallel, the r-axes are not, indicating distortion elsewhere in these films, even for such a large thickness.

A.7 Probing the Magnetic Anisotropies of $(1\bar{1}02)$ Orientated Hematite Thin Films

The discussion in Sec. 5.2.3 demonstrated that the inclined nature of the film c-axis with respect to the substrate led to additional SMR signals in the easy-axis phase of (0001) orientated films of hematite. In this section of the appendix, magnetoresistance measurements of 500 nm thick, $(1\bar{1}02)$ orientated thin films (i.e. r-plane, see Fig. A.5) of α-Fe_2O_3 grown on similarly orientated AlOx substrates by PLD will be shown. These films were grown through collaboration with the group of Prof. Avner Rothschild by Dr. D. Grave and Mr A. Kay. The characterisation of these films can be found in Appendix Sec.

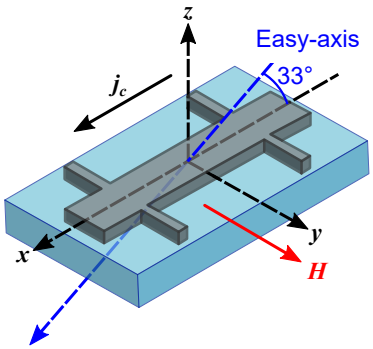

Figure A.5: Measurement geometry of a Pt Hall bar atop $(1\bar{1}02)$ orientated hematite films. A charge current $\boldsymbol{j}_c$ is passed parallel to the in-plane projection of the easy-axis and a magnetic field is applied perpendicular to $\boldsymbol{j}_c$

A.6, but a summary will be briefly discussed. Starting with the crystallographic structure of these films, investigation of the out-of-plane axis, the r-axis, finds that there is also a small deviation of this axis from the substrate axis, just as for the (0001) orientated films shown in Fig. 5.16. However, a reciprocal space map (RSM) shows that the film and substrate c-axes are parallel. Given that the axis of interest is the magnetic c-axis for temperatures both above and below the Morin transition temperature, the deviation of the out-of-plane axis can be disregarded. The Morin transition temperature can be investigated similar to Fig. 5.17 in these films, resulting in a value of $T_M \sim 200$ K (Fig. A.6a-b). Despite the fact that these films are thicker than those in Sec. 5.2.1, the Morin transition still occurs at a lower temperature than a bulk crystal and takes place over a large temperature range, rather than the sharp transition of a bulk crystal (Fig. 5.3). This

is likely due to the distortion of the crystal structure visible along the film r-axis (Fig. A.2) altering the magnetic anisotropies responsible for the Morin transition.

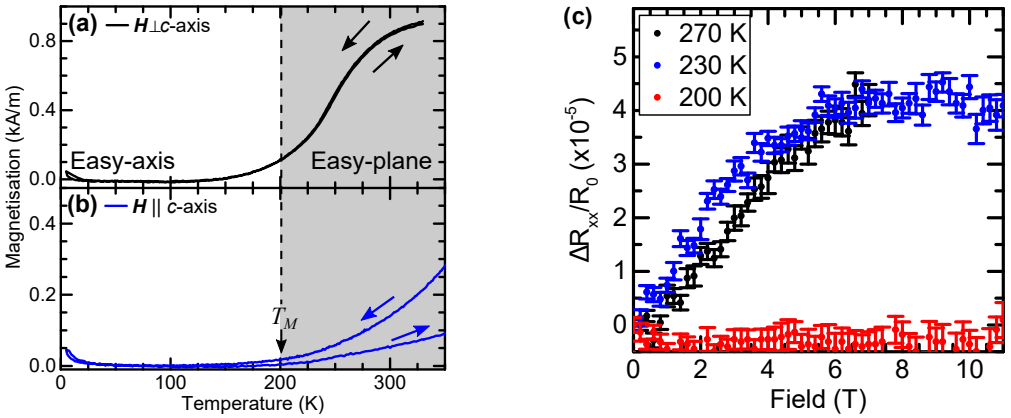

Figure A.6: Magnetometry measurements for 500 nm $(1\bar{1}02)$ orientated hematite thin films for a magnetic field applied a) within the basal plane and b) perpendicular to the basal plane for a probing field of 50 mT. The Morin transition is visible from a drop in the measured magnetisation and can be ascribed as $T_M = 200$ K. b) Longitudinal spin Hall magnetoresistance ΔR_{xx} for $(1\bar{1}02)$ orientated hematite and a Hall bar patterned parallel to the in-plane projection of the easy-axis at temperatures just below T_M (red), within the transition (blue) and above the transition (black). A magnetic field is applied perpendicular to the easy-axis. ΔR_{xx} is defined as the change in resistance from the zero-field resistance R_0. Figures adapted from Ref. [r14]. Copyright American Physical Society.

The magnetic imaging of similar films shown in Ch. 7, Fig. 7.13 demonstrated that these films have large domains separated by broad 180° domain walls below the Morin transition temperature. The large regions of contrast indicate that the Néel vector is parallel within large regions of the films, unlike in the (0001) films where a large distribution of the orientation of $\boldsymbol{n}$ was observed (Fig. 5.28). Based on the explanation of the signal given in Sec. 5.2.3 for $\boldsymbol{H} \| \boldsymbol{y}$, the magnetic domain structure of these $(1\bar{1}02)$ films would indicate that a similar signal should not be visible below the Morin transition temperature. To demonstrate this, Pt Hall bars were defined by EBL (Sec. 4.2.4) such that a charge current $\boldsymbol{j}_c$ is parallel to the in-plane projection of the magnetic easy-axis, termed the geometric $\boldsymbol{x}$ direction. The interfacial spin accumulation $\boldsymbol{\mu}_s$ is then parallel to the geometric $\boldsymbol{y}$ direction. The longitudinal SMR response ΔR_{xx} is then investigated as a function of the applied magnetic field perpendicular to $\boldsymbol{j}_c$ ($\boldsymbol{H} \| \boldsymbol{y}$) for temperatures above and below T_M. The reorientation of $\boldsymbol{n}$ expected for $T < T_M$ should then lead to no discernible signal as $\boldsymbol{n}$ will remain in the plane perpendicular to $\boldsymbol{H}$, leading to no variation in $\boldsymbol{n} \cdot \boldsymbol{\mu}_s$. This is represented by the measurements performed on bulk α-Fe_2O_3 of the same orientation (Sec. 5.1.4, Fig. 5.7) The variation of ΔR_{xx} for temperatures above and below T_M is shown in Fig. A.6b. Just below T_M (red points), there is no noticeable evidence of a rotation of $\boldsymbol{n}$ for any magnetic fields investigated here, even though the proximity to the Morin transition temperature should allow for a rotation of $\boldsymbol{n}$ at low magnetic fields. Meanwhile, for temperatures within the Morin transition (230 K, blue points) or above the Morin temperatures (280 K, black points), there is evidence of the reorientation of $\boldsymbol{n}$ occurring within the easy-plane from the change of the signal. These films can also be probed for $\boldsymbol{H}$ parallel to the easy-axis to try and discern the effective uniaxial anisotropy field H_{an}^{eff} below T_M, however, as demonstrated in Ch. 7, Sec. 7.2.1, the spin flop was not visible in magnon transport measurements below T_M. Although an

increase was seen, the subsequent decrease of the magnon transport above the spin flop was not observed placing a lower limit on the spin flop field $H_c^{\parallel}$ of 12 T (the maximum field available). This then places a lower limit on H_{an}^{eff} of 105 mT, more than three times larger than found in (0001) orientated films or bulk hematite (Ch. 5).

Something to note is that the absolute magnitude of the SMR in these films is one order of magnitude lower than the (0001) orientated films (Fig. 5.19 and 5.26). However, it is unclear whether this is related to the crystal orientation [299], which may be one possible origin of the differences seen bulk α-Fe_2O_3, or from effects related to the Pt itself, given that the devices on the two film orientations were deposited at different times to each other. Future studies could focus on the SMR in different crystal orientations to determine how the magnitude of the SMR varies.

A.8 Details of Hematite Orientations Investigated in This Thesis

In the course of this thesis, two principle orientations of hematite (α-Fe_2O_3) have been investigated, $(1\bar{1}02)$ (r-plane; bulk and thin film) and (0001) (c-plane; thin film) orientated hematite. This section of the appendix will detail the measurements performed in this thesis in a compact form to help provide a concise overview of which electrical measurements can be used to probe which magnetostatic or magnetotransport property. Considering the magnetic symmetry of hematite (c.f. Sec. 4.1), the two key orientations one would want to investigate would place the c-axis either in-plane or out-of-plane. This would mean that, above the Morin transition temperature, the easy-plane is perpendicular or parallel to the surface plane, respectively. Conversely, the easy-axis (EA) below the Morin transition temperature lies in-plane or out-of-plane, respectively. A large projection of the c-axis in-plane also offers the additional benefit of performing electronic measurements parallel or perpendicular to the c-axis. Ideally, one would make use of a-plane hematite in order to have the c-axis lie perfectly within the sample plane, however, this crystal orientation proved challenging to structure making use of electron beam lithography. The surface appears to be hydro-phobic and the photoresist suffered adhesion problems. Even with the introduction of an adhesion promoter, the photoresist coverage was poor. Finally, in the case of thin films with this orientation, there was no visible Morin transition in magnetometry measurements. For these reasons, the r-plane was chosen given the large in-plane projection of the c-axis, the chemically stable surface (see Sec. A.9) and furthermore, the finite angle between the surface plane and the c-axis helps to break the degeneracy of the easy-plane above the Morin transition temperature or the spin flop under an applied magnetic field. The downside is that, whilst the magnon dispersion for the $k = 0$ modes in hematite are known for a magnetic field parallel and perpendicular to the c-axis across the full temperature range, the magnon dispersion under a magnetic field at a finite angle to the easy-axis has not been investigated or calculated. Although within this thesis, the assumption of a magnetic field applied parallel to the in-plane component of the EA leads to a magnon dispersion similar to that of the field parallel to the easy-axis itself, this is an over-simplification.

A.8.1 Spin Hall Magnetoresistance Measurements

Tab. A.2 gives an overview of the electrical measurements performed on differently orientated hematite during the course of this thesis. Meanwhile, Tab. A.3 details which

Number	Crystal Orientation	Current Orientation	Field Orientation	Section
1.1	(1$\bar{1}$02) *bulk*	$\boldsymbol{j}_c \| EA$	$\boldsymbol{H} \| EA$	Sec. 5.1.3 ($T < T_M$)
1.2	(1$\bar{1}$02) *bulk*	$\boldsymbol{j}_c \| EA$	$\boldsymbol{H} \perp EA$	Sec. 5.1.3 ($T < T_M$)
2.1	(1$\bar{1}$02) *bulk*	$\boldsymbol{j}_c \perp EA$	$\boldsymbol{H} \| EA$	Sec. 5.1.4 ($T < T_M$)
2.2	(1$\bar{1}$02) *bulk*	$\boldsymbol{j}_c \perp EA$	$\boldsymbol{H} \perp EA$	Sec. 5.1.4 ($T < T_M$)
3	(1$\bar{1}$02) *bulk*	$\boldsymbol{j}_c \perp EA$	Plane $\perp \boldsymbol{j}_c$	Sec. 5.1.5 ($T < T_M$)
4	(1$\bar{1}$02) *bulk*	$\boldsymbol{j}_c \| / \perp EA$	Angular Dependence	Sec. 5.1.6 ($T > T_M$)
5	(1$\bar{1}$02) *thin film*	$\boldsymbol{j}_c \| EA$	$\boldsymbol{H} \perp EA$	Sec. A.7
6	(0001) *thin film*	$\boldsymbol{j}_c \perp HA$	$\boldsymbol{H} \perp HA$	Sec. 5.2.2.1 ($T > T_M$)
7	(0001) *thin film*	$\boldsymbol{j}_c \perp HA$	$\boldsymbol{H} \| HA$	Sec. 5.2.2.2 ($T > T_M$)
8	(0001) *thin film*	$\boldsymbol{j}_c \perp EA$	$\boldsymbol{H} \| EA$	Sec. 5.2.3.1 ($T < T_M$)
9	(0001) *thin film*	$\boldsymbol{j}_c \perp EA$	$\boldsymbol{H} \perp EA$	Sec. 5.2.3.2 ($T < T_M$)
10	(0001) *thin film*	$\boldsymbol{j}_c \perp EA$	$\boldsymbol{H} \| / \perp EA$	Sec. 5.2.3.5 (Temperature Dependence)

Table A.2: Table giving an overview of spin Hall magnetoresistance measurements in differently orientated hematite with respect to the current $\boldsymbol{j}_c$ and field $\boldsymbol{H}$ directions. (EA: Easy-axis, HA: Hard axis).

measurements provide information on certain magnetostatic properties for each sample. In order to access the strength of the effective uniaxial anisotropy H_{an}^{eff} directed along the [0001] direction, the c-axis, measurements with $\boldsymbol{H} \| EA$ are performed for $T < T_M$ in order to detect the spin flop of the Néel vector through spin Hall magnetoresistance measurements (see Tab. A.3). Meanwhile, the strength of the effective Dzyaloshinskii-

Moriya field can be resolved from investigations of the spin reorientation that occurs for $\boldsymbol{H} \perp EA$ and $T < T_M$ (see Tab. A.3). Finally, the effective anisotropy in the plane perpendicular to the c-axis $H_{an}^{\perp}$ can be resolved by measuring above T_M with a magnetic field perpendicular to the c-axis, which is now the hard-axis. Alternatively, by measuring for a field parallel to the easy-axis below T_M, information on the effective pinning field H_{ME} maintaining the spin flop state can be calculated. In (0001) orientated hematite, the orientation of $\boldsymbol{j}_c$ should not have a significant impact on the extraction of the magnetic anisotropies, however for (1$\bar{1}$02) orientated hematite, the choice of current direction relative to the anisotropy axis has a profound impact on the detected signal, however this should impact the extraction of the anisotropy field strengths providing the reorientation of the Néel vector is visible. For example, the spin-flop was not easily resolvable in

Crystal Orientation	Property	Measurement (from Tab. A.2)
(1$\bar{1}$02) *bulk*	H_{an}^{eff}	1.1, 2.1
(1$\bar{1}$02) *bulk*	H_D	1.2, 2.2, 3
(1$\bar{1}$02) *bulk*	$H_{an}^{\perp}$	4
(0001) *thin film*	H_{an}^{eff}	8, 10
(0001) *thin film*	H_D	9, 10
(0001) *thin film*	H_{ME}	8
(0001) *thin film*	$H_{an}^{\perp}$	7

Table A.3: Table indicating which measurements from Tab. A.2 can be used to investigate the magnetic anisotropies of hematite. H_{an}^{eff}: Effective anisotropy field acting along the c-axis, H_D: Effective field created due to the antisymmetric Dzyaloshinskii-Moriya interaction, $H_{an}^{\perp}$: Effective anisotropy field in the basal plane. This anisotropy can arise from the intrinsic crystalline anisotropy or from other effective fields such as the effective pinning potential created by defects. H_{ME}: Effective field stabilising the spin flop state due to pinning.

(1$\bar{1}$02) thin films for $\boldsymbol{H} \| EA$ due to the much larger effective uniaxial anisotropy placing the spin-flop field at the limits of the experimental setup utilised, even in close proximity to the Morin transition temperature. There are also measurements listed in Tab. A.2 that do not provide detailed information on the antiferromagnetic anisotropies and other properties, help to form a more complete picture of the system response, confirming the applicability of the measurements listed in Tab. A.3.

Future investigations could probe ways to reduce the magnetic anisotropy in thin films of hematite, which would facilitate lower magnetic fields required for spin flopping making use of spin Hall magnetoresistance to detect these events. There is also the possibility to dope thin films in order to alter the magnetic anisotropies and the equilibrium orientation of the Néel vector.

A.8.2 Magnon Transport Measurements

Tab. A.4 gives an overview of the magnon transport measurements in this thesis.

Number	Crystal Orientation	Current Orientation	Field Orientation	Section
1.1	(1$\bar{1}$02) *bulk*	$\boldsymbol{j}_c \| EA$ (R_{el})	$\boldsymbol{H} \| EA$	Sec. 6.2
1.2	(1$\bar{1}$02) *bulk*	$\boldsymbol{j}_c \| EA$ (R_{th})	$\boldsymbol{H} \| EA$	Sec. 6.2.1
2.1	(1$\bar{1}$02) *bulk*	$\boldsymbol{j}_c \| EA$ (R_{el})	$\boldsymbol{H} \perp EA$	Sec. 6.2
2.2	(1$\bar{1}$02) *bulk*	$\boldsymbol{j}_c \| EA$ (R_{th})	$\boldsymbol{H} \perp EA$	Sec. 6.2.1
3	(1$\bar{1}$02) *bulk*	$\boldsymbol{j}_c \| EA$	Angular Dependence	Sec. 6.2.2
4.1	(1$\bar{1}$02) *bulk*	$\boldsymbol{j}_c \perp EA$ (R_{el})	$\boldsymbol{H} \| EA$	Sec. 6.4
4.2	(1$\bar{1}$02) *bulk*	$\boldsymbol{j}_c \perp EA$ (R_{th})	$\boldsymbol{H} \| EA$	Sec. 6.4.1
5.1	(1$\bar{1}$02) *bulk*	$\boldsymbol{j}_c \perp EA$ (R_{el})	$\boldsymbol{H} \perp EA$	Sec. 6.4
5.2	(1$\bar{1}$02) *bulk*	$\boldsymbol{j}_c \perp EA$ (R_{th})	$\boldsymbol{H} \perp EA$	Sec. 6.4.1
6	(1$\bar{1}$02) *bulk*	$\boldsymbol{j}_c \| EA$ (R_{el})	$\boldsymbol{H} \| EA$	Sec. 7.4.3 (Temperature Dependence)
7	(1$\bar{1}$02) *thin film*	$\boldsymbol{j}_c \| EA$	$\boldsymbol{H} \| / \perp EA$	Sec. 7.2.1
8	(1$\bar{1}$02) *thin film*	$\boldsymbol{j}_c \perp EA$	$\boldsymbol{H} \| / \perp EA$	Sec. 7.2.2
9	(1$\bar{1}$02) *thin film*	$\boldsymbol{j}_c \perp EA$ (R_{el})	Angular Dependence	Sec. 7.2.3
10.1	(0001) *thin film*	$\boldsymbol{j}_c \perp EA$ (R_{el})	$\boldsymbol{H} \| EA$	Sec. 7.1.1
10.2	(0001) *thin film*	$\boldsymbol{j}_c \perp EA$ (R_{el})	$\boldsymbol{H} \perp EA$	Sec. 7.1.4
10.3	(0001) *thin film*	$\boldsymbol{j}_c \perp EA$ (R_{el})	Angular Dependence	Sec. 7.1.5
11	(0001) *thin film*	$\boldsymbol{j}_c \perp EA$ (R_{th})	$\boldsymbol{H} \| / \perp EA$	Sec. 7.1.6
12.1	(0001) *thin film*	$\boldsymbol{j}_c \perp EA$ (R_{el})	$\boldsymbol{H} \| / \perp EA$	Sec. 7.4.1 (Temperature Dependence $T < T_M$)
12.2	(0001) *thin film*	$\boldsymbol{j}_c \perp EA$ (R_{el})	$\boldsymbol{H} \| / \perp EA$	Sec. 7.4.2 (Temperature Dependence $T > T_M$)

Table A.4: Table giving an overview of magnon transport measurements in differently orientated hematite with respect to the current $\boldsymbol{j}_c$ and field $\boldsymbol{H}$ directions.

In ($1\bar{1}02$) orientated hematite, two geometries were investigated with the charge current parallel and perpendicular to the in-plane projection of the easy-axis, for the magnetic field also parallel or perpendicular to the in-plane projection of the easy-axis. This enables investigations of the transport of both electrically and thermally generated magnons as well as resolving the roles of the field induced magnetisation and Néel vector (see Tab. A.5). In thin films, the (0001) orientation allows for investigations of the magnon transport in the presence of a domain structure. By applying the magnetic field parallel to the easy-axis below T_M, a multi-domain state can be formed, whilst $\boldsymbol{H} \perp EA$ reduces the degeneracy of the resulting domain structure (see Tab. A.5). Such a feature would not be evident in bulk hematite of the same orientation as a field parallel to the easy-axis would result in domains that are far larger that the transport distances being involved and the impact of the multi-domain state would not be evident. Tab. A.4 also

Crystal Orientation	Property	Measurement (from Tab. A.4)
($1\bar{1}02$) *bulk*	R_{el}	1.1, 2.1, 4.1, 5.1, 6
($1\bar{1}02$) *bulk*	R_{th}	1.2, 2.2, 4.2, 5.2
($1\bar{1}02$) *thin film*	R_{el}/R_{th}	7, 8, 9
(0001) *thin film*	R_{el} (multi-domain)	10.1, 12.1, 12.2
(0001) *thin film*	R_{el} (mono-domain)	10.2, 12.1, 12.2
(0001) *thin film*	R_{th}	11

Table A.5: Table indicating which measurements from Tab. A.4 can be used to investigate the spin transport properties of hematite. R_{el}: Non-local resistance for electrically generated and detected magnons. R_{th}: Non-local thermal signal for thermally excited and electrically detected magnons.

lists other measurements, such as angular dependence, which do not provide as much information on the transport properties as some other. However, such measurements are important in terms of establishing the underlying symmetries of the transport mechanisms and how they evolve.

Other possibilities include altering the magnetic anisotropies of hematite films through dilute doping although this can suppress the Morin transition or increase the conductivity of the films making magnon transport more difficult to investigate. The suppression of the Morin transition may not be as critical as initially thought, with several very recent works demonstrating magnon transport in the easy-plane phase of hematite [r13, 327, 329]. There is also the possibility of tuning the antiferromagnetic domain structure through growth conditions and investigating the thickness dependence of the magnon transport in thin films of hematite.

A.9 Chemical Stability of Differently Orientated Hematite

This thesis has made use of two principle orientations of hematite, the (0001) or c-plane and the $(1\bar{1}02)$ or r-plane. These are by no means the only possible terminations of hematite, however, some orientations are not chemically stable under certain conditions. Both (0001) and $(10\bar{1}2)$ oriented hematite can restructure so that the surface is Fe_3O_4 when anneal in a low oxygen atmosphere following Ar-ion-bombardment induced disordering. This can be returned to a pure hematite surface by prolonged annealing at high temperatures in an O_2 atmosphere [357]. However, annealing too hot or in a low oxygen pressure can lead to the formation of $Fe_{1-x}O$ phases or layers of Fe at the surface [357]. Meanwhile the nonpolar $(1\bar{1}02)$ surface is stable, even when annealing in low oxygen pressure conditions. The ideal surface can be reduced from 1×1 to 2×1 for the first few layers, by annealing in an ultra high vacuum although it easily returns to the 1×1 termination under the introduction of oxygen [300]. (1000) orientated hematite has been theoretically discussed to be chemically stable and non-polar, however no experimental investigations have yet occurred to determine this [358]. This orientation would be particularly interesting if it indeed were stable under ambient conditions as it places the c-axis parallel to the surface. Regarding the stability of other orientations of hematite, there is limited available literature as most studies focus either on the natural faces of hematite, or those that are easier to prepare on, for example, conductive substrates.

Acknowledgements

Aus Datenschutzgründen entfernt / Removed due to data privacy

Curriculum Vitae

Aus Datenschutzgründen entfernt / Removed due to data privacy

Eidesstattliche Erklärung

Hiermit erkläre ich an Eides statt, dass ich meine Dissertation selbständig und ohne fremde Hilfe verfasst habe. Ich habe nur Quellen und Hilfsmittel verwendet, die von mir in der Bibliographie angegeben sind. Die Doktorarbeit ist weder abschnittsweise, noch in der vorliegender Form bei einer anderen Prüfungsbehörde zur Erlangung eines Doktorgrades eingereicht worden.

I declare under penalty of perjury, that I wrote this dissertation independently, without assistance and use of sources other than those indicated my bibliography. The thesis, in whole or in part, has never been submitted to any other examination committee that is able to admit a doctoral degree.

Mainz, den

Andrew Ross